# COMPUTATIONAL AND EXPERIMENTAL STUDIES OF THE PHOTOLUMINESCENCE, REACTIVITY AND STRUCTURAL PROPERTIES OF D10 AND D8 METAL COMPLEXES

Brooke Michelle Otten, B. Sc.

Dissertation Prepared for the Degree of

DOCTOR OF PHILOSOPHY

UNIVERSITY OF NORTH TEXAS

May 2019

APPROVED:

Thomas R. Cundari, Major Professor
Andrès Cisneros, Committee Member
Rebecca Weber, Committee Member
Bradley Smucker, Committee Member
Legrande Slaughter, Committee Member and
Chair of the Department of Chemistry
Su Gao, Dean of the College of Science
Victor Prybutok, Dean of the Toulouse
Graduate School

Otten, Brooke Michelle. *Computational and Experimental Studies of the Photoluminescence, Reactivity and Structural Properties of D10 and D8 Metal Complexes*. Doctor of Philosophy (Chemistry), May 2019, 150 pp., 25 tables, 62 figures, chapter references.

Computational chemistry has gained interest as a characterization tool to predict photoluminescence, reactivity and structural properties of organic and transition metal complexes. With the rise of methods including relativity, these studies have been expanded to the accurate modeling of luminescence spectra of complexes with considerable spin-orbit splitting due to heavy metal centers as well as the reaction pathways for these complexes to produce natural products such as hydrogen gas. These advances have led to the synthesis and utility of more effective catalysis as well as the development of more effective organic light emitting diodes (OLEDs) through the incorporation of organometallic complexes as emitters instead of typical organic emitters.

In terms of significant scientific advancement presented in this work is in relation to the discovery of significant spin-orbit splitting in a gold(I) alkylphosphine complex, where the splitting results in the states that emit in different colors of the visible region of the electromagnetic spectrum. This work also reveals the discovery both computationally and experimentally, of a genuine polar-covalent bond between two-closed shell metals. This work highlights a complex with an incredibly short gold(I) – copper(I) intermetallic distance leading to a vibrational frequency and dissociation energy that is on par with those of other systems with single-bonded metal centers. Lastly, this work outlines a strategy for the production of hydrogen gas through the use of trinuclear cyclic coinage metal complexes as catalysis to split hydrohalic acids.

ACKNOWLEDGMENTS

A special thanks goes out to the Department of Chemistry at UNT for all their support towards reaching this end. An extra special thanks goes out to Prof. Mohammad A. Omary (MO) for all his support and understanding. There are not enough kind words in the universe to express my gratitude. I would also like to take the time to thank my fellow TeamOmary members, without who the journey would have been a killer. I also want to thank Prof. Thomas R. Cundari for allowing me to start my research career as a sophomore in my undergrad – for what I learned from him and the TeamCundari members. I want to especially thank Erin Benton, Lauren Harris, Kortney Melancon and Megan Ericson for many girls' nights. I also want to thank my friends in the department outside of TeamOmary, Matt Ellison, Riffat Parveen, and my best friends, Dorie Mishael and Angelica Bigsby. A special thank you goes out to Dr. Dave Hrovat and Prof. Paul S. Bagus for all their helpful comments and discussions to uncover science through the years and more importantly, data that made sense. I want to thank my committee members for all their insight, suggestions and questions that have made my work stronger. Finally I would like to thank all my friends and family. I want to thank all my parents for all their support and continuing to brag about me to everyone, even though science is not their forte. I also want to thank my wife, Liz, for all her support and understanding through the years. Without her, I wouldn't remember to eat or drink anything so it's really thanks to her I'm alive. I want to thank my fathers-in-law for the many dinners and general distractions that made me remember I am allowed to have a life outside of work. And last but not least, I'd like to thank my tiny son, Odin and my fat daughter, Faye. When the going gets tough, pets don't abandon or judge you if you're sobbing.

TABLE OF CONTENTS

Page

ACKNOWLEDGMENTS ..... iii

LIST OF TABLES ..... vii

LIST OF FIGURES ..... ix

CHAPTER 1. INTRODUCTION AND MOTIVATIONS ..... 1

1.1 Overview of Dissertation ..... 1

1.2 Spin-Orbit Splitting in Gold (I) Alkylphosphine Complexes ..... 2

1.3 21st Century Alchemy: Cupriphication of Gold to Sensitize $d^{10}$-$d^{10}$ Metal-Metal Bonds and Near Phosphorescent Quantum Yields ..... 4

1.4 Oxidative Addition of Haloacids and Dihalogens to Trinuclear Cyclic Coinage Metal Complexes and the Photoinduced Reductive Elimination of $X_2$ and $H_2$ ..... 7

1.5 Luminescent, Redox-Active (Dithiolato)bis(imine) Divergent Complexes with Exchangeable Imine Ligands: An Experimental/Computational Study Versus Their (Diimine)(Dithiolato)Platinum(II) Convergent Congeners ..... 10

1.6 References ..... 11

CHAPTER 2. SPIN-ORBIT SPLITTING IN GOLD(I) ALKYLPHOSPHINE COMPLEXES ..... 16

2.1 Introduction ..... 16

2.2 Methods ..... 17

2.2.1 Experimental Methods ..... 17

2.2.2 Syntheses ..... 18

2.2.3 Computational Methods ..... 18

2.3 Results and Discussion ..... 20

2.3.1 Excited State Distortion and Bonding ..... 25

2.3.2 Electronic Spectroscopy – Time-Dependent DFT ..... 28

2.3.3 Experimental Results ..... 32

2.4 Conclusions ..... 35

2.5 References ..... 36

CHAPTER 3. 21ST CENTURY ALCHEMY: CUPRIPHICATION OF GOLD TO SENSITIZE $D^{10}$-$D^{10}$ METAL-METAL BONDS AND NEAR-UNITY PHOSPHORESCENCE QUANTUM YIELD ..... 39

3.1 Introduction ..... 39
3.2 Results and Discussion ..... 41
3.2.1 Synthetic Chemistry ..... 41
3.2.2 Crystal Structures ..... 42
3.2.3 Covalent $d^{10}$-$d^{10}$ Metal-Metal Bonding ..... 45
3.3 Conclusions and Prospects ..... 75
3.4 Materials and Methods ..... 76
3.4.1 Representing Synthesis Procedure of Heterobimetallic $Au_4Cu_2$ complex, **4a** ..... 76
3.5 Acknowledgements ..... 77
3.6 References ..... 77

CHAPTER 4. OXIDATIVE ADDITION OF HALOACIDS AND DIHALOGENS TO TRINUCLEAR CYCLIC COINAGE METAL COMPLEXES AND PHOTOINDUCED REDUCTIVE ELIMINATION OF $X_2$ AND $H_2$ . 82
4.1 Introduction ..... 82
4.2 Methods ..... 83
4.3 Results and Discussion ..... 87
4.4 Conclusions ..... 103
4.5 References ..... 104

CHAPTER 5. LUMINESCENT, REDOX-ACTIVE (DITHIOLATO)BIS(IMINE)PLATINUM(II) DIVERGENT COMPLEXES WITH EXCHANGEABLE IMINE LIGANDS: AN EXPERIMENTAL/COMPUTATIONAL STUDY VS THEIR (DIIMINE)(DITHIOLATO)PLATINUM(II) CONVERGENT CONGENERS ..... 107
5.1 Introduction ..... 107
5.2 Materials and Methods ..... 109
5.2.1 Syntheses ..... 109
5.2.2 X-Ray Crystallography ..... 112
5.2.3 Computational Studies ..... 113
5.3 Results and Discussion ..... 114
5.3.1 Synthetic Studies ..... 114
5.3.2 $^1$H NMR Spectroscopy ..... 115

5.3.3 Structural Studies ..... 116

5.3.4 Electrochemical and Photophysical Results ..... 120

5.4 Commentary on Divergent vs Convergent Pt(II)-Diimine Complexes ..... 129

5.5 Conclusions ..... 132

5.6 Acknowledgements ..... 133

5.7 References ..... 133

CHAPTER 6. CONCLUSIONS AND FUTURE WORK ..... 139

6.1 Spin-Orbit Splitting in Gold(I) Alkylphosphine Complexes ..... 139

6.1.1 Conclusions ..... 139

6.1.2 Future Work ..... 139

6.2 21st Century Alchemy: Cupriphication of Gold to Sensitize $d^{10}$-$d^{10}$ Metal-Metal Bonds and Near-Unity Phosphorescence Quantum Yields ..... 142

6.2.1 Conclusions ..... 142

6.2.2 Future Work ..... 143

6.3 Oxidative Addition of Haloacids and Dihalogens to Trinuclear Cyclic Coinage Metal Complexes and Photoinduced Reductive Elimination of $X_2$ and $H_2$ ..... 144

6.3.1 Conclusions ..... 144

6.3.2 Future Work ..... 145

6.4 Luminescent, Redox-Active (Dithiolato)Bis(Imine)Platinum(II) Divergent Complexes With Exchangeable Imine Ligands: An Experimental/Computational Study Versus Their (Diimine)(Dithiolato)Platinum(II) Convergent Congeners ... 146

6.4.1 Conclusions ..... 147

6.4.2 Future Work ..... 147

6.5 References ..... 148

LIST OF TABLES

Page

Table 2.1: Comparison of selected calculated geometric parameters for the ground state of $AuTPA_3$/$AuTPA_3X$ versus $Au(PH_3)_3$/$Au(PH_3)_3X$. ..... 21

Table 2.2: Comparison of selected calculated geometric parameters for the excited state of $AuTPA_3$/$AuTPA_3X$ versus $Au(PH_3)_3$/$Au(PH_3)_3X$. ..... 23

Table 2.3: Summary of Au-X bond length, vibrational frequency and dissociation energy for the ground and excited state. ..... 27

Table 3.1: Crystallographic Data and Refinement Parameters for 1, 3a, and 4a. ..... 44

Table 3.2: Selected Bond Lengths (Å), Intramolecular Contacts (Å) and Angles (°) for 1, 3a, and 4a ..... 48

Table 3.3: Morse potential fitting (MPF) and Dunham analysis (DA) of selected vibrational frequencies in the full $\{[Au_2Im`_2CuPz`)]\}_2$ hexanuclear dimer-of-trimer (DOT) model upon selected vertical vibrations in its two-component monomer-of-trimer (MOT) units. ..... 60

Table 3.4: Summary of photophysical parameters for homometallic and heterobimetallic complexes in this study.[a] ..... 69

Table 4.1: Bond angles between the donor atoms and the metal centers in $[M(\mu\text{-}C,N\text{-}L)]_3$ complexes. ..... 87

Table 4.2: Bond angles between the donor atoms and the metal centers in $[M(\mu\text{-}N,N\text{-}L)]_3$ complexes. ..... 87

Table 4.3: Halogen-metal-donor atom angles of $[M(\mu\text{-}C,N\text{-}Im)]_3$ oxidized complexes. ..... 88

Table 4.4: Comparison of energetics (ΔG) of the oxidative addition of $X_2$ to the ML trimers reported in kcal/mol. ..... 96

Table 4.5: Comparison of energetics (ΔG) of successive oxidative addition reactions of dihalogen substrates to the trimers reported in kcal/mol. ..... 97

Table 4.6: Comparison of oxidative addition energy (ΔG) of symmetric dihalogen substrates versus the hydrohalic acid for the MPz trimers reported in kcal/mol. ..... 98

Table 4.7: Comparison of energetics (ΔG) of successive oxidative addition reactions of the hydrohalic acid substrates to the trimers reported in kcal/mol. ..... 99

Table 4.8: Reductive elimination energies (ΔG) of the product of two successive oxidative addition steps for the hydrohalic acid substrates to produce $H_2$, $X_2$, and the original Au trimer reported in kcal/mol. ..... 100

Table 4.9: Calculated λmax for the oxidative addition products of Au trimers with HF, HCl, HBr, and HI. ..... 102

Table 5.1: Crystallographic Data for compounds 1 and $3•C_3H_6O•2H_2O$. ..... 113

Table 5.2: Select bond lengths, angles, and torsion angles for [Pt(pyz)$_2$(mnt)], 1, and [Pt(4-ap)$_2$(mnt)], 3. ..... 117

Table 5.3: Selected calculated bond lengths, angles and torsion angles for [Pt(4,4`-bpy)$_2$(mnt)], 2. ..... 119

Table 5.4: Redox potentials for compounds 1-3 at a scan rate of 0.1 V/s. ..... 122

Table 5.5: Comparison of experimental and calculated reduction/ oxidation potentials for 1, 2, 3, and [Pt(2,2'-bpy)(mnt)] ..... 122

Table 5.6: Summary of lifetime data for frozen glassy solutions of 1 ($10^{-3}$ M), 2 ($10^{-4}$ M), and 3 ($10^{-3}$ M) in acetone ..... 126

Table 5.7: Summary of lifetime data for solid samples of 1, 2, and 3 at 77K. ..... 127

Table 5.8: Comparison of calculated emission energies from the $T_1$ and $T_2$ states and excitation energy from $S_0 \rightarrow T_1$. ..... 128

Table 5.9: Select bond lengths, angles and torsion angles for [Pt(2,2'-bpy)(mnt)] ..... 129

LIST OF FIGURES

Page

Figure 2.1: Ground state structures of $AuTPA_3$/$AuTPA_3X$ versus $Au(PH_3)_3$/$Au(PH_3)_3X$ along with deviations from linearity and the Au-X bond length. ..... 21

Figure 2.2: Excited state structures of $AuTPA_3$/$AuTPA_3X$ versus $Au(PH_3)_3$/$Au(PH_3)_3X$ along with deviations from linearity and the Au-X bond length. ..... 23

Figure 2.3: Splitting of the 5d orbitals in the ground state ($D_{3h}$ geometry) (left) and the excited state ($C_{2v}$ geometry) (right). ..... 24

Figure 2.4: Excited state distortion for complexes $[AuTPA_3]^+$ (left), $[AuTPA_3]Cl$ (middle), and $[AuTPA_3]I$ (right) with diabatic excitation and emission energies and angle measurements. ..... 26

Figure 2.5: Migration of the halide counterion in the excited state for $[AuTPA_3]Cl$ (left) and $[AuTPA_3]I$ (right). ..... 27

Figure 2.6: Comparison of calculated absorption spectra with the inclusion of scalar and spin-orbit relativity for the cationic $[Au(PH_3)_3]^+$ complex at the geometry of the $[AuTPA_3]^+$ complex before (left) and after (right) normalization. ..... 28

Figure 2.7: Molecular orbital contours of the HOMO and LUMO of the singlet ground state of $[Au(PH_3)_3]^+$ (left) and SOMOs (right) of the lowest triplet state of $[Au(PH_3)_3]^+$ plotted using an isovalue of 0.03. ..... 29

Figure 2.8: Schematic of the transitions calculated when using the triplet geometry as an electronic singlet. ..... 30

Figure 2.9: Comparison of calculated emission spectra with the inclusion of scalar (blue) and spin-orbit (red) relativity for the cationic $[Au(PH_3)_3]^+$ complex at the geometry of the $[AuTPA_3]^+$ complex before (left) and after (right) normalization. ..... 31

Figure 2.10: Comparison of excitation (left) and emission spectra (right) for the experimental system $[AuTPA_3]Cl$ (blue) vs the theoretical model $[Au(PH_3)_3]^+$ (orange). ..... 32

Figure 2.11: Photoluminescence emission spectrum of $[AuTPA_3]Cl$ at 4 K. ..... 33

Figure 2.12: Photoluminescence emission spectrum of $[AuTPA_3]I$ at 4 K. ..... 33

Figure 2.13: Experimental splitting of the triplet state of Au(I) and the $[AuL_3]X$ complexes demonstrating the increased splitting seen for the iodide complex versus the chloride complex. ..... 35

Figure 3.1: Synthesis and solid-state luminescence of homometallic complexes, heterobimetallic and stacking product complexes ..... 40

Figure 3.2: Shows the steady state photoluminescence for a solid sample of $\{[Au(BzIm)]_3[Cu((CF_3)_2Pz)]_3\}$ at 77 K ..... 42

Figure 3.3: ORTEP plot for a) Crystal structure for one molecule of complex 1, b) Dimer-of-trimer formation found in the stacking of 1, and c) Fragment of crystal packing of 1 along the b axis. ..... 43

Figure 3.4: ORTEP plot for a) Crystal structure for one molecule of complex 3a, The box underneath it contains the intramolecular M-M distances, b) Dimer-of-trimer formation found in the stacking of 3a. c) Crystal packing of complex 3a along the c axis. ..... 43

Figure 3.5: ORTEP plot for a) Crystal structure for half the molecule, representing each monomer-of-trimer unit, of compound 4a. b) Crystal structure for one full molecule of compound 4a, c) A fragment of the crystal packing along the *a*-axis, and d) Extended crystal packing of 4a molecules along the *a*-axis. ..... 43

Figure 3.6: Infrared spectrum of neat solid powder of 4a in the far-IR region ..... 55

Figure 3.7: Potential energy surface plot upon varying only the vertical intertrimer separation in the optimized structure of a full {[Au2(μ-C2,N3-EtIm)2Cu(μ-3,5-(CF3)2Pz)]}2 hexanuclear dimer-of-trimer model of 4a ..... 56

Figure 3.8: Dispersive DFT (M06/CEP-31G(d)) optimized structure of 4a..... 58

Figure 3.9: Orbital mixing models that postulate Cu(I)···Au(I) polar-covalent metallophilic bonding formulism in an isolated $[CuAu]^{2+}$ diatomic unit ..... 64

Figure 3.10: Orbital mixing models that postulate Cu(I)-Au(I) polar-covalent bonding formulism of the Pz`Cu-AuIm` interaction in a) [Pz`Cu-AuIm`$\{_2$ tetranuclear cluster and b) the full $\{[Au_2Im`_2CuPz`]\}_2$ hexanuclear dimer-of-trimer (DOT), comprising two $[AuIm`_2CuPz`]$ monomer-of-trimer (MOT) units where Im`= μ-$C^2$,$N^3$-EtIm and Pz`= μ-3,5-$(CF_3)_2$Pz. ..... 65

Figure 3.11: Kohn-Sham contours of frontier molecular orbitals with significant electron density on metal atoms in a $[Cu_2Pz`_2Au_2Im`_2]$ tetranuclear model, where Im` = μ-$C^2$,$N^3$-EtIm and Pz` = μ-3,5-$(CF_3)_2$Pz ..... 66

Figure 3.12: Kohn-Sham contours of frontier molecular orbitals with significant electron density on metal atoms in the full $\{[Au_2Im'_2CuPz')]\}_2$ hexanuclear dimer-of-trimer model, where Im' = μ-$C^2$,$N^3$-EtIm and Pz' = μ-3,5-$(CF_3)_2$Pz..... 66

Figure 3.13: Kohn-Sham contours of all occupied frontier molecular orbitals (from the HOMO down to HOMO-37) plus the lowest unoccupied molecular orbital (LUMO) in a $[Cu_2Pz'_2Au_2Im'_2]$

tetranuclear cluster model, where Im' = μ-$C^2$,$N^3$-EtIm and Pz' = μ-3,5-$(CF_3)_2$Pz. Orbital energies are taken from DFT computations at the crystallographic geometry of 4a ..... 67

Figure 3.14: Kohn-Sham contours of occupied all frontier molecular orbitals (from the HOMO down to HOMO-43) plus the lowest unoccupied molecular orbital (LUMO) in the full $\{[Au_2Im'_2CuPz')]\}_2$ hexanuclear dimer-of-trimer model, where Im' = μ-$C^2$,$N^3$-EtIm and Pz' = μ-3,5-$(CF_3)_2$Pz. ..... 68

Figure 3.15: Steady-state photoluminescence spectra for a crystalline powder sample of 4a (i and ii), 3a (iii and iv), and 1 (v and vi) at 298 K (left) and 77 K (right). ..... 70

Figure 3.16: The comparison of normalized-emission spectra used for the absolute quantum yield ..... 71

Figure 3.17: Absorption spectra of $10^{-5}$ M dichloromethane solution of starting materials and heterobimetallic complexes. ..... 71

Figure 3.18: Photoluminescence spectra for a solid powder sample of $[Au(MeIm)Cu_2((CF_3)_2Pz)_2]$, 3b, at 298 K (top) and 77 K (bottom) ..... 72

Figure 3.19: A comparison of the steady state photoluminescence data (excitation spectra, emission spectra, and lifetimes) at room temperature vs 77 K for a solid sample of 4a ..... 72

Figure 3.20: Demonstration of the processability into OLED functional thin-film forms and the indifference of the photoluminescence spectra thereof vs powder forms for 3a (a) and $[Cu(\mu\text{-}3,5\text{-}(CF_3)_2Pz)]_3$ (b). ..... 73

Figure 4.1: Structures of products of successive oxidative addition of $Br_2/I_2$ to $[Au(CH_3OC{=}NCH_3)]_3$. ..... 83

Figure 4.2: $[Au(\mu\text{-}L)]_3$ structures where L = carbeniate (Cb) (top left), imidazolate (Im) (top middle), pyrazolate (Pz) (top right), triazolate (Tz) (bottom left) or tetrazolate (Ttz) (bottom right). ..... 84

Figure 4.3: Comparison of the change in enthalpy (x-axis) versus the change in the Gibbs free energy (y-axis) for the reaction of a trimer plus $X_2$ to produce [trimer$X_2$] ..... 86

Figure 4.4: Change in the geometry at the metal centers of [Au(μ-C,N-Im)] upon two successive oxidative additions. ..... 89

Figure 4.5: Mapping of the electrostatic potential of AuPz, CuPz, and AgPz on the surface of the electron density of the molecule (top) and a in space (bottom) where blue represents positive regions and red represents negative regions. ..... 90

Figure 4.6: PCA curves for the AuPz, CuPz, and AgPz trimers measuring the destabilization energy seen when a positive point charge is placed at the center of the trimer. ..... 91

Figure 4.7: Mapping of the electrostatic potential of AuL complexes on the surface of the electron density of the molecule (top) and in space (bottom) where blue represents positive regions and red represents negative regions. ..... 92

Figure 4.8: PCA curves for the AuL trimers measuring the destabilization energy seen when a positive point charge is placed at the center of the trimer. ..... 93

Figure 4.9: Mapping of the electrostatic potential of [Au(μ-Im-NS)] trimers where S = Me, H or $CF_3$, on the surface of the total electron density to give a gradient of electron density (top) and a localization of the electron density (bottom). ..... 94

Figure 4.10: PCA curves for the AuIm trimers measuring the destabilization energy seen when a positive point charge is placed at the center of the trimer. ..... 94

Figure 4.11: Comparison of the 1-electron oxidation energies (ΔG) versus the energy of the HOMO (a.u.). ..... 95

Figure 4.12: Comparison of oxidative addition energies of $X_2$ (left) or HX (right) to a monomer of trimer or dimer of trimer for AuPz. ..... 99

Figure 4.13: Comparison of calculated absorption spectra for oxidized products of Au trimers and HF (top left), HCl (top right), HBr (bottom left), and HI (bottom right). ..... 101

Figure 4.14: Orbital contributions that support metal-to-hydrogen charge transfer states with high contributions to strongly allowed transitions resulting in the formation of the bond in hydrogen gas for the AuIm trimer with HBr (top) and HI (bottom). ..... 102

Figure 5.1: a) Syntheses of 1 (L = pyz) and 2 (L = 4,4'-bpy) from $[Pt(\kappa^1\text{-}NN)_4]^{2+}$ and b) subsequent exchange of pyz ligands in 1 to form 2 or 3 (L = 4-ap)). ..... 115

Figure 5.2: $^1$H NMR Spectrum of $Pt(pyz)_2(mnt)$, 1 (a), $Pt(4\text{-}ap)_2(mnt)$, 3 (b) and $Pt(4,4'\text{-}bpy)_2(mnt)$, 2 (c). ..... 116

Figure 5.3: Crystal structures (ellipsoids at 50%) of the H-bonded quadrangle containing two units of $Pt(4\text{-}ap)_2(mnt)$, 3, and two water molecules ..... 118

Figure 5.4: Crystal structures (ellipsoids at 50%) of 1 (top) and 3 (bottom) showing head-to-tail packing. H-atoms and solvent molecules omitted for clarity. ..... 119

Figure 5.5: SOMO – 1 (top) and SOMO (bottom) contours for 1 (left), 2 (middle) and 3 (right) (plotted with an isovalue of 0.02) supporting assignment of oxidation and reduction processes. ..... 122

Figure 5.6: Cyclic voltammagram of 3 with five complete cycles from 0 to 1.5V (red) and one cycle from 0 to 0.9V (blue) indicating dependence of cathodic peak on oxidations at higher potential ..... 123

Figure 5.7: Cyclic voltammagrams of 1 in THF using 0.1M [n-$Bu_4N$][$PF_6$] electrolyte with a scan rate of 0.1V/s. ..... 123

Figure 5.8: Cyclic voltammagram of 3 with increasing concentrations (0.2mM, 0.4mM, and 0.8mM) indicating concentration dependence of cathodic peak at 0.32V ..... 123

Figure 5.9: Electronic adsorption spectra of compounds 1-3 exhibiting diimine-based $\pi$-$\pi$* absorptions in the mid-UV region and tunable MMLL'CT in the near-UV extending into the visible region. ..... 124

Figure 5.10: Calculated absorption spectra of 1 (a), 2 (b) and 3 (c) with orbital contours for the transitions with the highest oscillator strength. ..... 125

Figure 5.11: Photoluminescence excitation (left/thinner curves) and emission (right/thicker curves) spectra for frozen glassy solutions of 1, 2, and 3 in acetone. ..... 126

Figure 5.12: Photoluminescence excitation (left/thinner curves) and emission (right/thicker curves) spectra for solid samples of 1, 2, and 3 at 77K. ..... 127

Figure 5.13: SOMO and SOMO-1 for the convergent [Pt(2,2'-bpy)(mnt)] complex along with experimental oxidation and reduction values taken from ref. 48 and calculated oxidation and reduction potentials ..... 131

Figure 5.14: Calculated absorption spectra of [Pt(2,2'-bpy)(mnt)] with orbital contours for the transition with the highest oscillator strength. ..... 132

Figure 6.1: Schematic of a lighting device with the active layer being composed of a p- and n-type semiconductor.[2] ..... 141

# CHAPTER 1

# INTRODUCTION AND MOTIVATIONS

## 1.1 Overview of Dissertation

The following work represents a portion of the work I performed during my years as a graduate student within the chemistry department at the University of North Texas. Some of the works have been published or submitted[1, 2] to scientific journals while others await submission. The work shown herein represents only a portion of the completed work; I have co-authored manuscripts not presented in this work.[3-5] The focus of this work is to detail the photophysical, reactivity and structural properties of complexes containing $d^{10}$ and $d^8$ metals using computational and experimental means. This study starts with a detailed analysis of the excited state of $[AuTPA_3]X$, where X = Cl or I and determines the energy splitting of the lowest triplet state with metal-center emission character. This dissertation also includes a study of the first known genuine polar-covalent bonds between two $d^{10}$ metal centers achieved through the inclusion of relativistic effects on the mixing of nd and (n+1)s/p orbitals. This work has led to an expansion of the metal-metal bonding field to include these previously discounted metal centers. The study has been expanded to include the reactivity of $d^{10}$ trinuclear cyclic complexes with halogens and the hydrohalic acids to go through oxidative addition and photoinduced reductive elimination to produce halogen gases and hydrogen gas. This work culminates with a computational and experimental study of the structural, redox and photophysical properties of divergent Pt(II)(dithiolate)(diimine) complexes and how these properties compare to those seen for the convergent complexes.

## 1.2 Spin-Orbit Splitting in Gold (I) Alkylphosphine Complexes

Relativistic effects are corrections that must be made to non-relativistic theory to account for experimental phenomena, originating with the observation of superfine splitting in atomic spectra.[6] The two varieties of relativistic corrections are scalar and spin-orbit relativity. The first correction is the mass-velocity correction that results from the fact that as the size of the nucleus increases, the electrons in that atom orbit faster with speeds that approach the speed of light.[7] This increase in velocity leads to a mass increase of the electron with respect to its resting mass. The second scalar relativistic effect is the Darwin term that represents the random small motion of the electron around the average distance from the nucleus.[7] In addition to these two scalar relativistic effects there are two spin-orbit corrections. The first is the spin-orbit coupling correction that corrects for the interactions between the magnetic moment generated by the motion of the electrons as it moves relative to the magnetic moment generated by the orbital angular momentum. The last correction is a group of effects that are called the indirect relativistic effects and these effects account for the changes in electrostatic potential as a result of the effects of relativity on the valence and core electrons.[8, 9]

The physical consequences of relativistic effects include contraction and stabilization of the s and p orbitals and the expansion and destabilization of the f and d orbitals. This results in increased nuclear shielding by the s and p electrons, leading to the d and f electrons being more shielded from the nucleus, leading to orbital destabilization. This contraction of the s and p orbitals also leads to what is known as the lanthanide contraction. The expansion of the d and f orbitals also leads to higher oxidation states for elements with valence electrons in these shells.

Spin-orbit splitting in phosphorescent transition metal complexes is typically on the order

of 10 – 100 $cm^{-1}$ due to the prevalence of ligand-centered and charge transfer transitions. This is present in the $[Ru(II)(bpy)_3]Cl_2$ complex studied by Hager and Crosby in 1975.[10] For this complex there was no resolution of the spin-orbit splitting states in the steady state spectra or in the lifetime analysis, which gave single component decay. In order to deduce the splitting, computer modeling of the lifetime decay data versus temperature was analyzed to determine that there was splitting. To increase the spin-orbit splitting the Ru metal was traded with Os. While this approach led to a slight increase of the splitting, it was still on the order of 100 $cm^{-1}$. A similar study by Crosby et al. was performed in 1974[11] on $K_3M(CN)_6$ complexes where M = Ru(II), Os(II), Ir(III) and Rh(III). These studies led to similar spin-orbit splittings despite the change to heavier metals. In both of these studies, the ligands selected possess π-systems and so open the door for ligand-centered and charge transfer transitions.

More recently, work has continued on spin-orbit splitting in transition metal complexes and has led to discussion of how covalency at the metal center effects spin-oribt splitting. A recent study by Van Kuiken[12] shows that large covalent character between V(IV) and O leads to an increased probability for ligand-to-metal charge transfer due to the mixing of metal and ligand orbitals. Even upon cooling, for the $V(acac)_3$ complex they were only able to recover about 0.4 eV (3,200 $cm^{-1}$) for the spin-orbit splitting of the lowest triplet state. This amount is also predicted for a set of Rh complexes studied by Eng in 2015.[13] However, for another Au(I) complex ($AuS^-$) the recovery of the spin-orbit splitting is much smaller, comprising of only 45 $cm^{-1}$, which is similar to that seen for $Pt(pop)_2$ (41 $cm^{-1}$).[14, 15]

The motivation of the present work is to determine if using spectroscopically silent alkylphosphine ligands can help increase the probability of true metal-centered transitions and

recover a more appreciable amount of the spin-orbit splitting present in the Au(I) ion. This study will also aim to assess the effects of the counterion and whether increasing the size of the counterion increases the spin-orbit splitting seen for each complex. Additionally, given the selection of the counterion as the halides, we wish to assess excited state bonding between the metal center and the counterion to characterize the excited state as either 3- or 4-coordinate.

## 1.3 21st Century Alchemy: Cupriphication of Gold to Sensitize $d^{10}$-$d^{10}$ Metal-Metal Bonds and Near Phosphorescent Quantum Yields

Two of the most common interactions between metal centers are covalent and metallophilic interactions. Covalent systems typically have deep potential wells, leading to higher dissociation energies and vibrational frequencies as a result of the strong orbital overlap. Covalent interactions typically persist in solution and generally do not rely on solid-state packing effects and can be modeled computationally with high degrees of accuracy. Metallophilic interactions are an intermediate type of interaction between ionic, covalent and van der Waals interactions. Metallophilic interactions usually result from ligand-assisted and relativistically-allowed mixing of the (n+1)s and p orbitals with nd orbitals. Relativistic effects stabilize the (n+1)s and p orbitals and destabilize the nd orbitals, allowing for depopulation of the nd orbitals through orbital mixing. This results in an attractive interaction between metal centers. The most famous example of this is aurophilicity.[16] The solid-state packing effect observed for complexes with $d^{10}$ metal centers as a part of an extended lattice is attributed to theses attractive, metallophilic interactions. The potential wells for metallophilic interactions are shallow, and can be disallowed by solid-state packing effects and usually do not persistent in solution. Concurrent with the

shallow potential wells is the existence of lower dissociation energies and vibrational frequencies.

An example of these metallophilic interactions was discussed by Crespo in 2014.[17] A series of complexes containing $d^8$ and $d^{10}$ metal centers were synthesized. Each complex, with only one exception, displayed metallophilic interactions between the $d^8$ and $d^{10}$ metal centers; the Pt/Au containing complex exhibited a $d^8$-$d^{10}$ distance that resembled that of intermetallic interaction distances. The Pd/Cu and the Pd/Ag complex had even shorter distances. Crespo modeled the electronic structure of these complexes and found that the metallophilic interactions were not accounted for in the frontier orbitals. This led to the conclusion that the electronic transitions for these complexes are independent of the metallophilic interactions, which is further supported by the similarities in the absorption and emission spectra for each complex, despite varying the identity of the metals. Going further back, there is an example of metallophilic interactions between Pd-Pd and Ag-Ag reported by Perreault in 1993.[18] An $Ag_2$ complex was synthesized with dmb bridging ligands as well as bridging halogens. The distance between the Ag metal centers was determined to be at the limit of the sum of the van der Waals radii, leading to the conclusion that this system exhibits weak argentophilic interactions. It was also shown that based on the Ag-X bond lengths, the Ag-X bonds possesses significant ionic character. The Pd-Pd complex exhibited metallophilic interactions through association of monomer units into dimers. These dimers yielded Pd-Pd distances within the sum of the van der Waals radii. Any prediction for covalent interactions can be excluded as these dimers do not persist in solution. A spectroscopic study was conducted and found both complexes possess low metal-metal stretching vibrational frequencies ($Ag_2$: 40 $cm^{-1}$ and $Pd_2$: 32 $cm^{-1}$). These low vibrational frequencies show that

metallophilic interactions are weak, but should not be overlooked.

Elbjeirami reported trinuclear Au(I) complexes that have crystals structures that reveal these molecules stack in a prismatic manner in the solid state, with short Au-Au distances of 3.3465 Å.[19] This shows that the dimers of this trinuclear complex are held together by aurophilic interactions, resulting in one long Au-Au distance and two shorter distances. Another example of solid state packing for Au(I) trinuclear complexes was reported by Vickery in 1997.[20] The crystal structure showed that this trinuclear Au(I) complex also associates as a dimer, with shorter than 3.6 Å Au-Au intertrimer distances. These intertrimer distances indicate that there is some attractive interactions between the Au atoms.

While these examples demonstrate that metal-metal bonds are possible, they don't reflect the situation we are motivated to illustrate. In 2001, Catalano[21] reported an unsupported bond between Pt(0), a $d^{10}$ metal, and Tl(I), a closed-shell metal ion. While an abundance of examples exist with bonds between Pt(II) and Tl(I), there are few examples of genuine bonds between Pt(0) and Tl(I). Support for the covalent character of this bond involves the FAB-mass spectra, which displays a peak corresponding to an intact $[Pt(PPh_2Py)_3Tl]^+$ (where Py = pyridine) that indicates that this bond persists in the gas phase. There is another peak that points to dissociation of one of the phosphine ligands, but the Pt-Tl bond remains intact. Additionally, Baya[22] in 2016 synthesized a dinuclear Pt-Au complex that exhibited [PtCNC]→Au interactions that are dative in nature.

Studies have also been completed on bonding between Au(II) metal centers. In 2003, Irwin[23] reported Au(II)-Au(II) distances that were shorter than those seen in metallic gold. These short distances can be described by bond formation between the Au(II) centers aided by bonding

with the halides. This discovery showed that covalent bonding can be induced in Au(II) complexes that contain bridging ligands. In 2013, Xiong and Pyykkö[24] studied the possibility of unbridged Au(II)-Au(II) bonding and they found that the test complexes exhibited bond dissociation energies on the order of 200 kJ/mol. Through the use of the electron localization function they were able to determine that significant electron density exists between the Au(II) centers. The Kohn-Sham orbitals were modeled to find that metal-metal bonding orbitals showed significant mixing between 6s/6p orbitals and the 5d orbitals.

All the covalent bonding examples mentioned above demonstrate the possibility of metal-metal bonds and for some of the examples the low d-count of the metals leads to high bond orders. There are examples of covalent type interactions between pseudo-closed shell and closed shell metal centers, like Pt(II) and Au(I) as well as Pt(0) and Tl(I) and these models demonstrate the possibility of producing non-zero bond orders between these pseudo-closed shell and closed shell metals, or pseudo-closed shell metals. While these examples are present, to our knowledge, there are no examples of genuine covalent bonds between $d^{10}$ metal centers.

## 1.4 Oxidative Addition of Haloacids and Dihalogens to Trinuclear Cyclic Coinage Metal Complexes and the Photoinduced Reductive Elimination of $X_2$ and $H_2$

Oxidative addition is a reaction pathway that transition metal complexes can go through that involves an increase in the oxidation state of the metal (usually by two) and an increase in the coordination number at the metal center. Due to the increase of the coordination number at the metal center, steric bulk often inhibits oxidative addition. Typically, sterically unencumbered complexes such as square planar and linear complexes, undergo oxidative addition more readily than a trigonal bipyramidal or octahedral complex. Coordination complexes with more ligands

are incapable of undergoing oxidative addition; however, the process usually involves the dissociation of an existing ligands that is more labile. In addition to these steric factors, there are also electronic factors that can affect the ability of a complex to go through oxidative addition. Since the metal center will be oxidized, there must be stable neighboring oxidation states. To go through 2-electron oxidation, a metal center must have a stable *n* and *n+2* formal oxidation states such as Au(I)/Au(III) or Mn(II)/Mn(IV). In addition to this requirement, metals that have higher basicity will be oxidized more easily, and therefore complexes with these metal centers will be more likely to go through oxidative addition. These steric and electronic factors also extend to the substrate. Substrates that are bulky and sterically encumbered will not go through oxidative addition as quickly as less hindered substrates.

There are different mechanistic pathways for oxidative addition that complexes can undergo. One of the popular mechanisms of oxidative addition is a concerted mechanism and involves the formation of a three-centered transition state, which involves the binding of both ends of the substrate to the metal center and leads to the breakage of the substrate bond to form the oxidized species. This mechanism is seen mostly with complexes where the substrate has a permanent dipole (i.e., asymmetric substrates) and requires the metal center to be a strong electron-donor to break the substrate bond. Another popular mechanism of oxidative addition is a polar mechanism involving the coordination of an electrophile to the metal center followed by the coordination of the leaving group. This is seen typically with strongly polarizable substrates that make good leaving groups. A final popular mechanism usually seen for hydrohalic acids, is an $S_N1$-type addition, where the substrate dissociates before the nucleophiles bind to the metal centers.

Reductive elimination is the reverse process of oxidative addition and causes a decrease in both the coordination number and the oxidation state of the metal center. Reductive elimination is favored by electron rich ligands that will dissociate from the metal center, donating electrons to the metal center, which should be electron poor. Since sterically unencumbered ligands favor oxidative addition, sterically bulky ligands favor reductive elimination. Similar to oxidative addition there are three main mechanisms: concerted, $S_N2$ and $S_N1$ type eliminations.

Previous work involving the splitting of hydrohalic acids to produce hydrogen and dihalogen gases has been completed by Teets and Nocera[25] where they studied the photocatalytic reduction of the halogens from heterobimetallic complexes involving both Au and Pt centers. They showed that once the hydrohalic acid has been added to the heterobimetallic complex, the elimination is more efficient if there is little to no excited state distortion upon excitation of the complex. It was also found that the presence of ligand-to-metal charge transfer states induce a lengthening of the M-X bonds, which leads to more effective reductive elimination. Their proposed mechanism suggests that upon irradiation of the oxidized complex, hydrogen gas is lost first and then the dihalogen gas is lost second.

Another important work was completed by de Jong[26] which focused on Pd complexes. This work lead to subtle differences between the transition states of the addition of dihalogens and hydrohalic acids to the Pd centers. For the dihalogens, it was found that the activation barrier increases with halogen size and the Pd-X-X angle in the transition state is around 150°. For the hydrohalic acids, the trend was reversed with larger halogens leading to decreased activation barriers. The transition state Pd-X-H angle was found to be around 90° versus the 150° for the dihalogens.

While studies have been completed on the oxidative addition properties of cyclic coinage metal complexes,[27-29] these studies have not focused on the trinuclear cyclic complexes such as those studied by Balch[20,30-32] and Raptis.[33,34] Our motivation for investigating the oxidative addition reactions of trinuclear coinage metal complexes comes from the desire to study the production of hydrogen gas for use in fuel cells. In this work, oxidative addition of symmetric and asymmetric substrates allows for the study of the effects of substitutions and substrate identity on the oxidative addition trends in these molecules.

## 1.5 Luminescent, Redox-Active (Dithiolato)bis(imine) Divergent Complexes with Exchangeable Imine Ligands: An Experimental/Computational Study Versus Their (Diimine)(Dithiolato)Platinum(II) Convergent Congeners

Pt(II) $\kappa^2$-diimine complexes have been studied widely by experimental chemist. These complexes have many well-known electrochemical properties as well photophysical properties[35-37] which have led to applications in MOFs[38-41] and light-harvesting devices.[42,43] While these so-called convergent Pt(II) complexes have been extensively studied, their divergent congeners have received less attention. These $\kappa^1$-imine complexes are of particular interest when it comes to the synthesis and utility of supramolecular coordination complexes.

Through this computational and experimental study, a new synthetic strategy has been carried out to produce divergent ($\kappa^1$-imine) complexes with exchangeable imine ligands, leading to complexes with similar redox and photophysical properties. This would allow for these complexes to be used in similar applications as the convergent complexes, but the structural differences between the two shows broader applications in supramolecular coordination complexes for the divergent complexes, given the $\kappa^1$ nature of the imine ligands. This leads to

complexes with rotatable imine ligands, leading to a change in the dihedral of these imine ligands, which is absent in the $\kappa^2$-diimine complexes.

Computationally, there is agreement between the crystal structure and the calculated geometry which includes reproduction of the dihedral angles between the two imine ligands in the divergent complexes. There is also good qualitative agreement between the experimental and calculated absorption spectra, which shows the spectra to be based on metal-to-ligand-to-ligand*-charge transfers as well as higher lying excitations which correspond to π-π* transitions, which is consistent with previous work on the convergent congeners.[44]

## 1.6 References


1. Galassi, R.; Ghimire, M. M.; Otten, B. M.; Ricci, S.; McDougald, R. N.; Almotawa, R. M.; Alhmoud, D.; Ivy, J. F.; Rawashdeh, A.-M. M.; Nesterov, V. N.; Reinheimer, E. W.; Daniels, L. M.; Burini, A.; Omary, M. A. Cupriphication of gold to sensitize $d^{10}$–$d^{10}$ metal–metal bonds and near-unity phosphorescence quantum yields. *Proc. Natl. Acad. Sci.*, **2017**, 114(*26*), E5042-E5051.

2. Smith, J. B.; Otten, B. M.; Derry, P. J.; Browning, C.; Bodenstedt, K. W.; Sandridge, J.; Satumtira, N. T.; Zilaie, M.; Payne, J.; Nuti, R.; Omary, M. A.; Smucker, B. W. Luminescent, redox-active (dithiolato)bis(imine)platinum(II) divergent complexes with exchangable imine ligands: an experimental/computational study versus their (diimine)(dothiolato)platinum(II) convergent congeners. *Comments Inorg. Chem.*, **Accepted**.

3. Nicholas, A. D.; Otten, B. M.; Ayala, G.; Hutchinson, J.; Wojtas, L.; Omary, M. A.; Pike, R. D.; Patterson, H. H. Light-Induced Photochemical Changes in Copper(I) Thiocyanate Complexes Decorated with Halopyridines: Optical Memory Manifestation. *J. Phys. Chem. C*, **2017**, 121(*45*), 25430-25439.

4. Otten, B. M.; Melançon, K. M.; Omary, M. A. All That Glitters Is Not Gold: A Computational Study of Covalent vs Metallophilic Bonding in Bimetallic Complexes of $d^{10}$ Metal Centers—A Tribute to Al Cotton on the Tenth Anniversary of His Passing *Comments Inorg. Chem.*, **2018**, 38(*1*), 1-35.

5. Yaseen, W. K.; Sanders, S. F.; Almotawa, R. M.; Otten, B. M.; Bhat, S.; Alamo, D. C.; Marpu, S. B.; Golden, T. D.; Omary, M. A. Are metal complexes “organic”, “inorganic”, “organometallic”, or “metal-organic” materials? A case study for the use of trinuclear coinage metal complexes as “metal-organic coatings” for corrosion suppression on Aluminum substrates. *Comments Inorg. Chem.*, **2019**, 39(*1*), 1-26.

6. Thomas, L. H. The Motion of the Spinning Electron. *Nature*, **1926**, 117, 514.

7. Cowan, R. D.; Griffin, D. C. Approximate relativistic corrections to atomic radial wave functions. *J. Opt. Soc. Am.*, **1976**, 66(*10*), 1010-1014.

8. Marian, C. M. Spin–orbit coupling and intersystem crossing in molecules. *Wiley Interdisciplinary Reviews: Computational Molecular Science*, **2012**, 2(*2*), 187-203.

9. Marian, C. M. Spin-Orbit Coupling in Molecules. Reviews in Computational Chemistry. **2001**, John Wiley & Sons, Inc.

10. Hager, G. D.; Crosby, G. A. Charge-transfer exited states of ruthenium(II) complexes. I. Quantum yield and decay measurements. *J. Am. Chem. Soc.*, **1975**, 97(*24*), 7031-7037.

11. Hager, G. D.; Watts, R. J.; Crosby, G. A. Charge-Transfer Excited States of Ruthenium(II) Complexes. II. Relationship of Level Parameters to Molecular Structure. *J. Am. Chem. Soc.*, **1974**, 97(*24*), 7037-7042.

12. Van Kuiken, B. E.; Hahn, A. W.; Maganas, D.; DeBeer, S. Measuring Spin-Allowed and Spin-Forbidden d–d Excitations in Vanadium Complexes with 2p3d Resonant Inelastic X-ray Scattering. *Inorg. Chem.*, **2016**, 55(*21*), 11497-11501.

13. Eng, J.; Gourlaouen, C.; Gindensperger, E.; Daniel, C. Spin-Vibronic Quantum Dynamics for Ultrafast Excited-State Processes. *Acc. Chem. Res.*, **2015**, 48(*3*), 809-817.

14. Liu, H.-T.; Huang, D.-L.; Liu, Y.; Cheung, L.-F.; Dau, P. D.; Ning, C.-G.; Wang, L.-S. Vibrational State-Selective Resonant Two-Photon Photoelectron Spectroscopy of $AuS^-$ via a Spin-Forbidden Excited State. *J. Phys. Chem. Lett.*, **2015**, 6(*4*), 637-642.

15. Záliš, S.; Lam, Y.-C.; Gray, H. B.; Vlček, A. Spin–Orbit TDDFT Electronic Structure of Diplatinum(II,II) Complexes. *Inorg. Chem.*, **2015**, 54(*7*), 3491-3500.

16. Schimdbaur, H. The aurophilicity phenomenon: A decade of experimental findings, theoretical concepts and emerging applications. *Gold Bull.*, **2000**, 33(*1*), 3-10.

17. Crespo, O.; Gimeno, M. C.; Laguna, A.; Lehtonen, O.; Ospino, I.; Pyykkö, P.; Villacampa, M. D. Structural and Photophysical Study on Heterobimetallic Complexes with $d^8$–$d^{10}$ Interactions Supported by Carborane Ligands: Theoretical Analysis of the Emissive Behaviour. *Chem. - Eur. J.*, **2014**, 20(*11*), 3120-3127.

18. Perreault, D.; Drouin, M.; Michel, A.; Harvey, P. D. Relationships between metal-metal force constants and metal-metal separations for disilver and dipalladium systems. Crystal and molecular structures of $Ag_2(dmb)_2X_2$ (X = Cl, Br, I; dmb = 1,8-diisocyano-p-menthane) and cis-$Pd(CNC(CH_3)_3)_2Cl_2$ complexes. *Inorg. Chem.*, **1993**, 32(*10*), 1903-1912.

19. Elbjeirami, O.; Rashdan, M. D.; Nesterov, V.; Rawashdeh-Omary, M. A. Structure and luminescence properties of a well-known macrometallocyclic trinuclear Au(I) complex and its adduct with a perfluorinated fluorophore showing cooperative anisotropic supramolecular interactions. *Dalton Trans.*, **2010**, 39(*40*), 9465-9468.

20. Vickery, J. C.; Olmstead, M. M.; Fung, E. Y.; Balch, A. L. Solvent-Stimulated Luminescence from the Supramolecular Aggregation of a Trinuclear Gold(I) Complex that Displays Extensive Intermolecular Au···Au Interactions. *Angew. Chem., Int. Ed.*, **1997**, 36(*11*), 1179-1181.

21. Catalano, V. J.; Bennett, B. L.; Muratidis, S.; Noll, B. C. Unsupported Pt(0)−Tl(I) Bonds in the Simple $[Pt(PPh_2Py)_3Tl]+$ Complexes. *J. Am. Chem. Soc.*, **2001**, 123(*1*), 173-174.

22. Baya, M.; Belío, Ú.; Fernández, I.; Fuertes, S.; Martín, A. Unusual Metal–Metal Bonding in a Dinuclear Pt–Au Complex: Snapshot of a Transmetalation Process. *Angew. Chem., Int. Ed.*, **2016**, 55(*24*), 6978-6982.

23. Irwin, M. D.; Abdou, H. E.; Mohamed, A. A.; Fackler, J. J. P. Synthesis and X-ray structures of silver and gold guanidinate-like complexes. A Au(II) complex with a 2.47 Å Au–Au distance. *Chem. Commun.*, **2003**, 23, 2882-2883.

24. Xiong, X.-G.; Pyykkö, P. Unbridged Au(II)–Au(II) bonds are theoretically allowed. *Chem. Commun.*, **2013**, 49(*21*), 2103-2105.

25. Teets, T. S.; Nocera, D. G. Photocatalytic hydrogen production. *Chem. Commun.*, **2011**, 47(*33*), 9268-9274.

26. de Jong, G. T.; Kovács, A.; Bickelhaupt, F. M. Oxidative Addition of Hydrogen Halides and Dihalogens to Pd. Trends in Reactivity and Relativistic Effects. *J. Phys. Chem. A*, **2006**, 110(*25*), 7943-7951.

27. Lin, J. C. Y.; Huang, R. T. W.; Lee, C. S.; Bhattacharyya, A.; Hwang, W. S.; Lin, I. J. B. Coinage Metal−N-Heterocyclic Carbene Complexes. *Chem. Rev.*, **2009**, 109(*8*), 3561-3598.

28. Mohamed, A. A. Advances in the coordination chemistry of nitrogen ligand complexes of coinage metals. *Coord. Chem. Rev.*, **2010**, 254(*17*), 1918-1947.

29. Díaz-Requejo, M. M.; Pérez, P. J. Coinage Metal Catalyzed C−H Bond Functionalization of Hydrocarbons. *Chem. Rev.*, **2008**, 108(*8*), 3379-3394.

30. Balch, A. L.; Doonan, D. J. Mixed valence gold chemistry: Stepwise oxidation of a cyclic trigold(I) complex. *J. Organomet. Chem.*, **1977**, 131(*1*), 137-146.

31. Balch, A. L.; Nagle, J. K.; Oram, D. E.; Reedy, P. E. Oxidative additions and luminescence involving iridium-gold-iridium chains formed by binding of gold(I) to the metallamacrocycle $Ir_2Cl_2(CO)_2[\mu\text{-}Ph_2PCH_2As(Ph)CH_2PPh_2]_2$. *J. Am. Chem. Soc.*, **1988**, 110(*2*), 454-462.

32. Vickery, J. C.; Balch, A. L. X-ray Crystallographic Studies of the Products of Oxidative Additions of Iodine to Cyclic Trinuclear Gold(I) Complexes: Directional Effects for Au−I···I−Au Interactions. *Inorg. Chem.*, **1997**, 36(*26*), 5978-5983.

33. Raptis, R. G.; Murray, H. H.; Fackler, J. P., Jnr The structure of $[Au\text{-}[\mu]\text{-}\{3,5\text{-}(C_6H_5)_2C_3HN_2\}]_3Cl_2$: a trinuclear mixed-valence gold pyrazolate complex. *Acta Crystallogr., Sect. C: Struct. Chem.*, **1988**, 44(*6*), 970-973.

34. Raptis, R. G.; Porter, L. C.; Emrich, R. J.; Murray, H. H.; Fackler, J. P. Synthesis of a mixed-valence gold(I)/gold(III) complex, $[Au(CH_2)_2PPh_2]_2Br_2$, and its characterization by x-ray crystallography and x-ray photoelectron spectroscopy. *Inorg. Chem.*, **1990**, 29(*22*), 4408-4412.

35. Eisenberg, R.; Gray, H. B. Noninnocence in Metal Complexes: A Dithiolene Dawn. *Inorg. Chem.*, **2011**, 50(*20*), 9741-9751.

36. Espa, D.; Pilia, L.; Makedonas, C.; Marchiò, L.; Mercuri, M. L.; Serpe, A.; Barsella, A.; Fort, A.; Mitsopoulou, C. A.; Deplano, P. Role of the Acceptor in Tuning the Properties of Metal [M(II) = Ni, Pd, Pt] Dithiolato/Dithione (Donor/Acceptor) Second-Order Nonlinear Chromophores: Combined Experimental and Theoretical Studies. *Inorg. Chem.*, **2014**, 53(*2*), 1170-1183.

37. Smucker, B. W.; Hudson, J. M.; Omary, M. A.; Dunbar, K. R. Structural, Magnetic, and Optoelectronic Properties of (Diimine)(dithiolato)platinum(II) and -palladium(II) Complexes and Their Charge-Transfer Adducts with Nitrile Acceptors. *Inorg. Chem.*, **2003**, 42(*15*), 4714-4723.

38. Corma, A.; García, H.; Llabrés i Xamena, F. X. Engineering Metal Organic Frameworks for Heterogeneous Catalysis. *Chem. Rev.*, **2010**, 110(*8*), 4606-4655.

39. Cook, T. R.; Zheng, Y.-R.; Stang, P. J. Metal–Organic Frameworks and Self-Assembled Supramolecular Coordination Complexes: Comparing and Contrasting the Design, Synthesis, and Functionality of Metal–Organic Materials. *Chem. Rev.*, **2013**, 113(*1*), 734-777.

40. Guo, Z.; Kobayashi, T.; Wang, L.-L.; Goh, T. W.; Xiao, C.; Caporini, M. A.; Rosay, M.; Johnson, D. D.; Pruski, M.; Huang, W. Selective Host–Guest Interaction between Metal

Ions and Metal–Organic Frameworks Using Dynamic Nuclear Polarization Enhanced Solid-State NMR Spectroscopy. *Chem. - Eur. J.*, **2014**, 20(*49*), 16308-16313.

41. Cui, J.; Xu, Z. An electroactive porous network from covalent metal–dithiolene links. *Chem. Commun.*, **2014**, 50(*30*), 3986-3988.

42. Islam, A.; Sugihara, H.; Hara, K.; Singh, L. P.; Katoh, R.; Yanagida, M.; Takahashi, Y.; Murata, S.; Arakawa, H.; Fujihashi, G. Dye Sensitization of Nanocrystalline Titanium Dioxide with Square Planar Platinum(II) Diimine Dithiolate Complexes. *Inorg. Chem.*, **2001**, 40(*21*), 5371-5380.

43. Browning, C.; Hudson, J. M.; Reinheimer, E. W.; Kuo, F.-L.; McDougald, R. N.; Rabaâ, H.; Pan, H.; Bacsa, J.; Wang, X.; Dunbar, K. R.; Shepherd, N. D.; Omary, M. A. Synthesis, Spectroscopic Properties, and Photoconductivity of Black Absorbers Consisting of Pt(Bipyridine)(Dithiolate) Charge Transfer Complexes in the Presence and Absence of Nitrofluorenone Acceptors. *J. Am. Chem. Soc.*, **2014**, 136(*46*), 16185-16200.

44. Cummings, S. D.; Eisenberg, R. Tuning the Excited-State Properties of Platinum(II) Diimine Dithiolate Complexes. *J. Am. Chem. Soc.*, **1996**, 118(*8*), 1949-1960.

# CHAPTER 2

# SPIN-ORBIT SPLITTING IN GOLD(I) ALKYLPHOSPHINE COMPLEXES[1]

## 2.1 Introduction

In previous work by the Omary group on spin-orbit splitting in Au(I) alkylphosphine complexes, the $[Au(TPA)_3]Cl$ complex was shown to have spin-orbit splitting through the separation of three separate emission bands (500 nm, 650 nm and 660 nm).[1] These bands were separated at low temperatures (4 K, achieved through the use of liquid helium) using a method called gated emission, where the detector was delayed in order to separate two overlapping bands based upon the lifetimes of these bands. This led to the conclusion that while SOC splitting is seen for this complex and is comparable to the splitting seen in the Au(I) ion, the energy difference between the bands is not large enough to separate the bands based on energy alone.

In order to better understand the splitting phenomenon seen for this Au(I) chloride complex, the complex was first studied as a trigonal planar complex, with the exclusion of the counter ion. In this case the main effects seen where a result of the Jahn-Teller excited state distortion, which are seen as an effect of an electron being promoted from the 5d orbitals to the 6p. Given that the Au(I) complex has a $5d^{10}$ configuration, the promotion of an electron leads to an unequal occupation of degenerate orbitals, leading to the distortion of the geometry. Previous studies of this Jahn-Teller distortion were reported by Omary et al. and showed that the main effect on the distortion in these complexes were due to the ligand size or the ligand cone angle.[2] Other studies were also completed to show the shifting of the emission band based on the

[1] Previous experimental work on the $[AuTPA_3]Cl$ was performed by Pankaj Sinah while experimental work on the $[AuTPA_3]I$ was completed by the author. Previous calculations with the GAMESS software package were completed by Tom Grimes and all Gaussian and ADF calculations were completed by the author.

counter ion to show a blue shift as the counter ion was increased in size.[3] This led to the conclusion that the identity of the counter ion does matter and thus in these future studies, the complex is treated as a neutral complex while varying the counter ion. This study aims to rationalize the shifting and degree of SOC splitting seen in these Au(I)-alkylphosphine halide complexes as the counterion size is increased from chloride to iodide in order to determine the trends in the spin-orbit splitting.

## 2.2 Methods

### 2.2.1 Experimental Methods

Unless stated otherwise, all syntheses were performed in an air and water free atmosphere of argon gas through the use of a Schlenck line. All complexes were characterized through the use of infrared (IR), nuclear magnetic resonance (NMR) spectroscopies and photoluminescent studies. IR spectroscopy was performed on solid materials through the use of the Thermo Scientific Nicolet 6700 with both far and mid-IR detectors. Phosphorous-31 NMR was performed on solutions of the samples in $D_2O$ versus an 85% phosphoric acid standard in $D_2O$ on a Varian spectrometer operating at 300 MHz. Photoluminscent studies were performed on solid samples with the PTI QuantaMaster Spectrofluorometer for the UV-Vis and Near IR regions with the use of an arc lamp, at both room temperature and cryogenic temperatures. Cryogenic temperatures were achieved through the use of the Oxford Instruments OptistateCF Continuous Helium Flow cryostat with gas flow and temperature controls in conjunction with a turbopump. Lifetimes were performed using the QuantaMaster using a pulsed lamp.

### 2.2.2 Syntheses

**$AuTPA_3Cl$**. 100 mg of AuTHTCl (Chlorotetrahydrofurangold(I)) was suspended in 9 mL of 2:1 methanol:acetonitrile. To this stirring suspension, 49 mg of TPA(1,3,5-triaza-7-phosphaadamantane) was added and allowed to stir for two hours in the dark. An additional 49 mg of TPA was added and allowed to stir for three hours in the dark. 49 mg of TPA was added to the stirring solution and was allowed to stir until the precipitate dissolved upon which 10 mg of TPA was added and allowed to stir for three hours. The solution was filtered to remove any suspended solid and $Et_2O$ was added to the solution to form the precipitate. The precipitate was collected and allowed to dry under vacuum overnight.

**$AuTPA_3I$**. 100 mg of AuTHTCl was suspended in 9 mL of 2:1 methanol:acetonitrile. To this stirring suspension, 49 mg of TPA was added and allowed to stir for two hours in the dark. An additional 49 mg of TPA was added and allowed to stir for three hours in the dark. 49 mg of TPA was added to the stirring solution and was allowed to stir until the precipitate dissolved upon which 10 mg of TPA was added and allowed to stir for three hours. The solution was filtered to remove any suspended solid and a stoichiometric amount of KI was added. The solution was allowed to stir until the yellow color disappeared. A drop of water was added to rid the excess KI. Then a small amount of $AgNO_3$ was added to the solution to precipitate out the excess $Cl^-$ as AgCl. $Et_2O$ was added to the solution to form the precipitate. The precipitate was collected and allowed to dry under vacuum overnight.

### 2.2.3 Computational Methods

For this work, geometry optimizations of the ground and excited state of $[Au(TPA)_3]Cl$ and

$[Au(TPA)_3]I$ were performed using the Gaussian 09 suite of programs[4] using the hybrid functional B3PW91[5-9] in conjunction with the compact-electron potential basis set, CEP-31G[10-12] with added d-polarization functions on the main group elements excluding hydrogen. Test calculations were also performed using the same functional but with the augmented correlation-consistent triplet-ζ which is an all electron basis set through chlorine,[13, 14] with pseudo-potentials added for the core electrons of gold[15] and iodide.[16] For each optimized geometry, a frequency calculation was performed to ensure the geometry was a true minimum. To predict spectroscopic properties, the diabatic (vertical) excitation and emission energies were calculated as well as the adiabatic absorption spectra. The main issue with using Gaussian to calculate these properties for these complexes is that the time-dependent DFT (TD-DFT) algorithm follows the Laporte transition rules which state that there is only a non-zero transition probability between states with the same multiplicity. Given that these complexes are expected to exhibit spin-orbit coupling, transitions between states with different multiplicities are expected to have non-zero transition probabilities. This led to the use of the Amsterdam Density Functional (ADF) program.[17-19] This program was selected for its inclusion of relativistic effects through the use the zeroth-order regular approximation (ZORA).[20-22] ZORA is capable of including both scalar and spin-orbit relativistic effects through a two- or four-component Hamiltonian, respectively. The two-component Hamiltonian is based on Dirac's spin-free Hamiltonian while the four-component Hamiltonian includes spin terms. The BPW91[6-9, 23] functional was used in conjunction with a quadruple-ζ relativistic basis set on gold and iodide with a triple-ζ relativistic basis set on all other atoms.[24] The model $[Au(PH_3)_3]X$ complex was used to perform calculations in ADF. This complex was selected as a reasonable model given the similar cone angle of the phosphine and the TPA

ligand, leading to a similar excited state distortion. ADF was used to calculate the excitation and emission spectra of each complex and an orbital analysis was completed to determine the different types of transitions and whether these complexes truly exhibit the expected metal-centered transitions anticipated for complexes that exhibit spin-orbit coupling with spectroscopically silent ligands.[25-28]

## 2.3 Results and Discussion

The ground state geometries of $[AuTPA_3]X$ and $[Au(PH_3)_3]X$ (where X = Cl, or I) are compared below in **Table 2.1** (structures depicted in **Figure 2.1**). This comparison is drawn to demonstrate that the phosphine model is an appropriate model to replace the TPA ligand. The main focus of comparison is the phosphine cone angle and the angles containing a phosphorous atom, a gold atom and another phosphorous atom. While there is significant variation of the cone angle in the cationic complexes, the differences are smaller in the species containing the halide. Not only that, but there is a larger variation from the cationic complex to the halide containing species with the phosphine. Both of these variations are attributed to the ring structure seen in the TPA ligand. The ring structure keeps the carbon atoms in place while the hydrogens in the phosphine have more space to move and separate. The addition of the halides contracts this allowed movement and accounts for the fact that the cone angles are similar for the halide containing complexes. Additionally, the P-Au-P angles experience small variations for the cationic and neutral complexes. All complexes exhibit bond angles that are close to the ideal $D_{3h}$ symmetry expected. While the angles vary, the degree of planarity of the core of the molecule possess is a more important parameter to consider.

**Table 2.1: Comparison of selected calculated geometric parameters for the ground state of $AuTPA_3$/$AuTPA_3X$ versus $Au(PH_3)_3$/$Au(PH_3)_3X$.**

| Complex | Phosphine Cone Angle* (°) | $P_1$-Au-$P_2$ (°) | $P_2$-Au-$P_3$ (°) | $P_3$-Au-$P_1$ (°) | $P_1$-Au (Å) | $P_2$-Au (Å) | $P_3$-Au (Å) |
|---|---|---|---|---|---|---|---|
| $[AuTPA_3]^+$ | 291.4 ± 0.5 | 120.8 | 119.8 | 119.4 | 2.4440 | 2.4094 | 2.4243 |
| $[AuTPA_3]Cl$ | 290.9 ± 0.2 | 120.0 | 120.0 | 120.0 | 2.3989 | 2.4015 | 2.3985 |
| $[AuTPA_3]I$ | 290.6 ± 0.1 | 120.3 | 120.1 | 119.3 | 2.4015 | 2.4038 | 2.4031 |
| $[Au(PH_3)_3]^+$ | 297.1 ± 0.3 | 120.2 | 119.6 | 120.1 | 2.4298 | 2.4306 | 2.4294 |
| $[Au(PH_3)_3]Cl$ | 290.1 ± 0.5 | 118.2 | 118.1 | 118.1 | 2.4314 | 2.4324 | 2.4326 |
| $[Au(PH_3)_3]I$ | 290.5 ± 0.2 | 117.9 | 117.8 | 117.8 | 2.4362 | 2.4360 | 2.4358 |

*Denotes an average

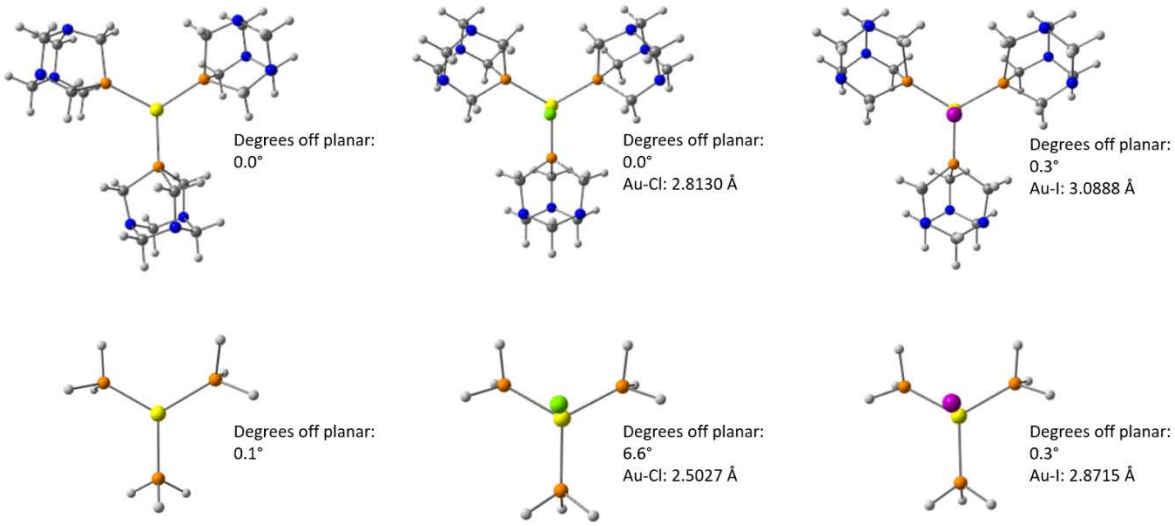


**Figure 2.1**: **Ground state structures of $AuTPA_3$/$AuTPA_3X$ versus $Au(PH_3)_3$/$Au(PH_3)_3X$ along with deviations from linearity and the Au-X bond length.**

This parameter is determined by the summation of all three P-Au-P angles (**Figure 2.1**) and the deviation of this sum from 360°. All TPA complexes remain extremely close to planar (within ± 1°) while there are slight deviations for the phosphine complexes. These deviations are attributed to the increased interaction of the Au center and the halide due to the lack of steric bulk. The final

factor to determine if the phosphine complexes can be used in place of the TPA models is the Au halide bond distance (**Figure 2.1**). These distances show that the phosphine model have much shorter Au halide bonds than those seen with the TPA complex. While the bond lengths are different, both ligands given bond lengths that are outside the sum of the covalent radii for Au and the halide. This could point to the fact that the bond lengths are different mostly due to the steric bulk of the ligands and not that there is a covalent interaction in one model and an ionic interaction in the other.

The same structural analysis has been carried out for the excited state and the results are summarized in **Table 2.2** and **Figure 2.2**. For the excited state the cone angle of the phosphine ligand experiences less variation than in the ground state. (**Figure 2.2**). The degree of planarity also shows significant deviation from the TPA complex to the phosphine. While all three complexes with the TPA ligand experience deviations from planarity, the neutral phosphines experience this deviation while the cationic complex does not. This is attributed to the fact that the interaction between the Au and halide in the excited state causes a puckering of the structure. While the geometric parameters may vary with the ligand choice, the overall character of the ground to excited state excitation is the same. Given that the ideal geometry is $D_{3h}$, the 5d-orbitals are split into three groups (**Figure 2.3**). Since $Au^{+}$ has 10 d-electrons, the HOMO is a set of degenerate e`` orbitals and when an electron is excited from this level to either $a_2$`` or $a_1$` (6$p_z$ and 6s, respectively) there is unequal occupation of these orbitals. As a result, the geometry of the molecule will distort to break the degeneracy of the e`` orbitals. This Jahn-Teller distortion accounts for the breaking of the symmetry from $D_{3h}$ to $C_{2v}$ upon excitation.

**Table 2.2: Comparison of selected calculated geometric parameters for the excited state of $AuTPA_3$/$AuTPA_3X$ versus $Au(PH_3)_3$/$Au(PH_3)_3X$.**

| Complex | Phosphine Cone Angle* (°) | $P_1$-Au-$P_2$ (°) | $P_2$-Au-$P_3$ (°) | $P_3$-Au-$P_1$ (°) | $P_1$-Au (Å) | $P_2$-Au (Å) | $P_3$-Au (Å) |
|---|---|---|---|---|---|---|---|
| $[AuTPA_3]^+$ | 291.4 ± 0.0 | 146.2 | 103.8 | 103.8 | 2.3879 | 2.3879 | 2.3892 |
| $[AuTPA_3]Cl$ | 290.2 ± 0.2 | 151.7 | 103.7 | 100.2 | 2.4094 | 2.4121 | 2.4332 |
| $[AuTPA_3]I$ | 288.8 ± 0.1 | 158.2 | 99.5 | 101.2 | 2.4801 | 2.4780 | 2.4656 |
| $[Au(PH_3)_3]^+$ | 298.5 ± 0.6 | 170.4 | 92.0 | 97.6 | 2.6141 | 2.6209 | 2.4470 |
| $[Au(PH_3)_3]Cl$ | 290.5 ± 1.0 | 160.8 | 97.0 | 96.9 | 2.4846 | 2.4844 | 2.5330 |
| $[Au(PH_3)_3]I$ | 289.3 ± 2.0 | 163.3 | 95.4 | 95.4 | 2.4887 | 2.4887 | 2.6077 |

*Denotes an average

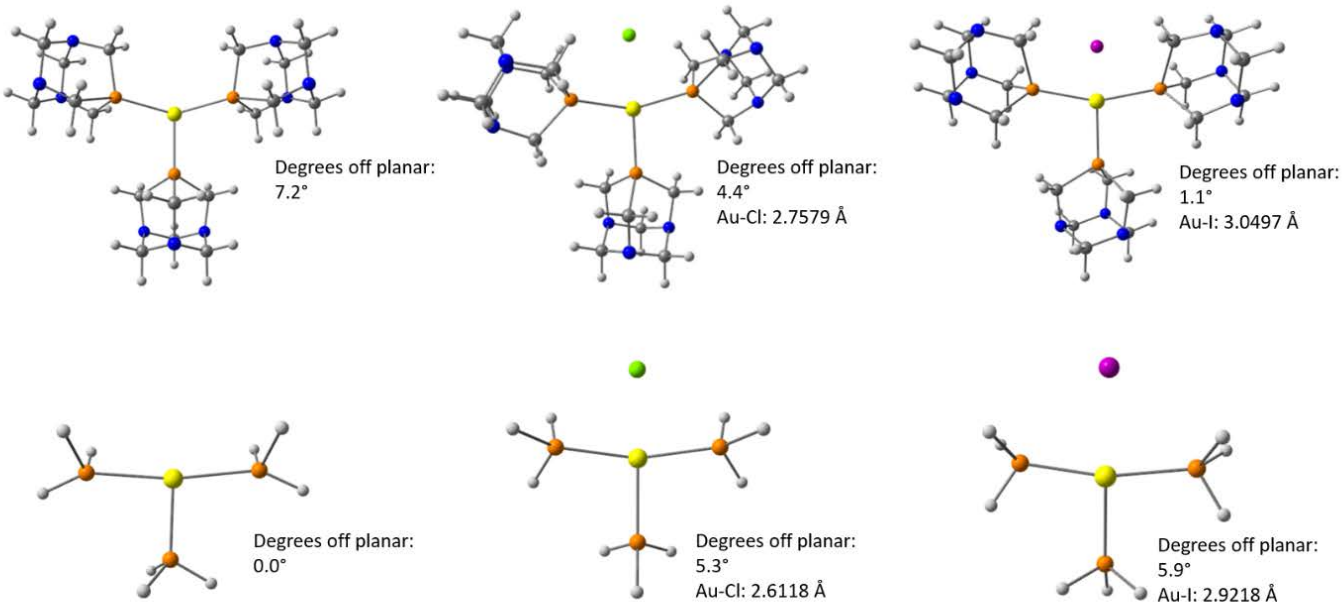


**Figure 2.2: Excited state structures of $AuTPA_3$/$AuTPA_3X$ versus $Au(PH_3)_3$/$Au(PH_3)_3X$ along with deviations from linearity and the Au-X bond length.**

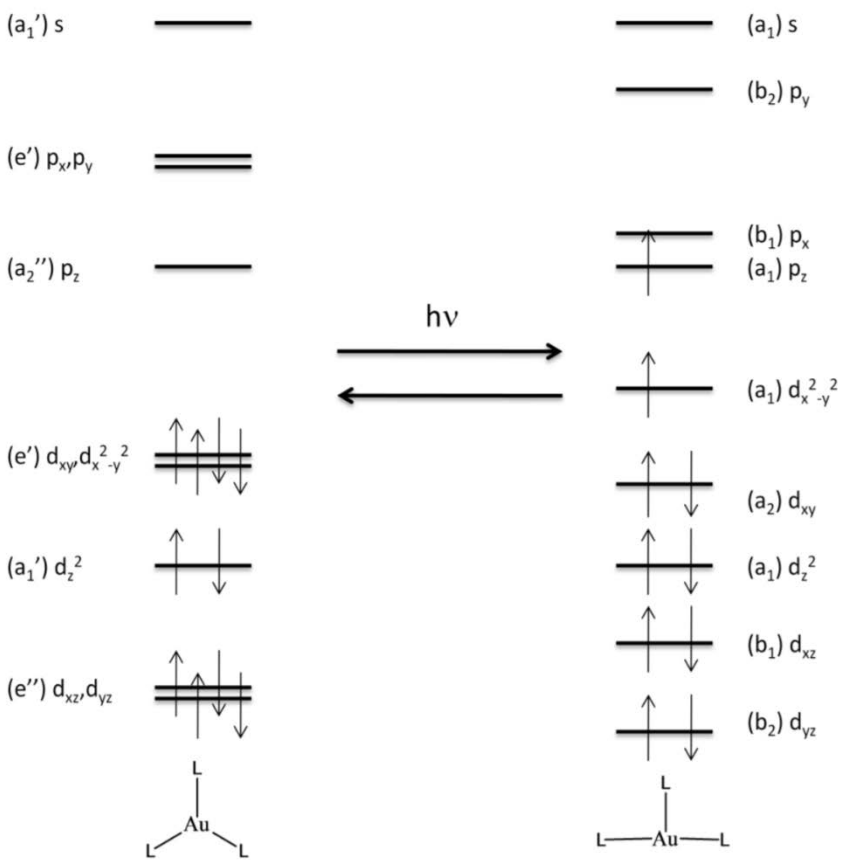


**Figure 2.3: Splitting of the 5d orbitals in the ground state ($D_{3h}$ geometry) (left) and the excited state ($C_{2v}$ geometry) (right).**

Based on these geometric and electronic arguments, the phosphine ligand seems suitable to model the phenomena seen in the TPA complexes. While some of the geometric parameters are significantly different due to the lack of steric bulk in the phosphine ligand, electronically they are similar complexes. Both complexes experience the same type of distortion and the excited states are similar. To account for the differences in the geometric parameters, the phosphine complexes will be altered to match the geometry of the TPA complexes. Since the TPA ligand is spectroscopically silent and not involved in the transitions of interest, this will ease computational cost for the calculation of the excitation and emission spectra with and without spin-orbit relativity.

### 2.3.1 Excited State Distortion and Bonding

As discussed above, upon excitation there is a geometric distortion from trigonal planar $D_{3h}$ geometry to a t-shape $C_{2v}$ geometry. The degree of distortion seen in Au(I) three-coordinate complexes has been shown to be dependent upon the cone angle of the ligands.[2] In this study the degree of distortion is also shown to be dependent upon the presence and identity of the counterion. In the excited there is significant distortion of one of the P-Au-P angles and there is migration of the counterion for the neutral complexes (**Figure 2.4**). The cationic version of the complex experiences a smaller distortion of the P-Au-P angle than the neutral complexes. For the neutral complexes, there is a larger distortion seen for the iodo complex versus the chloro complex. This is reasoned to be due to the fact that the iodide is a larger anion and as it moves closer to the Au and in between the two ligands, it forces a larger angle.

As for the migration of the counterion in the excited state, there is a change in the Au halide distance as well as a change in the placement of the counterion in relation to the Au-P plane (**Figure 2.5**). For the ground state, the Au halide distance remains outside the sum of the covalent radii (2.41 Å for chloride and 2.75 Å for iodide)[29] but there is a small contraction upon excitation (2.81 vs 2.76 Å for chloro and 3.09 vs 3.05 Å for the iodo complex). This bond contraction is also accompanied by a blue-shift of the Au halide stretching frequency and an increase in the interaction energy between the Au and the halide (**Table 2.3**). These factors lead to the conclusion that in the excited state, there is a stronger interaction energy than in the ground state. This is a phenomena also seen in $[AuTPA_2]Cl$ complex.[3] There is also movement of the halides closer to the plane of the Au-P in the excited state (**Figure 2.5**). In the ground state, the $AuP_3$ is completely planar and so the angle between this plane and the counterion is close to 90°

(88.6° in the chloro complex and 91.0° in the iodo complex). This in addition to the lack of puckering of the $AuP_3$ moiety leads to the conclusion that this is a non-interacting counterion in the ground state. However, once excited these angles increase to 173.2° and 135.1°. This result in conjunction with the puckering of the $AuP_3$ center leads to the conclusion that there is some interaction of the Au center with the halides in the excited state. These geometric analysis lead to the conclusion that while $[AuTPA_3]^+$ and $[AuTPA_3]X$ may have similar ground state properties, the excited state properties of these complexes may differ.

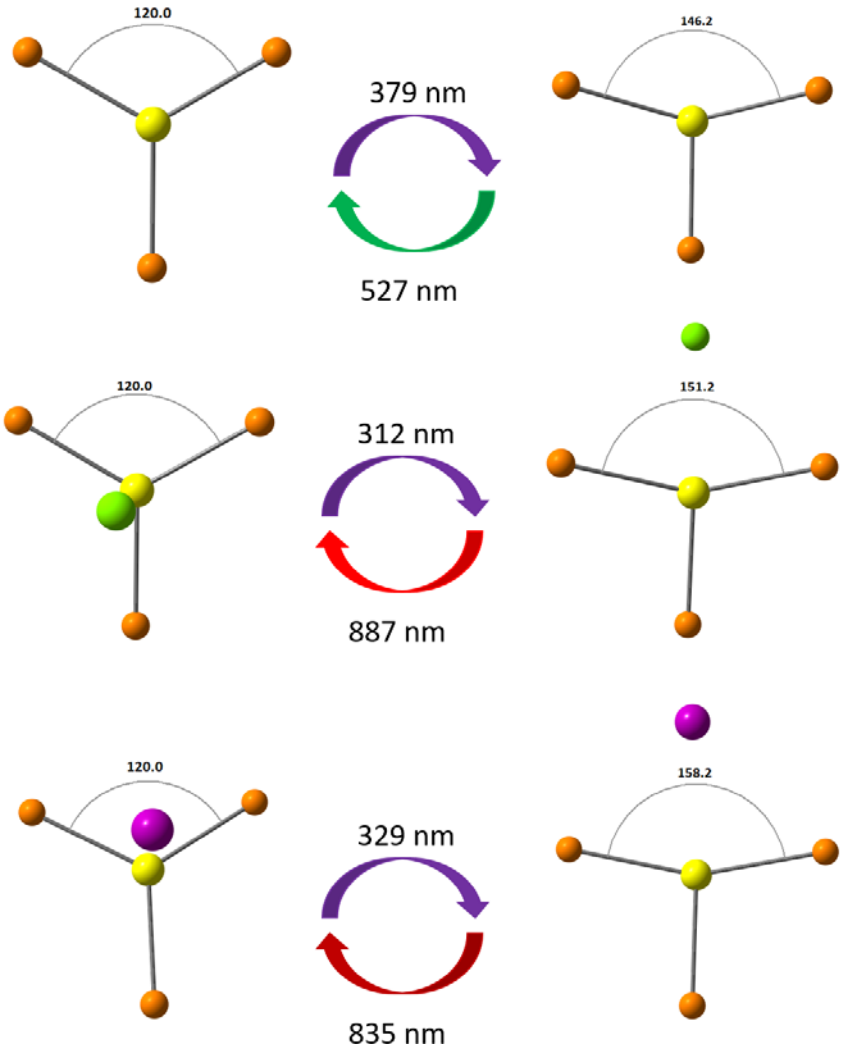


**Figure 2.4: Excited state distortion for complexes $[AuTPA_3]^+$ (left), $[AuTPA_3]Cl$ (middle), and $[AuTPA_3]I$ (right) with diabatic excitation and emission energies and angle measurements.**

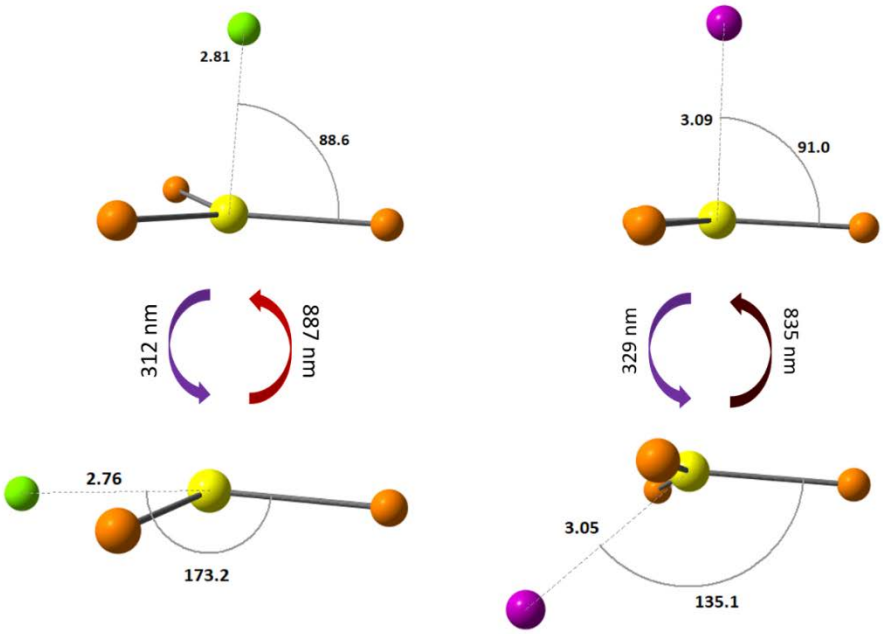


**Figure 2.5: Migration of the halide counterion in the excited state for [AuTPA$_3$]Cl (left) and [AuTPA$_3$]I (right).**

**Table 2.3: Summary of Au-X bond length, vibrational frequency and dissociation energy for the ground and excited state.**

| | Au-X bond length (Å) | Au-X vibrational frequency ($cm^{-1}$) | $TPA_3$Au-X Dissociation Energy ($cm^{-1}$) |
|---|---|---|---|
| $^1$[AuTPA$_3$]Cl | 2.81 | 162.6 | 35139.3 |
| $^3$[AuTPA$_3$]Cl | 2.76 | 169.0 | 36386.0 |
| $^1$[AuTPA$_3$]I | 3.09 | 110.0 | 31467.8 |
| $^3$[AuTPA$_3$]I | 3.05 | 123.7 | 32555.1 |

Given the changes in the geometry of the excited state with the inclusion of the counterion, it is reasonable to surmise that the excited state geometry of the neutral complexes are different from the cationic complex. However, both states possess approximate $C_{2v}$ symmetry

so the group theory analysis of the dipole allowed transitions and the double group analysis remains the same whether the cation is considered or not.

### 2.3.2 Electronic Spectroscopy – Time-Dependent DFT

In order to look at the electronic properties of these systems, time-dependent DFT was used in order to classify the types of transitions these complexes exhibit. To begin with, a comparison was done between the absorption spectra as calculated using scalar relativity and spin-orbit relativity (**Figure 2.6**).

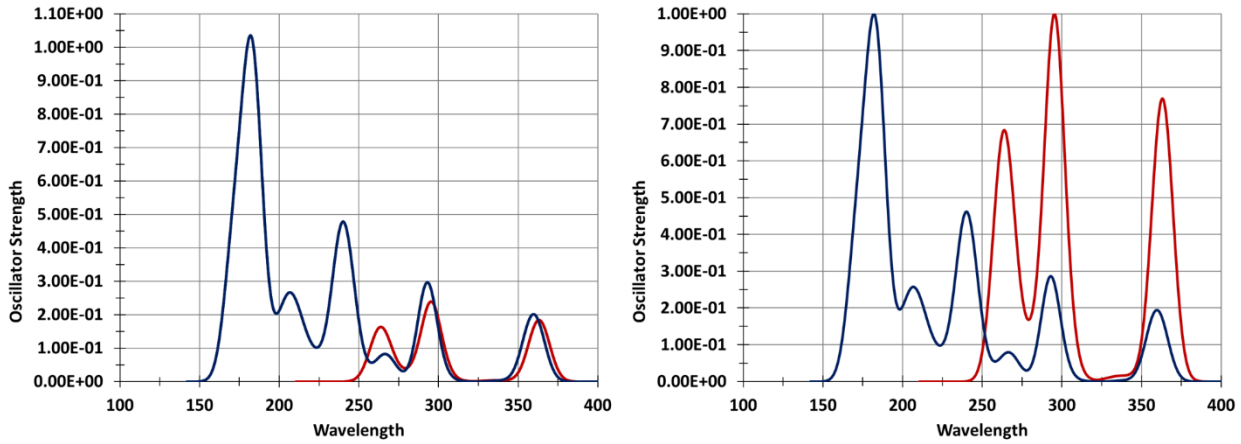


**Figure 2.6: Comparison of calculated absorption spectra with the inclusion of scalar and spin-orbit relativity for the cationic $[Au(PH_3)_3]^+$ complex at the geometry of the $[AuTPA_3]^+$ complex before (left) and after (right) normalization.**

Scalar relativity still follows the Laporte selection rules for electronic transitions; hence, the transitions that take place between a singlet and a triplet state have an oscillator strength that is equal to zero. In the spin-orbit relativistic calculations, this spin rule is relaxed and transitions between states of different multiplicities become allowed and are calculated have non-zero oscillator strengths. Due to the limitations of the fragment size for use in these calculations, the scalar relativistic spectra always show transitions at higher energies than those seen in the spin-

orbit relativistic calculations. Given that these higher energy transitions are calculated to have higher oscillator strengths, before normalization, the scalar relativistic calculations tend to make the spin-orbit spectra look weaker by comparison. However, when the spectra are overlapped, it is apparent there is some qualitative alignment of the spectra. This is due to the fact that the singlet-to-singlet transitions are still allowed so the shape of the spectra stays roughly the same. There is minor shifting of observed peaks and new peaks emerge due to the fact that states with different multiplicities have non-zero transition probabilities.

In the above spectra, the peaks can be assigned as either metal centered transitions or as metal-to-ligand charge transfer bands with the Au d-orbitals donating electron density to the phosphorous atoms. Given that the ligand is expected to spectroscopically silent whether it is the full adamantane-type cage seen in TPA or the $PH_3$ groups, these are the expected types of transitions. The HOMO of this complex is doubly degenerate as is predicted by group theory and is comprised of the $d_{xy}$ and $d_{x2-y2}$. The LUMO of this complex is based primarily on the Au 6s orbital. As for the excited state, the d-orbitals split as predicted and the SOMOs are based on the Au 6s orbital and the $d_{x2-y2}$ (**Figure 2.7**).

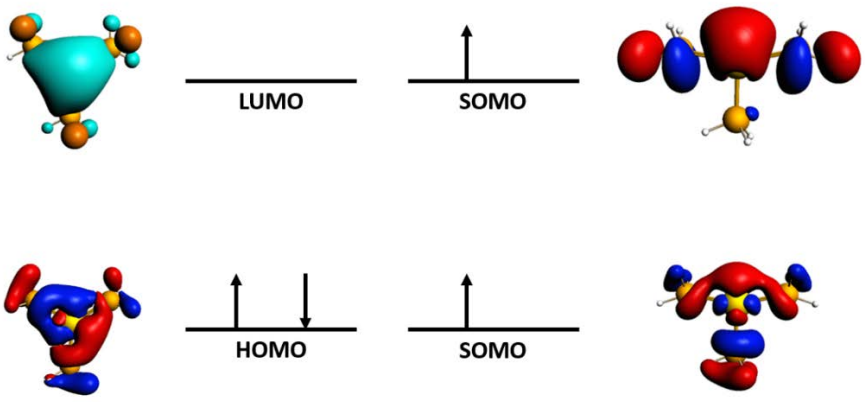


**Figure 2.7: Molecular orbital contours of the HOMO and LUMO of the singlet ground state of $[Au(PH_3)_3]^+$ (left) and SOMOs (right) of the lowest triplet state of $[Au(PH_3)_3]^+$ plotted using an isovalue of 0.03.**

In addition to calculating the absorption spectra, or with the inclusion of SOC the excitation spectra of the cationic complex, the optimized triplet geometry was used to calculate the emission spectra, both with and without SOC. This was done using the triplet geometry at an electronic singlet state and calculating the transitions at this geometry. This is depicted below in **Figure 2.8**.

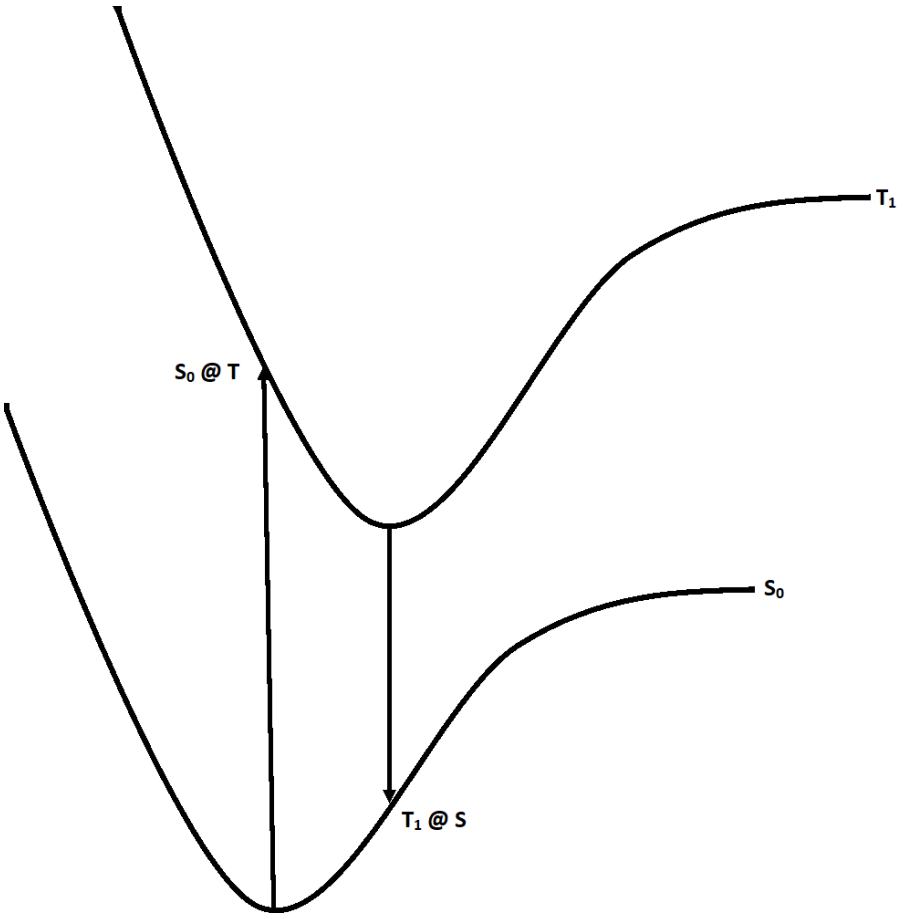


**Figure 2.8: Schematic of the transitions calculated when using the triplet geometry as an electronic singlet.**

The spectra offer the same qualitative agreement between the scalar and spin-orbit relativistic spectra seen for the excitation spectra (**Figure 2.9**). In order to determine the splitting of the lowest triplet state, transitions containing the appropriate orbital transitions were identified. In the case of this cationic complex, this included metal centered transitions and excluded

transitions that had major contributions from ligand-to-metal or metal-to-ligand charge transfer states.

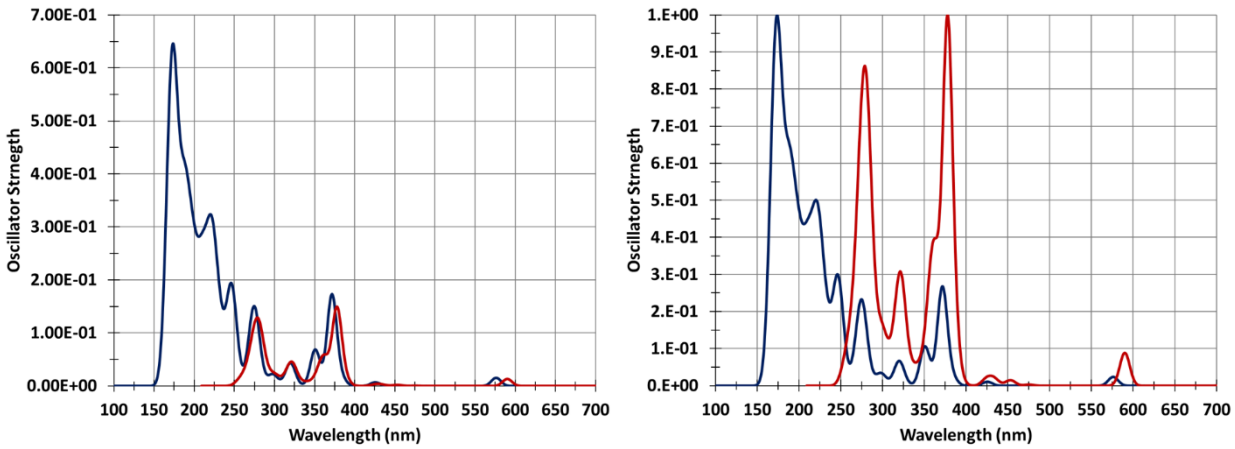


**Figure 2.9: Comparison of calculated emission spectra with the inclusion of scalar (blue) and spin-orbit (red) relativity for the cationic $[Au(PH_3)_3]^+$ complex at the geometry of the $[AuTPA_3]^+$ complex before (left) and after (right) normalization.**

However, due to the orbital rearrangement in the excited state, there is a stabilization of the virtual halide orbitals that mix with the 6s and 6p orbitals, this leads to the lowest triplet being halide based instead of Au based. This led to smaller than expected triplet splittings (15 $cm^{-1}$ for the chloro complex and 85 $cm^{-1}$ for the iodo complex). Thus, while there is still an increase in the splitting of the lowest triplet, it is less than expected.

However, previous calculations completed by Grimes[30] using multi-configurational SCF calculations using GAMESS found the second lowest excited triplet state to be 2 eVs higher in energy. Therefore, it was deemed inaccessible and unlikely to be responsible for the additional excitation and emission bands seen in the experimental spectra. These calculations supported the claims of the drastic spin-orbit splitting seen in these complexes (**Figure 2.10**).

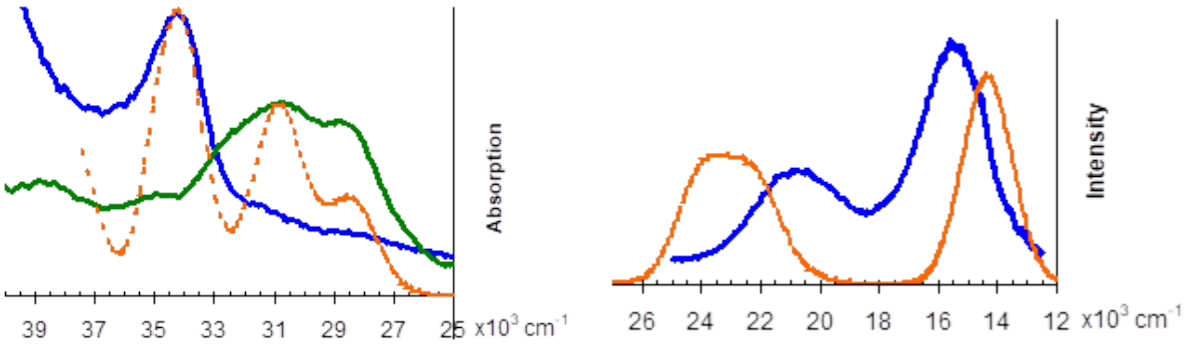


**Figure 2.10: Comparison of excitation (left) and emission spectra (right) for the experimental system [AuTPA$_3$]Cl (blue) vs the theoretical model [Au(PH$_3$)$_3$]$^+$ (orange).**

### 2.3.3 Experimental Results

The photoluminescence spectra for the [AuTPA$_3$]Cl complex was previously completed by Sinha[1] and has been reproduced below for comparison purposes (**Figure 2.11**). At 4 K the green emission at 500 nm has larger emission intensity than that of the 650 nm emission. When warmed to 70 K, the relative intensity of the 650 nm emission increases in relation to the 500 nm emission. In addition to the green and red emissions present when excited with 384 nm light, another red emission band is uncovered at 660 nm when [Au(TPA)$_3$]Cl is excited at 275 nm. For the iodide complex, at 4K the yellow emission at 570 nm has larger emission intensity than the blue emission band at 480 nm (**Figure 2.12**). This trend in intensity is also seen at 70 K. There is also an emergence of a red band at 700 nm when the sample was excited at 465 nm that is resolvable through the use of steady-state measurements until 110 K.

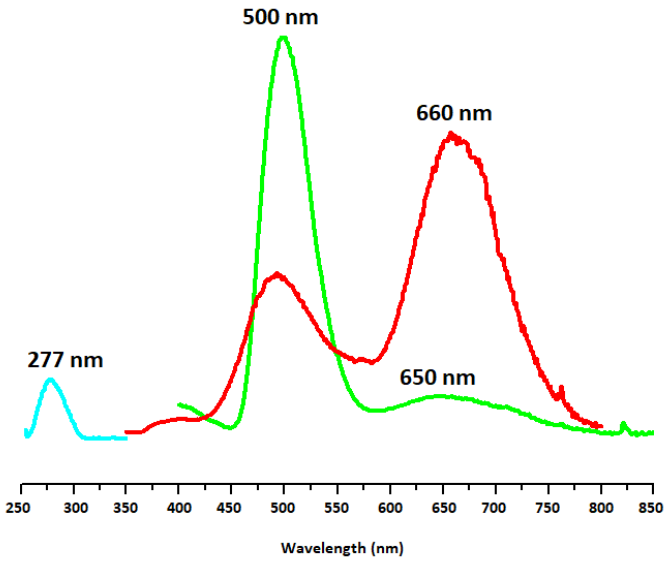


**Figure 2.11: Photoluminescence emission spectrum of [AuTPA$_3$]Cl at 4 K.**

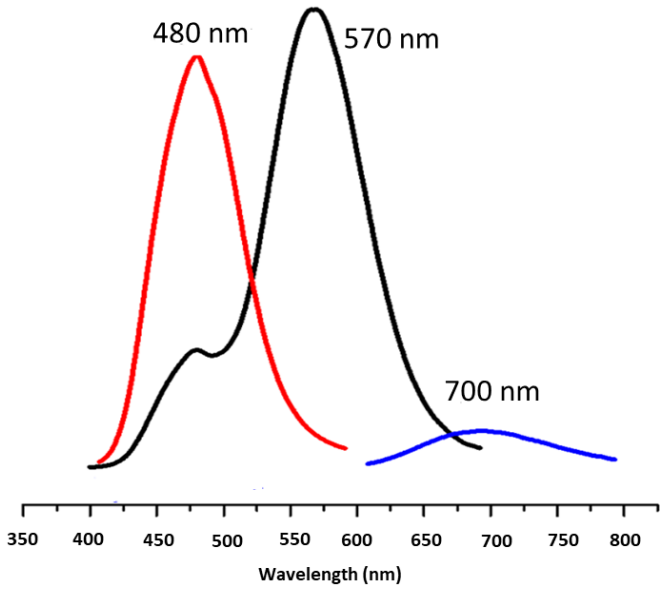


**Figure 2.12: Photoluminescence emission spectrum of [AuTPA$_3$]I at 4 K.**

As shown in **Figure 2.3**, the lowest phosphorescent transition should be from the $^3A_1$state to a $^1A_1$ state, where the electron falls from the $a_1$ ($p_z$) orbital to the $a_1$ ($d_{x^2-y^2}$). Spin-orbit coupling splits this state into three components: $A_2$ + $B_1$ + $B_2$. For the $C_{2v}$ geometry, this leads to the

transition from the $A_1$ state to the $B_1$ and $B_2$ state being dipole allowed while the $A_1$ to $A_2$ transition is dipole forbidden. This leads to the assignment of the two bands with the highest emission intensity being labeled as the $A_1$ to $B_1$ and $A_1$ to $B_2$ transitions. Given the decrease in the bond length and the increase in the vibrational frequency between the Au(I) center and the chloride, it is believed that in the excited state the chloride coordinates to the Au(I) center, leading to a deviation of the excited state geometry from the idealized $C_{2v}$ symmetry, which gives rise to the $A_1$ to $A_2$ transition having a small non-zero transition probability, which results in a low intensity emission band even at 4 K. This same analysis can be applied to the iodide version of the complex. There are still three phosphorescent energy bands and upon excitation of the complex, there is a decrease in the Au(I) iodide bond distance and an increase in the vibrational frequency between them. However, the shifting of the red band from 660 nm for the chloride complex to 700 nm for the iodide complex does lead to an increased splitting seen for the iodide complex, taking the spin-orbit splitting from about 4500 $cm^{-1}$ to about 6500 $cm^{-1}$.

For the Au(I) cation, the splitting between the $^3D_1$ and $^3D_2$ is 10300 $cm^{-1}$ while the splitting between $^3D_2$ and $^3D_3$ is 2600 $cm^{-1}$, giving rise to a total splitting between the $^3D_1$ and $^3D_3$ states of about 13000 $cm^{-1}$. There is significant mixing between levels with the same j-value which leads to the stabilization of the $^1D_2$ and destabilization of the $^3D_2$ state, which accounts for the small energy gap between the $^3D_2$ and $^3D_3$, according to Lande's interval rule. When this splitting is compared to the splitting seen in the $[AuTPA_3]Cl$ complex, there is a stabilization in the three triplet component levels which leads to a smaller splitting. When the counterion was switched to the iodide, there was a red-shift of the $A_1$ to $A_2$ transition from 650 to 700 nm and a blue shift of the $A_1$ to $B_1$ from 660 to 570 nm, which increased the splitting between the two bands. This also

led to a higher splitting between the three triplet components than that seen for the chloride complex (**Figure 2.13**).

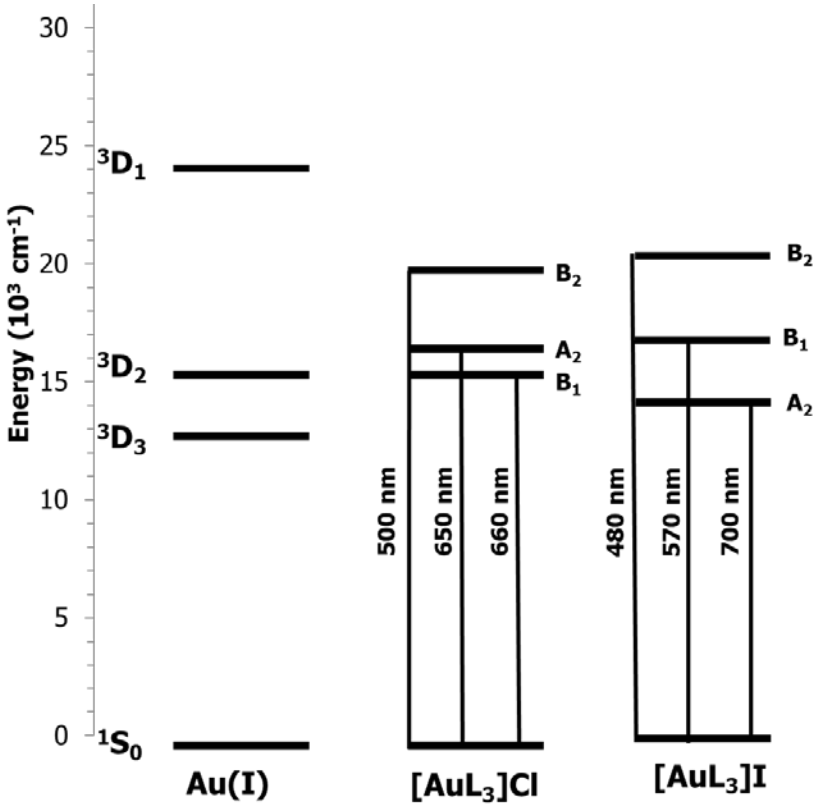


**Figure 2.13: Experimental splitting of the triplet state of Au(I) and the [$AuL_3$]X complexes demonstrating the increased splitting seen for the iodide complex versus the chloride complex.**

## 2.4 Conclusions

The spin-orbit splitting of [$AuTPA_3$]Cl and [$AuTPA_3$]I have been observed and resolved through the use of cryogenic temperature photoluminescent measurements. The splitting between the spin-orbit microstates has been determined to be about 4500 $cm^{-1}$ for the chloride complex while the splitting is increased to 6500 $cm^{-1}$ upon exchanging the chloride counterion for iodide. This degree of spin-orbit splitting has not been previously reported for any transition metal complex to the knowledge of the author. These complexes are of particular interest due to the fact that the spin-orbit splitting results in emission bands that span the visible light region

of the electromagnetic radiation spectrum. These complexes are anticipated to lead to promising applications in the world of light devices, such as organic light emitting diodes.

## 2.5 References


1. Sinha, P. *Phosphorescent Emissions of Coinage Metal-Phosphine Complexes: Theory and Photophysics (Dissertation)*. Sinha, P. Univeristy of North Texas, **2009**.

2. Barakat, K. A.; Cundari, T. R.; Omary, M. A. Jahn−Teller Distortion in the Phosphorescent Excited State of Three-Coordinate Au(I) Phosphine Complexes. *J. Am. Chem. Soc.*, **2003**, 125(*47*), 14228-14229.

3. Sinha, P.; Wilson, A. K.; Omary, M. A. Beyond a T-Shape. *J. Am. Chem. Soc.*, **2005**, 127(*36*), 12488-12489.

4. M. J. Frisch, G. W. T., H. B. Schlegel, G. E. Scuseria, M. A. Robb, J. R. Cheeseman, G. Scalmani, V. Barone, G. A. Petersson, H. Nakatsuji, X. Li, M. Caricato, A. Marenich, J. Bloino, B. G. Janesko, R. Gomperts, B. Mennucci, H. P. Hratchian, J. V. Ortiz, A. F. Izmaylov, J. L. Sonnenberg, D. Williams-Young, F. Ding, F. Lipparini, F. Egidi, J. Goings, B. Peng, A. Petrone, T. Henderson, D. Ranasinghe, V. G. Zakrzewski, J. Gao, N. Rega, G. Zheng, W. Liang, M. Hada, M. Ehara, K. Toyota, R. Fukuda, J. Hasegawa, M. Ishida, T. Nakajima, Y. Honda, O. Kitao, H. Nakai, T. Vreven, K. Throssell, J. A. Montgomery, Jr., J. E. Peralta, F. Ogliaro, M. Bearpark, J. J. Heyd, E. Brothers, K. N. Kudin, V. N. Staroverov, T. Keith, R. Kobayashi, J. Normand, K. Raghavachari, A. Rendell, J. C. Burant, S. S. Iyengar, J. Tomasi, M. Cossi, J. M. Millam, M. Klene, C. Adamo, R. Cammi, J. W. Ochterski, R. L. Martin, K. Morokuma, O. Farkas, J. B. Foresman, and D. J. Fox Gaussian 09 Revision E01. **2016**.Wallingford, CT, USA.

5. Becke, A. D. Density-functional thermochemistry. III. The role of exact exchange. *J. Chem. Phys.*, **1993**, 98(*7*), 5648-5652.

6. Burke, K.; Perdew, J. P.; Wang, Y. Electronic Density Functional Theory: Recent Progress and New Directions. **1998**. Plenum.

7. Perdew, J. P.; Burke, K.; Wang, Y. Generalized gradient approximation for the exchange-correlation hole of a many-electron system. *Phys. Rev. B*, **1996**, 54(*23*), 16533-16539.

8. Perdew, J. P.; Chevary, J. A.; Vosko, S. H.; Jackson, K. A.; Pederson, M. R.; Singh, D. J.; Fiolhais, C. Atoms, molecules, solids, and surfaces: Applications of the generalized gradient approximation for exchange and correlation. *Phys. Rev. B*, **1992**, 46(*11*), 6671-6687.

9. Perdew, J. P.; Chevary, J. A.; Vosko, S. H.; Jackson, K. A.; Pederson, M. R.; Singh, D. J.; Fiolhais, C. Erratum: Atoms, molecules, solids, and surfaces: Applications of the generalized gradient approximation for exchange and correlation. *Phys. Rev. B*, **1993**, 48(*7*), 4978-4978.

10. Cundari, T. R.; Stevens, W. J. Effective core potential methods for the lanthanides. *J. Chem. Phys.*, **1993**, 98(*7*), 5555-5565.

11. Stevens, W. J.; Basch, H.; Krauss, M. Compact effective potentials and efficient shared-exponent basis sets for the first- and second-row atoms. *J. Chem. Phys.*, **1984**, 81(*12*), 6026-6033.

12. Stevens, W. J.; Krauss, M.; Basch, H.; Jasien, P. G. Relativistic compact effective potentials and efficient, shared-exponent basis sets for the third-, fourth-, and fifth-row atoms. *Can. J. Chem.*, **1992**, 70(*2*), 612-630.

13. Woon, D. E.; Jr., T. H. D. Gaussian basis sets for use in correlated molecular calculations. III. The atoms aluminum through argon. *J. Chem. Phys.*, **1993**, 98(*2*), 1358-1371.

14. Jr., T. H. D. Gaussian basis sets for use in correlated molecular calculations. I. The atoms boron through neon and hydrogen. *J. Chem. Phys.*, **1989**, 90(*2*), 1007-1023.

15. Peterson, K. A.; Puzzarini, C. Systematically convergent basis sets for transition metals. II. Pseudopotential-based correlation consistent basis sets for the group 11 (Cu, Ag, Au) and 12 (Zn, Cd, Hg) elements. *Theor. Chem. Acc.*, **2005**, 114(*4*), 283-296.

16. Peterson, K. A.; Shepler, B. C.; Figgen, D.; Stoll, H. On the Spectroscopic and Thermochemical Properties of ClO, BrO, IO, and Their Anions. *J. Phys. Chem. A*, **2006**, 110(*51*), 13877-13883.

17. ADF2014, SCM, Theoretical Chemistry **2014**.Amsterdam.

18. Fonseca Guerra, C.; Snijders, J. G.; te Velde, G.; Baerends, E. J. Towards an order-N DFT method. *Theor. Chem. Acc.*, **1998**, 99(*6*), 391-403.

19. te Velde, G.; Bickelhaupt, F. M.; Baerends, E. J.; Fonseca Guerra, C.; van Gisbergen, S. J. A.; Snijders, J. G.; Ziegler, T. Chemistry with ADF. *J. Comp. Chem.*, **2001**, 22(*9*), 931-967.

20. Lenthe, E. v.; Baerends, E. J.; Snijders, J. G. Relativistic regular two-component Hamiltonians. *J. Chem. Phys.*, **1993**, 99(*6*), 4597-4610.

21. Lenthe, E. v.; Snijders, J. G.; Baerends, E. J. The zero-order regular approximation for relativistic effects: The effect of spin–orbit coupling in closed shell molecules. *J. Chem. Phys.*, **1996**, 105(*15*), 6505-6516.

22. van Lenthe, E.; van Leeuwen, R.; Baerends, E. J.; Snijders, J. G. Relativistic regular two-component Hamiltonians. *Int. J. Quant. Chem.*, **1996**, 57(*3*), 281-293.

23. Becke, A. D. Density-functional exchange-energy approximation with correct asymptotic behavior. *Phys. Rev. A*, **1988**, 38(*6*), 3098-3100.

24. Van Lenthe, E.; Baerends, E. J. Optimized Slater-type basis sets for the elements 1–118. *J. Comp. Chem.*, **2003**, 24(*9*), 1142-1156.

25. van Gisbergen, S. J. A.; Snijders, J. G.; Baerends, E. J. Implementation of time-dependent density functional response equations. *Comp. Phys. Comm.*, **1999**, 118(*2*), 119-138.

26. Rosa, A.; Baerends, E. J.; van Gisbergen, S. J. A.; van Lenthe, E.; Groeneveld, J. A.; Snijders, J. G. Electronic Spectra of M(CO)6 (M = Cr, Mo, W) Revisited by a Relativistic TDDFT Approach. *J. Am. Chem. Soc.*, **1999**, 121(*44*), 10356-10365.

27. Wang, F.; Ziegler, T.; Lenthe, E. v.; Gisbergen, S. v.; Baerends, E. J. The calculation of excitation energies based on the relativistic two-component zeroth-order regular approximation and time-dependent density-functional with full use of symmetry. *J. Chem. Phys.*, **2005**, 122(*20*), 204103.

28. Wang, F.; Ziegler, T. A simplified relativistic time-dependent density-functional theory formalism for the calculations of excitation energies including spin-orbit coupling effect. *J. Chem. Phys.*, **2005**, 123(*15*), 154102.

29. Coredeo, B.; Gómez, V.; Platero-Prats, A. E.; Revés, M.; Echeverría, J.; Cremades, E.; Barragán, F.; Alvarez, S. Covalent radii revisited. *Dalton Trans.*, **2008**, 21, 2832-2838.

30. Sinha, P.; Grimes, T. V.; Cundari, T. R.; Omary, M. A. Photoluminescent resolution of the spin-orbit split microstates of Au(I) complexes. **Unpublished Work**.

# CHAPTER 3

# 21ST CENTURY ALCHEMY: CUPRIPHICATION OF GOLD TO SENSITIZE $D^{10}$-$D^{10}$ METAL-METAL BONDS AND NEAR-UNITY PHOSPHORESCENCE QUANTUM YIELD[2]

## 3.1 Introduction

A novel synthesis of heterobimetallic **$Au_4Cu_2$**, **$Au_2Cu$** and **$AuCu_2$** complexes is reported for the first time. This paper documents the unprecedented formation of a bona fide polar-covalent, ligand-unassisted $d^{10}$-$d^{10}$ bond between Cu(I) and Au(I) atoms of an **$Au_4Cu_2$** hexanuclear complex. Moreover, cupriphication of gold in **$Au_4Cu_2$** and **$Au_2Cu$** species leads to near-unity photoluminescence quantum yields and higher extinction coefficients vs **$Au_3$** and **$Cu_3$** precursors, challenging stereotypical Alchemy-based perceptions and paving the way for utilizing such novel materials in optoelectronic devices for which we have successfully demonstrated the fabrication of functional thin-film forms. Novel scientific phenomena enabling societally-useful technologies are discovered, embodied by counterintuitive metal-metal bonds and high-efficiency, Ir-/rare-earth-free phosphorescent-organic-light-emitting-diode (PhOLED)/phosphor-converted-inorganic-light-emitting-diode (pcLED) emitters of use in more-environmentally-friendly lighting and/or video-display products.

Seminal work by Cotton and co-workers addressed "the question raised by many compounds in which short metal-metal distances might be taken to imply the existence of M-M bonds…, the answer depending on the degree of participation of outer (s,p) valence

[2]Entire chapter is a reprint of Galassi, R.; Ghimire, M. M.; Otten, B. M.; Ricci, S.; McDougald Jr., R. N.; Almotawa, R. M.; Almoud, D.; Ivy, J. F.; Rawashdeh, A-M. M.; Nesterov, V. N.; Reinheimer, E. W.; Daniels, L. M.; Burini, A.; Omary, M. A. Cupriphication of gold to sensitize $d^{10}$-$d^{10}$ metal-metal bonds and near-unity phosphorescence quantum yields. *Proc. Nat.'l Acad. Sci.*, **2017**, 114(*16*), E5042-E5051. Experimental work kept for context. Computational work performed by author.

orbitals….Although the metal-metal distances are short (Cu-Cu = 2.497(2) and Ag-Ag = 2.705(1) Å), we conclude that there is little or no direct metal-metal bonding."[1] Here, we show that outer 4s ($Cu^{I}$) and 6s ($Au^{I}$) orbitals can admix with the respective valence 3d and 5d orbitals to sensitize a bona fide polar-covalent metal-metal bond between two $d^{10}$ centers manifest by two quanta of a rather short, 2.8750(8) Å, Cu(I)-Au(I) distance without any ligand-bite-size assistance. Other complexes of the same family did not exhibit such a bond but, instead, favored cupro-aurophilic intermolecular interactions to either cuprophilic or aurophilic analogues in their supramolecular structures. The reduced symmetry in this family of complexes is also shown to impart higher extinction coefficients and phosphorescence quantum yields than those attained by the parent homometallic precursor complexes.

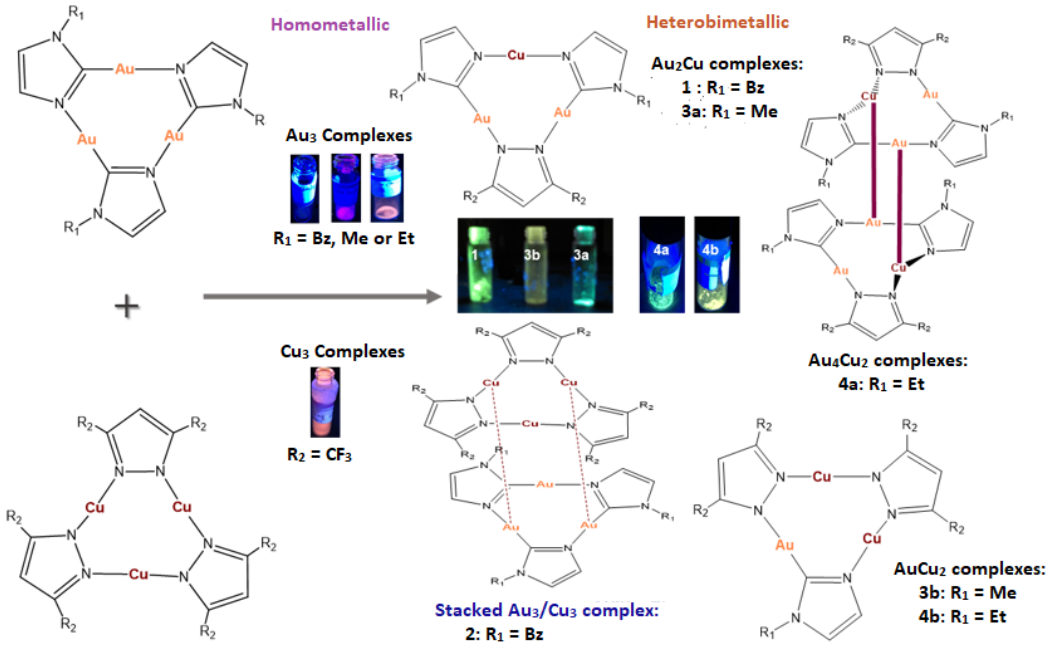


**Figure 3.1: Synthesis and solid-state luminescence of homometallic complexes, heterobimetallic and stacking product complexes. The stacking product does not exhibit detectable luminescence at room temperature.**

Heterometallic complexes are remarkable molecules owing to their unique catalytic and

optoelectronic properties.[2, 3] Heterometallic species involving coinage metals have received immense attention owing to their fascinating structural and photophysical properties, including polar-metallophilic interactions and stimulus-responsive luminescence.[3-9] Notable examples include Balch's luminescent Ir-Au-Ir chains,[4] Fackler's luminescence-thermochromic $Ag^{I}Au^{I}$-pyrazolates,[7] and Catalano's Au-Cu[8] and Laguna's Au-Tl vapochromic-sensors.[9] Herein, we report heterobimetallic Au(I)/Cu(I) complexes shown in **Figure 3.1**, including their synthetic chemistry and unusual structural and photophysical properties.

## 3.2 Results and Discussion

### 3.2.1 Synthetic Chemistry

Reacting π-basic $[Au(\mu\text{-}C^2,N^3\text{-BzIm})]_3$, $[Au(\mu\text{-}C^2,N^3\text{-EtIm})]_3$, or $[Au(\mu\text{-}C^2,N^3\text{-MeIm})]_3$ with π-acidic $[Cu(\mu\text{-}3,5\text{-}(CF_3)_2Pz)]_3$ attains new metal clusters, composition of which is sensitive to precursor stoichiometry (**Figure 3.1**). The four product categories are *heterobimetallic* ***$Au_4Cu_2$,*** $[Au_2(\mu\text{-}C^2,N^3\text{-EtIm})_2Cu(\mu\text{-}3,5\text{-}(CF_3)_2Pz)]_2$ (**4a**), ***$Au_2Cu$*** $[Au_2(\mu\text{-}C^2,N^3\text{-BzIm})_2Cu(\mu\text{-}3,5\text{-}(CF_3)_2Pz)]$ (**1**) and $[Au_2(\mu\text{-}C^2,N^3\text{-MeIm})_2Cu(\mu\text{-}3,5\text{-}(CF_3)_2Pz)]$ (**3a**), and ***$AuCu_2$*** $[Au(\mu\text{-}C^2,N^3\text{-MeIm})Cu_2(\mu\text{-}3,5\text{-}(CF_3)_2Pz)_2]$ **(3b)** and $[Au(\mu\text{-}C^2,N^3\text{-EtIm})Cu_2(\mu\text{-}3,5\text{-}(CF_3)_2Pz)_2]$ **(4b)** complexes and the *π-acid/π-base* ***$Au_3/Cu_3$*** *stacked complex* $[Au(\mu\text{-}C^2,N^3\text{-BzIm})]_3$ $[Cu(\mu\text{-}3,5\text{-}(CF_3)_2Pz)]_3$ (**2**). Either $[Au(\mu\text{-}C^2,N^3\text{-MeIm})]_3$ or $[Au(\mu\text{-}C^2,N^3\text{-EtIm})]_3$ react with $[Cu(\mu\text{-}3,5\text{-}(CF_3)_2Pz)]_3$ in a 2:1 or 1:2 stoichiometric ratio to affords **3a**, **4a**, **3b**, or **4b**, respectively, whereas 2:1 and 1:2 reactions of $[Au(\mu\text{-}C^2,N^3\text{-BzIm})]_3$ and $[Cu(\mu\text{-}3,5\text{-}(CF_3)_2Pz)]_3$ yielded **1** and **2**, respectively. Formation of **2** hypothesizes that the first step in the other reactions might entail an π-acid/π-base stacked intermediate preceding subsequent ligand and/or metal exchange. Besides FT-IR, $^{1}$HNMR and $^{13}$CNMR characterizations,

crystallographic analysis of complexes **1**, **3a**, and **4a** highlight the formation of heterobimetallic **$Au_2Cu$** or **$Au_4Cu_2$** or **$AuCu_2$** metallocycles, whereas **2** and **3b** are confirmed by elemental analysis. Crystallographic evidence (*vide infra*) suggests ligand exchange *vs* the homometallic **$Au_3$** and **$Cu_3$** precursors, in contrast with the behavior for analogous Ag(I)/Au(I) complexes.[7] Crystals of **1**, **3a** and **4a** show bright-green photoluminescence *vs* yellow for **3b** and **4b** (**Figure 3.1**), with no detectable luminescence for stack **2** at room temperature (bright-yellow at 77 K; **Figure 3.2**).

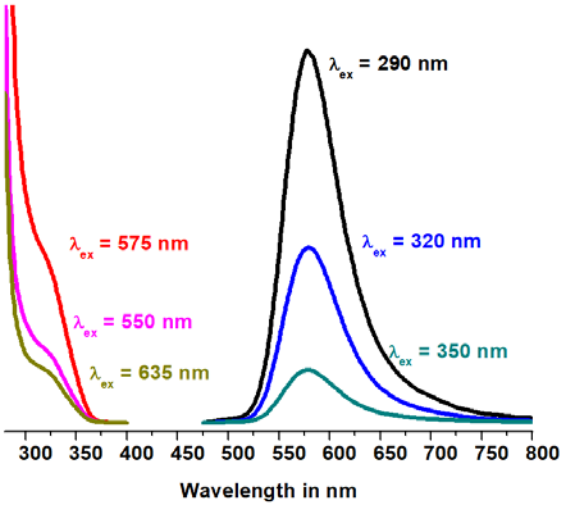


**Figure 3.2: Shows the steady state photoluminescence for a solid sample of {[Au(BzIm)]$_3$[Cu((CF$_3$)$_2$Pz)]$_3$} at 77 K. Excitation and emission wavelengths used in the emission and excitation spectra, respectively, are labeled on each trace.**

### 3.2.2 Crystal Structures

**Figure 3.3**, **Figure 3.4**, and **Figure 3.5** illustrate the crystal structures for **1**, **3a**, and **4a** while **Table 3.1** summarizes the corresponding structural parameters. The heterobimetallic complexes **1**, **3a** and **4a** crystallize in orthorhombic, monoclinic and triclinic crystal systems with space groups *Pbcn*, *C*2/*c*, and *P-1*, respectively (**Table 3.1**). The crystal structure of **3a** is disordered in metal centers and *N*-methylimidazolate ligands sharing position, whereas no disorder is found for **1** or **4a**.

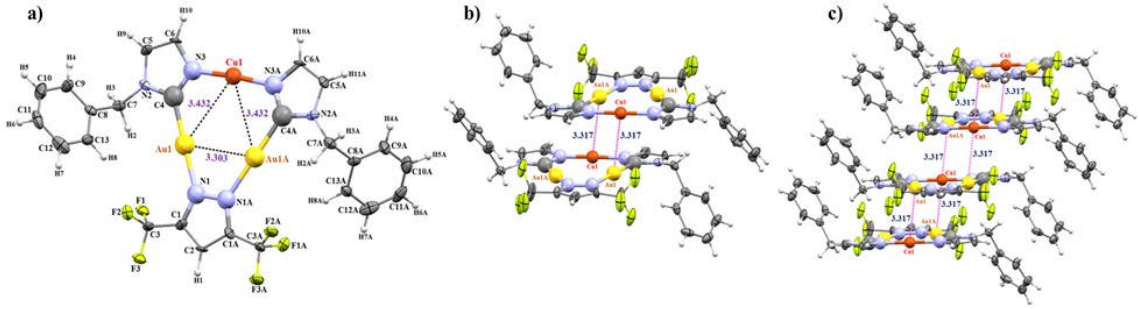


**Figure 3.3: ORTEP plot for a) Crystal structure for one molecule of complex 1, b) Dimer-of-trimer formation found in the stacking of 1, and c) Fragment of crystal packing of 1 along the b axis.**

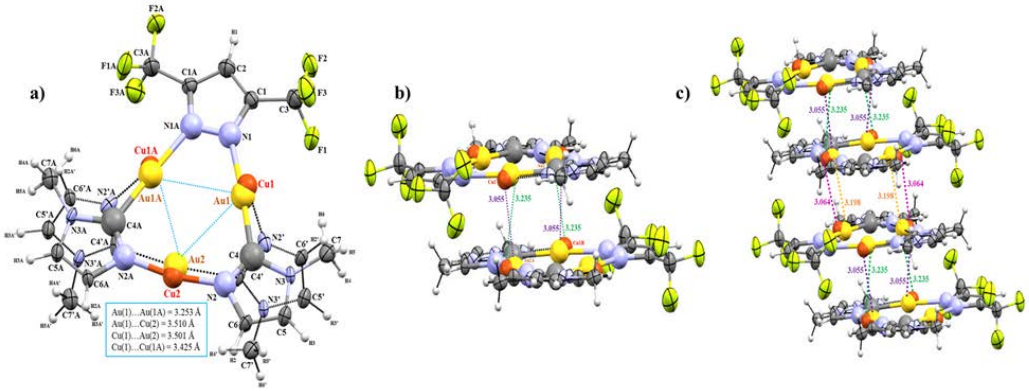


**Figure 3.4: ORTEP plot for a) Crystal structure for one molecule of complex 3a, The box underneath it contains the intramolecular M-M distances, b) Dimer-of-trimer formation found in the stacking of 3a. c) Crystal packing of complex 3a along the c axis.**

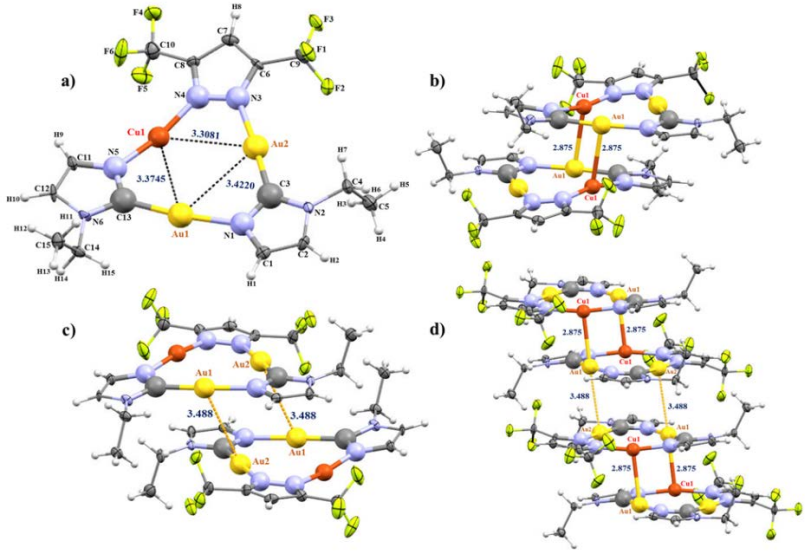


**Figure 3.5: ORTEP plot for a) Crystal structure for half the molecule, representing each monomer-of-trimer unit, of compound 4a. b) Crystal structure for one full molecule of compound 4a, c) A fragment of the crystal packing along the *a*-axis, and d) Extended crystal packing of 4a molecules along the *a*-axis.**

**Table 3.1: Crystallographic Data and Refinement Parameters for 1, 3a, and 4a.**

| | Complex **1** | Complex **3a** | Complex **4a** |
|---|---|---|---|
| Empirical formula | $C_{25}H_{19}Au_2CuF_6N_6$ | $C_{13}H_{11}Au_2CuF_6N_6$ | $C_{30}H_{30}Au_4Cu_2F_{12}N_{12}$ |
| Molecular Weight | 974.94 | 822.75 | 1701.60 |
| Crystal System | Orthorhombic | Monoclinic | Triclinic |
| Space group | *Pbcn* | *C2/c* | *P-1* |
| *a* (Å) | 27.205 (16) | 19.094 (2) | 8.09925 (14) |
| *b* (Å) | 12.118 (7) | 12.486 (1) | 10.7781 (2) |
| *c* (Å) | 7.937 (5) | 7.8003 (6) | 12.8747 (3) |
| α (°) | 90 | 90 | 114.6079 (19) |
| β (°) | 90 | 102.329 (1) | 92.4118 (16) |
| γ (°) | 90 | 90 | 92.7737 (15) |
| *V* (Å$^3$) | 2617 (3) | 1816.7 (3) | 1018.22 (4) |
| *Z* | 4 | 4 | 1 |
| T (K) | 100 (2) | 100 (2) | 100 (2) |
| $\rho_{calcd}$ (mg/m$^3$) | 2.475 | 3.008 | 2.775 |
| μ (mm$^{-1}$) | 12.063 | 17.342 | 15.476 |
| F(000) | 1808 | 1488 | 776 |
| Reflections Collected | 19771 | 10607 | 12099 |
| Independent Reflections | 2317 | 1918 | 4155 |
| $R_{int}$ | 0.1778 | 0.0260 | 0.0334 |
| $^aR_1[I>2\sigma(I)]$ | 0.0508 | 0.0386 | 0.0235 |
| $^bwR_2[I>2\sigma(I)]$ | 0.1152 | 0.0966 | 0.0507 |

$^aR_1[I>2\sigma(I)] = \Sigma||F_o| - |F_c||/\Sigma|F_o|$. $^bwR_2[I>2\sigma(I)] = \{\Sigma[w(F_o^2 - wF_c^2)^2/\Sigma[w(F_o^2)^2]\}^{1/2}$

Units of **1** and **3a** are crystallographically-packed such that (C-Au-N, N-Cu-N) angles slightly deviate from linearity, attaining (177.6°, 175.7°) in **1** and (175.4°, *167.8°-170.6°*) in **3a** – *range/uncertainty/untrustworthiness in the latter* due to disorder. Likewise, the Au-C bond and the Au-N bond distances in **3a** are slightly shorter than those found in **1**, whereas the Cu-N bond

lengths are extremely long when compared to those obtained for **1** (**Table 3.1**). When compared to those reported for the starting homometallic complexes $[Au(\mu\text{-}C^2,N^3\text{-}BzIm)]_3$ and $[Cu(\mu\text{-}3,5\text{-}(CF_3)_2Pz)]_3$,[10, 11] the bond angles around Au atoms are longer while those around Cu atoms are shorter in **1** and **3a**. In the context of non-covalent metallophilic interactions in **1**, two intermolecular Au···Cu contacts (3.317 Å) link cyclotrimer molecules, forming extended stacks (**Figure 3.3**). Next-neighbor dimer-of-trimer units form a $Cu_2Au_4$ metal framework that adopts a chair-like configuration with two equal intertrimer Cu···Au separations (**Figure 3.3**). Similarly, there are four intermolecular Au···Cu contacts for each molecule in **3a** (**Figure 3.4**), two interactions above and two below each molecule. This allows extended-chain formation in a staircase motif of dimer-of-trimer units in a chair-like configuration (**Figure 3.4**). Remarkably, these intertrimer separations in **1** and **3a** are significantly shorter than the intratrimer Cu···Au distances (**Figure 3.3**; **Figure 3.4**). The configuration of packed units is not atypical for non-covalently-bonded **$Au_3$···$Au_3$** or **$Cu_3$···$Cu_3$** metallophilic structures. For example, the packing herein for **1** or **3a** – notwithstanding the latter's disorder – is similar to that in [Au-*C,N*-(ethoxy)(*p*-tolyl)carbeniate]$_3$ or $[Au(\mu\text{-}3,5\text{-}(CF_3)_2Pz)]_3$.[12]

### 3.2.3 Covalent $d^{10}$-$d^{10}$ Metal-Metal Bonding

The specific situation for **4a** merits a multi-faceted discussion of structural, spectral, and computational data analyses to scrutinize its possible $3d^{10}$-$5d^{10}$ polar-covalent metal-metal bonds.

#### 3.2.3.1 Crystallographic Considerations

The principal piece of evidence to validate such a bond is the presence of two quanta of

a ligand-unassisted short distance of 2.875 Å between the two crystallographically-equivalent Cu(1) atoms with their next-neighbor two crystallographically-congruent Au(1) atoms in the adjacent cyclotrimer, as shown in the crystal structure of compound **4a** (**Figure 3.5**) in lieu of the shortest such an intermolecular distance ever reported between any two $d^{10}$ centers so as to deem it a "metal-metal bond" *vis-à-vis* "metallophilic interaction". The affinity of copper to gold is manifest by a rather significant under-deviation from linearity in the N(4)-Cu(1)-N(5) angles of 167° in the two adjacent cyclotrimers to effect attractive shortening of the two Cu(1)-Au(1) ligand-unassisted covalent bonds (**Figure 3.5** and **Table 3.2**). This is exactly opposite to the situation in Cotton's work on $M_2(form)_2$ systems (M = Cu(I) or Ag(I); form = *N,N'*-di-*p*-formamidinate) whereby the N(1)-Cu-N(2) or N(1)-Ag-N(2) angles of 185.5° and 191.2°, respectively, over-deviated from linearity to effect repulsive elongation of Cu···Cu or Ag···Ag ligand-assisted non-covalent bonds/interactions beyond what the bite size allows with linear bonds.[1] The situation here, represents a greater affinity of copper to gold than it does gold to copper, given the smaller deviation from linearity in the C(13)-Au(1)-N(1) angle of 173° (which is an attractive under-deviation nonetheless). By the same token, the pair of C(3)-Au(2)-N(3) angles of 176° each associated with the Au(2)···Au(2) interaction comprise the least deviation from linearity among the three metal centers in each **4a** molecule. The attractive deviation from linearity can be used to substantiate the involvement of $3d_\pi$-$5d_\pi$ component of the Cu(I)-Au(I) (or $d^{10}$-$d^{10}$) bonding claimed herein for the Cu(1)-Au(1) ligand-unassisted polar-covalent bonds in **4a** crystals – in addition to the $3d_\sigma$-$5d_\sigma$ component – in the same manner by which Cotton *et al*. have justified the opposite repulsive deviation to imply the lack of involvement of $nd_\pi$ orbitals in M-M bonding in favor of M-L $\pi$-bonding in $M_2(form)_2$ species.[1] Additional theoretical insights for $3d_\sigma$-

$5d_\sigma/3d_\pi$-$5d_\pi/3d_\delta$-$5d_\delta$ bonding are addressed based on dispersive DFT computations (*vide infra*). To end this crystallographic argument, however, we draw attention to the recently-discovered quintuple M-M bond by Power and co-workers for trigonal Cr(I) $d^5$ centers[13] and the related less-than-quintuple M-M bonds in trigonal paddlewheels of non-$d^5$ systems that nonetheless involve the use of all five d orbitals in M-M bonding, as commented upon and reviewed very recently by Murillo, on the heels of the 50th anniversary of the delta bond.[14] The reduction of symmetry from tetragonal to trigonal (idealistically $D_{4h}$ to $D_{3h}$) allows stronger d-d orbital mixing when the number of bridging ligands were reduced, liberating $d_{(x2-y2)}$ – indeed all d orbitals with x and y components – to render them available for M-M bonding instead of being used solely for M-L bonding.[15] In a similar manner, the symmetry reduction from an idealized $D_{\infty h}$ to $C_{2v}$ in the coordination sphere of specially the Cu1 atom in **4a** crystals renders stronger mixing of $3d_{\sigma/\pi/\delta}$ orbitals with the corresponding $5d_{\sigma/\pi/\delta}$ orbitals of the Au1 atom in the next-neighbor molecule at the expense of mixing with the orbitals of the two pyrazolate ligands or the Au2 and Au1 atoms in the same molecule. Additionally, there is significant deviation from planarity of the Cu and Au atoms with respect to the centroid plain defined by the four N and two C atoms of the Im and Pz ligands in each monomer-of-trimer unit (**Figure 3.5**); this deviation also acts to facilitate the Cu(I)-Au(I) intertrimer interaction. To quantify the deviation from planarity experienced by the Cu1 atom, we define three independent centroids. Centroid 1 ($c_1$) is calculated between atoms C3 and N1 as this position was *ortho* to the copper atom in the trimetallic cluster. Centroid 2 ($c_2$) corresponds to the plane defined by the atoms Au1, Au2, C3, C13, N1, N3, N4 and N5, which define the primary region of planarity within the cluster except for the Cu1 atom in question. The final centroid calculated ($c_3$) is located between atoms N4 and N5 and is superimposed upon the

position occupied by Cu1 within the trimetallic cluster. The angle between the three centroids is 178.123(10)° while the angle between $c_1$, $c_2$, and Cu1 is 173.012(19)°. The nearly 5° deviation from approximate linearity, together with a rather significant 0.204 Å separation between $c_3$ and Cu1, both offer further crystallographic support for the position of Cu1 to be clearly out of the primary plane of the cluster, hence making it available to bond with the Au1 atom of the adjacent cyclotrimer. The deviation from planarity and linearity no longer keeps Cu(I) and Au(I) as linear, 2-coordinate centers but, indeed, closer to 3-coordinate trigonal-planar and T-shaped centers, respectively, while taking into consideration the bond with one another. This is akin to the metal geometries in *bona fide* covalent M-M bonds; for example, the Au(II)-Au(II) bond is part of the square-planar arrangement as in typical $d^9$ systems.[15]

**Table 3.2: Selected Bond Lengths (Å), Intramolecular Contacts (Å) and Angles (°) for 1, 3a, and 4a.**

| Complex **1** | |
|---|---|
| Au(1)-N(1) | 2.079 (11) |
| Au(1)-C(4) | 2.007 (14) |
| Au(1)···Au(1A)#1[a] | 3.303 (2) |
| Cu(1)-N(3) | 1.860 (2) |
| Cu(1)···Au(1) | 3.432 (2) |
| Cu(1)···Au(1A)#1[a] | 3.432 (2) |
| N(1)-Au(1)-C(4) | 177.6 (5) |
| Au(1)-C(4)-N(2) | 126 (1) |
| Au(1)-C(4)-N(3) | 123 (1) |
| N(3)-Cu(1)-N(3A)#1[a] | 175.7 (7) |
| Cu(1)-N(3)-C(4) | 123 (1) |
| Cu(1)-N(3)-C(6) | 131 (1) |
| Complex **3a** | |
| Au(1)-C(4) | 2.021 (15) |

| | |
|---|---|
| Au(1)-N(1) | 2.077 (7) |
| Au(1)···Au(1A)#2[a] | 3.253 (7) |
| Au(1)···Cu(2) | 3.510 (7) |
| Cu(2)-N(2) | 1.781 (14) |
| C(4)-Au(1)-N(1) | 175.4 (4) |
| N(2A)#2[a]-Cu(2)-N(2) | 168 (1) |
| Cu(1)···Au(2) | 3.501 (7) |
| Cu(1)···Cu(1A)#2[a] | 3.425 (7) |
| Cu(1)-N(2`) | 1.91 (3) |
| Cu(1)-N(1) | 1.88 (2) |
| Au(2)-C(4`) | 2.24 (3) |
| C(4`A)-Au(2)-C(4`)#2[a] | 172 (2) |
| N(2`)-Cu(1)-N(1) | 171 (1) |
| Complex **4a** | |
| Au(1)-Cu(1)[‡] | 2.8750 (8) |
| Au(1)···Au(2)[‡] | 3.4883 (8) |
| Au(1)···Au(2)* | 3.4220 (3) |
| Au(1)···Cu(1)* | 3.3745 (7) |
| Au(1)···Cu(2)* | 3.3081 (7) |
| Au(1)-C(13) | 1.983 (6) |
| Au(1)-N(1) | 2.051 (5) |
| Au(2)-C(3) | 1.973 (6) |
| Au(3)-N(3) | 2.056 (5) |
| Cu(1)-N(4) | 1.889 (5) |
| Cu(1)-N(5) | 1.866 (5) |
| N(5)-Cu(1)-N(4) | 167.5 (2) |
| C(13)-Au(1)-N(1) | 173.4 (2) |
| C(3)-Au(2)-N(3) | 176.4 (2) |
| C(8)-N(4)-Cu(1) | 131.2 (4) |

| | |
|---|---|
| C(11)-N(5)-Cu(1) | 130.6 (4) |
| C(13)-N(5)-Cu(1) | 121.0 (4) |
| C(3)-N(1)-Au(1) | 117.3 (4) |
| C(1)-N(1)-Au(1) | 133.8 (4) |
| N(5)-C(13)-Au(1) | 122.1 (4) |
| N(6)-C(13)-Au(1) | 130.9 (4) |
| C(6)-N(3)-Au(2) | 133.6 (4) |

[a]Symmetry transformation to generate equivalent atoms: #1 –x+1, y, -z+3/2; #2: -x+1, y, -z+1/2. ‡Intermolecular separation. *Intramolecular separation.

The pertinent situation herein is somewhat akin to three other literature systems with varying degrees of similarity in M-M' distances found in complex **4a**. The first analogy – albeit less extensively – is with respect to the rather strong Pt(II)-Tl(III) polar-covalent bonding in $Tl[(NC)_5Pt\text{-}Tl(CN)_n]^{n-}$ complexes discovered by Glaser and co-workers to attain exceptionally short distances of 2.60(1), 2.62(1), and 2.64(1) Å for *n* = 1-3, respectively.[16] The electronegativity gradient and corresponding orbital mismatch between the Pt(II) and Tl(III) centers therein are greater than those for Cu(I) and Au(I) centers herein of complex **4a**, leading to a much greater shortening of the M-M' distances than those allowed by the summed van der Waals radii in the former situation 3.68 Å for Pt(II)-Tl(III) and 3.06 Å for Cu(I)-Au(I)).[17, 18] Clearly, however, the interaction is significantly "softer" and less electrostatic in nature in our situation given the smaller concentration of charge on two monovalent metals *vs* a divalent and trivalent metals. A closer similarity perhaps exists *vs* the Tl(I)-Pt(0) polar covalent bonding discovered by Catalano and co-workers for $[Pt(PPh_2py)_3Tl]X$ complexes, which led to Tl(1)-Pt(1) bond distances of 2.8888(5) and 2.8653(4) Å with X = $NO_3^-$ and $C_2H_3O_2^-$, respectively.[19] Both the distances and "softness"/electrostatic compatibility between the M-M' centers are rather similar for the

Catalano system and **4a** herein, despite the drastic difference in the coordination geometries of the corresponding M and M' centers. At the other extreme, we finally draw attention to the similarity with $AgAu(MTP)_2$ (MTP = diphenylmethylenethiophosphinate) described by Fackler and co-workers as an Ag(I)···Au(I) heterobimetallic argento-aurophilic interaction (as opposed to polar-covalent bonding) type, whereby the Ag atom exhibited attractive deviation from linearity of its S-Ag-S coordination so as to intramolecularly interact with the Au atom in the bridged-dimer molecule, leading to an Ag···Au distance of 2.9124(13) Å.[20] This ligand-assisted Ag(I)···Au(I) intramolecular distance is longer than the ligand-unassisted Cu(I)-Au(I) intermolecular distance in **4a** and, likewise, the attractive deviation from linearity is less extensive for the M···M' centers (171.71(13)° for S1-Ag-S1A and 179.1(6)° for C1-Au-C1A in $AgAu(MTP)_2$ *vs* 167.5(2)° for N5-Cu1-N4 and 173.4(2)° for C13-Au1-N1 in **4a**). The analogous ligand-unassisted intermolecular argento-aurophilic interaction in $AgAu(MTP)_2$ is much weaker at 3.635 Å (*i.e.*, > 1 Å longer than the polar-covalent intertrimer bond distance of 2.875 Å in **4a**).

In terms of literature comparisons with relevant homometallic M···M metallophilic and/or M-M covalent bonding systems, we start with the two most direct precedents – cyclotrimeric Au(I)-imidazolate and Cu(I)-pyrazolate analogues of the systems herein. Although some of us and our scientific ancestors have been studying the same compound for decades,[21, 22] it took until 2010 for the Rawashdeh-Omary group to publish the crystal structure of $[Au(\mu\text{-}C^2,N^3\text{-}BzIm)]_3$; it exhibited a semi-prismatic conformation with one long (3.558 Å) and two short (3.346 Å) intertrimer distances to manifest its strong aurophilic interactions.[10] The copper precursor for **1-4** has been studied by Dias, Omary, and co-workers and revealed rather long Cu(I)···Cu(I) cuprophilic separations of 3.813 and 3.987 Å; other partially-fluorinated analogues likewise

showed similar separations in loosely-connected extended chains, whereas alkylated analogues exhibited non-covalent dimer-of-trimer structures with much shorter separations of ca. 2.95-3.00 Å while aryl-substituted congeners attain segregated trimers.[23] Expanding beyond Au(I)-imidazolate and Cu(I)-pyrazolate to include cyclotrimers with other bridging ligands, the *strongest* intertrimer metallophilic interactions are manifest by two Au(I)-carbeniate complexes: the hexagonal polymorph of $[Au_3(MeN{=}COMe)_3]$ described originally by the Balch group in 1997,[24] and a recent modification thereof, $[Au_3(MeN{=}CO^nBu)_3]$, reported by Omary and co-workers,[25] which exhibited strongly-connected extended chains with three quanta of intertrimer aurophilic interactions of ca. 3.34 Å and 3.44 Å, respectively; the latter also exhibited reinforcing N=C···C=N electrostatic attractions to strengthen the intermolecular/supramolecular interactions. A significantly *shorter* Au···Au separation of ca. 3.22 Å was exhibited by triclinic of $[Au_3(MeN{=}COMe)_3]$ that nonetheless represented weaker aurophilic interaction *vs* its hexagonal polymorph, given that the supramolecular structure of the triclinic polymorph exhibited two instead of three quanta of that short separation in dimer-of-trimer units that are more loosely-separated from one another by a single quantum of a much longer Au···Au distance of ca. 3.53 Å.[26] Even with partial oxidation upon reaction with organic electron acceptors, some of the aforementioned cyclotrimers exhibited shortened Au···Au intertrimer distances that nevertheless remained > 3.15 Å,[21, 22] which are still much longer than the two 2.875 Å "intertrimer" separations (or $Cu^I$-$Au^I$ "bonds" within the hexanuclear cluster) in **4a** herein. Likewise, the Cu(I) precursor for **1**-**4** herein, exhibit colossal shortening of Cu···Cu intertrimer and interplanar separations by ca. 0.56 Å and 0.65 Å, respectively, upon photo-excitation according to an elegant time-resolved diffraction study by Coppens and co-workers; nevertheless, the resulting

separations remained too long to be deemed a "metal-metal bond" as the shortest Cu···Cu intertrimer distance in the resulting excimer was 3.46(1) Å – given that the longer ground-state distance that was > 4.0 Å was the one to shrink.[27] Although de-population of a formally anti-bonding highest-occupied molecular orbital, HOMO, occurs in these redox/photoexcitation examples (concomitant with population of a formally bonding lowest-unoccupied molecular orbital, LUMO, in the latter example), the resulting M-M bonding enhancement is distributed among multiple quanta of adjacent metal atoms in the hexanuclear dimer-of-trimer cluster as opposed to classical metal-metal bonding situations whereby the bonding exists in a single M-M bond. *Bona fide* single bonds in such "simple" systems exist upon full oxidation to Au(II) attain ligand-assisted separations of anywhere between 2.4752(9) Å, as described by Fackler and co-workers for $[Au_2(hpp)_2Cl_2]$ (hpp =1,3,4,6,7,8-hexahydro-pyrimido[1,2-*a*]pyrimidinate),(20) and up to 2.977(10) Å in $[Au_2(i\text{-MNT})_2]^{2-}$ species (*i*-MNT = 1,1-dicyanoethene-2,2-dithiolate), whereas more rare ligand-unassisted versions with ca. 2.49-2.64 Å have been described and validated theoretically by Pyykkö and co-workers.[28] The two quanta of 2.875 Å intertrimer Cu(I)-Au(I) separations in **4a** herein are each within the range of the longest such Au(II)-Au(II) single bonds and other conventional, well-established systems (*i.e.*, 2.96-2.99 Å known for Mo-Mo and W-W single bonds from their nd-$\sigma^2$ electronic configuration).[29]

### 3.2.3.2 Vibrational Spectral Considerations

**Figure 3.6** shows the infrared spectrum of a neat solid powder of **4a** in the far-IR region. The strong, broad main bands at ca. 470 and 270 $cm^{-1}$ are easily assignable to $\nu_{M\text{-}L}$ ($\nu_{Cu\text{-}N}$; $\nu_{Au\text{-}C}$; $\nu_{Au\text{-}AN}$) and $\delta_{L\text{-}M\text{-}L/MLL}$ ($\delta_{N\text{-}Cu\text{-}N}$; $\delta_{C\text{-}Au\text{-}N}$; $\delta_{Cu\text{-}N\text{-}C}$; $\delta_{Au\text{-}C\text{-}N}$; $\delta_{Cu\text{-}N\text{-}N}$; $\delta_{Au\text{-}N\text{-}C}$; etc.) vibrations, respectively, as this

is the general spectral region for M-L bond vibrations;[30-32] animation of our DFT simulations on **4a** models substantiated both this assignment. We have scrutinized the bands at < 200 $cm^{-1}$ to evaluate whether they exhibit significant $\nu_{Cu\text{-}Au}$ contribution based on the Harvey-Gray method of correlating the crystallographic M-M distance to the corresponding force constant,[32] as well as based on DFT simulations (*vide infra*). The infrared spectrum of **4a** shown in **Figure 3.6** entails multiple bands within 65-200 $cm^{-1}$ that are potentially assignable to $\nu_{Cu\text{-}Au}$ vibrations within the rectangular Cu1-Au1'···Au1-Cu1' cluster (primes designate the adjacent trimer). The general pattern of such far-IR bands, comprising doublets each of which with a stronger and weaker component, is consistent with a group theory analysis for a $D_{2h}$ symmetry of such a tetranuclear metal cluster rectangle, which entails one IR-allowed ($B_{2u}$) and one IR-forbidden ($B_{1g}$) $\nu_{Cu\text{-}Au}$ band; the "forbidden" $B_{1g}$ band gains intensity due to the symmetry reduction from $D_{2h}$ when one considers the rest of the hexanuclear dimer-of-trimer molecule besides the rectangular cluster. Utilizing the Harvey-Gray method,[32] the crystallographic Cu1-Au1' distance of 2.875 Å gives rise to a force constant of 0.8287 mdyn/Å or 82.87 N/m, which corresponds to a $\nu_{Cu\text{-}Au}$ value of 171.0 $cm^{-1}$ – in very good agreement with the band at 173.6 $cm^{-1}$ in the experimental spectrum of the neat solid of **4a** in (**Figure 3.6**) as well as the computational data shown in **Figure 3.7**. This estimation corresponds to our modification of the Harvey-Gray method by utilizing the Woodruff formula for 4d-4d $\nu_{M\text{-}M}$ homometallic vibrations – given the absence of such correlations for 3d-5d $\nu_{M\text{-}M'}$ or any heterometallic vibrations – on the premise that the average or reduced mass is similar between the two types of bonds; obviously, we have used the accurate reduced mass for the Cu-Au bond. (Indeed, this reduced mass falls well-within the range of reduced masses of the diatomic species used in the 4d-4d $\nu_{M\text{-}M}$ homometallic correlation).[32]

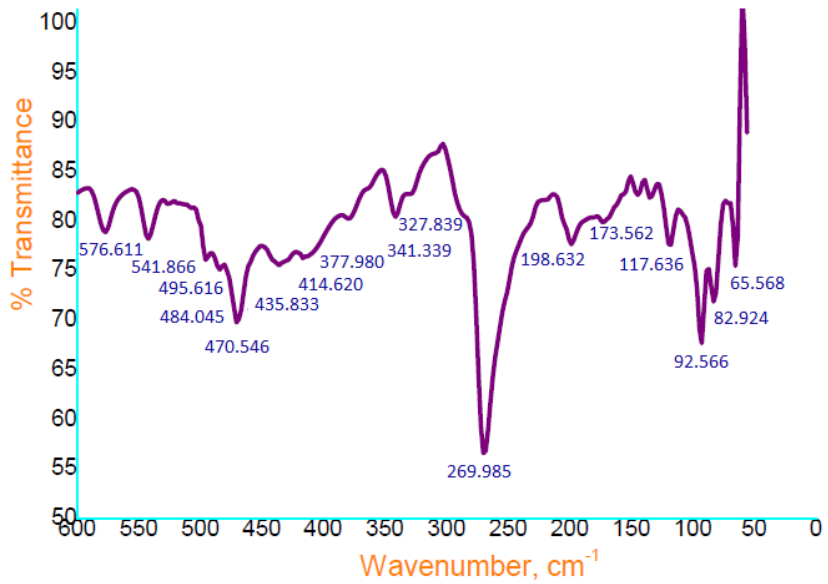


**Figure 3.6: Infrared spectrum of neat solid powder of** 4a **in the far-IR region. Most bands at <200 cm$^{-1}$ have significant $\nu_{Cu\text{-}Au}$ contributions based on animations and high reduced masses shown in DFT simulations or based on the Gray-Harvey correlation method.**

We have also validated this correlation by applying it to the $\nu_{Ag\text{-}Ag}$ homometallic vibrations in $TlAg(CN)_2$, for which Patterson and co-workers reported Raman bands in the ca. 85-130 cm$^{-1}$ region with varying spectral resolution *vs* temperature, which they have assigned to $\nu_{Ag\text{-}Ag}$.[30] Applying the same Woodruff formula we used here for $TlAg(CN)_2$ attains $\nu_{Ag\text{-}Ag}$ values of 99.60 cm$^{-1}$ for a dimer and 122.0 cm$^{-1}$ for a trimer of Ag atoms separated by 3.110 Å; these are in excellent agreement with the experimental Raman spectral bands at ca. 98.7 cm$^{-1}$ (average position of the broad band for room and cryogenic temperature data) and 119.5 cm$^{-1}$ (average of the higher-energy peaks in the resolved spectra at cryogenic temperatures), respectively.[30, 32] We have attempted to likewise investigate the effect of clustering on the calculated position of the $\nu_{Cu\text{-}Au}$ band, by making the correlation to be between two Cu-Au reduced masses separated by the crystallographic intra-trimer separation of 3.3745 Å. Unfortunately, however, the pertinent Woodruff formula is not applicable at such long separations. On the one hand,

clustering further decreases the reduced mass so as to increase $\nu_{Cu\text{-}Au}$ whereas the large separation between the two Cu-Au intertrimer bonds should decrease the $\nu_{Cu\text{-}Au}$ frequency. We, therefore, settle to considering the problem associated with the 171.0 $cm^{-1}$ Woodruff formula prediction *vs* the corresponding 173.6 $cm^{-1}$ closest experimental band for **4a** to be a problem between two orthogonal Cu-Au intertrimer polar-covalent bonds separated by non-covalent Cu···Au cupro-aurophilic intratrimer interactions. The broadness of the relevant experimental band in **Figure 3.6** (spanning the 150-212 $cm^{-1}$ range) coupled with the "estimation" nature of the Harvey-Gray method,[30-32] the two aforementioned opposing factors for the clustering effect, temperature effects (given the IR spectrum is gathered at ambient temperature *vs* 100 K for the crystal structure) – all are factors that beg for theoretical strengthening of this assignment.

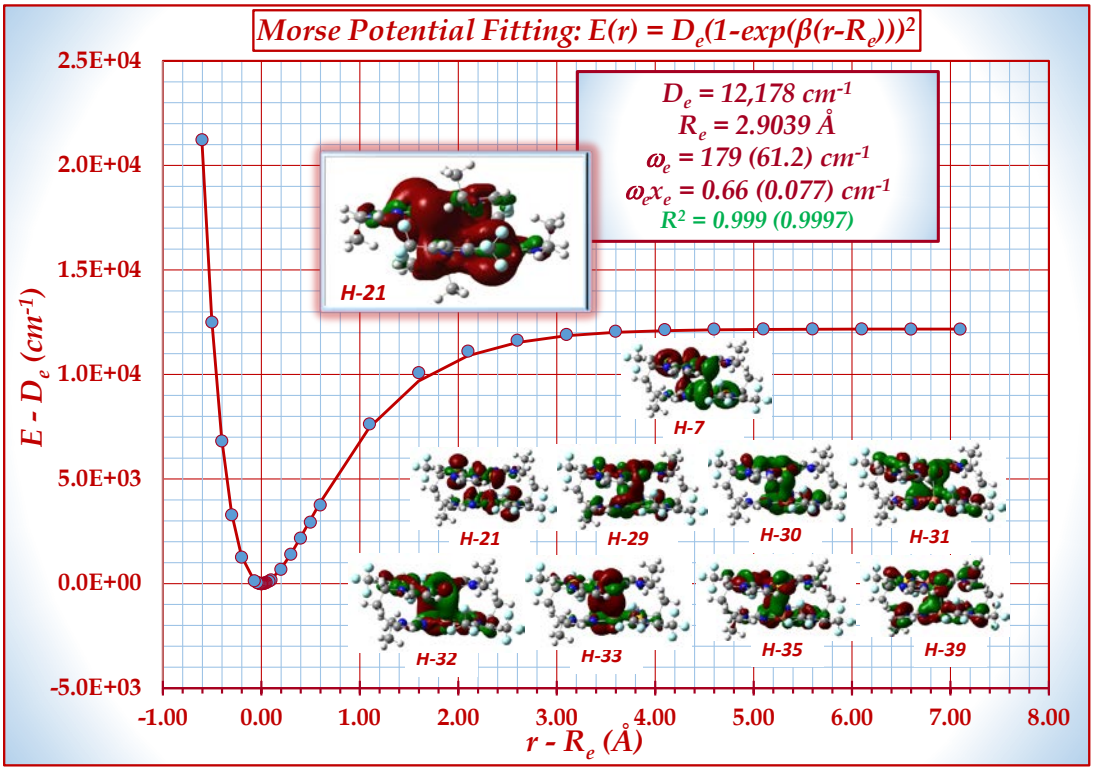


**Figure 3.7: Potential energy surface plot upon varying only the vertical intertrimer separation in the optimized structure of a full {[Au2(μ-C2,N3-EtIm)2Cu(μ-3,5-(CF3)2Pz)]}2 hexanuclear dimer-of-trimer model of 4a. Bonding and spectroscopic constants are given with main vs (parenthesized) ωe and ωexe values given based on the reduced masses of CuAu atoms vs (entire molecule). Also shown are the**

**Kohn-Sham contours of the nine Cu-Au strongly-bonding molecular orbitals in the full 4a molecule (isodensity = 0.01 for the zoomed-out H-21 and 0.02 for all others). Orbital notation is given to describe the relative energy (e.g., H-35 = the occupied molecular orbital that lies 35th below the HOMO). See SI for a more comprehensive illustration of molecular orbitals.**

### 3.2.3.3 Theoretical Considerations

Dispersive DFT computations using Truhlar's M06 "desert island" functional,[33, 34] which we have demonstrated its ability to describe both weak metallophilic $d^{10}$-$d^{10}$ interactions and chemisorption interactions in our previous collaborative work,[35] is used to substantiate the polar-covalent bonding in **4a**. The computed structure shown in **Figure 3.8** is, overall, in good agreement with the experimental structural data shown in **Figure 3.5** and **Table 3.2**. This is so not only for the coordination sphere of the Cu(I) and Au(I) centers but also for the two pertinent Cu(I)-Au(I) intertrimer bonds, both quanta of which have been attained with an excellent qualitative and reasonable quantitative agreement with the crystal structure – within 0.02 Å from experiment (2.9039 Å *vs* 2.8750 Å). In addition to the bond distance, the large deviation from planarity in the N-Cu-N bond angle was also reproduced reasonably well (within 3.5°, 171.0° *vs* 167.5°) and likewise for the N-Au-C bonds that are engaged in the Cu-Au bond (within 0.6°, 172.8° *vs* 173.4°), which is significantly greater than the deviation from planarity for the other N-Au-C bonds that are not engaged in the Cu-Au bond (within 0.2°, 176.7° *vs* 176.4°) – again in good overall agreement with experiment – at least qualitatively – given the density-functional level of theory employed; a higher-level *ab initio* method, such as MP2 or CCSD(T), will likely attain a closer agreement to experiment in such structural parameters but at the expense of a much higher computation cost for such a large hexanuclear dimer-trimer model with a very large number of atoms (90), valence electrons explicitly treated (408), and basis functions (1020).

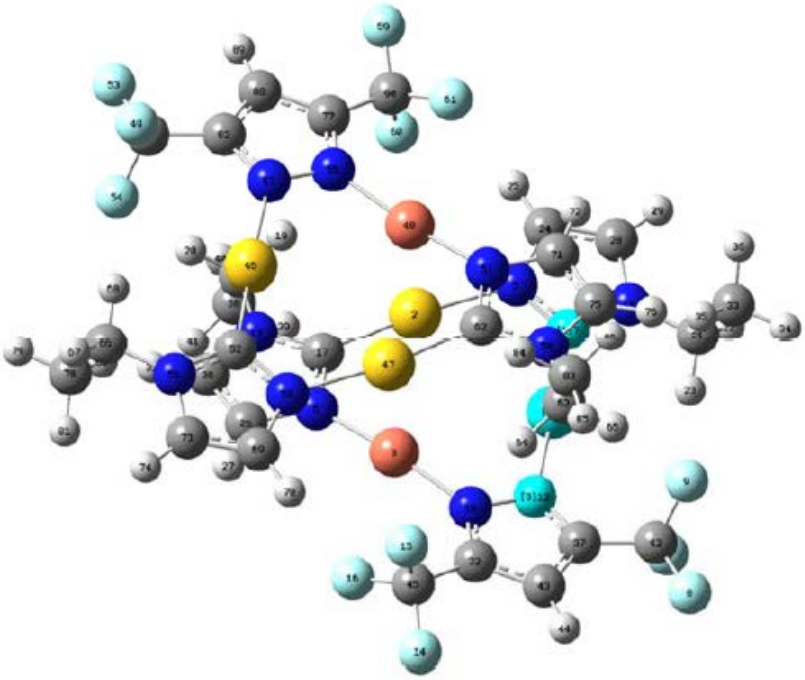

| M06-Optimized | Length (Å)/Angle (°) |
|---|---|
| Au(2)-Cu(48) | 2.9039 |
| Cu(3)-Au(47) | 2.9039 |
| Cu(3)-Au(2) | 3.5018 |
| Cu(3)-Au(1) | 3.3878 |
| Cu(48)-Au(47) | 3.5018 |
| Cu(48)-Au(46) | 3.3878 |
| Cu(3)-N(6) | 1.8810 |
| Cu(3)-N(10) | 1.9062 |
| Au(2)-N(5) | 2.1081 |
| Au(2)-C(17) | 2.0344 |
| Au(1)-N(12) | 2.1159 |
| Au(1)-C(7) | 2.0284 |
| Cu(48)-N(51) | 1.8810 |
| Cu(48)-N(55) | 1.9062 |
| Au(47)-N(50) | 2.1081 |
| Au(47)-C(62) | 2.0344 |
| Au(46)-N(57) | 2.1159 |
| Au(46)-C(52) | 2.0284 |
| N(51)-Cu(40)-N(55) | 171.0 |
| N(50)-Au(47)-C(62) | 172.8 |
| N(57)-Au(46)-C(52) | 176.7 |
| N(6)-Cu(3)-N(10) | 171.0 |
| N(5)-Au(2)-N(5) | 172.7 |
| N(12)-Au(1)-N(12) | 176.7 |

**Figure 3.8: Dispersive DFT (M06/CEP-31G(d)) optimized structure of 4a.**

The M06/CEP-31G(d)[36, 37] density-functional computations quite conservatively given the aforementioned merely qualitative agreement with the structural bonding parameters, estimate the Cu(I)-Au(I) bond energy in **4a** as ca. 30-35 kcal/mol. We have derived this binding energy by two methodologies: (a) full optimization of the hexanuclear dimer-of-trimer model to attain the structure in **Figure 3.8** then subtracting from its total energy the summed energies of two units of an independently-fully-optimized monomer-of-trimer molecule; and (b) potential energy surface (PES) scan calculations whereby the vertical separation is varied between the two monomer-of-trimer half-molecular units that comprise the hexanuclear dimer-of-trimer optimized structure. Method (a) gives rise to -31.5 kcal/mol, whereas method (b) attains -34.8 kcal/mol or $D_e$ = 12,178 $cm^{-1}$ (**Figure 3.7**). Further analysis of the PES, by fitting it to a Morse function, attains a stretching frequency for this vertical motion, presumed as inter-trimer

symmetric $\nu_{Cu\text{-}Au}$, of 179 $cm^{-1}$, hence validating the estimation based on the modified Harvey-Gray correlation method in the preceding section. Indeed, the under-description of the Cu(I)-Au(I) polar-covalent bonding in **4a** surmised from the crystallographic arguments in the previous paragraph leads us to speculate that the computed $D_e$ and $\nu_{Cu\text{-}Au}$ values from the PES analysis in **Figure 3.7** is a lower limit. Hence, if we were to assign the experimental $\nu_{Cu\text{-}Au}$ value as the stronger 198.6 $cm^{-1}$ peak (IR-allowed $B_{2u}$) instead of the weaker 173.6 $cm^{-1}$ shoulder (IR-forbidden $B_{1g}$) in **Figure 3.8** – although the weaker shoulder was in a better agreement with the DFT and Harvey-Gray values – then we would estimate the experimental $D_e$ as ca. 15,000 $cm^{-1}$ or 43 kcal/mol, given the quadratic relationship between the stretching frequency and $D_e$. The longer DFT-computed $R_e$ vs experiment and the aforementioned limitations of DFT methods are also consistent with this assignment of higher $\nu_{Cu\text{-}Au}$ and $D_e$ values. With or without this "adjustment", such values of 12,000-15,000 $cm^{-1}$ or 34-43 kcal/mol are commensurate with the bond energies of *bona fide* single M-M covalent bonds such as those in Cotton's classical $d^1$-$d^1$ or $d^9$-$d^9$ ground-state species,[29] more recent manifestations of the latter such as the (halo)pyridyl Au(II)-Au(II) dimers, for which Pyykkö calculated $D_e$ values of 15,000-17,000 $cm^{-1}$ *via* GGA/TZ2P (SR-ZORA) ADF calculations,[28] and excimeric group 12 ligand-free neutral metallic dimers, for which Wilson and co-workers calculated $D_e$ values of ca. 8,000-10,000 $cm^{-1}$ *via* CCSD(T)/complete basis set limit *ab initio* calculations of their phosphorescent $^3\sum^+$ state.[38, 39] The aforementioned calculated $\nu_{Cu\text{-}Au}$ of ~179 $cm^{-1}$ is found to be insensitive as to whether one considers three alternative approaches: (a) The one employed in **Figure 3.8** whereby the Morse potential is assembled for the symmetric vertical inter-trimer vibration of the two monomer-of-trimer units in the hexanuclear dimer-of-trimer **4a** but using an "effective reduced mass" corresponding to only the Cu and Au atoms (akin

to the insensitivity of $\nu_{C=C}$ in a diene such as cyclobutadiene or 1,5-cyclooctadiene *vs* ethylene; considering the reduced mass of the two cyclotrimer molecules gives rise to ~61 $cm^{-1}$, which also accounts for the experimental peak at ~ 65 $cm^{-1}$ in **Figure 3.6**). (b) Another set of scan calculations whereby we varied only the out-of-plane Cu-Au distance in the proximity of the optimized geometry by displacing both Cu and Au atoms of each intermolecular bond equally; this attains a pure $\nu_{Cu\text{-}Au}$ of 182 $cm^{-1}$ *via* Dunham analysis,[40] very similar to the value from approach (a) and, indeed, identical – within 0.1 $cm^{-1}$ – to the value obtained by subjecting selected **Figure 3.7** data near the potential minimum to the same Dunham analysis for approach (a) instead of fitting the entire dataset to a Morse potential – see **Table 3.3**. (c) A third set of scan calculations whereby we varied only the out-of-plane Cu-Au distance in the proximity of the optimized geometry by displacing only the Cu atom of each intermolecular bond to approach a stagnant Au atom in the next molecule; this attains an asymmetric $\nu_{Cu\text{-}Au}$ of 173 $cm^{-1}$ *via* Dunham analysis, again very similar to the frequency from both approaches (a) and (b).

**Table 3.3: Morse potential fitting (MPF) and Dunham analysis (DA) of selected vibrational frequencies in the full $\{[Au_2Im`_2CuPz`)]\}_2$ hexanuclear dimer-of-trimer (DOT) model upon selected vertical vibrations in its two-component monomer-of-trimer (MOT) units.**

| Vibration | Method | μ (a.u.) | $R_e$ (Å) | $\omega_e$ ($cm^{-1}$) | $\omega_e\chi_e$ ($cm^{-1}$) |
|---|---|---|---|---|---|
| $\nu_{Cu\leftrightarrow Au(symm)}$ in MOT↔MOT | MPF | 48* | 2.9039 | 179 | 0.658 |
| $\nu_{MOT\leftrightarrow MOT(symm)}$ | MPF | 425 | 2.9039 | 61.2 | 0.077 |
| $\nu_{Cu\leftrightarrow Au(symm)}$ in MOT↔MOT | DA | 48* | 2.9036 | 182.3 | 3.14 |
| $\nu_{MOT\leftrightarrow MOT(symm)}$ | DA | 425 | 2.9036 | 61.3 | 0.35 |
| Pure $\nu_{Cu\leftrightarrow Au(symm)}$ | DA | 48 | 2.9020 | 182.3 | 44.67 |
| Pure $\nu_{Cu\leftrightarrow Au(asymm)}$ | DA | 48** | 2.9019 | 172.7 | 31.8 |

*: Effective reduced mass assumed to be that of the Cu and Au atoms within the symmetric intertrimer vibration of the two entire MOT units. See vibrations designated "Pure" for analogous values from the scan calculations whereby only the metal atoms were motioned and the intertrimer vibration while the rest of the two MOT units remained stagnant.

**: Effective reduced mass assumed to be that of the Cu and Au atoms within the asymmetric intertrimer vibration whereby only the two Cu atoms were motioned towards the corresponding Au atoms, which remained stagnant.

Additional theoretical considerations must be accounted for besides the computational validation of the short $R_e$ and high $\nu_{Cu\text{-}Au}$ and $D_e$ values in order to ascertain the polar-covalency of the Cu-Au bonds in the crystal structure of **4a**. While the covalency of a $d^{10}$-$d^{10}$ "bond" is certainly counterintuitive, the discrepancy in electronegativity between not only the $Au^+$ and $Cu^+$ atomic ions but also the heavily-fluorinated 3,5-$(CF_3)_2Pz^-$ and alkylated $EtIm^-$ ligands bonded to them, respectively, greatly alters the otherwise perfectly-matched energies of nd and (n+1)s orbitals between two identical metal atoms. **Figure 3.12** and **Figure 3.10** show that this leads to important distinctions between polar *vs* non-polar covalent M-M bonds. Two manifestations of this distinction are exhibited even by the simple Cu(I)-Au(I) ligand-free or "naked" model, namely: (a) the (n+1)s/p orbital mixing is more likely to occur as one between the 6s/p orbitals of Au(I) on the one hand with the 3d orbitals of Cu(I) instead of 4s/p (Cu)/5d(Au) orbital mixing; and (b) the $\delta$ bond, which is generally accepted to be the "weakest link" in Cotton's M-M bonding scheme, so much so $\delta$ orbitals are often described as non-bonding molecular orbitals,[29] is greatly strengthened such that the $\delta^*$ orbital is no longer the first anti-bonding orbital and the $\delta$-$\delta^*$ orbital splitting (0.664 eV) is almost on par with the $\pi$-$\pi^*$ splitting (0.761 eV) – as illustrated in **Figure 3.12**. This situation is akin to that for $\pi_{(n)p}$ bonding orbitals becoming lower in energy than $\sigma_{(n)p}$ bonding orbitals in the bonding scheme of heteronuclear *vs* homonuclear diatomics of main-group elements due to greater (n)p/(n)s orbital mixing in the former, as postulated in typical inorganic chemistry textbooks.[41] Such influences of polar covalency are magnified in ligand-containing models of **4a**, including the full $\{[Au_2(\mu\text{-}C^2,N^3\text{-}EtIm)_2Cu(\mu\text{-}3,5\text{-}(CF_3)_2Pz)]\}_2$ hexanuclear dimer-of-trimer model and the $[Au_2(\mu\text{-}C^2,N^3\text{-}EtIm)_2Cu_2(\mu\text{-}3,5\text{-}(CF_3)_2Pz)_2]$ tetranuclear cluster model of inter-connected corner units; see **Figure 3.10**. As a consequence, the anti-bonding $d_{z2}$-

$d_{z2}$ $\sigma$* in Cotton's M-M bonding scheme becomes a non-bonding orbital when one considers, as a second step, the interaction of this molecular orbital with the (n+1)s/$p_z$ atomic orbital of the second atom. As a result, the formal bond order becomes 1 instead of 0 in the resulting heterobimetallic molecule. Although we shall address the formal bond order in a follow-up theoretical investigation, the Kohn-Sham frontier molecular orbital contours of the two aforementioned ligand-containing models of **4a** clearly bear out this formalism. **Figure 3.11** show that, whilst all 6 Cu-Au bonding molecular orbitals demonstrate a rather unmistakable strongly-bonding character based on both the strong electron density in bonding regions and their rather low relative energy below the HOMO, the other occupied molecular orbitals with strong metal contributions include a significant number of either non-bonding (*i.e.*, HOMO-1 and HOMO-16) or only weakly-anti-bonding (*i.e.*, HOMO-9 and HOMO-15) orbitals of the $[Au_2(\mu\text{-}C^2,N^3\text{-}EtIm)_2Cu_2(\mu\text{-}3,5\text{-}(CF_3)_2Pz)_2]$ tetranuclear cluster model. The same conclusion holds true for the full $\{[Au_2(\mu\text{-}C^2,N^3\text{-}EtIm)_2Cu(\mu\text{-}3,5\text{-}(CF_3)_2Pz)]\}_2$ hexanuclear dimer-of-trimer model, indeed to a greater extent, as manifest by the strongly-bonding nature of nine occupied molecular orbitals that exhibit such a clear Cu-Au bonding character (**Figure 3.7** insets) *vs* only three exhibiting a clear Cu-Au anti-bonding character among frontier molecular orbitals that are occupied and exhibit strong metal contribution. (For a more comprehensive illustration of molecular orbitals for both the full $\{[Au_2(\mu\text{-}C^2,N^3\text{-}EtIm)_2Cu(\mu\text{-}3,5\text{-}(CF_3)_2Pz)]\}_2$ hexanuclear dimer-of-trimer model – **Figure 3.12** and **Figure 3.14** – and the $[Au_2(\mu\text{-}C^2,N^3\text{-}EtIm)_2Cu_2(\mu\text{-}3,5\text{-}(CF_3)_2Pz)_2]$ tetranuclear cluster model – **Figure 3.11**and **Figure 3.13**). The Cu-Au bonding formalism in the full hexanuclear dimer-of-trimer model of **4a** involves initial metal-metal bonding within a monomer-of-trimer that leads to equally-occupied bonding and anti-bonding orbitals with a formal 0 bond order, as

a 1st step. Upon intertrimer Cu-Au bonding in the hexanuclear dimer-of-trimer as a 2nd step, however, one needs to consider two factors: (a) the interaction of the two "corner units" considered hitherto for the $[Au_2(\mu\text{-}C^2,N^3\text{-}EtIm)_2Cu_2(\mu\text{-}3,5\text{-}(CF_3)_2Pz)_2]$ tetranuclear cluster model, which generates 6 Cu-Au bonding orbitals (**Figure 3.11**); and (b) given that crystal field theory considerations dictate stronger *intratrimer* interactions for $d_{xy}$ and $d_{x2-y2}$ orbitals as well as, albeit to a lesser extent, $d_{z2}$ orbitals of the two Au(I) and one Cu(I) atoms in the trigonal-planar monomer-of-trimer model to initially form three $\delta$ bonding orbitals and three $\delta^*$ anti-bonding orbitals, the latter approach the (n+1) shell such that they become subject to more energy-favorable orbital mixing upon the *intertrimer* interactions in the hexanuclear dimer-of-trimer within the 2nd step, hence reversing their bonding characters to become bonding with respect to the intertrimer Cu-Au bonds pertinent herein for **4a**. While this formalism justifies the presence of nine Cu-Au strongly-bonding molecular orbitals shown in (**Figure 3.7** insets; **Figure 3.12** and **Figure 3.14**), additional rigorous theoretical scrutiny (bond order calculation schemes; breakdown of bonding forces *via* projections, corresponding orbitals, constrained variations, *etc.*) is warranted.

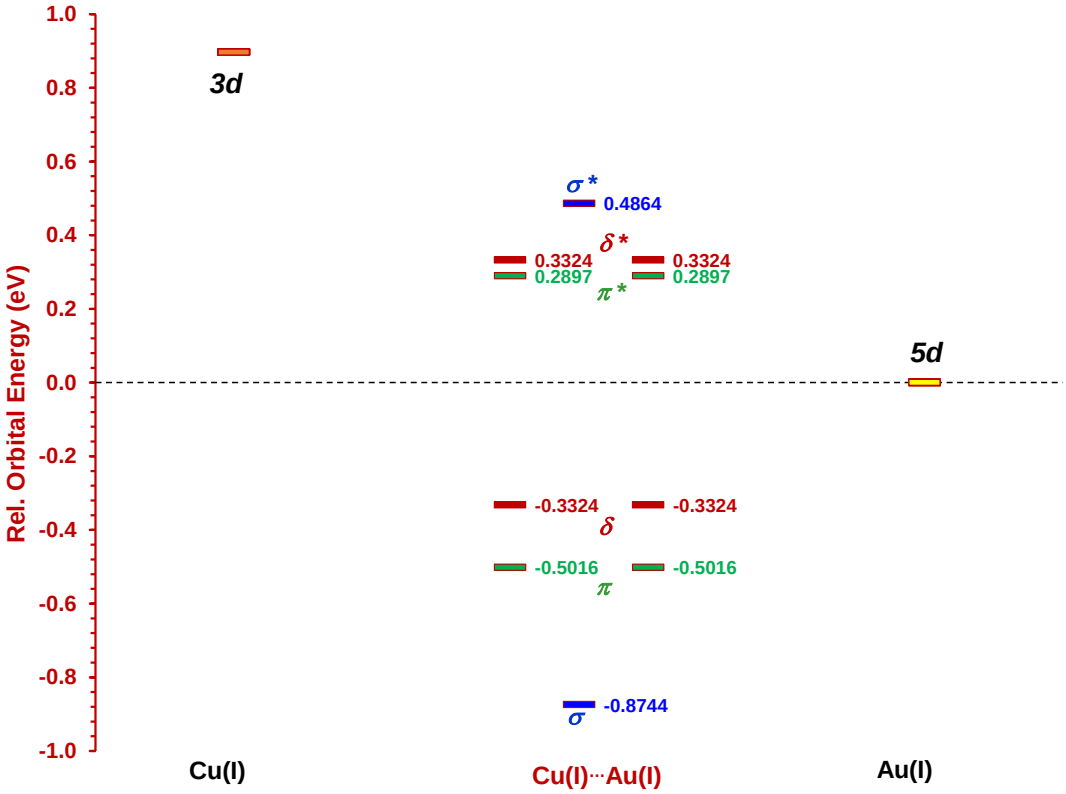


**Figure 3.9: Orbital mixing models that postulate Cu(I)···Au(I) polar-covalent metallophilic bonding formulism in an isolated $[CuAu]^{2+}$ diatomic unit. Orbital energies are taken from DFT computations at the crystallographic geometry of 4a for the Cu(I)-Au(I) diatomic model. The asymmetric splitting of the σ and π orbitals is attributed to the lowering of the σ* and the π* energy levels due to interactions with the 4s and 4p vacant orbitals of Cu(I); however, there (and δ*) remain anti-bonding in nature so the lowering is interpreted as metallophilic stabilization without increasing the formal bond order from zero in this naked $[CuAu]^{2+}$ heternuclear diatomic model.**

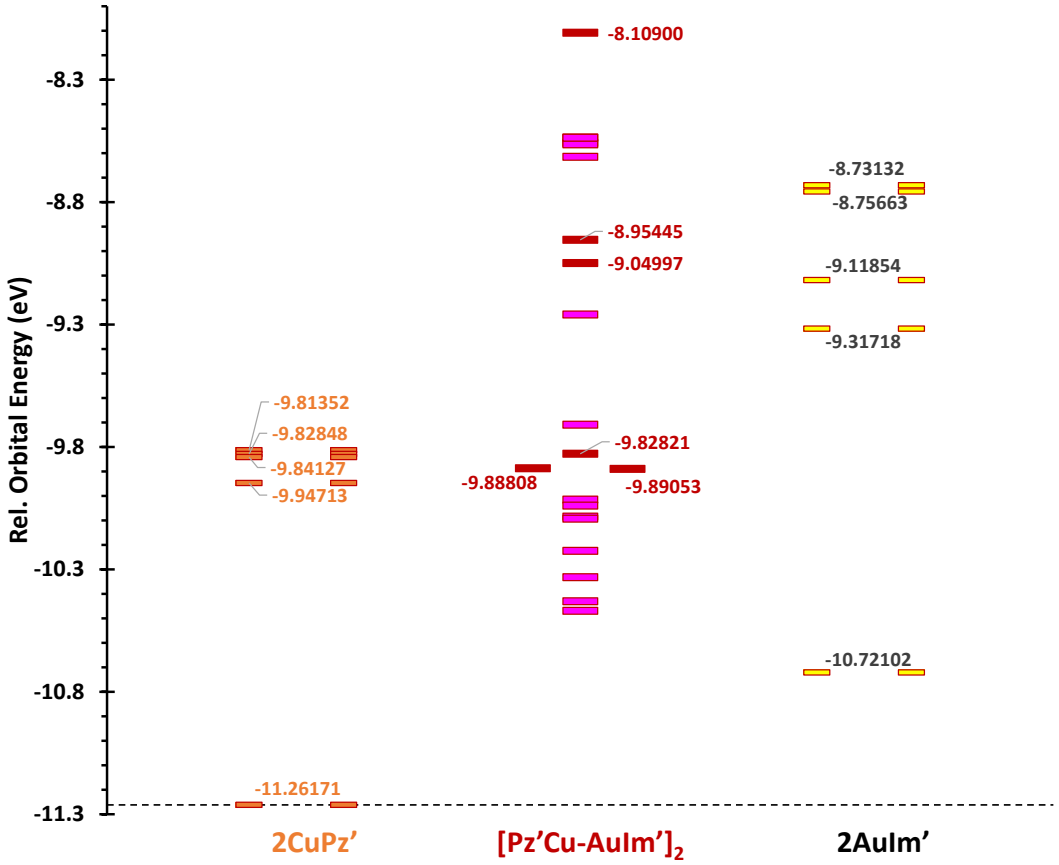


**Figure 3.10: Orbital mixing models that postulate Cu(I)-Au(I) polar-covalent bonding formulism of the Pz`Cu-AuIm` interaction in a) [Pz`Cu-AuIm`{$_2$ tetranuclear cluster and b) the full {[Au$_2$Im`$_2$CuPz`]}$_2$ hexanuclear dimer-of-trimer (DOT), comprising two [AuIm`$_2$CuPz`] monomer-of-trimer (MOT) units where Im`= μ-C$^2$,N$^3$-EtIm and Pz`= μ-3,5-(CF$_3$)$_2$Pz. Orbital energies are taken from DFT computations at the crystallographic geometry of 4a for the [Pz`Cu-AuIm`]$_2$ model and its CuPz` and AuIm` components but at the fully optimized geometry of the full MOT and full {[Au$_2$Im`$_2$CuPz`)]}$_2$ hexanuclear DOT model. The strong orbital mixing of the d-based filled atomic orbitals with the 6s and 6p vacant orbitals of Au(I) as well as 4s and 4p vacant orbitals of Cu(I) in these ligand-containing models alter the nature of at least one formally anti-bonding orbital from the formulism in Figure 3.9 above to render it bonding instead, resulting in a total of at least 6 strongly-bonding orbitals – instead of 5 – in both models (designated in maroon colors for orbital energy levels and labeled orbital energy values; see highlighted orbitals in Figure 3.13 below). The full hexanuclear DOT model exhibits 3 additional bonding orbitals due to the additionally-strengthened (n+1) outer-shell orbital mixing for MOT molecular orbitals with $d_{xy}$, $d_{x2-y2}$ and (to a lesser extent) $d_{z2}$ δ-character of each trigonal planar molecule; this results in 3 additional strongly-bonding orbitals for a total of 9 strongly-bonding orbitals in the hexanuclear DOT (designated in maroon colors for orbital energy levels and labeled energy values; see highlighted orbitals in Figure 3.14 below as well as Figure 3.7 insets).**

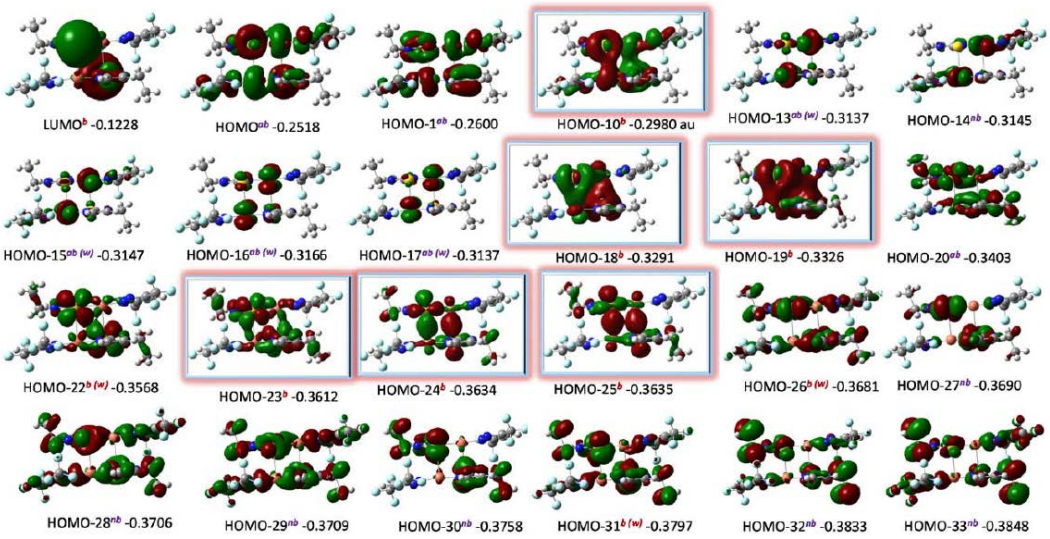


**Figure 3.11: Kohn-Sham contours of frontier molecular orbitals with significant electron density on metal atoms in a [$Cu_2Pz`_2Au_2Im`_2$] tetranuclear model, where Im` = μ-$C^2$,$N^3$-EtIm and Pz` = μ-3,5-$(CF_3)_2$Pz. Orbital energies are taken from DFT computations at the crystallographic geometry of 4a. Orbital notation is given to describe both the relative energy (e.g. HOMO = highest occupied molecular orbital; HOMO – 24 = the occupied molecular orbital that lies 24$^{th}$ below the HOMO) and the absolute energy, given in atomic units next to orbital designations, as well as the Cu-Au bonding character (superscripts "b", "nb", "ab" and "ab (w)' indicate bonding, non-bonding, anti-bonding and weakly-antin-bonding respectively). The 6 occupied orbitals that exhibit a particularly strong Cu-Au bonding character are highlighted. The isodensity = 0.01 for all orbitals.**

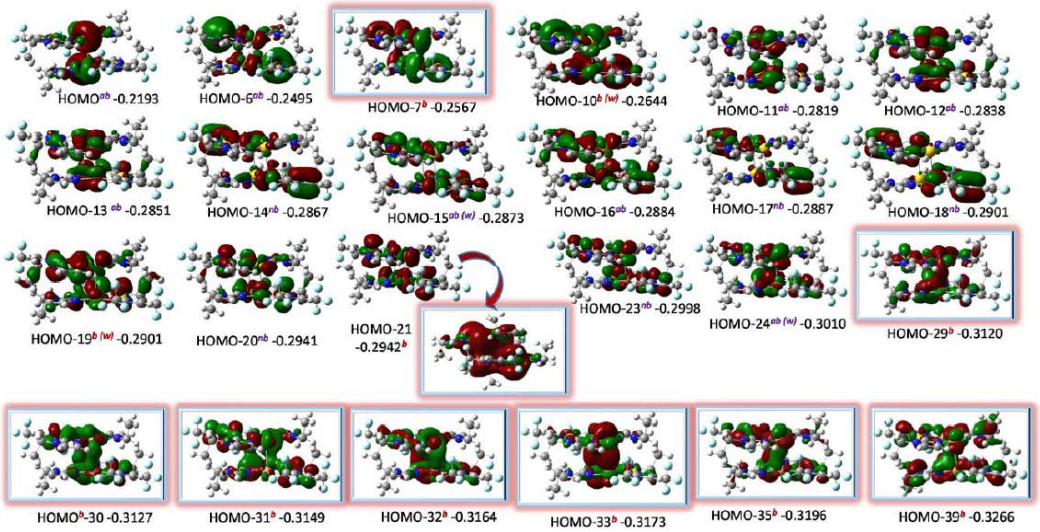


**Figure 3.12: Kohn-Sham contours of frontier molecular orbitals with significant electron density on metal atoms in the full {[$Au_2Im'_2CuPz')$]}$_2$ hexanuclear dimer-of-trimer model, where Im' = μ-$C^2$,$N^3$-EtIm and Pz' = μ-3,5-$(CF_3)_2$Pz. Orbital energies are taken from DFT computations of the optimized geometry of 4a shown in Figure 3.8. Orbital notation is given to describe both the relative energy (e.g., HOMO = highest occupied molecular orbital; HOMO-35 = the occupied molecular orbital that lies 35th below the**

**HOMO) and absolute energy, given in atomic units next to orbital designations, as well as the Cu-Au bonding character (superscripts "b", "nb", "ab", and "ab (w)" indicate bonding, non-bonding, anti-bonding, and weakly- anti-bonding, respectively). The 9 occupied orbitals that exhibit a particularly strong intertrimer Cu-Au bonding character are highlighted. The isodensity = 0.01 for the zoomed out HOMO-21 and 0.02 for all other orbitals.**

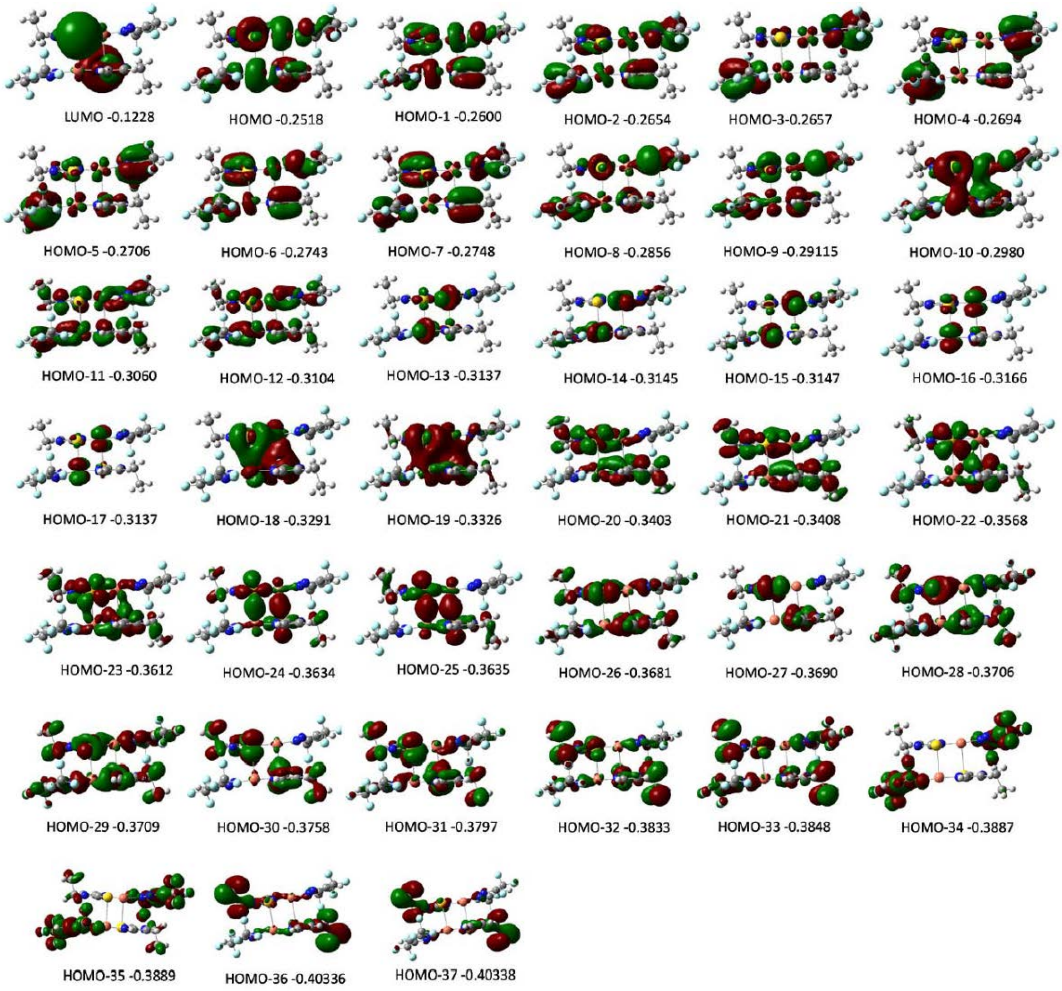


**Figure 3.13: Kohn-Sham contours of all occupied frontier molecular orbitals (from the HOMO down to HOMO-37) plus the lowest unoccupied molecular orbital (LUMO) in a $[Cu_2Pz'_2Au_2Im'_2]$ tetranuclear cluster model, where Im' = μ-$C^2$,$N^3$-EtIm and Pz' = μ-3,5-$(CF_3)_2$Pz. Orbital energies are taken from DFT computations at the crystallographic geometry of 4a. Orbital notation is given to describe both the relative energy (e.g., HOMO = highest occupied molecular orbital; HOMO-32 = the occupied molecular orbital that lies 32$^{nd}$ below the HOMO) and absolute energy, given in atomic units next to orbital designations. The isodensity = 0.01 for all orbitals.**

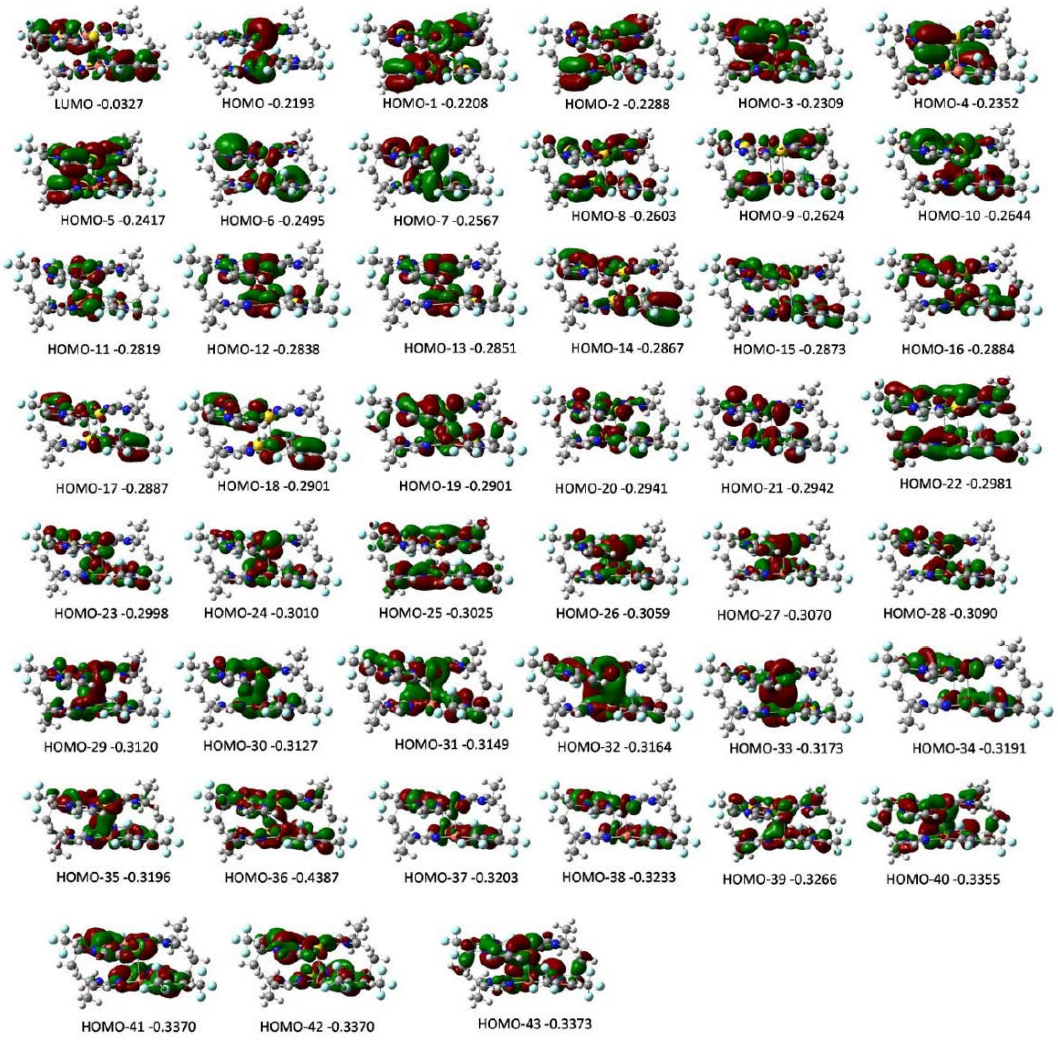


**Figure 3.14: Kohn-Sham contours of occupied all frontier molecular orbitals (from the HOMO down to HOMO-43) plus the lowest unoccupied molecular orbital (LUMO) in the full $\{[Au_2Im'_2CuPz')]\}_2$ hexanuclear dimer-of-trimer model, where Im' = μ-$C^2$,$N^3$-EtIm and Pz' = μ-3,5-$(CF_3)_2$Pz. Orbital energies are taken from DFT computations of the optimized geometry of 4a shown in Figure 3.8. Orbital notation is given to describe the relative energy (e.g., HOMO = highest occupied molecular orbital; HOMO-41 = the occupied molecular orbital that lies 41st below the HOMO) and absolute energy, given in atomic units next to orbital designations. The isodensity = 0.01 for all orbitals.**

### 3.2.3.4 Photophysical Studies

**Table 3.4** summarizes the photophysical data for homometallic and heterobimetallic complexes studied while **Figure 3.2**, **Figure 3.15 – Figure 3.20** compile the detailed electronic spectra. The spectral profiles are relatively simple for **4a** crystalline powder (**Figure 3.15**),

showing a single emission in the green region with a peak maximum at 510 nm for the broad, unstructured band, and a single excitation feature at 330 nm that is independent to temperature or excitation wavelength. These are assignable to $T_1 \rightarrow S_0$ phosphorescence emission and $S_0 \rightarrow T_1$ spin-forbidden excitation, respectively, whereas the rise in the blue edge of the excitation spectrum is the $S_0 \rightarrow S_1$ spin-allowed absorption given the microsecond lifetimes (6-7 μs) and the higher-energy solution absorption at $\lambda_{max} \leq 300$ nm (**Table 3.4** and **Figure 3. 17**). This assignment gives rise to a *genuine* Stokes' shift of 10,700 $cm^{-1}$ suggesting a large *excited state distortion* of a dodecanuclear tetramer-of-trimer unit whereby the aurophilic interactions undergo excimeric contraction of Au(I)···Au(I) distances from 3.488 Å to significantly shorter distances. If the excited state distortion were due to the contraction of the polar-covalent Cu(I)-Au(I) bond, instead, a much smaller Stokes' shift than the > 1.3 eV value would be expected, as it is hard to envision such a bond shortening way beyond 2.875 Å as supported by an elegant work by Coppens and co-worker using time-resolved X-ray diffraction;[27] such studies would be needed to ascertain or refute the speculation herein about the analogous excited state structure of solid **4a**.

**Table 3.4: Summary of photophysical parameters for homometallic and heterobimetallic complexes in this study.[a]**

| Complex | ε ($M^{-1}cm^{-1}$) | $\Phi_{PL}$ (%) | τ (μs) |
|---|---|---|---|
| [Au (μ-$C^2$, $N^3$-MeIm)]$_3$ | 4 800 | 56.88±3.58 | 11.5 (298 K) 34.6 & 15.4 (77 K) |
| [Au (μ-$C^2$, $N^3$-BzIm)]$_3$ | 7 880 | N/A | N/A |
| [Cu(μ-3,5-$(CF_3)_2$Pz)]$_3$ | 2 600 | 82.17± 0.16 | N/A |
| [$Au_2$(μ-$C^2$,$N^3$-BzIm)$_2$Cu(μ-3,5-$(CF_3)_2$Pz)] (**1**) | 11 560 | 85.16±1.57 | 12.2 (298 K) 47.0 & 38.3 (77 K) |
| [$Au_2$(μ-$C^2$,$N^3$-MeIm)$_2$Cu(μ-3,5-$(CF_3)_2$Pz)] (**3a**) | 20 590 | 97.13± 0.80 | 12.3 (298 K) 10.8 & 11.2 (77 K) |
| [Au(μ-$C^2$,$N^3$-MeIm)$Cu_2$(μ-3,5-$(CF_3)_2$Pz)$_2$] (**3b**) | 2 850 | 17.51± 0.25 | 26.2 & 4.88 (298 K) & 179.7 & 95.7 (77 K) |

| Complex | ε ($M^{-1}cm^{-1}$) | $\Phi_{PL}$ (%) | τ (μs) |
|---|---|---|---|
| {Au(μ-$C^2$,$N^3$-BzIm)}$_3${Cu(μ-3,5-$(CF_3)_2$Pz)}$_3$ (**2**) | N/A | N/A | 61.5 & 22.5 (77 K) |
| [$Au_4$(μ-$C^2$,$N^3$-EtIm)$_4$$Cu_2$(μ-3,5-$(CF_3)_2$Pz)$_2$] (**4a**) | 17 260 | 90.31± 0.70 | 6.92 (298 K) & 6.57 (77 K) |
| [Au(μ-$C^2$,$N^3$-EtIm)]$_3$ | 3 950 | N/A | 11.8 (298 K) & 59.8 (77 K) |

[a]: Notation: $\varepsilon$ = extinction coefficient at 268 nm for dilute (ca. 0.1 μM) solutions. $\Phi_{PL}$ = photoluminescence quantum yield in the solid-state powder form. τ = photoluminescence lifetime at the characteristic $\lambda_{max}$. Some entries are designated with "N/A" for "Not Applicable" because the emission is too weak to measure its lifetime or quantum yield, or the extinction coefficient could not be measured in solution due to lack of solubility.

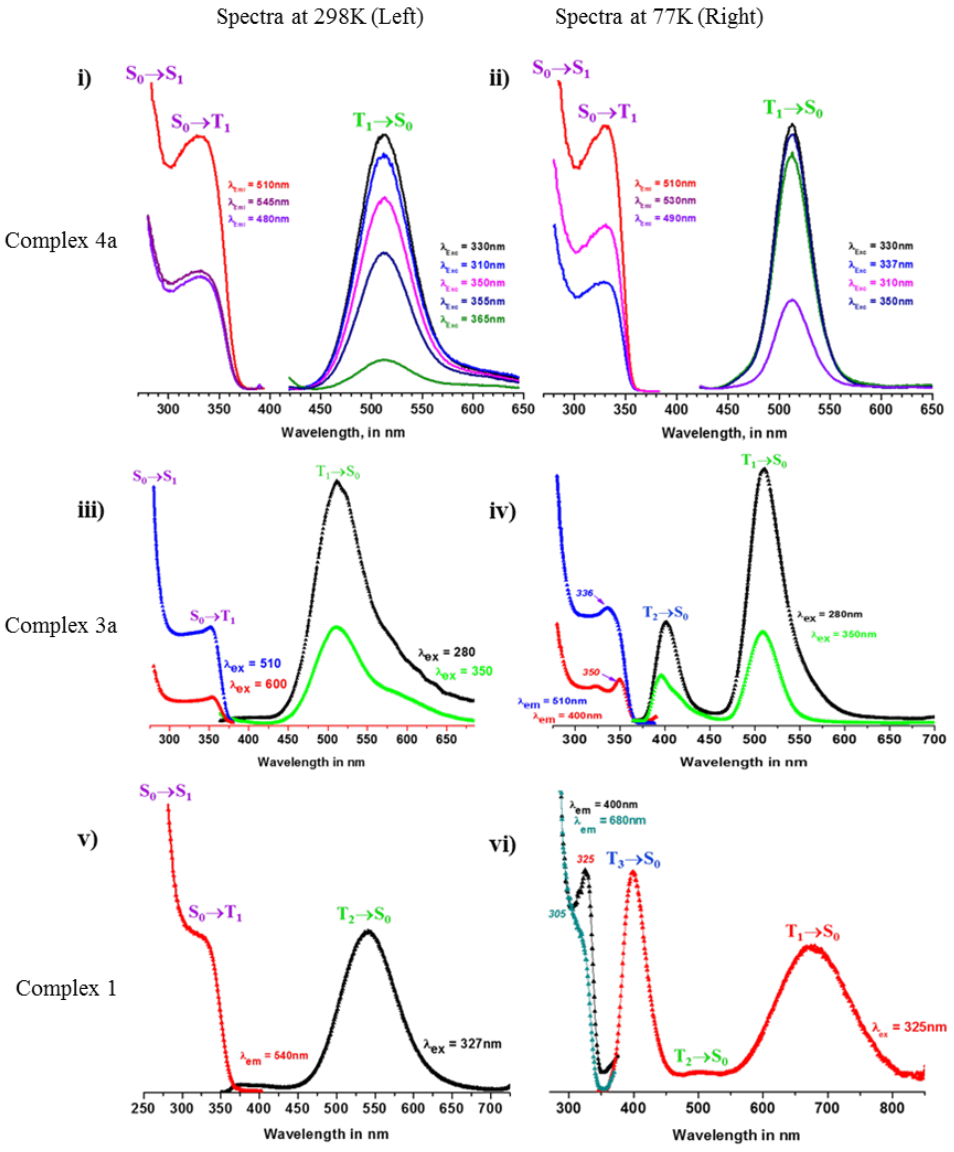


**Figure 3.15: Steady-state photoluminescence spectra for a crystalline powder sample of 4a (i and ii), 3a (iii and iv), and 1 (v and vi) at 298 K (left) and 77 K (right).**

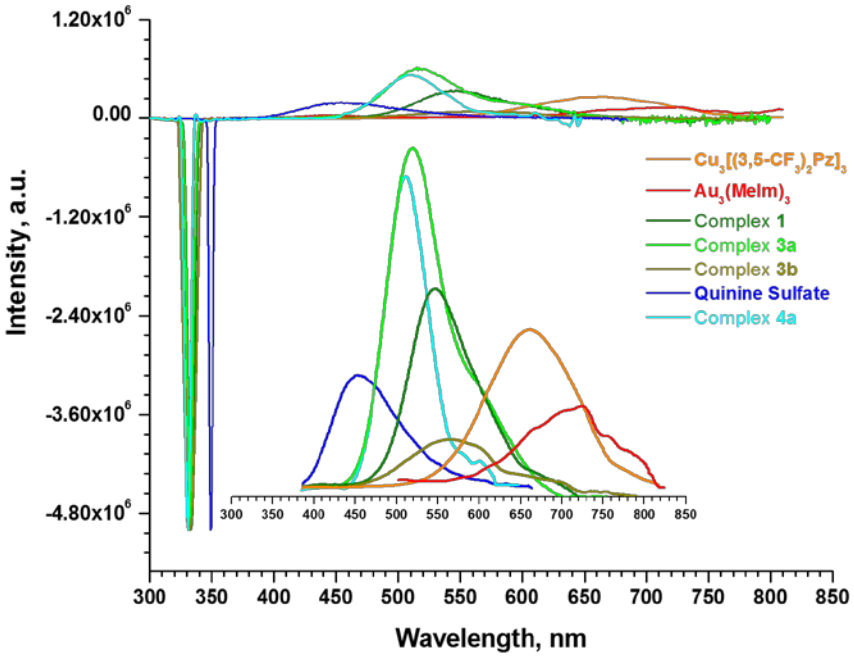


**Figure 3.16: The comparison of normalized-emission spectra used for the absolute quantum yield. The inset shows the zoomed out emission spectra within 300-850 nm for clarity purposes.**

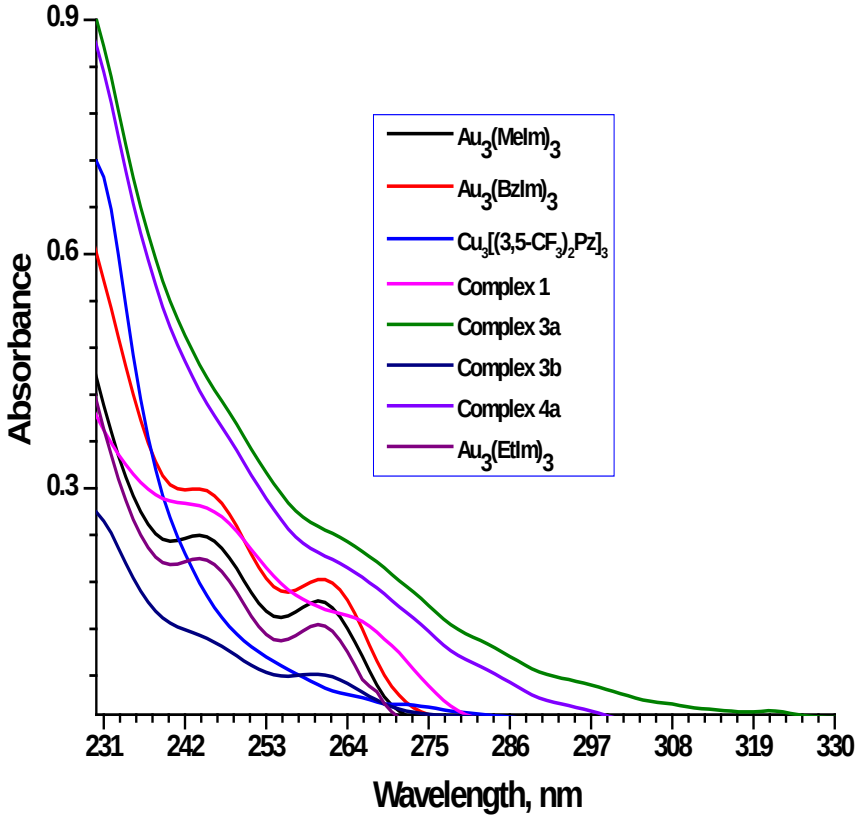


**Figure 3.17: Absorption spectra of $10^{-5}$ M dichloromethane solution of starting materials and heterobimetallic complexes.**

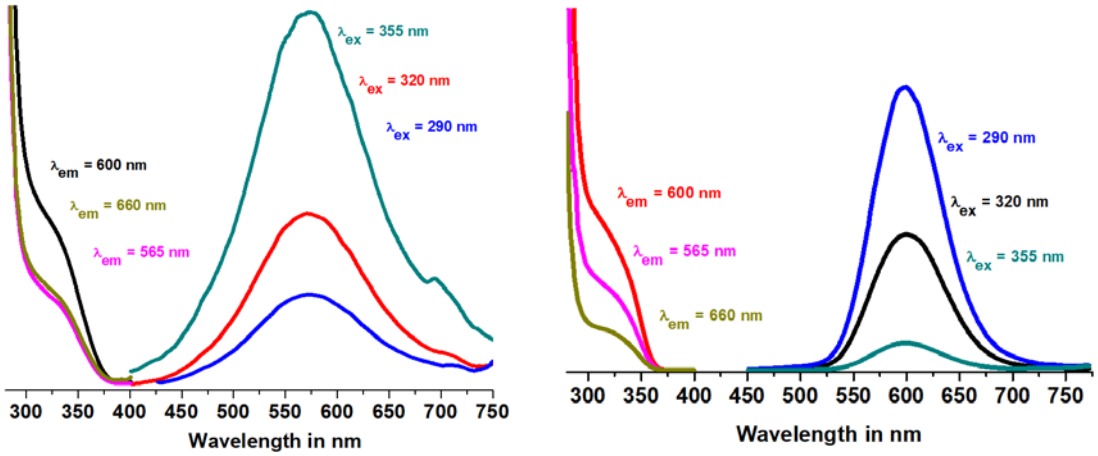


**Figure 3.18: Photoluminescence spectra for a solid powder sample of [Au(MeIm)Cu$_2$((CF$_3$)$_2$Pz)$_2$], 3b, at 298 K (top) and 77 K (bottom). Excitation and emission wavelengths used in the emission and excitation spectra, respectively, are labeled on each trace.**

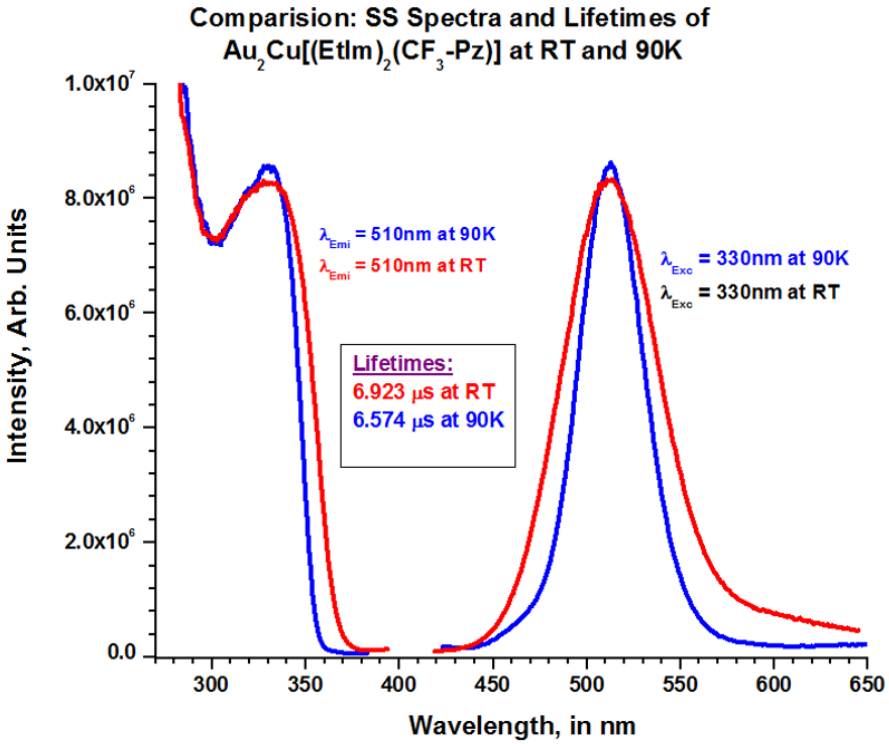


**Figure 3.19: A comparison of the steady state photoluminescence data (excitation spectra, emission spectra, and lifetimes) at room temperature vs 77 K for a solid sample of 4a. Excitation and emission wavelengths used in the emission and excitation spectra, respectively, are labeled on each trace. Note the near indifference of emission intensity and lifetime to temperature, consistent with the high $\Phi_{PL}$ found for this complex at ambient temperature (Table 3.4).**

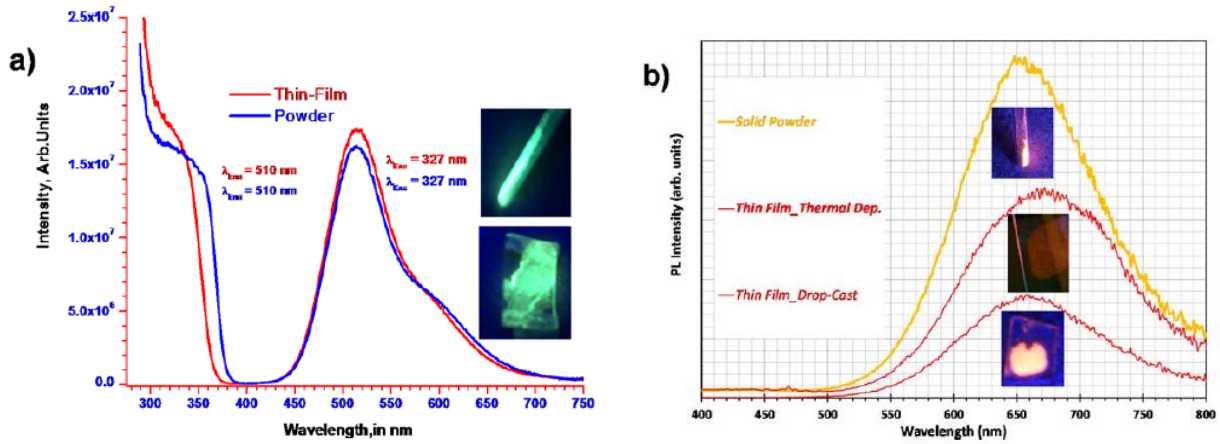


**Figure 3.20: Demonstration of the processability into OLED functional thin-film forms and the indifference of the photoluminescence spectra thereof vs powder forms for 3a (a) and [Cu(μ-3,5-$(CF_3)_2$Pz)]$_3$ (b).**

The photoluminescence spectra of complexes **3a** and **1** show multiple temperature/excitation-dependent emission bands (**Figure 3.15**). Also, the large intensity difference in excitation spectra **(3a;** $\lambda_{ex}$ ~ 350 nm and $\lambda_{ex}$ < 300 nm; *e.g.*, $\lambda_{ex}$ = 280 nm and **1;** $\lambda_{ex}$ ~ 325 nm and $\lambda_{ex}$ < 300 nm; *e.g.*, $\lambda_{ex}$ = 280 nm) indicates the involvement of spin-forbidden ($S_0 \rightarrow T_1$) and spin-allowed ($S_0 \rightarrow S_1$) transitions. The 298 K lower-energy emission of **3a** ($\lambda_{max}$ = 510 nm, $T_1 \rightarrow S_0$) undergoes thermal broadening at 77K and an additional higher-energy band ($\lambda_{max}$ = 400 nm, $T_2 \rightarrow S_0$) appears. This $T_2$ band disappears at room temperature *via* internal conversion process to $T_1$ state, given the lifetime data in microseconds regime for both bands which are metal-centered excimeric in nature without a clear vibronic structure.[42] Similarly, the emission spectra of complex **1** at 298K ($\lambda_{max}$ = 540 nm, $T_2 \rightarrow S_0$) becomes dual emission bands at 77K ($\lambda_{max}$ = 680 nm, $T_1 \rightarrow S_0$; violet-emission, 400 nm, $T_3 \rightarrow S_0$) through either by modest compression of Au(I)···Cu(I) intertrimer distances across the entire stack of chains leading to a higher-energy $T_3$ band or by a strong compression of Au(I)···Cu(I) intertrimer distances leading to lower-energy $T_1$ band as described in our previous work.[25] The benzyl groups in complex **1** provide a steric effect

that could cause an increase in Cu···Au intermolecular distances which explains the slight increase in the Stokes' shift for the 540 nm green-emission band at 298 K for this complex when compared to the corresponding green-emission that appears at 510 nm in the methyl imidazolate analogue complex **3a**.

The luminescence data for complexes **3b** and **2**, are shown in **Table 3.4**, **Figure 3.2** and **Figure 3.18** respectively. The solid of both **3b** and **2** have a low-energy excitation (**3b**; $\lambda_{max}$ = 330 nm and **2**; 325 nm).The emission profile of the complex **3b** at 298 K shows a band with $\lambda_{max}$ = 575 nm which is red shifted to $\lambda_{max}$ = 600 nm at 77 K and complex **2** shows an emission band with $\lambda_{max}$ = 575 nm at 77K. Both **3b** and **2** exhibits long lifetimes (in μs) with significantly large Stokes' shift suggesting excimeric excited states with contracted intertrimer M···M distances vs the corresponding ground state of either solid complex **3b** or **2**.

**Figure 3. 16** shows absolute $\Phi_{PL}$ spectral data acquired by using an integrating sphere technique proposed by Kawamura et al.,[43] for solid samples of selected complexes and the standard reference material quinine sulfate (1N sulfuric acid/ethanol solution, $\Phi_{PL}$ of 55%).[44] The heterobimetallic complexes **1** (~85%), **3a** (~97%), and **4a** (~90%) exhibit extremely high quantum yields (**Table 3.4**) that is supported by the temperature-independent emission intensity (**Figure 3.20**) and lifetimes of **4a** and **3a**. We believe that these higher quantum yields are bestowed by the lowered symmetry from $D_{3h}$ in the homometallic species to $C_{2v}$ in the heterobimetallic species by cuprophication of gold to lead to enhanced extinction coefficients in solution (**Figure 3. 17**) and sensitized $\Phi_{PL}$ in the solid state, respectively at both the molecular and supramolecular levels.

Finally, we have subjected two representative high-quantum-yield complexes analyzed in this work to a screening study aimed to assess their possible use in optoelectronic devices such as organic light-emitting diodes (OLEDs). Both the heterobimetallic **3a** and homometallic [Cu(μ-3,5-$(CF_3)_2$Pz)]$_3$ complexes have demonstrated their processability into OLED functional thin-film forms by thermal evaporation (vacuum sublimation) and/or solution drop-casting with identical photoluminescence spectra to those for solid powder forms of the same material, as illustrated in **Figure 3.20**. These findings are encouraging for pursuing the use of the high-quantum-yield solid materials in this work into high efficiency phosphorescent Ir-free OLED device architectures as well as down-conversion phosphors for inorganic LEDs to replace rare earth-based phosphor materials.

## 3.3 Conclusions and Prospects

In conclusion, a novel synthesis method for the preparation heterobimetallic $Au_2Cu$, $Cu_2Au$ and stacking complexes is hereby documented and discussed for the first time. Crystallographic, far-IR, and dispersive DFT methods data reinforce the formation of a *bona fide* polar-covalent bond between Cu(I) and Au(I) atoms of the {[$Au_2$(μ-$C^2$,$N^3$-EtIm)$_2$Cu(μ-3,5-$(CF_3)_2$Pz)]}$c_2$ hexanuclear dimer-of-trimer **4a**, whereas the analogous [$Au_2$(μ-$C^2$,$N^3$-BzIm)$_2$Cu(μ-3,5-$(CF_3)_2$Pz)] (**1**) and [$Au_2$(μ-$C^2$,$N^3$-MeIm)$_2$Cu(μ-3,5-$(CF_3)_2$Pz)] (**3a**) species are found to exhibit cupro-aurophilic as opposed to aurophilic or cuprophilic non-covalent metal···metal interactions. The reaction mechanism occurring is not completely understood but it likely proceeds *via* π-acid/π-base interactions - a well-known chemistry for this type of complexes. The reduced symmetry in the $Au_2Cu$ compounds has been demonstrated to attain greater extinction

coefficient in solution and higher solid-state photoluminescence quantum yield than those for the homometallic complexes, indeed approaching unity for **3a** and **4a**, which opens promising applications of such materials in OLEDs as light-emitting layers and/or inorganic LEDs as down-conversion phosphors.

## 3.4 Materials and Methods

The photoluminescence measurements were carried out with a PTI Quanta Master Model QM-4 scanning spectrofluorometer. OLED thin films were prepared *via* both vacuum sublimation by using a 12-source Trovato Model 300C vacuum deposition system, and drop-casting. Geometry optimization and single-point calculations were performed using the Gaussian 09 suite of programs. Single crystal structural data analysis and refinement was done by using Bruker APEX2, SAINT, SADABS, SHELXTL; Bruker AXS Inc.: Madison, WI, 2007 as well as CrysAlisPro (V 1.171.39.7f) software system and AutoChem 2.1 software system in conjunction with Olex2 1.2; Rigaku Corporation (2015), Oxford, UK. The experimental details and computational methods are provided in supporting information.

### 3.4.1 Representing Synthesis Procedure of Heterobimetallic $Au_4Cu_2$ complex, **4a**

1 mol of $[Au(\mu\text{-}C^2,N^3\text{-}EtIm)]_3$ and 0.5 mol of $[Cu(\mu\text{-}3,5\text{-}(CF_3)_2Pz)]_3$ were dissolved in dichloromethane, separately. The latter solution was transferred into the solution containing the gold metallocycle and a white precipitate formed. The resulting suspension was stirred for 2 hours then filtered and washed with hexane twice. Yellowish white single crystals were obtained by slow evaporation.

## 3.5 Acknowledgements

M.A.O., A.B., and R.G. dedicate this work to the memory of F. Albert Cotton. M.A.O. thanks Harry B. Gray, Pierre D. Harvey, Donald G. Truhlar, Pekka Pyykkö, Paul S. Bagus, John P. Fackler, Jr., and Thomas R. Cundari for helpful discussions. M.A.O. gratefully acknowledges support to his group's contributions by the Robert A. Welch Foundation (Grant B-1542) and the U.S. National Science Foundation (Grant CHE-1413641 and its corresponding international supplement CHE-1545934 for the collaboration with R.G. and A.M.R.). R.G. and A.B. acknowledge the FAR (Fondi di Ateneo per la Ricerca) grant from University of Camerino and the CIRCMSB (Consortium Inter-universities for the Research on Chemistry of Metals with Biological Systems). A.M.R. and M.A.O. acknowledge support of their OLED/LED-related efforts by the Scientific Research Support Fund (SRSF) of the Ministry of Higher Education and Scientific Research in Jordan.

## 3.6 References

1. Cotton, F. A.; Feng, X.; Matusz, M.; Poli, R. Experimental and theoretical studies of the copper(I) and silver(I) dinuclear N,N'-di-p-tolylformamidinato complexes. *J. Am. Chem. Soc.*, **1988**, 110(*21*), 7077-7083.

2. Napoline, J. W.; Thomas, C. M. catalytic applications of early/late heterobimetallic complexes AU - Cooper, Benjamin G. *Catal. Rev.*, **2012**, 54(*1*), 1-40.

3. Fernández, E. J.; Laguna, A.; López-de-Luzuriaga, J. M. Gold–heterometal complexes. Evolution of a new class of luminescent materials. *Dalton Trans.*, **2007**, *20*), 1969-1981.

4. Balch, A. L.; Nagle, J. K.; Oram, D. E.; Reedy, P. E. Oxidative additions and luminescence involving iridium-gold-iridium chains formed by binding of gold(I) to the metallamacrocycle $Ir_2Cl_2(CO)_2[\mu\text{-}Ph_2PCH_2As(Ph)CH_2PPh_2]_2$. *J. Am. Chem. Soc.*, **1988**, 110(*2*), 454-462.

5. Fernández, E. J.; López-de-Luzuriaga, J. M.; Monge, M.; Olmos, M. E.; Pérez, J.; Laguna, A. $[Au_2Tl_2(C_6Cl_5)_4]\cdot(CH_3)_2CO$: A luminescent loosely bound butterfly cluster with a Tl(I)−Tl(I) interaction. *J. Am. Chem. Soc.*, **2002**, 124(*21*), 5942-5943.

6. Fernández, E. J.; López-de-Luzuriaga, J. M.; Olmos, M. E.; Pérez, J.; Laguna, A.; Lagunas, M. C. A family of Au−Tl loosely bound butterfly clusters. *Inorg. Chem.*, **2005**, 44(*17*), 6012-6018.

7. Mohamed, A. A.; Galassi, R.; Papa, F.; Burini, A.; Fackler, J. P. Gold(I) and silver(I) mixed-metal trinuclear complexes: Dimeric products from the reaction of gold(I) carbeniates or benzylimidazolates with silver(I) 3,5-diphenylpyrazolate. *Inorg. Chem.*, **2006**, 45(*19*), 7770-7776.

8. Strasser, C. E.; Catalano, V. J. "On−off" Au(I)···Cu(I) Interactions in a $Au(NHC)_2$ luminescent vapochromic sensor. *J. Am. Chem. Soc.*, **2010**, 132(*29*), 10009-10011.

9. Fernández, E. J.; López-de-Luzuriaga, J. M.; Monge, M.; Olmos, M. E.; Pérez, J.; Laguna, A.; Mohamed, A. A.; Fackler, J. P. $\{Tl[Au(C_6Cl_5)_2]\}_n$: A vapochromic complex. *J. Am. Chem. Soc.*, **2003**, 125(*8*), 2022-2023.

10. Elbjeirami, O.; Rashdan, M. D.; Nesterov, V.; Rawashdeh-Omary, M. A. Structure and luminescence properties of a well-known macrometallocyclic trinuclear Au(I) complex and its adduct with a perfluorinated fluorophore showing cooperative anisotropic supramolecular interactions. *Dalton Trans.*, **2010**, 39(*40*), 9465-9468.

11. Rasika Dias, H. V.; Polach, S. A.; Wang, Z. Coinage metal complexes of 3,5-bis(trifluoromethyl)pyrazolate ligand: Synthesis and characterization of $\{[3,5\text{-}(CF_3)_2Pz]Cu\}_3$ and $\{[3,5\text{-}(CF_3)_2Pz]Ag\}_3$. *J. Fluorine Chem.*, **2000**, 103(*2*), 163-169.

12. Bonati, F.; Burini, A.; Pietroni, B. R.; Bovio, B. Reactions of C-imidazolyllithium derivatives with Group Ib compounds: Tris[μ-(1-alkylimidazolato-$N^3$,$C^2$)]tri-gold(I) and -silver(I). Crystal structure of bis(1-benzylimidazolin-2-yliden)gold(I) chloride. *J. Organomet. Chem.*, **1989**, 375(*1*), 147-160.

13. Nguyen, T.; Sutton, A. D.; Brynda, M.; Fettinger, J. C.; Long, G. J.; Power, P. P. Synthesis of a stable compound with fivefold bonding between two chromium(I) centers. *Science*, **2005**, 310(*5749*), 844-847.

14. Murillo, C. A. The δ bond and trigonal paddlewheels before the dawn of the quintuple bond AU - Murillo, Carlos A. *Comments Inorg. Chem.*, **2015**, 35(*1*), 39-58.

15. Irwin, M. D.; Abdou, H. E.; Mohamed, A. A.; Fackler, J. J. P. Synthesis and X-ray structures of silver and gold guanidinate-like complexes. A Au(II) complex with a 2.47 Å Au–Au distance. *Chem. Commun.*, **2003**, *23*), 2882-2883.

16. Jalilehvand, F.; Maliarik, M.; Sandström, M.; Mink, J.; Persson, I.; Persson, P.; Tóth, I.; Glaser, J. New class of oligonuclear platinum−thallium compounds with a direct metal-metal bond. 5. Structure Determination of heterodimetallic cyano complexes in aqueous solution by EXAFS and vibrational spectroscopy. *Inorg. Chem.*, **2001**, 40(*16*), 3889-3899.

17. Hu, S.-Z.; Zhou, Z.-H.; Robertson, B. E. Consistent approaches to van der Waals radii for the metallic elements. *Zeitschrift für Kristallographie International journal for structural, physical, and chemical aspects of crystalline materials*, **2009**, 224(*8*), 375.

18. Bondi, A. van der Waals Volumes and Radii. *J. Phys. Chem.*, **1964**, 68(*3*), 441-451.

19. Catalano, V. J.; Bennett, B. L.; Muratidis, S.; Noll, B. C. Unsupported Pt(0)−Tl(I) bonds in the simple $[Pt(PPh_2Py)_3Tl]+$ complexes. *J. Am. Chem. Soc.*, **2001**, 123(*1*), 173-174.

20. Rawashdeh-Omary, M. A.; Omary, M. A.; Fackler, J. P. Argento–aurophilic bonding in organosulfur complexes. The molecular and electronic structures of the heterobimetallic complex $AgAu(MTP)_2$. *Inorg. Chim. Acta*, **2002**, 334(376-384.

21. Burini, A.; Mohamed, A. A.; Fackler, J. P. Cyclic trinuclear gold(I) compunds: synthesis, structures and supramolecular aicd-case π-stacks. *Comments Inorg. Chem.*, **2003**, 24(*5-6*), 253-280.

22. Omary, M. A.; Mohamed, A. A.; Rawashdeh-Omary, M. A.; Fackler, J. P. Photophysics of supramolecular binary stacks consisting of electron-rich trinuclear Au(I) complexes and organic electrophiles. *Coord. Chem. Rev.*, **2005**, 249(*13*), 1372-1381.

23. Dias, H. V. R.; Diyabalanage, H. V. K.; Eldabaja, M. G.; Elbjeirami, O.; Rawashdeh-Omary, M. A.; Omary, M. A. Brightly phosphorescent trinuclear copper(I) complexes of pyrazolates: Substituent effects on the supramolecular structure and photophysics. *J. Am. Chem. Soc.*, **2005**, 127(*20*), 7489-7501.

24. Vickery, J. C.; Olmstead, M. M.; Fung, E. Y.; Balch, A. L. Solvent-stimulated luminescence from the supramolecular aggregation of a trinuclear gold(I) complex that displays extensive intermolecular Au···Au interactions. *Angew. Chem., Int. Ed.*, **1997**, 36(*11*), 1179-1181.

25. McDougald, R. N.; Chilukuri, B.; Jia, H.; Perez, M. R.; Rabaâ, H.; Wang, X.; Nesterov, V. N.; Cundari, T. R.; Gnade, B. E.; Omary, M. A. Molecular and electronic structure of cyclic trinuclear gold(I) carbeniate complexes: Insights for structure/luminescence/conductivity relationships. *Inorg. Chem.*, **2014**, 53(*14*), 7485-7499.

26. White-Morris, R. L.; Olmstead, M. M.; Attar, S.; Balch, A. L. Intermolecular interactions in polymorphs of trinuclear gold(I) Complexes: Insight into the solvoluminescence of $AuI_3(MeNCOMe)_3$. *Inorg. Chem.*, **2005**, 44(*14*), 5021-5029.

27. Vorontsov, I. I.; Kovalevsky, A. Y.; Chen, Y.-S.; Graber, T.; Gembicky, M.; Novozhilova, I. V.; Omary, M. A.; Coppens, P. Shedding light on the structure of a photoinduced transient excimer by time-resolved diffraction. *Phys. Rev. Lett.*, **2005**, 94(*19*), 193003.

28. Xiong, X.-G.; Pyykkö, P. Unbridged Au(ii)–Au(ii) bonds are theoretically allowed. *Chem. Commun.*, **2013**, 49(*21*), 2103-2105.

29. Cotton, F. A.; Walton, R. A. *Multiple bonds between metal atoms.* **1982**. Wiley.

30. Omary, M. A.; Webb, T. R.; Assefa, Z.; Shankle, G. E.; Patterson, H. H. Crystal structure, electronic structure, and temperature-dependent raman spectra of $Tl[Ag(CN)_2]$: Evidence for ligand-unsupported argentophilic interactions. *Inorg. Chem.*, **1998**, 37(*6*), 1380-1386.

31. Chadwick, B. M.; Frankiss, S. G. Vibrational spectra and structures of some dicyanoaurate(I) complexes. *J. Mole. Struct.*, **1976**, 31(*1*), 1-9.

32. Harvey, P. D. Reparameterized Herschbach-Laurie empirical relationships between metal-metal distances and force constants applied to homonuclear bi- and polynuclear complexes (M = Cr, Mo, Rh, Pd, Ag, W, Re, Ir, Pt, Au, Hg). *Coord. Chem. Rev.*, **1996**, 153(175-198.

33. Zhao, Y.; Truhlar, D. G. The M06 suite of density functionals for main group thermochemistry, thermochemical kinetics, noncovalent interactions, excited states, and transition elements: two new functionals and systematic testing of four M06-class functionals and 12 other functionals. *Theor. Chem. Acc.*, **2008**, 120(*1*), 215-241.

34. Zhao, Y.; Truhlar, D. G. Density functionals with broad applicability in chemistry. *Acc. Chem. Res.*, **2008**, 41(*2*), 157-167.

35. Galassi, R.; Ricci, S.; Burini, A.; Macchioni, A.; Rocchigiani, L.; Marmottini, F.; Tekarli, S. M.; Nesterov, V. N.; Omary, M. A. Solventless supramolecular chemistry via vapor diffusion of volatile small molecules upon a new trinuclear silver(I)-nitrated pyrazolate macrometallocyclic solid: An experimental/theoretical investigation of the dipole/ quadrupole chemisorption phenomena. *Inorg. Chem.*, **2013**, 52(*24*), 14124-14137.

36. Cundari, T. R.; Stevens, W. J. Effective core potential methods for the lanthanides. *J. Chem. Phys.*, **1993**, 98(*7*), 5555-5565.

37. Stevens, W. J.; Krauss, M.; Basch, H.; Jasien, P. G. Relativistic compact effective potentials and efficient, shared-exponent basis sets for the third-, fourth-, and fifth-row atoms. *Can, J. Chem.*, **1992**, 70(*2*), 612-630.

38. Determan, J. J.; Omary, M. A.; Wilson, A. K. Modeling the photophysics of Zn and Cd monomers, metallophilic dimers, and covalent excimers. *J. Phys. Chem. A*, **2011**, 115(*4*), 374-382.

39. Determan, J. J.; Sinha, P.; Wilson, A. K.; Omary, M. A. Bonding and phosphorescence trends in 1-D, 2-D, and 3-D oligomers and extended excimers of group 12 metals: Validation of cooperativity in both metallophilic and excimeric bonding. *J. Phys. Chem. C*, **2015**, 119(*4*), 2015-2028.

40. Dunham, J. L. The energy levels of a rotating vibrator. *Phys. Rev.*, **1932**, 41(*6*), 721-731.

41. Miessler, G.; Fischer, P.; Tarr, D. *Inorganic Chemistry.* **2014**. Prentice Hall.

42. Omary, M. A.; Rawashdeh-Omary, M. A.; Gonser, M. W. A.; Elbjeirami, O.; Grimes, T.; Cundari, T. R.; Diyabalanage, H. V. K.; Gamage, C. S. P.; Dias, H. V. R. Metal effect on the supramolecular structure, photophysics, and acid−base character of trinuclear pyrazolato coinage metal complexes. *Inorg. Chem.*, **2005**, 44(*23*), 8200-8210.

43. Kawamura, Y.; Sasabe, H.; Adachi, C. Simple accurate system for measuring absolute photoluminescence quantum efficiency in organic solid-state thin films. *Japanese J. Appl. Phys.*, **2004**, 43(*11A*), 7729-7730.

44. Turro, N. *Modern Molecular Photochemistry.* **1978**. Benjamin/Cummings.

# CHAPTER 4

# OXIDATIVE ADDITION OF HALOACIDS AND DIHALOGENS TO TRINUCLEAR CYCLIC COINAGE METAL COMPLEXES AND PHOTOINDUCED REDUCTIVE ELIMINATION OF $X_2$ AND $H_2$

## 4.1 Introduction

The oxidative addition properties of cyclic trinuclear gold(I) complexes have been an area of active research since 1977 with Balch and Doonan's report of stepwise oxidative addition of a gold(I) carbeniate complex that showed mixed valence gold metal center after the addition of $Br_2/I_2$.[1] This study resulted the conclusion of oxidative addition of $Br_2/I_2$ occurs across one gold center, taking it from a linear gold(I) center to a square planar gold(III) center (**Figure 4.1**), instead of the formation of gold-gold bonds as seen in the partially oxidized dimeric bridged gold(I) complexes studies conducted by Raptis.[2] Balch was also able to determine that the gold centers in these trimer complexes "communicate" with one another, given the separation of three distinct different oxidative addition products. It was hypothesized that the gold centers could communicate the difference in their chemical environments either through gold-gold interactions or through the π-system of the ligands. The addition of the halogen would change the electronic structure at not just the gold center but also tune the electronics of the ligands, which could be responsible for the stepwise oxidative additions.

This study quickly led to the study of other cyclic trinuclear gold(I) complexes featuring pyrazolate ligands[3-5] as well as imidazolate ligands.[6, 7] These studies ultimately led to the same conclusions. Vickery[5] found that the oxidative addition of the halogens disrupted the aurophilic interactions that usually hold these cyclic trinuclear complexes as aggregates and found that

there are no intermolecular interactions between the partially oxidized products but the fully oxidized products exhibited I---I interactions.

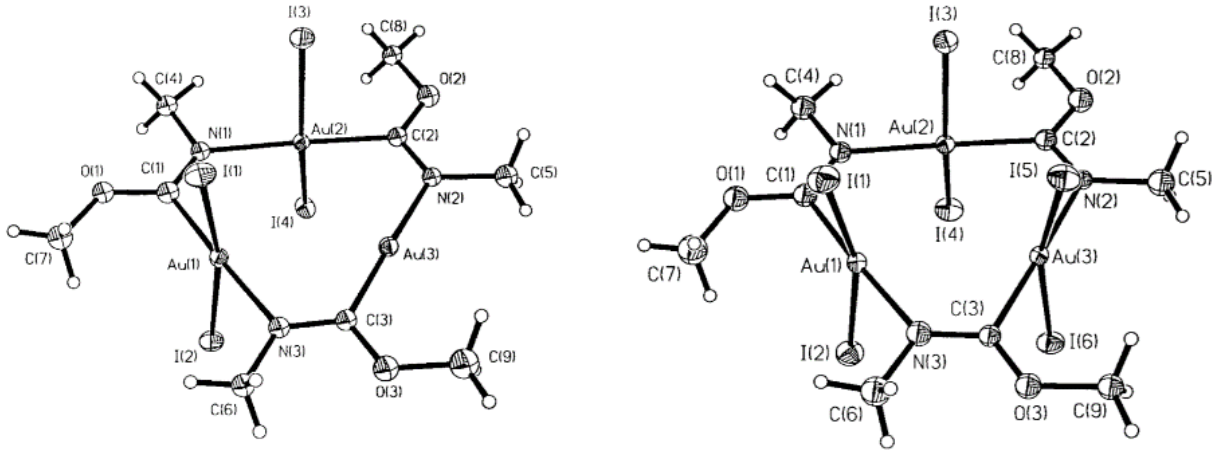


**Figure 4.1: Structures of products of successive oxidative addition of $Br_2/I_2$ to $[Au(CH_3OC{=}NCH_3)]_3$.**

All these studies have led to the conclusion that the oxidative addition of halogens is possible for the complexes, but the mechanism remains questionable. It also remains questionable whether these complexes can go through the reverse of oxidative addition, reductive elimination. This work has inspired us to delve into the oxidative addition properties of not only cyclic trinuclear Au(I) complexes, but to also consider the oxidative addition properties of Ag(I) and Cu(I) complexes as well. The work herein strives to determine trends in the thermodynamics of these oxidative additions as well as the reductive eliminations.

## 4.2 Methods

All calculations were performed using the Gaussian 09 suite of programs[8] except the positive charge attraction curves which were generated with GAMESS.[9, 10] Truhlar's functional M06[11, 12] was employed in conjunction with the CEP-31G(d) pseudopotential/valence basis set.[13-15] This functional was selected due to its performance in modeling weak interactions.[12] Weak

intermolecular interactions are important in this work due to the $d^{10}$ metal centers, which exhibit metallophilic interactions prior to being oxidized. The CEP-31G(d) basis set has been used previously by the Omary Group to model various phenomena dealing with these trimeric coinage metal complexes.[16] Calculations include geometry optimizations along with frequency calculations to ensure stationary points have been achieved. Time-dependent DFT (TD-DFT) calculations were performed to determine the transition types the oxidized complexes experience to validate photoinduced reductive elimination of hydrogen gas occurs for these complexes.

A wide variety of ligands were sampled in order to deduce trends across both metal selection and ligand selection (**Figure 4.2**). An additional consideration was whether the ligands were "naked" (with hydrogens as substituents) or if the ligand has a methyl or trifluoromethyl substituents. This allowed for the analysis of the effect of electron withdrawing and electron donating substituents upon the π-acidity or –basicity of the trimers.

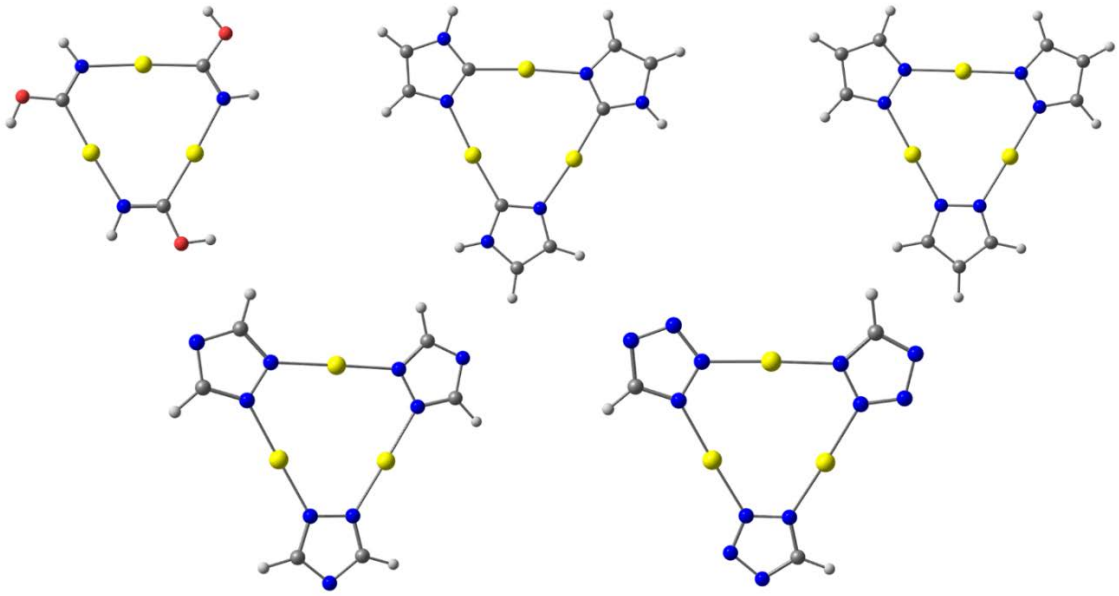

**Figure 4.2: $[Au(\mu\text{-}L)]_3$ structures where L = carbeniate (Cb) (top left), imidazolate (Im) (top middle), pyrazolate (Pz) (top right), triazolate (Tz) (bottom left) or tetrazolate (Ttz) (bottom right).**

Dimers-of-trimer (DOTs) were also optimized in addition to trimers. In order to determine the most stable dimer conformation, four conformations were calculated: (i) eclipsed or prismatic, (ii) staggered, (iii) chair and (iv) extended chain. Dimerization energies were calculated according to **Equation 4.1**. It was found that there was no consensus across all metals and ligands for which conformation would be the most stable, but experimental results show that the eclipsed or staggered versions of the DOTs appear in crystal structures with some examples of chair conformations or extended chain conformations. Given this observation, all further calculations were performed with eclipsed or staggered conformations, depending on which is lower in energy for the particular metal, ligand and substituent combination.

$$E_{dimerization} = E_{DOT} - 2E_{trimer} \qquad \textbf{Equation 4.1}$$

The energetics of oxidative additions involving the trimers was determined *via* **Equation 4.2** and **4.3** where $E_{ox.add.}$ is the energy of the overall oxidative addition process, $E_{TX2}$ and $E_{THX}$ are the energy of the oxidized product with either $X_2$ (where X= F, Cl, Br or I) or HX. $E_T$ is the energy of the trimer by itself and $E_{X2}$ or $E_{HX}$ is the energy of the substrate. From here the energies of multiple oxidative additions can be calculated according to similar equations, substituting the $E_T$ with the energy of oxidized product. These same equations can also be applied to the DOT systems, by substituting $E_T$ with $E_{DOT}$.

$$E_{ox.add.} = E_{TX_2} - E_T - E_{X_2} \qquad \textbf{Equation 4.1}$$

$$E_{ox.add.} = E_{THX} - E_T - E_{HX} \qquad \textbf{Equation 4.2}$$

Conversely, the energy for the reductive elimination process when two successive additions have occurred is represented by **Equation 4.4** or **4.5**. Where $E_{red.elm.}$ is the energy of the reductive elimination process, $E_{(TX2)2}$ or $E_{(THX)2}$ represents the product of two successive oxidative

addition processes. For **Equation 4.4**, the $E_{red.elm.}$ should be equal to $-E_{ox.add.}$ because the products are the same as the reactants. For **Equation 4.5**, $E_{red.elm.}$ will be different than $E_{ox.add.}$ given the products will be rearranged from the reactants.

$$E_{red.elm.} = E_T + 2E_{x_2} - E_{(TX_2)2} \qquad \textbf{Equation 4.3}$$

$$E_{red.elm.} = E_T + E_{H_2} + E_{X_2} - E_{(THX)2} \qquad \textbf{Equation 4.4}$$

All energies are a reflection of the change in the Gibbs free energy and are reported in kcal/mol for these complexes. It was found that all addition reactions had similar change in entropy leading to the change in enthalpy for each complex having a similar relationship to the change in the Gibbs free energy. The range of the change in enthalpy and the change in the Gibbs free energy is similar as is demonstrated by **Figure 4.3**.

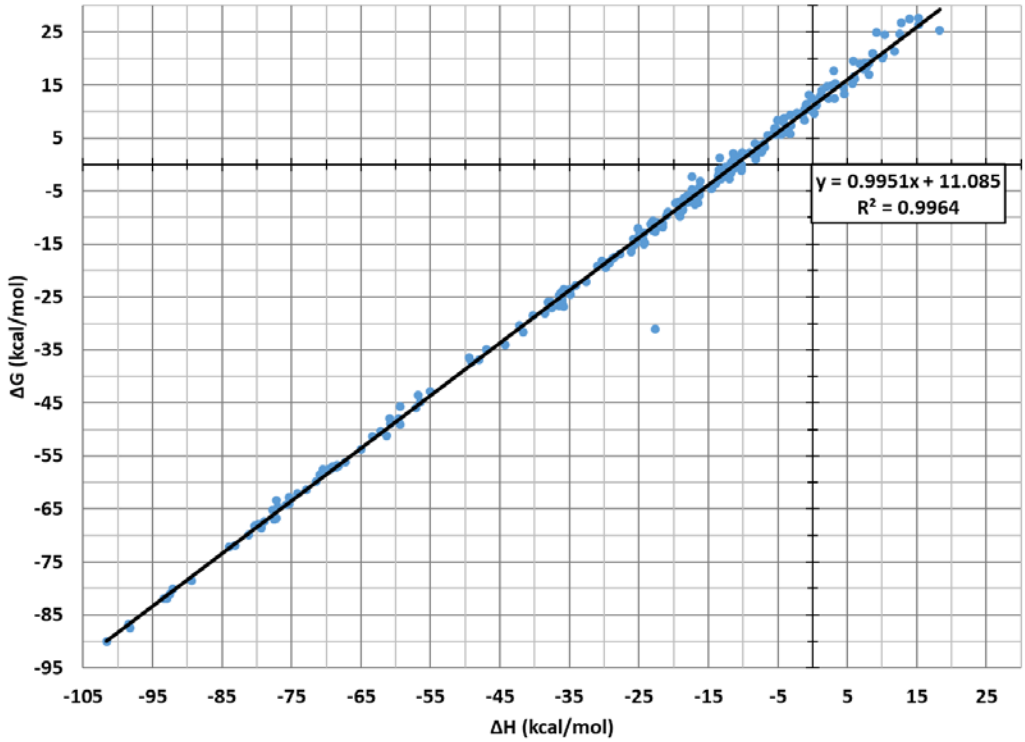


**Figure 4.3: Comparison of the change in enthalpy (x-axis) versus the change in the Gibbs free energy (y-axis) for the reaction of a trimer plus $X_2$ to produce [trimer$X_2$]. Trend line has been added to demonstrate how well the data fits a straight line to justify reporting the changes in Gibbs free energy versus the change in enthalpy.**

## 4.3 Results and Discussion

The metal centers in these trimers are expected to have an oxidation state of 1 due to the negative charge on the coordinating ligands due to deprotonation before the ligands coordinates to the metal atom. The donor atom-metal-donor atom angles are expected to be around 180°, supporting linear two coordinate geometry at the metal centers. This is seen computationally as all angles are within 4° of being linear (**Table 4.1** and **4.2**). This is similar to other linear two coordinate complexes of the coinage metals, including the crystal structures of some of these trimeric materials, as well as Au phosphine complexes. This geometric approach to oxidation state verification is also supported by the natural bond order (NBO) analysis of these complexes, where each metal center possess 5 lone pairs in predominantly d-character orbitals, giving the metal centers 10 d-electrons.

**Table 4.1: Bond angles between the donor atoms and the metal centers in $[M(\mu\text{-}C,N\text{-}L)]_3$ complexes.**

| Complex | N-M-C, ° | N-M-C, ° | N-M-C, ° |
|---|---|---|---|
| $[Cu(\mu\text{-}C,N\text{-}Cb)]_3$ | 178.3 | 178.3 | 178.3 |
| $[Ag(\mu\text{-}C,N\text{-}Cb)]_3$ | 178.4 | 178.4 | 178.4 |
| $[Au(\mu\text{-}C,N\text{-}Cb)]_3$ | 177.1 | 177.1 | 177.1 |
| $[Cu(\mu\text{-}C,N\text{-}Im)]_3$ | 176.8 | 176.8 | 176.8 |
| $[Ag(\mu\text{-}C,N\text{-}Im)]_3$ | 177.2 | 177.2 | 177.2 |
| $[Au(\mu\text{-}C,N\text{-}Im)]_3$ | 175.9 | 175.9 | 175.9 |

**Table 4.2: Bond angles between the donor atoms and the metal centers in $[M(\mu\text{-}N,N\text{-}L)]_3$ complexes.**

| Complex | N-M-N, ° | N-M-N, ° | N-M-N, ° |
|---|---|---|---|
| $[Cu(\mu\text{-}N,N\text{-}Pz)]_3$ | 179.4 | 179.4 | 179.4 |
| $[Ag(\mu\text{-}N,N\text{-}Pz)]_3$ | 179.6 | 179.6 | 179.6 |
| $[Au(\mu\text{-}N,N\text{-}Pz)]_3$ | 179.4 | 179.4 | 179.4 |

| Complex | N-M-N, ° | N-M-N, ° | N-M-N, ° |
|---|---|---|---|
| $[Cu(\mu\text{-}N,N\text{-}Tz)]_3$ | 180.0 | 180.0 | 180.0 |
| $[Ag(\mu\text{-}N,N\text{-}Tz)]_3$ | 179.9 | 179.9 | 179.9 |
| $[Au(\mu\text{-}N,N\text{-}Tz)]_3$ | 179.2 | 179.2 | 179.2 |
| $[Cu(\mu\text{-}N,N\text{-}Ttz)]_3$ | 178.2 | 178.2 | 178.2 |
| $[Ag(\mu\text{-}N,N\text{-}Ttz)]_3$ | 177.3 | 177.3 | 177.3 |
| $[Au(\mu\text{-}N,N\text{-}Ttz)]_3$ | 178.0 | 178.0 | 178.0 |

Given that these complexes are expected to go through oxidative addition at the metal centers, it is expected that upon oxidation, the geometry should change at the metal center to be approximately square-planar with M(III) centers. This is based off previous work done by Balch that is supported by crystal structures of the oxidized materials. Selected complexes are shown below to have this approximately square planar geometry (**Table 4.3**) as well as an NBO analysis that shows that the metal center loses two d-electrons, leading to the M(III) oxidation state. Another interesting geometric phenomena that was observed is that upon successive oxidative addition, the geometries at the metal centers becomes less square planar (**Figure 4.4**). This is presumed to be from the repulsion of the halogens/hydrogens, which is also seen experimentally.

**Table 4.3: Halogen-metal-donor atom angles of $[M(\mu\text{-}C,N\text{-}Im)]_3$ oxidized complexes.**

| Complex | X-M-C, ° | X-M-C, ° | X-M-N, ° | X-M-N, ° |
|---|---|---|---|---|
| $\{[Cu(\mu\text{-}C,N\text{-}Im)]_3Br_2\}$ | 86.6 | 85.3 | 94.3 | 95.1 |
| $\{[Cu(\mu\text{-}C,N\text{-}Im)]_3I_2\}$ | 85.7 | 85.7 | 94.7 | 94.7 |
| $\{[Ag(\mu\text{-}C,N\text{-}Im)]_3Br_2\}$ | 87.7 | 87.1 | 92.7 | 93.4 |
| $\{[Ag(\mu\text{-}C,N\text{-}Im)]_3I_2\}$ | 85.9 | 85.8 | 94.0 | 94.4 |
| $\{[Au(\mu\text{-}C,N\text{-}Im)]_3Br_2\}$ | 88.4 | 88.4 | 91.7 | 91.7 |
| $\{[Au(\mu\text{-}C,N\text{-}Im)]_3I_2\}$ | 88.3 | 88.3 | 91.9 | 91.9 |

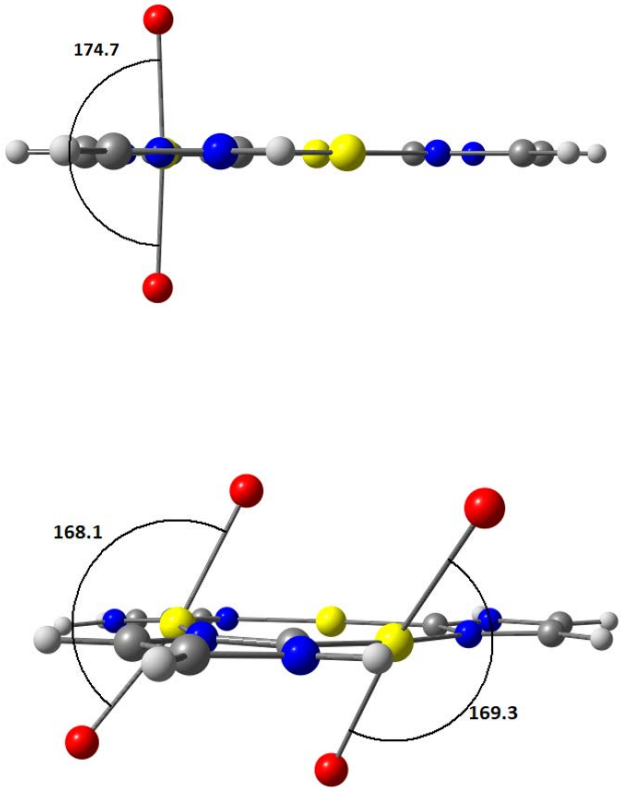


**Figure 4.4**: **Change in the geometry at the metal centers of [Au(μ-C,N-Im)] upon two successive oxidative additions.**

After verifying that the oxidative addition occurs as expected by previous work, the π-basicity (or π-acidity) of the trimers was monitored through three effects: (i) varying the metal; (ii) varying the ligand; and (iii) varying the substituents. These changes were characterized based on three methods. The first is the molecular electrostatic potential (MEP) which is a plot of the electron density of the molecule plotted on the surface of the total electron density of the molecule and can be used to determine where the concentration of electron density is highest. The second is another type MEP surface referred to as an MEP in space. These two methods are the same in the fact that the second is an exaggeration of the first. They are both qualitative ways of describing and comparing π-basicity. The third method is known as a positive charge attraction curve (PCA). These calculations are done by placing a naked positive charge at the center of the

trimer and monitors the energy as that charge moves regular to the plane of the trimer. Given that the charge is naked, it possesses no orbitals so the energy measures only the electrostatic potential between the point charge and the center of the trimer. This also used to determine the π-basicity of the trimers but this is a more qualitative method. These methods have previously been used to characterize the π-acidity and –basicity of these trimers by Tekarli et al. in 2008.[17]

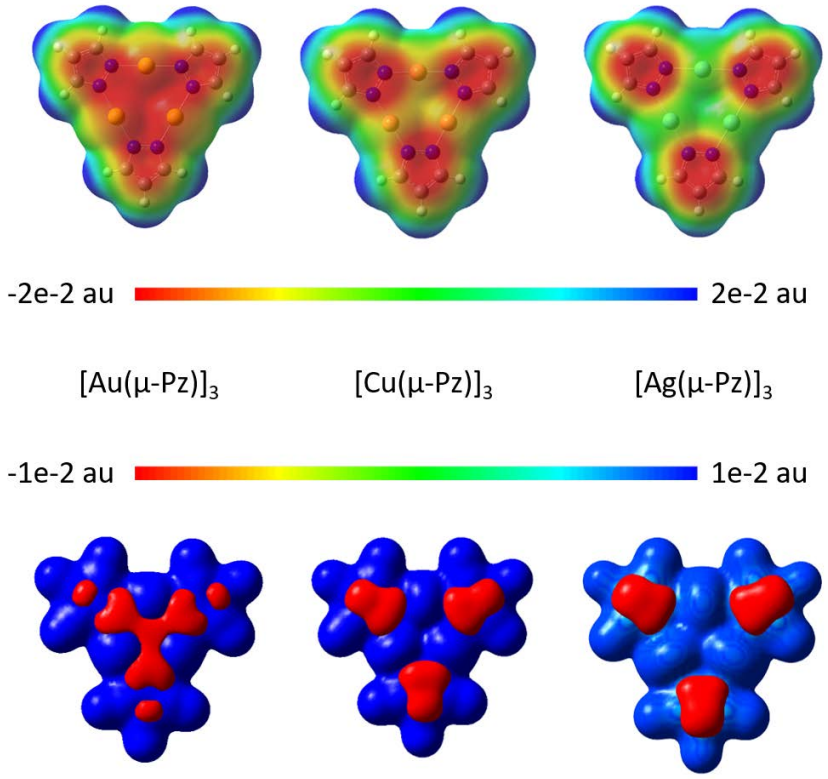


**Figure 4.5: Mapping of the electrostatic potential of AuPz, CuPz, and AgPz on the surface of the electron density of the molecule (top) and a in space (bottom) where blue represents positive regions and red represents negative regions.**

These methods were applied to these trimer systems to ascertain which coinage metal affords the most π-basic and π-acidic trimers (**Figure 4.5**). When considering the $[M(\mu\text{-Pz})]_3$, the MEP surfaces show that the Au trimer would have the largest amount of electron density at the center of the trimer (denoted by the red color), making it the most π-basic. The Ag trimer has the smallest amount of electron density (denoted by the blue color) at the center making it the most

π-acidic. These results correlate with what is known about the metal centers, which the electronegativity of Au being larger than Cu which is only slightly larger than Ag. This accounts for the reason the difference between the Au and Cu trimer is very obvious while the difference between the Cu and Ag trimer is less obvious.

As discussed in the methods section above, a way to quantitatively measure π-basicity is to look at the interaction of the electron density at the center of the trimer with a naked positive point charge. The AuPz trimer experiences the smallest destabilization when the point charge is placed at its center, supporting the claims above that it is the most basic trimer. The difference in the destabilization energies mirrors the results from the electrostatic potential maps. Namely, there is a large difference when switching from the Au to the Cu trimer and a smaller difference between the Cu and the Ag trimer (**Figure 4.5**).

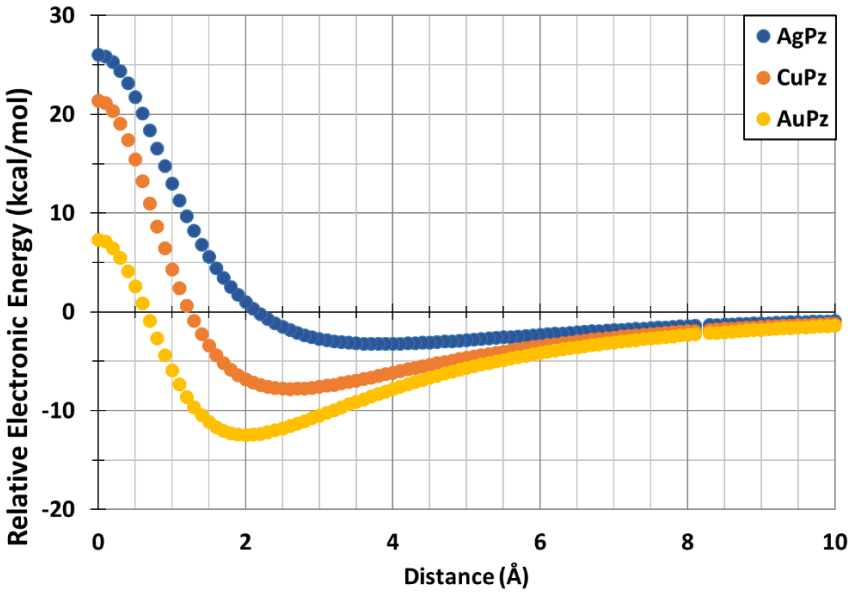


**Figure 4.6: PCA curves for the AuPz, CuPz, and AgPz trimers measuring the destabilization energy seen when a positive point charge is placed at the center of the trimer.**

After investigating the metals, the ligands were varied and analyzed the same way. It became clear that the $[AuL]_3$ trimers could be separated into two groups: the π-basic and π-acidic

trimers. The π-basic trimers consist of the trimers formed from the carbeniate (Cb), imidizolate (Im), and pyrazolate (Pz) ligands. These ligands combined with the Au center all lead to a high concentration of electron density at the center of the trimers. The π-acidic trimers result from the triazolate (Tz) and tetrazolate (Ttz) ligands which lead to a lack of electron density at the center of the trimers (**Figure 4.7**). The degree of electron density in the center of the trimers can modulated through changing the number and placement of nitrogen atoms on the ligand rings. For example, the imidazolate ligand yields the most π-basic trimer. It has nitrogen atoms at the one and three position while the pyrazolate trimer has two nitrogen atoms at the one and two position. The nitrogen atoms appear to be responsible for withdrawing electrons from the center of the trimer, which would explain why the tetrazolate and triazolate ligands lead to π-acidic trimers. The PCA curves for these ligand modulated trimers also show the same qualitative agreement that was seen for the pyrazolate trimers when the metal was varied (**Figure 4.8**).

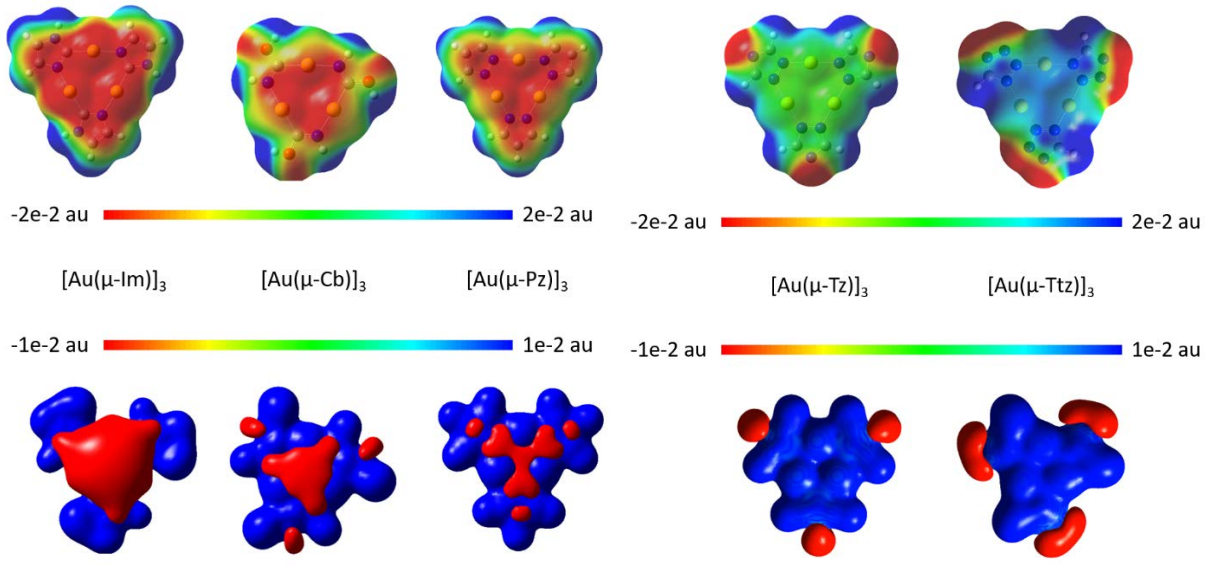


**Figure 4.7: Mapping of the electrostatic potential of AuL complexes on the surface of the electron density of the molecule (top) and in space (bottom) where blue represents positive regions and red represents negative regions.**

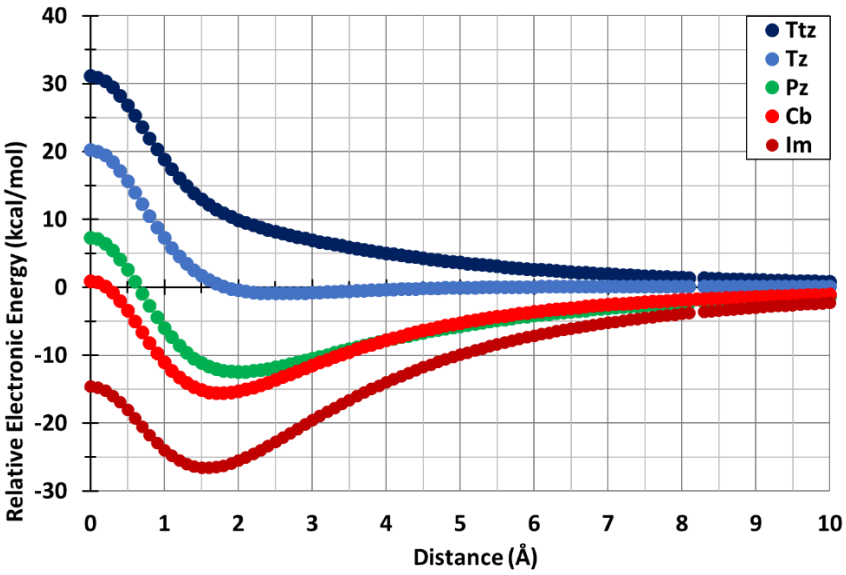


**Figure 4.8: PCA curves for the AuL trimers measuring the destabilization energy seen when a positive point charge is placed at the center of the trimer.**

After investigating the metal and ligand effects, the most π-basic trimer was used to determine the effects of substituent, which was determined to be the AuIm trimer. For the imidazolate ligand, the substitution occurs at the nitrogen atom at the three position. When the hydrogen at this position was substituted for a methyl group, there were little changes observed in the electrostatic potential and in the stabilization energy seen in the PCA curves. The methylated trimer was determined to be more π-basic based on the fact that the methyl group is weakly electron donating *via* induction. When the hydrogen group was substituted with the trifluoromethyl group the change was more drastic. This group is extremely electron withdrawing and as a result there is an obvious difference between the unsubstituted trimer versus the fluorinated trimer (**Figure 4.9** and **4.10**).

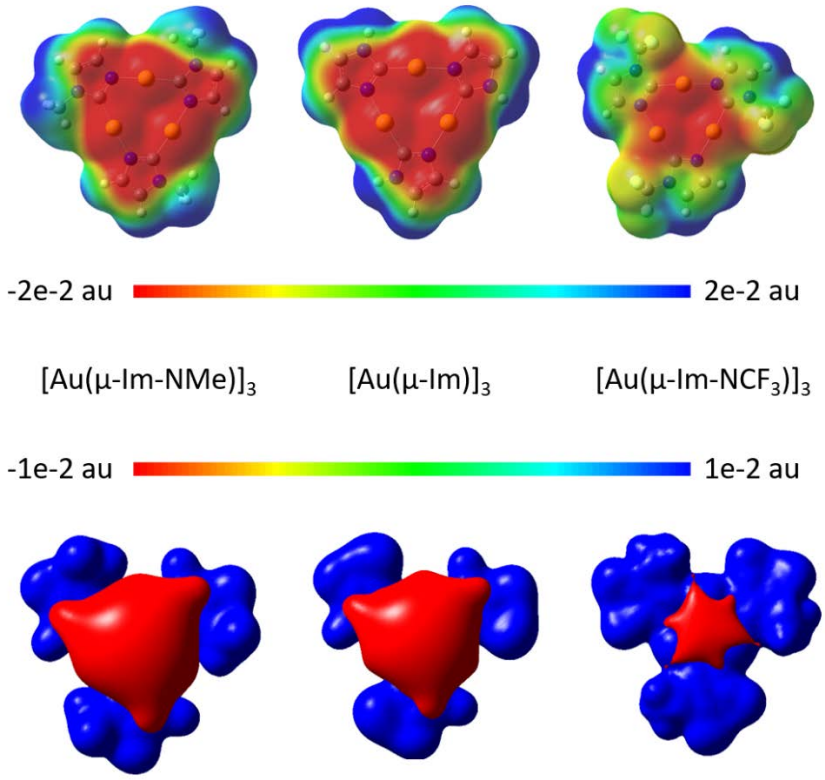


**Figure 4.9: Mapping of the electrostatic potential of [Au(μ-Im-NS)] trimers where S = Me, H or $CF_3$, on the surface of the total electron density to give a gradient of electron density (top) and a localization of the electron density (bottom).**

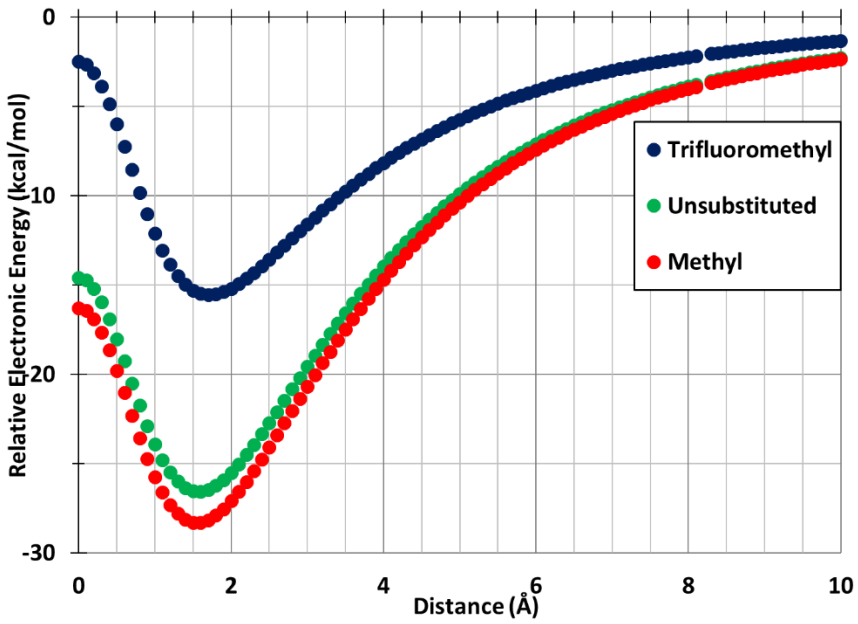


**Figure 4.10: PCA curves for the AuIm trimers measuring the destabilization energy seen when a positive point charge is placed at the center of the trimer.**

While π-basicity can be used to judge which trimers will act more effectively as nucleophiles, these characteristics are not directly correlated with the oxidation energies of the trimers. In order to deduce trends for the oxidative addition to these trimers, the energy of the highest-occupied molecular orbital (HOMO) was compared against the one-electron oxidation of the trimers (**Figure 4.11**). These results show that the trimers that have the more favorable oxidative addition energies are the trimers that have HOMO energies that are the highest in energy (i.e. – less negative). Therefore, the trimers with the Ttz ligands have the least favorable oxidation energies while the trimers from the Im ligand have the most favorable oxidation energies. In this case, the trends seen for the one-electron oxidations closely follow that of the trends of π-basicity.

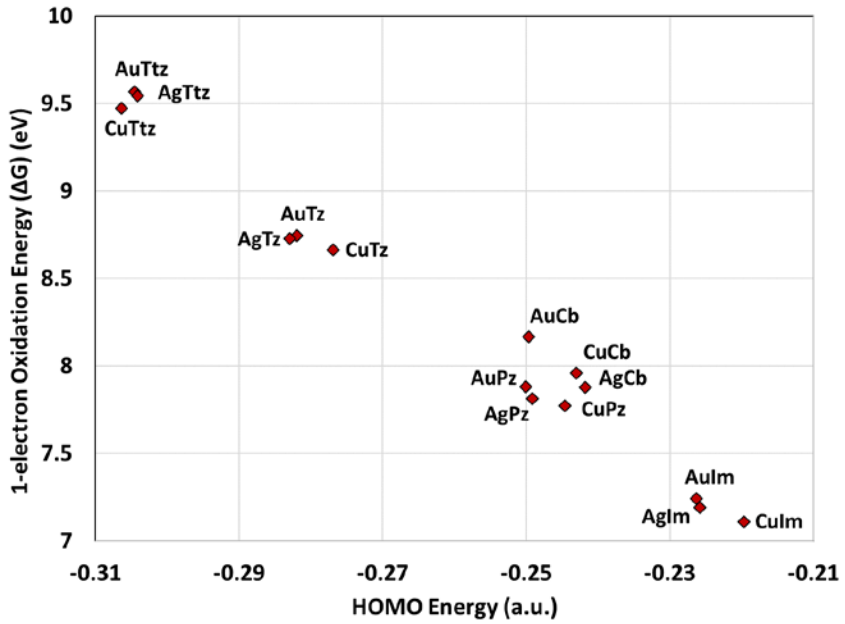


**Figure 4.11: Comparison of the 1-electron oxidation energies (ΔG) versus the energy of the HOMO (a.u.).**

After determining which trimers were π-acidic or -basic, and which trimers had more favorable 1-electron oxidations, the effects of these characteristics on the energetics of the oxidative addition reactions with $X_2$ and HX were determined as well as the energetics of the

reductive elimination of $X_2$ and $H_2$. To determine these trends, the thermodynamics of the addition of symmetric dihalogen substrates were studied. In order to look at the trends with respect to π-basicity the reactions involving the MPz trimers were analyzed first (**Table 4.4**). The oxidative addition of the later dihalogen substrates ($Cl_2$, $Br_2$, and $I_2$) show a preference for the more π-basic trimers. This is believed to be a result of the increased electron density at the metal centers, supporting an $S_N2$ type reaction, which is expected for these complexes. However, the energy of the $F_2$ to the trimers sees a deviation from this trend. The CuPz trimer and $F_2$ would have a larger orbital overlap compared to the Au/AgPz trimers, which leads to a stronger interaction between the Cu metal center and the F, leading to the inflated energy of the oxidative addition reaction (**Table 4.4**). From these results it was hypothesized that the more π-basic trimers will have more favorable oxidative additions and this is a trend seen across as dihalogen substrates. There is also a trend that is revealed to be related to the length of the dihalogen bond. For the dihalogens that have smaller bond lengths, the oxidative addition energy was found to be more favorable (**Table 4.4**).

**Table 4.4: Comparison of energetics (ΔG) of the oxidative addition of $X_2$ to the ML trimers reported in kcal/mol.**

| Trimer | $F_2$ | $Cl_2$ | $Br_2$ | $I_2$ |
|---|---|---|---|---|
| $[Cu(\mu\text{-Im})]_3$ | -81.9 | -24.5 | -9.3 | -0.6 |
| $[Cu(\mu\text{-Cb})]_3$ | -86.8 | -28.1 | -12.7 | -2.7 |
| $[Cu(\mu\text{-Pz})]_3$ | -68.2 | -7.2 | 7.3 | 15.3 |
| $[Cu(\mu\text{-Tz})]_3$ | -64.7 | -4.7 | 9.8 | 18.0 |
| $[Cu(\mu\text{-Ttz})]_3$ | -57.1 | -0.8 | 12.5 | 14.7 |
| $[Ag(\mu\text{-Im})]_3$ | -64.1 | -18.6 | -5.9 | 1.0 |
| $[Ag(\mu\text{-Cb})]_3$ | -71.9 | -22.1 | -8.9 | -1.1 |
| $[Ag(\mu\text{-Pz})]_3$ | -48.9 | -2.2 | 9.6 | 16.2 |

| Trimer | $F_2$ | $Cl_2$ | $Br_2$ | $I_2$ |
|---|---|---|---|---|
| $[Ag(\mu\text{-Tz})]_3$ | -44.8 | 0.6 | 12.4 | 18.6 |
| $[Ag(\mu\text{-Ttz})]_3$ | -36.9 | 6.0 | 16.5 | 21.4 |
| $[Au(\mu\text{-Im})]_3$ | -66.9 | -26.1 | -15.0 | -7.5 |
| $[Au(\mu\text{-Cb})]_3$ | -68.6 | -26.8 | -14.8 | -7.2 |
| $[Au(\mu\text{-Pz})]_3$ | -56.9 | -16.5 | -4.3 | 3.2 |
| $[Au(\mu\text{-Tz})]_3$ | -53.7 | -12.4 | -1.6 | 5.6 |
| $[Au(\mu\text{-Ttz})]_3$ | -49.0 | -9.8 | 1.6 | 8.3 |

For the studied trimers, it was found that the second oxidative addition is less favorable than the first (**Table 4.5**). This can be attributed to the fact that the first oxidative addition results in a decrease in the electron density at the center of the trimer, as the metal center donates two electrons to form the metal halogen bonds. The oxidative addition product is then less π-basic and as a result further oxidative addition is less favorable. It can also be account for through steric arguments as the center of the trimer becomes less available to coordinate the incoming substrate.

**Table 4.5: Comparison of energetics (ΔG) of successive oxidative addition reactions of dihalogen substrates to the trimers reported in kcal/mol.**

| Trimer | $Br_2$ | $2Br_2$ | $I_2$ | $2I_2$ |
|---|---|---|---|---|
| $[Cu(\mu\text{-Im})]_3$ | -9.3 | -9.0 | -0.6 | 3.9 |
| $[Cu(\mu\text{-Cb})]_3$ | -12.7 | -13.2 | -2.7 | -0.5 |
| $[Cu(\mu\text{-Pz})]_3$ | 7.3 | 8.8 | 15.3 | 26.3 |
| $[Cu(\mu\text{-Tz})]_3$ | 9.8 | 9.3 | 18.0 | 21.0 |
| $[Cu(\mu\text{-Ttz})]_3$ | 12.5 | 14.7 | 20.1 | 24.6 |
| $[Ag(\mu\text{-Im})]_3$ | -5.9 | -5.7 | 1.0 | 4.0 |
| $[Ag(\mu\text{-Cb})]_3$ | -8.9 | -9.6 | -1.1 | 0.8 |
| $[Ag(\mu\text{-Pz})]_3$ | 9.6 | 11.2 | 16.2 | 18.0 |

| Trimer | $Br_2$ | $2Br_2$ | $I_2$ | $2I_2$ |
|---|---|---|---|---|
| $[Ag(\mu\text{-Tz})]_3$ | 12.4 | 13.2 | 18.6 | 20.9 |
| $[Ag(\mu\text{-Ttz})]_3$ | 16.5 | 19.0 | 21.4 | 27.6 |
| $[Au(\mu\text{-Im})]_3$ | -15.0 | -11.2 | -7.5 | -2.3 |
| $[Au(\mu\text{-Cb})]_3$ | -14.8 | 2.4 | -7.2 | -2.1 |
| $[Au(\mu\text{-Pz})]_3$ | -4.3 | 0.3 | 3.2 | 9.8 |
| $[Au(\mu\text{-Tz})]_3$ | -1.6 | 2.2 | 5.6 | 11.4 |
| $[Au(\mu\text{-Ttz})]_3$ | 1.6 | 6.8 | 8.3 | 15.3 |

In general the oxidative addition of the hydrohalic acids is less favorable than the addition of the dihalogen (**Table 4.6**). For the oxidative addition for these substrates, it is observed that the stronger acids (i.e., smaller dissociation energies) have more favorable addition energies. This is consistent with previous work whereby the acids are expected to dissociate before nucleophilic attack by the metal centers or an $S_N1$ mechanism.[18] It also holds true for these substrates that the second oxidative addition is expected to be less favorable than the first (**Table 4.7**).

**Table 4.6: Comparison of oxidative addition energy (ΔG) of symmetric dihalogen substrates versus the hydrohalic acid for the MPz trimers reported in kcal/mol.**

| Complex | $[Cu(\mu\text{-Pz})]_3$ | $[Ag(\mu\text{-Pz})]_3$ | $[Au(\mu\text{-Pz})]_3$ |
|---|---|---|---|
| $F_2$ | -68.2 | -48.9 | -56.9 |
| HF | 49.7 | 62.0 | 46.2 |
| $Cl_2$ | -7.2 | -2.2 | -16.5 |
| HCl | 39.7 | 46.6 | 27.7 |
| $Br_2$ | 7.3 | 9.6 | -4.3 |
| HBr | 36.7 | 41.9 | 23.8 |
| $I_2$ | 15.3 | 16.2 | 3.2 |
| HI | 34.3 | 38.0 | 21.0 |

**Table 4.7: Comparison of energetics (ΔG) of successive oxidative addition reactions of the hydrohalic acid substrates to the trimers reported in kcal/mol.**

| Trimer | HBr | 2HBr | HI | 2HI |
|---|---|---|---|---|
| $[Cu(\mu\text{-}Pz)]_3$ | 36.7 | 24.1 | 34.3 | 33.0 |
| $[Ag(\mu\text{-}Pz)]_3$ | 41.9 | NA | 38.0 | 41.2 |
| $[Au(\mu\text{-}Pz)]_3$ | 23.8 | 27.9 | 21.0 | 23.5 |

In solutions of low concentrations, these trimers exist as monomers but in solutions of higher concentration, or in the solid state, these molecules exist as loosely associated dimers, due to metallophilic interactions. The question then becomes, if the oxidative addition will disrupt the metallophilic interactions that hold these dimers together? Previous work by Vickery and Balch[5] showed that the oxidative addition does disrupt the aurophilic interactions of the AuCb trimers they studied. This conclusion is also supported by our calculations which show the DOTs to have significantly less favorable oxidative addition energies than the corresponding trimers (**Figure 4.12**). Given the previous work in the field and our results showing that the oxidative addition does not occur to DOTs, these models were not carried through to study the reductive elimination reactions.

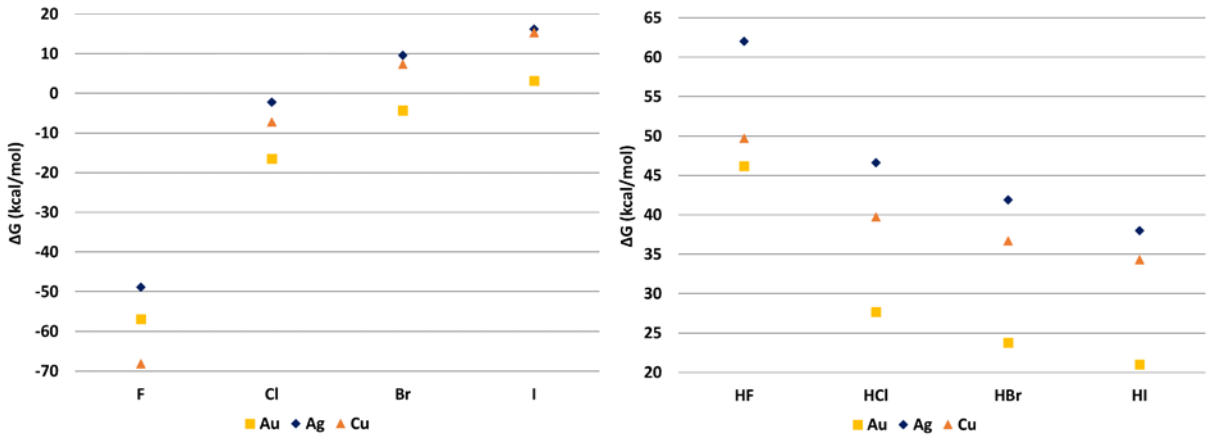


**Figure 4.12: Comparison of oxidative addition energies of $X_2$ (left) or HX (right) to a monomer of trimer or dimer of trimer for AuPz.**

The next step after oxidative addition is reductive elimination which allows for the collection of rearranged products when asymmetric substrates are used. The trends for reductive elimination are the reverse of the trends for oxidative addition, as is expected, given that the factors that increase the ability of a complex to go through oxidative addition decrease the ability of the complex to go through reductive elimination. The energetics of reductive elimination of the symmetric substrates are not of as much interest as the energetics of the elimination of rearranged products due to the fact the energy of the reductive elimination is equal and opposite of the energy of the oxidative addition. For the energetic study, the energies of the reductive elimination of $X_2$ and $H_2$ are tabulated to show the expected trends (**Table 4.8**).

**Table 4.8: Reductive elimination energies (ΔG) of the product of two successive oxidative addition steps for the hydrohalic acid substrates to produce $H_2$, $X_2$, and the original Au trimer reported in kcal/mol.**

| Complex | HF | HCl | HBr | HI |
|---|---|---|---|---|
| $[Au(\mu\text{-Im})]_3$ | 47.9 | 7.2 | -4.8 | -16.6 |
| $[Au(\mu\text{-Cb})]_3$ | 49.0 | 0.5 | -10.0 | -22.0 |
| $[Au(\mu\text{-Pz})]_3$ | 27.8 | -16.8 | -27.4 | -38.2 |
| $[Au(\mu\text{-Tz})]_3$ | 22.9 | -20.0 | -30.5 | -41.2 |
| $[Au(\mu\text{-Ttz})]_3$ | 17.9 | -28.9 | -39.7 | -46.7 |

For the applications of this study, we are more interested in the possibility of photoinduced reductive elimination, which carries the criteria that the frequency of the incident light must be high enough to break or distort the metal-halogen or metal-hydrogen bond. In order to encourage this bond distortion or breaking, there must be metal-to-ligand charge transfer states, specifically from the trimer to the halogen/hydrogen. In order to quantify the likelihood of photoinduced reductive elimination, the absorption spectra of the product of two successive

oxidative addition steps to the Au trimers have been modeled (**Figure 4.13**) and major contributions have been analyzed.

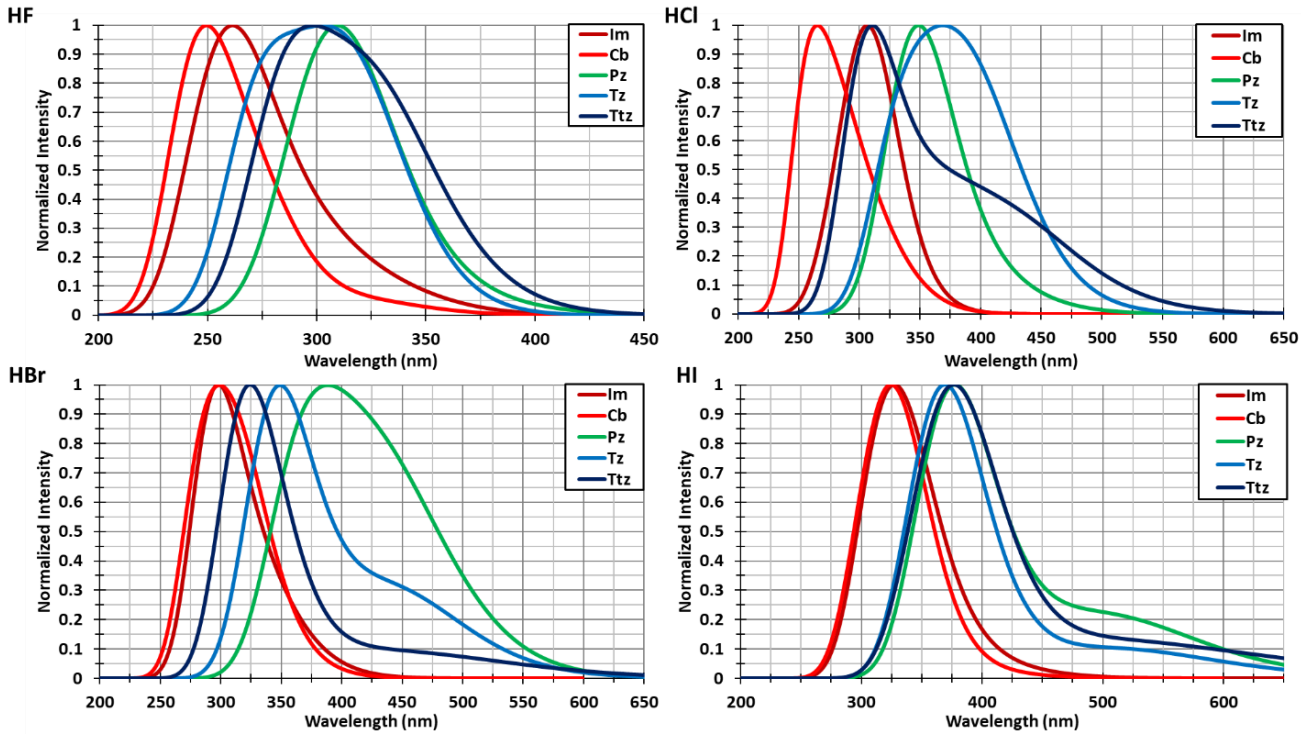


**Figure 4.13: Comparison of calculated absorption spectra for oxidized products of Au trimers and HF (top left), HCl (top right), HBr (bottom left), and HI (bottom right).**

The calculated absorption spectra for the Cb and Im trimers does not change shape or appear to broaden with the changing of the substrate identity, while it does show some shifting of the $\lambda_{max}$ that is substrate dependent (**Table 4.9**). As the π-basicity of the trimer is decreased, starting with the Pz ligand, there appears to be a significant change in broadness and shape of the overall spectra that is dependent on the substrate, accompanied with the development of shoulders in the blue and yellow region for the π-acidic trimers and the AuPz trimer, respectively. However, the shifting does not result in the shifting of the $\lambda_{max}$ out of the UV region.

**Table 4.9: Calculated λmax for the oxidative addition products of Au trimers with HF, HCl, HBr, and HI.**

| Complex | HF | HCl | HBr | HI |
|---|---|---|---|---|
| $[Au(\mu\text{-Im})]_3$ | 261 nm | 307 nm | 298 nm | 324 nm |
| $[Au(\mu\text{-Cb})]_3$ | 250 nm | 266 nm | 299 nm | 327 nm |
| $[Au(\mu\text{-Pz})]_3$ | 310 nm | 349 nm | 389 nm | 378 nm |
| $[Au(\mu\text{-Tz})]_3$ | 303 nm | 369 nm | 349 nm | 369 nm |
| $[Au(\mu\text{-Ttz})]_3$ | 298 nm | 311 nm | 324 nm | 377 nm |

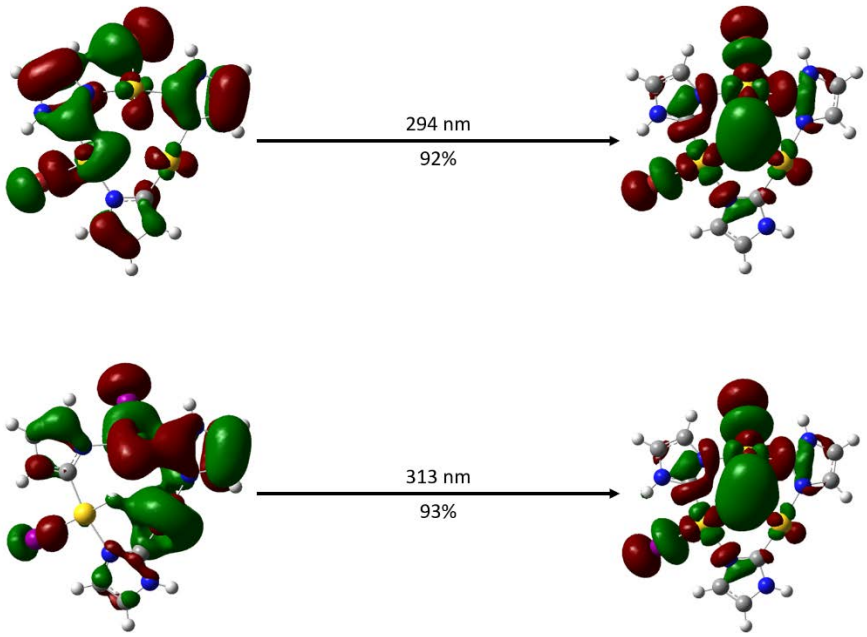


**Figure 4.14**: **Orbital contributions that support metal-to-hydrogen charge transfer states with high contributions to strongly allowed transitions resulting in the formation of the bond in hydrogen gas for the AuIm trimer with HBr (top) and HI (bottom).**

To definitively identify the differences in these spectra and determine if these complexes have suitable transitions for the photoinduced reductive elimination process, the orbitals that contribute significantly to the transitions with the highest oscillator strength have been analyzed. Each adduct displays orbital transitions that are consistent with metal-to-hydrogen bond charge transfer states (an example of this is shown in **Figure 4.14**). The electron density is donated from

the metal to form the hydrogen gas bond, but there are no significant transitions that display metal-to-halide charge transfer states. This is supported by previous work that suggested that the photoinduced reductive elimination should lead to the elimination of hydrogen gas first, and then the halogen gas will be lost.[18] The orbital analysis also shows the breaking of the Au-H bond via the phasing of the orbitals. For the selected trimer shown below, the only orbitals that contributed to the transitions with the largest oscillator strength were those supporting the Au(III)-to-hydrogen charge transfer, while the other trimers also demonstrated Au-to-bridging ligand charge transfer states.

## 4.4 Conclusions

Oxidative addition reactions of cyclic trinuclear complexes with dihalogens has been a field of interest since 1977 starting with the work done by Balch.[1-6] The use of these compounds to produce hydrogen gas has not been studied previously to the author's knowledge. This work shows the expected trends in oxidative addition, with the more π-basic trimers resulting in more favorable oxidative additions, and the expected energetics of reductive elimination of hydrogen gas and dihalogen gas when the substrates are the asymmetric hydrohalic acids. The present time-dependent DFT results show the possibility of UV light to be used as a trigger to produce hydrogen gas through the transfer of electron density from the Au(III) centers of the adduct to the hydrogen bond. The most promising results are for the combination of the AuIm trimer with either HBr or HI, given the strongly allowed transitions, indicated by large oscillator strengths. For both of these acids, there is a red-shifting of the absorption energy leading to the elimination of the hydrogen gas, compared to the other trimers. The major transitions for these complexes

are consistent with Au(III)-to-hydrogen charge transfer states, while other complex and acid combinations also lead to other metal-to-ligand charge transfer states involving the halogens as well as the bridging ligands. This work demonstrates the possibility of the use of UV light to aid the production of hydrogen gas through the utilization of oxidative addition reactions of cyclic trinuclear gold(I) complexes.

## 4.5 References


1. Balch, A. L.; Doonan, D. J. Mixed valence gold chemistry: Stepwise oxidation of a cyclic trigold(I) complex. *J. Organomet. Chem.*, **1977**, 131(*1*), 137-146.

2. Raptis, R. G.; Porter, L. C.; Emrich, R. J.; Murray, H. H.; Fackler, J. P. Synthesis of a mixed-valence gold(I)/gold(III) complex, $[Au(CH_2)_2PPh_2]_2Br_2$, and its characterization by x-ray crystallography and x-ray photoelectron spectroscopy. *Inorg. Chem.*, **1990**, 29(*22*), 4408-4412.

3. Minghetti, G.; Banditelli, G.; Bonati, F. Metal derivatives of azoles. 3. The pyrazolato anion (and homologs) as a mono- or bidentate ligand: Preparation and reactivity of tri-, bi-, and mononuclear gold(I) derivatives. *Inorg. Chem.*, **1979**, 18(*3*), 658-663.

4. Raptis, R. G.; Murray, H. H.; Fackler, J. P., Jnr The structure of [Au-[μ]-{3,5-$(C_6H_5)_2C_3HN_2$}]$_3Cl_2$: a trinuclear mixed-valence gold pyrazolate complex. *Acta Crystallogr., Sect. C: Struct. Chem.*, **1988**, 44(*6*), 970-973.

5. Vickery, J. C.; Balch, A. L. X-ray crystallographic studies of the products of oxidative additions of iodine to cyclic trinuclear gold(I) complexes: Directional effects for Au−I···I−Au interactions. *Inorg. Chem.*, **1997**, 36(*26*), 5978-5983.

6. Bonati, F.; Burini, A.; Rosa Pietroni, B.; Bovio, B. Reactions of symmetric C-imidazolylgold(I) leading to Au1 carbene complexes or mixed valence or AuIII imidazolyl derivatives. Crystal structure of [1-benzyl-3-(carboethoxy)imidazolin-2-yliden]chlorogold(I). *J. Organomet. Chem.*, **1991**, 408(*2*), 271-280.

7. Bovio, B.; Burini, A.; Pietroni, B. R. Reactions of trimeric 1-benzyl-2-gold(I)imidazole leading to AuI carbene complexes. Crystal structure of [1-benzyl-3-benzoyl-imidazolin-2-yliden]chlorogold(I). *J. Organomet. Chem.*, **1993**, 452(*1*), 287-291.

8. M. J. Frisch, G. W. T., H. B. Schlegel, G. E. Scuseria, M. A. Robb, J. R. Cheeseman, G. Scalmani, V. Barone, G. A. Petersson, H. Nakatsuji, X. Li, M. Caricato, A. Marenich, J.

Bloino, B. G. Janesko, R. Gomperts, B. Mennucci, H. P. Hratchian, J. V. Ortiz, A. F. Izmaylov, J. L. Sonnenberg, D. Williams-Young, F. Ding, F. Lipparini, F. Egidi, J. Goings, B. Peng, A. Petrone, T. Henderson, D. Ranasinghe, V. G. Zakrzewski, J. Gao, N. Rega, G. Zheng, W. Liang, M. Hada, M. Ehara, K. Toyota, R. Fukuda, J. Hasegawa, M. Ishida, T. Nakajima, Y. Honda, O. Kitao, H. Nakai, T. Vreven, K. Throssell, J. A. Montgomery, Jr., J. E. Peralta, F. Ogliaro, M. Bearpark, J. J. Heyd, E. Brothers, K. N. Kudin, V. N. Staroverov, T. Keith, R. Kobayashi, J. Normand, K. Raghavachari, A. Rendell, J. C. Burant, S. S. Iyengar, J. Tomasi, M. Cossi, J. M. Millam, M. Klene, C. Adamo, R. Cammi, J. W. Ochterski, R. L. Martin, K. Morokuma, O. Farkas, J. B. Foresman, and D. J. Fox Gaussian 09 Revision E01. **2016**.Wallingford, CT, USA.

9. Schmidt, M. W.; Baldridge, K. K.; Boatz, J. A.; Elbert, S. T.; Gordon, M. S.; Jensen, J. H.; Koseki, S.; Matsunaga, N.; Nguyen, K. A.; Su, F.; Windus, T. L.; Montgomery, M. D. J. A. General atomic and molecular electronic structure system. *J. Comp. Chem.*, **1993**, 14(1347-1363.

10. Gordon, M. S.; Schmidt, M. W. Advances in electronic structure theory: GAMESS a decade later. *Theory and Applications of Computational Chemistry: The First Forty Years*. **2005**. Dykstra, C. E.; Frenking, G.; Kim, K. S. ; Scuseria, G. E., Elsevier. Amsterdam.

11. Zhao, Y.; Truhlar, D. G. The M06 suite of density functionals for main group thermochemistry, thermochemical kinetics, noncovalent interactions, excited states, and transition elements: two new functionals and systematic testing of four M06-class functionals and 12 other functionals. *Theor. Chem. Acc.*, **2008**, 120(*1*), 215-241.

12. Zhao, Y.; Truhlar, D. G. Density functionals with broad applicability in chemistry. *Acc. Chem. Res.*, **2008**, 41(*2*), 157-167.

13. Stevens, W. J.; Basch, H.; Krauss, M. Compact effective potentials and efficient shared-exponent basis sets for the first- and second-row atoms. *J. Chem. Phys.*, **1984**, 81(*12*), 6026-6033.

14. Stevens, W. J.; Krauss, M.; Basch, H.; Jasien, P. G. Relativistic compact effective potentials and efficient, shared-exponent basis sets for the third-, fourth-, and fifth-row atoms. *Can, J. Chem.*, **1992**, 70(*2*), 612-630.

15. Cundari, T. R.; Stevens, W. J. Effective core potential methods for the lanthanides. *J. Chem. Phys.*, **1993**, 98(*7*), 5555-5565.

16. McDougald, R. N.; Chilukuri, B.; Jia, H.; Perez, M. R.; Rabaâ, H.; Wang, X.; Nesterov, V. N.; Cundari, T. R.; Gnade, B. E.; Omary, M. A. Molecular and electronic structure of cyclic trinuclear gold(I) carbeniate complexes: Insights for structure/luminescence/conductivity relationships. *Inorg. Chem.*, **2014**, 53(*14*), 7485-7499.

17. Tekarli, S. M.; Cundari, T.R.; Omary, M. A. Rational design of macrometallocyclic trinucelar complexes with superior π-acidity and π-basicity. *J. Am. Chem. Soc.*, **2008**, 130(*5*), 1669-1675.

18. Teets, T. S.; Nocera, D. G. Photocatalytic hydrogen production. *Chem. Comm.*, **2011**, 47, 9268-9274.

# CHAPTER 5

# LUMINESCENT, REDOX-ACTIVE (DITHIOLATO)BIS(IMINE)PLATINUM(II) DIVERGENT COMPLEXES WITH EXCHANGEABLE IMINE LIGANDS: AN EXPERIMENTAL/COMPUTATIONAL STUDY VS THEIR (DIIMINE)(DITHIOLATO)PLATINUM(II) CONVERGENT CONGENERS[3]

## 5.1 Introduction

Supramolecular coordination compounds exhibit extensive properties including light-harvesting capabilities,[1] magnetic behavior,[2] redox functionality,[3] electron transfer,[4] and gas storage and separation for porous metal-organic frameworks (MOFs).[5, 6] Further advancements in this field depend upon the creative development and utilization of building blocks possessing both form and function. Traditionally, the geometry and stability of platinum(II) complexes make them commonly-used precursors for supramolecular polygons, polyhedral,[6] and MOFs.[7, 8] The addition of photophysical functionality to the square-planar form of platinum(II) is emerging as a new way of generating fluorescent organometallic metallacycles[9, 10] or microcrystalline fibers.[11]

The redox and photophysical behavior of platinum(II) dithiolate complexes[12-14] offer an intriguing avenue to engender location specific functionality to supramolecular coordination complexes. In particular, the photophysical properties of platinum(II) diimine-dithiolate complexes foster applications in light-harvesting devices,[15, 16] 2$^{nd}$-order non-linear optical materials,[17] and water splitting photocatalysts.[18, 19] Supramolecular coordination complexes, however, are typically synthesized using divergent ditopic diimine ligands rather than the

[3] Entire chapter is a reprint of Smith, J. B.; Otten, B. M.; Derry, P. J.; Browning, C.; Bodenstedt, K. W.; Sandridge, J. H.; Satumtira, N. T.; Zilaie, M.; Payne, J.; Nuti, R.; Omary, M. A.; Smucker, B. W. Luminescent, redox-active (dithiolato)bis(imine)platinum(II) divergent complexes with exchangeable imine ligands: An experimental/computational study versus their (diimine)(dithiolato)platinum(II) convergent congeners. *Comments Inorg. Chem.*, **Accepted**. Experimental work kept for context. Computational work performed by author.

terminal chelating diimine ligands employed in platinum(II) diimine-dithiolate compounds. By combining the divergent bridging imine ligands with the *cis*-directing form and functionality of dithiolatoplatinum(II), a new family of supramolecular building blocks with tunable photophysical and electrochemical properties can be generated. Herein we report on the rational design of luminescent (dithiolato)(*bis*-imine)platinum(II) complexes with two divergent imine ligands, both experimentally and computationally. The presence of two $\kappa^1$-*NN* ligands in the family of Pt($\kappa^1$-arylimine)$_2$(dithiolate) complexes herein allows for greater torsion in the independent arylamine ring planes than the situation in the analogous Pt($\kappa^2$-arylimine)(dithiolate) complexes. The extent of this distortion in the neutral/singlet ground, excited/triplet, and the radical cation/doublet and radical anion/doublet electronic states responsible for the photophysical and redox processes is investigated for both classes of complexes using density functional theory (DFT) computations. The role of ligand-field (dd) vs charge transfer transitions in quenching the phosphorescence intensity and altering the redox potentials in **1**-**3** vs Pt(2,2'-bpy)(mnt) models has been found to be central.

In the typical syntheses of platinum(II) diimine-dithiolate complexes, the dithiolate ligand is added to a Pt(diimine)$Cl_2$ complex.[20] Utilizing this methodology with two monotopically-coordinated pyridine ligands results in lower yields and the potential formation of the thermodynamically stable bis(dithiolato)platinate(II) salt.[21, 22] We employ an alternative high-yield route to make neutral Pt($\kappa^1$-*NN*)$_2$(mnt) complexes which minimizes the formation of bis-dithiolate salts. The products are promising candidates for yet further reactivity to form hetero- or homo-metallic supramolecular assemblies, including MOFs and coordination polymers whereby the divergent complexes herein will be secondary building blocks or linkers with active

optoelectronic functionalities. These linkers may be altered to improve their potential use in pertinent devices due to coordination polymer formation that will facilitate electronic communication between such active centers. As such, it is critical to understand the structure and properties of the light-emitting/harvesting excitons and redox-active polarons of such active components, as aspired in this investigation.

## 5.2 Materials and Methods

Unless otherwise indicated, all operations were performed under a nitrogen atmosphere using standard Schlenk-line techniques with reaction flasks covered with aluminum foil to exclude light. Solvents were purchased from Pharmco-AAPER and reagents were purchased from Aldrich and used as received. $[Pt(pyz)_4](BF_4)_2$, **4**,[23] $[Pt(NCMe)_4](BF_4)_2$,[24] and $(TBA)_2[Pt(mnt)_2]$,[25] were synthesized according to previously published work. Electrochemical measurements were conducted using a CHI 620B electrochemical analyzer in a 0.1 M tetra-*n*-butylammonium hexafluorophosphate ($Bu_4NPF_6$) solutions using a platinum disk working electrode, a platinum wire counter electrode, and an Ag/AgCl reference electrode with a scan rate of 0.1V/s. $^1$H NMR spectra were obtained on a JEOL Eclipse Plus 300 instrument. UV-Vis spectra were obtained using a Hewlett-Packard UV-Vis 8453 diode array spectrophotometer. FTIR spectra measurements were obtained using a Thermo Nicolett 6700 FT-IR spectrometer with FAR-IR range. The photoluminescence measurements were carried out with a PTI Quanta Master Model QM-4 scanning spectrofluorometer.

### 5.2.1 Syntheses

**$Pt(pyz)_2(mnt)$, 1.** 82.5 mg (0.120 mmol) of $[Pt(pyz)_4](BF_4)_2$ is dissolved with 322.2 mg (4.02

mmol) pyrazine in 25 mL DI water. A solution of 23.2 mg (0.125 mmol) $Na_2$(mnt) dissolved in 15 mL DI water is added slowly *via* cannula to the Pt solution while rapidly stirring. The solution is stirred for 2 hours and the resulting yellow-orange precipitate is filtered through a frit in air and washed with 2 x 5 mL DI water, 2 x 5 mL cold MeOH, and 5 mL $Et_2O$ yielding 57.4 mg (97% yield). FT−IR (CsI pressed pellet): ($cm^{-1}$) 2212, 2200, 2190 (*m*, C≡N), 1594(C=N), 1425, 2256, 122, 1071, 1062, 812, 806, 694, and 474. $^1$H NMR (d-acetone): 9.00 (dd, $J_a$ = 3.2 Hz, $J_b$ = 1.4 Hz, 4H) and 8.90 (dd, $J_a$ = 3.2 Hz, $J_b$ = 1.4 Hz, 4H) ppm. ESI-*M*.S. (MeOH with 1% KBr) 534 $[K(Pt(N_2C_4H_4)_2)(S_2C_4N_2)]^+$.

**Pt(4,4'-bpy)$_2$(mnt), 2.** A solution of $Na_2$mnt (7.5mg, 0.040mmol) dissolved in 10 mL of water was slowly added, via addition funnel, to a stirring solution of 4,4'bipyridine (164.8mg, 1.1mmol) and $[Pt(4,4'\text{-bpy})_4](BF_4)_2$ (40.2mg, 0.040mmol) dissolved in 60ml of 5:4 methanol: water. After stirring for 15 minutes, the resulting cloudy orange slurry is filtered and resulting orange solid is washed with water and dried in air to give 0.0247g (95% yield) of an orange solid. FT-IR (CsI pellet): ($cm^{-1}$) 2203 & 2192 (C≡N), 1678, 1647(C=N), 1405, 1352, 1313, 993, 832, 695, 662, 631, and 506. $^1$H NMR (d-DMSO): 9.10 (dd, $J_a$ = 6.9 Hz, 4H), 8.76 (dd, $J_a$ = 6.0 Hz, 4H), 8.08 (dd, $J_a$ = 6.9 Hz, 4H), and 7.89 (dd, $J_a$ = 6.3 Hz, 4H) ppm.

**Pt(4,4'-bpy)$_2$(mnt), 2, by pyrazine replacement.** $Pt(pyz)_2$(mnt) (52.2 mg, 0.105 mmol) is dissolved with 4,4'-bipyridine (165.2 mg, 1.06 mmol) in 10 mL degassed $MeNO_2$ and is stirred for 1 day. The solution is concentrated under reduced pressure to ~5 mL, and the orange product is precipitated with 35 mL degassed $Et_2O$. After isolation by vacuum filtration, the solid is washed with 5 mL cold THF and 2 x 5 mL cold acetone yielding 57.8 mg (85% yield). FT−IR (CsI pressed pellet): ($cm^{-1}$) 2203 (*m*, C≡N), 1647(C=N), 1405, 994, 833, 808, 695, 662, and 631. $^1$H NMR (d-

DMSO): 9.10 (dd, $J_a$ = 6.9 Hz, 4H), 8.76 (dd, $J_a$ = 6.0 Hz, 4H), 8.08 (dd, $J_a$ = 6.9 Hz, 4H) and 7.89 (dd, $J_a$ = 6.3 Hz, 4H) ppm.

**[Pt(4-ap)$_2$(mnt)], 3.** [Pt(pyz)$_2$(mnt)] (53.7 mg, 0.108 mmol) is dissolved with 4-aminopyridine (105 mg, 1.12 mmol) in 10 mL degassed $MeNO_2$ and stirred overnight. The solution is concentrated under reduced pressure to ~5 mL and combined with 30 mL degassed $Et_2O$ and filtered. Further product was obtained by condensing the filtrate under reduced pressure to dryness, re-dissolving the solid in 10 mL acetone then precipitating with 30 mL DI $H_2O$ and isolating via frit filtration. Both yellow solids are combined and washed with 2 x 10 mL DI $H_2O$ and dried in air to yield 52.8 mg (93% yield). FT−IR (CsI pressed pellet): ($cm^{-1}$) 3350 (N-H), 2200 (*m*, C≡N), 1641 (C=N), 1518, 1355, 1210, 827 and 525. $^1$H NMR (d-acetone): 8.12 (dd, $J_a$ = 6.7 Hz, 4H), 6.66 (dd, $J_a$ = 7.1 Hz, 4H) and 6.46 (4H, s) ppm.

**[Pt(4,4'-bpy)$_4$](BF$_4$)$_2$**, **5**. A solution containing 3.87 g (24.8 mmol) of 4,4'-bpy in 30 mL of degassed $CH_3NO_2$ is transferred, via cannula, to 0.44 g (0.83 mmol) of [Pt(NCMe)$_4$](BF$_4$)$_2$ to make a peach solution. This solution is mildly heated for 2 days. The slight orange solution is partially condensed using reduced pressure and then combined with 50 mL of a 1:1 ratio of degassed diethyl ether and THF. The resulting beige precipitate is filtered in air and washed with 15mL of 1:1 diethyl ether and THF to give 0.414g (50% yield). FT-IR (CsI): ($cm^{-1}$), 1678, 1641(C=N), 1621, 1594, 1408, 1353, 1261, 1082 (B-F), 1022, 832, 809, 695, 635, 516, 499, and 395. $^1$H NMR (d-DMSO): 9.31 (dd, 8H), 8.76 (dd, 8H), 8.21 (dd, 8H) and 7.84 (dd, 8H) ppm. UV-vis (nm, $\varepsilon$ ($Lmol^{-1}cm^{-1}$)) 240 ($1.2x10^5$). ESI-M.S. (MeOH) 410 $[(Pt(N_2C_{10}H_8)_4)]^{2+}$.

**[Pt(pyz)$_4$][Pt(mnt)$_2$], 6.** A solution of (TBA)$_2$[Pt(mnt)$_2$] (24.7mg, .026mmol) in 5mL degassed acetone is added to a solution of [Pt(pyz)$_4$](BF$_4$)$_2$ (19.6mg, 0.028mmol) and pyrazine

(154mg, 1.91mmol) dissolved in 5 mL degassed acetone and one drop of DMF. The solution is stirred for 1 hour. The red product is filtered over a frit in air yielding 16.9mg (66% yield). $^{1}$H NMR (d-DMSO): δ 9.06(dd) and 8.89(dd) ppm. FT-IR (nujol, CsI plates): ($cm^{-1}$) 2196 (C≡N), 1418, 1151, 1107, 1023.

**[Pt(4,4'-bpy)$_4$][Pt(mnt)$_2$], 7.** A red solution of 24.9mg (0.030mmol) (TBA)$_2$[Pt(mnt)$_2$] in 15mL of acetone is transferred, via cannula, to a tan solution containing 30.2mg (0.030 mmol) [Pt(4,4'-bpy)$_4$](BF$_4$)$_2$ in 10mL of acetone and 5mL of methanol to immediately form an orange solid. The solid is isolated by filtration and washed with 2 x 5mL of acetone and 1mL of Et$_2$O to yield 29.8mg (85%) of product. $^{1}$HNMR (d-DMSO) 9.32 (dd, 8H), 8.76 (dd, 8H), 8.20 (dd, 8H), 7.83(dd, 8H) ppm. ESI-M.S. (DMSO) 409 [(Pt($N_2C_{10}H_8$)$_4$)]$^{2+}$, 237 [Pt($S_2C_4N_2$)$_2$]$^{2-}$.

### 5.2.2 X-Ray Crystallography

Slow evaporation at -20°C of saturated acetone/xylenes solutions of either **1** or **3** generated orange crystals or orange-yellow crystals, respectively. A hemisphere of data was collected for compounds **1** at 295 K and for **3**•$C_3H_6O$•2$H_2O$ at 291 K**.** Data were integrated using Bruker SAINT[26] and corrected for absorption effects using SADABS.[27] Space groups were assigned via XPREP.[28] Structures were solved by charge flipping solution method through the use of the Olex2 program,[29, 30] which was also employed to refine all non-hydrogen atoms with anisotropic thermal parameters. Hydrogen atoms were inserted at ideal positions and refined using a riding model with an isotropic thermal parameter. **Table 5.1** has the crystal data for compounds **1** and **3**•$C_3H_6O$•2$H_2O$.

**Table 5.1: Crystallographic Data for compounds 1 and 3•$C_3H_6O$•$2H_2O$.**

| | **1** | **3•$C_3H_6O$•$2H_2O$** |
|---|---|---|
| Formula | $C_{12}H_8N_6PtS_2$ | $C_{17}H_{22}N_6O_3PtS_2$ |
| space group | P-1 | P-1 |
| a, Å | 8.8424(18) | 9.1050(18) |
| b, Å | 9.0440(18) | 11.153(2) |
| c, Å | 10.693(2) | 11.709(2) |
| α, deg | 86.08(3) | 80.66(3) |
| β, deg | 78.61(3) | 74.95(3) |
| γ, deg | 64.08(3) | 85.53(3) |
| V, $Å^3$ | 753.8(3) | 1129.9(4) |
| Z | 2 | 2 |
| T, K | 295 | 291 |
| D, g/cm | 2.1826 | 1.8152 |
| R1 | 0.0187 | 0.0468 |
| R1 (all data) | 0.0218 | 0.0655 |
| wR2 (all data) | 0.0458 | 0.0993 |
| GOF | 1.040 | 0.9897 |

### 5.2.3 Computational Studies

All geometry optimizations of **1**, **2**, **3**, and the comparative model Pt(2,2'-bpy)(mnt) were performed using the Gaussian 09 suite of programs.[31] The B3LYP hybrid[32, 33] and M06 meta-hybrid[34] functionals were utilized in conjunction with the CEP-31G(d) basis set,[35-37] where d signifies the addition of a polarization function to main group elements besides hydrogen. Geometry optimizations were performed for the ground state ($S_0$), lowest-triplet excited state ($T_1$), and the lowest-doublet radical-cation and radical-anion states ($DC_1$ and $DA_1$, respectively).

Adiabatic and diabatic transition and redox energies were calculated. Time-dependent DFT (TD-DFT) method was utilized in order to accurately simulate the absorption spectra as well as to determine transition types. These results have been used to verify and support the experimental results herein.

## 5.3 Results and Discussion

### 5.3.1 Synthetic Studies

The neutral Pt($\kappa^1$-*NN*)$_2$(mnt), ($\kappa^1$-*NN* = pyz, **1**, or 4,4'-bpy, **2**), complexes were synthesized by reacting either [Pt(pyz)$_4$](BF$_4$)$_2$, **4**, (16) or [Pt(4,4'-bpy)$_4$](BF$_4$)$_2$, **5**, with Na$_2$mnt in a methanol/water mixture with an excess of the divergent *NN* ligand (**Scheme 5.1a**). The corresponding ion-paired complexes, [Pt($\kappa^1$-*NN*)$_4$][Pt(mnt)$_2$], ($\kappa^1$-*NN* = pyz, **6**, or 4,4'-bpy, **7**), which are coordination isomers of **1** and **2**, respectively, were also synthesized and used to confirm the syntheses of Pt($\kappa^1$-*NN*)$_2$(mnt).

In the process of characterizing **1**, we observed a solvent-dependent exchange of the $\kappa^1$-pyrazine (in DMSO or MeNO$_2$). This behavior could be utilized to generate building blocks with larger divergent ligands (such as 4,4'-bpy) or to directly synthesize supramolecular coordination complexes bearing dithiolate corners.[38] As a proof of concept, we exchanged the pyrazine ligands with two less labile $\kappa^1$-*NN* ligands in the high yield syntheses of Pt(4-ap)$_2$(mnt), **3**, and an alternative route to form **2** (**Figure 5.1**).

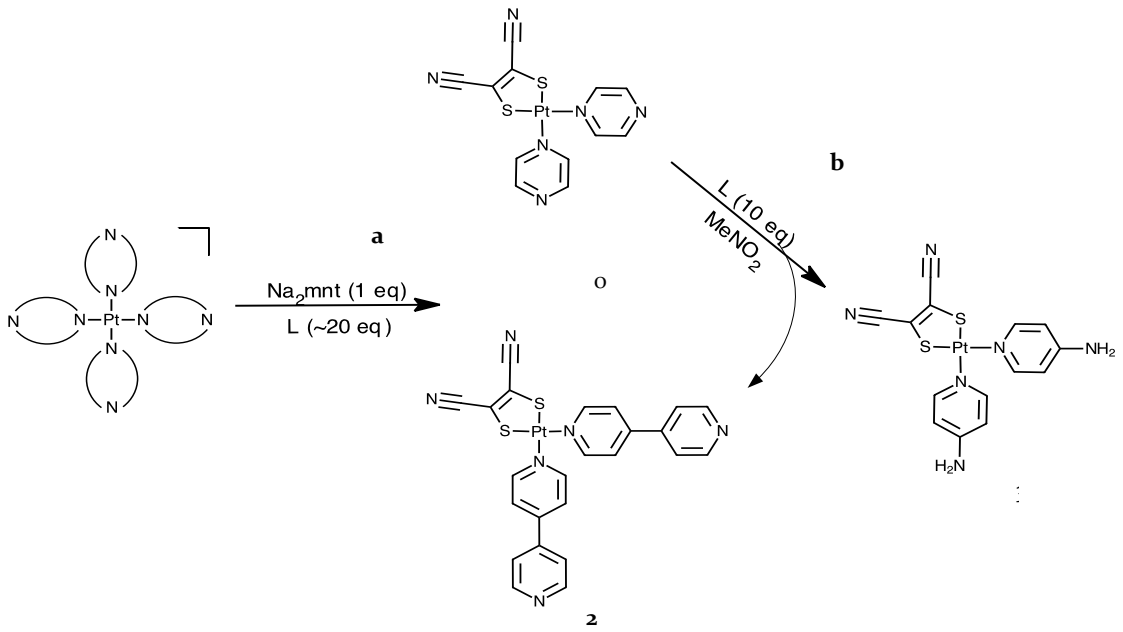


**Figure 5.1: a) Syntheses of 1 (L = pyz) and 2 (L = 4,4'-bpy) from $[Pt(\kappa^1\text{-}NN)_4]^{2+}$ and b) subsequent exchange of pyz ligands in 1 to form 2 or 3 (L = 4-ap)).**

### 5.3.2 $^1$H NMR Spectroscopy

The $^1$H NMR resonances of compounds **1-7** were consistent with those for the monotopic coordination mode of the pyz, 4,4'-bpy, or 4-ap ligands. The resonances of the ring protons in compounds **1** (9.00 and 8.90 ppm) and **3** (8.12, 6.66, and 6.46 ppm) exhibited $^1$H-$^{195}$Pt coupling (*J* = 34 and 25 Hz, respectively) for the downfield resonances associated with the hydrogen atoms nearest the coordinated nitrogen in the ring (see **Figure 5.2**), which is in range with other pyridyl/pyrazine-containing complexes.[39] The resonances for the coordinated pyridyl group of the ($\kappa^1$-4,4'-bpy) complexes shift upfield (9.10 and 8.08 ppm for **2** and from 9.31 and 8.21 ppm for **5**; see **Figure 5.2**) upon coordination of the anionic mnt ligand. This is consistent with the larger *trans*-influence of the chelating dithiolate.[40] The $^1$H resonances for the ion-paired complexes **6** and **7** are equivalent to the tetrakis($\kappa^1$-*NN*)platinum(II) complexes **4** and **5,** respectively.

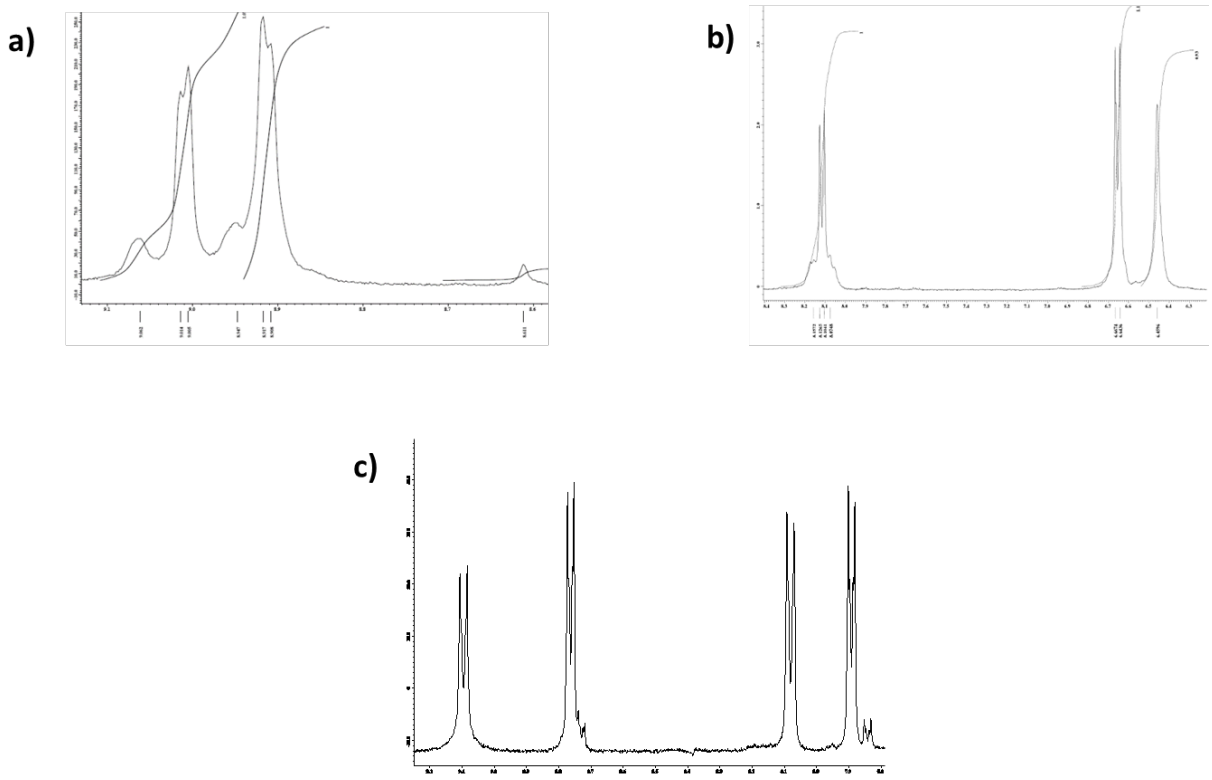


**Figure 5.2**: **$^1$H NMR Spectrum of Pt(pyz)$_2$(mnt), 1 (a), Pt(4-ap)$_2$(mnt), 3 (b) and Pt(4,4'-bpy)$_2$(mnt), 2 (c).**

5.3.3 Structural Studies

**Table 5.2** shows the pertinent interatomic distances and bond and torsion angles for **1** and **3** as revealed via single-crystal X-ray diffraction analysis as well as the computational structural parameters. The structures in **Figure 5. 3** confirm the monotopic coordination of the ligands in both **1** and **3**, as well as the solvent-dependent stability of **1** (grown in acetone). Intramolecular Pt-S bond lengths are comparable to other complexes of the type ($\kappa^2$-diimine)(dithiolate)Pt (II).[41-44] The intramolecular Pt-N bond lengths (2.063(5) and 2.049(6) Å) in **3** are within the range of these diimine analogous complexes. The Pt-N distances are longer in the structure of **1**, (2.077(3) and 2.078(3) Å), than in **3**, which further supports the tendency of **1** to be more labile. These Pt-N bond distances are also longer than those in the tetrakispyrazineplatinum(II) (2.012(5) and 2.026(6) Å)[23] or tetrakispyridineplatinum(II) (2.016(3)

- 2.031 (2) Å)[45] providing further support for the stronger *trans*-influence of the mnt ligand.[46] The calculated bond lengths are elongated when compared to the crystal structure due to the loss of solvation and packing effects seen in the crystal structure that are absent in the calculated structures (**Table 5.2**). There is also deviation seen for these reasons for the N-Pt-N and S-Pt-S angles. In comparison to the crystal structure of Pt(2,2'-bpy)(mnt)[47] where the $\kappa^2$-(2,2'-bpy) is essentially in the same plane as the Pt(mnt), the $\kappa^1$-*NN* ligands have a substantial torsion angle from the $PtS_2C_2$ plane in both **1** (49.24(12) and 61.33(12)°) and **3** (56.9(2) and 60.8(2)°), which is also reproduced well by the calculations. The loss of planarity of the pyridyl-based ligand is a factor which improves the performance of these types of molecules in light-harvesting materials.[21, 22] Both complexes pack in a slipped head-to-tail dimer arrangement (**Figure 5.4**), with plane-to-plane vertical distances of 3.618(2) and 3.607(4) Å, for **1** and **3**, respectively. The calculated geometry for **2** is summarized in **Table 5. 3**.

**Table 5.2: Select bond lengths, angles, and torsion angles for $[Pt(pyz)_2(mnt)]$, 1, and $[Pt(4\text{-}ap)_2(mnt)]$, 3.**

| Bond Length (Å), 1 | | | Angle (°), 1 | | |
|---|---|---|---|---|---|
| | Experimental | Theoretical | | Experimental | Theoretical |
| Pt1—S2 | 2.2460(12) | 2.3084 | S1—Pt1—S2 | 90.97(3) | 90.32 |
| Pt1—S1 | 2.2429(11) | 2.3804 | N5—Pt1—S2 | 90.46(7) | 89.30 |
| Pt1—N5 | 2.077(3) | 2.1268 | N5—Pt1—S1 | 178.22(7) | 179.18 |
| Pt1—N3 | 2.078(3) | 2.1270 | N3—Pt1—N5 | 88.36(10) | 91.09 |
| S1—C1 | 1.739(3) | 1.7588 | C1—S1—Pt1 | 102.54(12) | 102.49 |
| S2—C2 | 1.739(3) | 1.7588 | C2—C1—S1 | 122.1(2) | 122.35 |
| N1—C3 | 1.150(4) | 1.1874 | Torsion Angle (°), 1 | | |
| C2—C4 | 1.431(4) | 1.4506 | | Experimental | Theoretical |
| C2—C1 | 1.360(5) | 1.3915 | $PtS_2C_2$—N3 Ring | 49.24(12) | 54.03 |
| C4—N2 | 1.141(4) | 1.1873 | $PtS_2C_2$—N5 Ring | 61.33(12) | 54.07 |
| C3—C1 | 1.429(5) | 1.4506 | N3 Ring—N5 Ring | 72.50(13) | 70.97 |

| Bond Length (Å), 3 | | | Angle (°), 3 | | |
|---|---|---|---|---|---|
| | Experimental | Theoretical | | Experimental | Theoretical |
| Pt1—S2 | 2.249(2) | 2.3103 | S1—Pt1—S2 | 90.89(7) | 90.52 |
| Pt1—S1 | 2.2446(18) | 2.3103 | N5—Pt1—S1 | 91.25(16) | 89.89 |
| Pt1—N5 | 2.049(6) | 2.1312 | N5—Pt1—S2 | 175.81(17) | 179.01 |
| Pt1—N3 | 2.062(5) | 2.1312 | N3—Pt1—N5 | 86.6(2) | 89.90 |
| S1—C2 | 1.741(7) | 1.7595 | C1—S2—Pt1 | 102.1(2) | 102.28 |
| S2—C1 | 1.737(7) | 1.7585 | C1—C2—S1 | 122.6(5) | 122.46 |
| N1—C3 | 1.154(10) | 1.1880 | Torsion Angle (°), 3 | | |
| C2—C4 | 1.435(10) | 1.4506 | | Experimental | Theoretical |
| C2—C1 | 1.342(9) | 1.3935 | PtS2C2—N3 Ring | 56.9(2) | 56.03 |
| C4—N2 | 1.132(9) | 1.1880 | PtS2C2—N5 Ring | 60.8(2) | 56.92 |
| C3—C1 | 1.413(10) | 1.4506 | N3 Ring—N5 Ring | 74.0(2) | 74.55 |

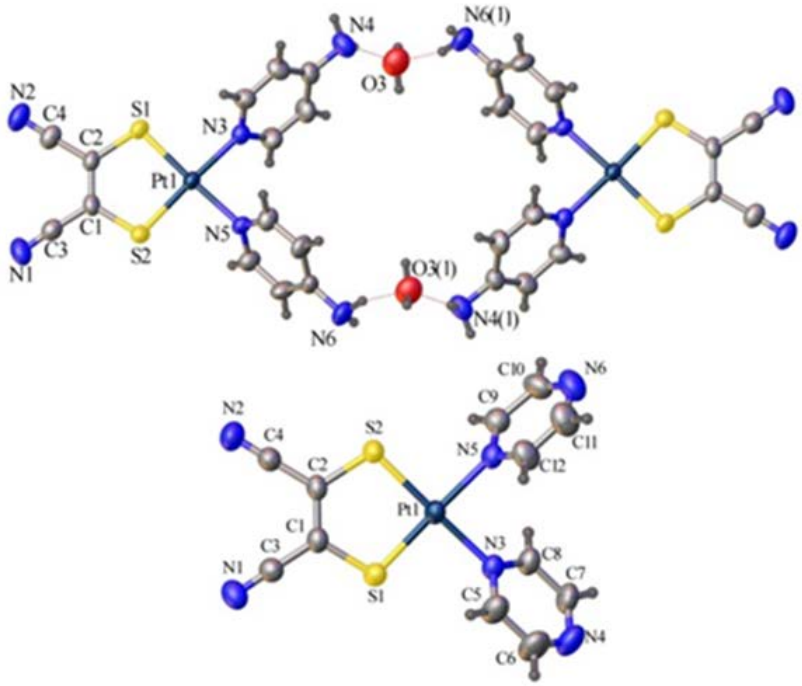


**Figure 5.3: Crystal structures (ellipsoids at 50%) of the H-bonded quadrangle containing two units of Pt(4-ap)$_2$(mnt), 3, and two water molecules. Other solvent molecules omitted for clarity (top) and Pt(pyz)$_2$(mnt), 1, (bottom).**

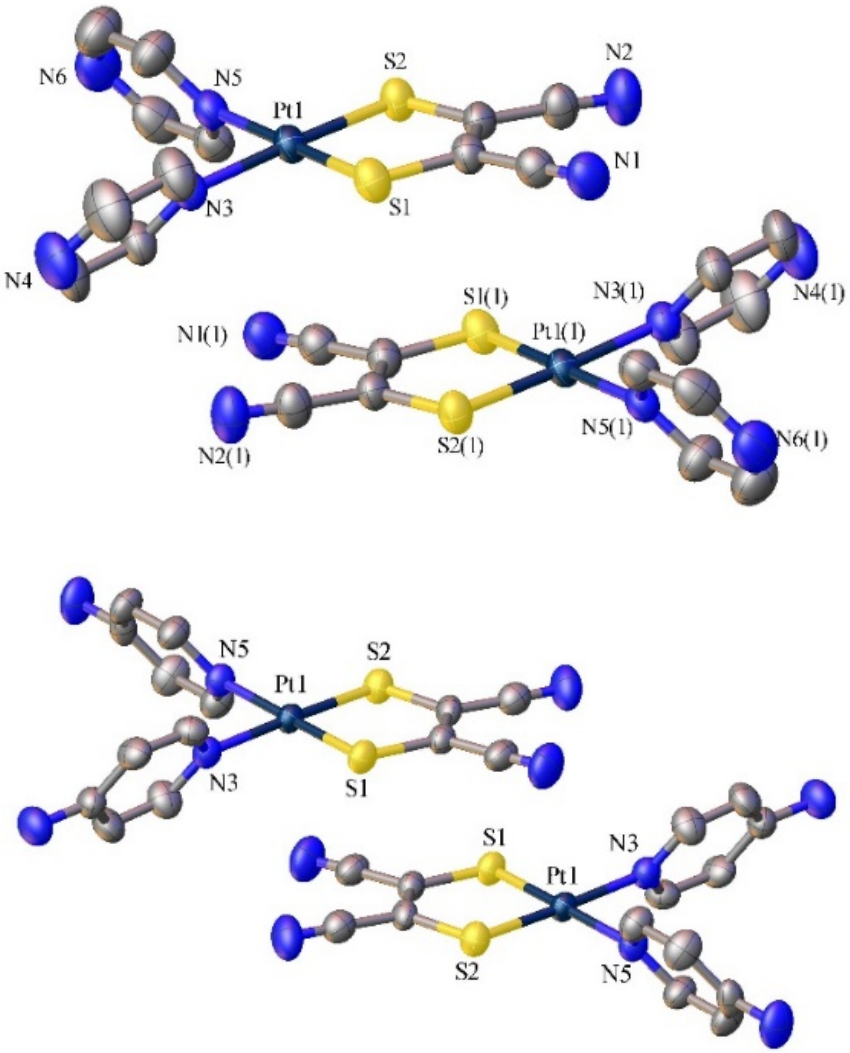


**Figure 5.4: Crystal structures (ellipsoids at 50%) of 1 (top) and 3 (bottom) showing head-to-tail packing. H-atoms and solvent molecules omitted for clarity.**

**Table 5.3: Selected calculated bond lengths, angles and torsion angles for [Pt(4,4`-bpy)$_2$(mnt)], 2.**

| Bond Length (Å), 2 | | Angle (°), 2 | |
|---|---|---|---|
| Pt1—S2 | 2.309 | S1—Pt1—S2 | 90.45 |
| Pt1—S1 | 2.309 | N5—Pt1—S1 | 89.53 |
| Pt1—N5 | 2.131 | N5—Pt1—S2 | 179.31 |
| Pt1—N3 | 2.131 | N3—Pt1—N5 | 90.49 |
| S1—C2 | 1.759 | C1—S2—Pt1 | 102.37 |

| Bond Length (Å), 2 | | Angle (°), 2 | |
|---|---|---|---|
| S2—C1 | 1.759 | C1—C2—S1 | 122.41 |
| N1—C3 | 1.188 | Torsion Angle (°), 2 | |
| C2—C1 | 1.392 | PtS2C2—N3 Ring | 56.30 |
| C4—N2 | 1.188 | PtS2C2—N5 Ring | 56.30 |
| C3—C1 | 1.451 | N3 Ring—N5 Ring | 73.91 |

The solid state packing of **3** reveals both $NH_2$ groups of two distinct complexes are H-bonded with two water molecules (**Figure 5.3**). This generates a supramolecular quadrangular (Pt···Pt distance of 1.2743(4) nm and O···O distance of 0.9624(13) nm), resulting in a cavity (occupied by the remaining solvate molecules; not shown in **Figure 5.3** for clarity). Such H-bonding interactions may be further utilized with customized building blocks to generate supramolecular complexes with specific properties. Investigation of self-assembly reactions to form optoelectronically-active supramolecular assemblies, MOFs, and other extended coordination polymer structures whereby such complexes act as building blocks are warranted.

### 5.3.4 Electrochemical and Photophysical Results

Compounds **1-3** all exhibit quasi-reversible or irreversible redox properties (**Table 5.4** contains experimental data while **Table 5.5** compares experimental data versus computational data) consistent with reductions centralized on the pyridyl/pyrazine ligands and oxidations originating from the Pt(mnt) components.[15, 16, 21, 22, 48, 49] This observation is further supported *via* orbital analysis of the SOMO and SOMO-1 of the anionic doublet at the optimized ground state structures of **1**-**3** (**Figure 5.5**). The orbitals of the doublet anion are used in this justification because in DFT the orbital shapes and energies are computed based on the electron density.

While the HOMO of the ground state should adequately show the nature of the oxidation, the LUMO is not trust-worthy to determine the nature of the reduction based on the fact it has no electron density.[50] Since the HOMO of the ground state is still occupied in this doublet anion, the character of this orbital does not change appreciably. However, the former LUMO is now a SOMO, leading to a more reliable description of this orbital. These orbital contours reveal that the SOMO – 1 (HOMO of the ground state) of each complex is Pt(mnt) based, supporting the conclusion that the oxidation is based on this moiety, while the SOMOs (LUMO of the ground state) are based on the pyridyl ligands, supporting that reduction should be pyridyl based. This orbital analysis is also supported by previous computational work on divergent [Pt(II)(dithiolate)(diimine)] complexes.[21, 22] The splitting of the oxidation peaks for **3**, observed at 1.06 and 1.21 V (**Figure 5.6** and **Table 5.4**) is indicative of dimerization in solution, analogous to related well-documented phenomena in TTF species,[51-54] and in Pt($^t$bpy)(benzenedithiolate). The oxidative potential shifts by ~25mV more negative for a ten-fold increase in scan rate, confirming this dimerization behavior (**Figure 5.7**).[55] Interestingly, a cathodic peak at the low potential of 0.32 V is also observed for **3** post the thiolate-based oxidation, and the cycle was reproduced at least five times. This unexpected peak[52] did not appear for **1** or **2**, or even more dilute solutions of **3** (**Figure 5.8**) and likely represents a Pt(II)-based reduction that takes place following the thiolate-based oxidation; a control experiment whereby the cyclic voltammetry was limited to 0.0-0.9 V did not show this unexpected peak (**Figure 5.6**). Metal-based redox processes for Pt(II) square-planar complexes aid their association because the pertinent HOMO ($\sigma^*_{dz2}$) for the oligomer is a formally anti-bonding orbital while the LUMO ($\sigma_{pz}$) is bonding; this phenomenon is known for simple $[Pt(CN)_4]^{2-}$ aqueous solutions, which become redox-active only at high

concentration.[56] An alternative hypothesis of a ligand rearrangement to form $[Pt(mnt)_2]^{2-}$ is ruled out; although this complex is oxidized at a similar potential, it has a completely reversible oxidation profile ($E_{½}$ = 0.37 V), which was not observed upon repeated cycles for **3** (**Figure 5.6**).

**Table 5.4: Redox potentials for compounds 1-3 at a scan rate of 0.1 V/s. *Quasi-reversible while others are irreversible. All $E_c$ and $E_a$ values represent peak potentials.**

| Compound (Solvent) | $E_c$ (V) | $E_a$ (V) |
|---|---|---|
| **1** (THF) | -1.37, -1.77 | 1.37 |
| **2** (DMF) | -1.30*, -1.41* | 1.23 |
| **3** (MeCN) | -1.42, -1.65 | 1.06*, 1.21* |

**Table 5.5: Comparison of experimental and calculated reduction/ oxidation potentials for 1, 2, 3, and [Pt(2,2'-bpy)(mnt)]. $E^{abs}_{exp}$ was calculated according to $E^{abs} = E_{exp} + 4.696$ V to convert from a Ag/AgCl reference electrode to vacuum and $E^{abs}_{calc} = \Delta G_{sol}/nF$ where $\Delta G_{sol} = \Delta G^{ox}_{sol} - \Delta G^{red}_{sol}$.**

| Complex (solvent) | Oxidation | | Reduction | |
|---|---|---|---|---|
| | $E^{abs}_{calc}$ (V) | $E^{abs}_{exp.}$ (V) | $E^{abs}_{calc}$ (V) | $E^{abs}_{exp.}$ (V) |
| **1** (in THF) | 5.60 | 6.07 | 2.94 | 3.33 |
| **2** (in DMF) | 5.00 | 5.93 | 3.32 | 3.40 |
| **3** (in AMeCN) | 5.20 | 5.91 | 2.47 | 3.28 |

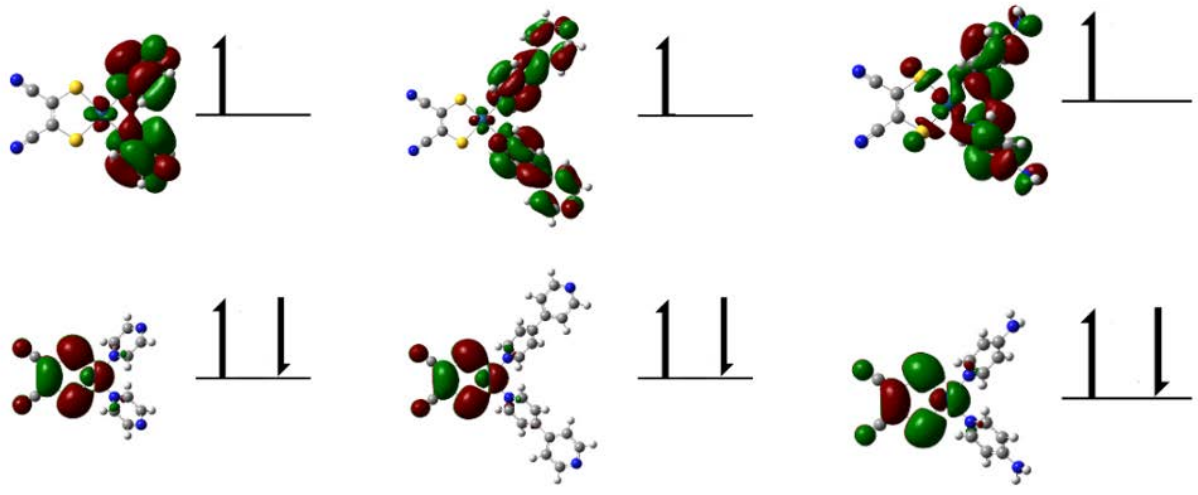

**Figure 5.5: SOMO – 1 (top) and SOMO (bottom) contours for 1 (left), 2 (middle) and 3 (right) (plotted with an isovalue of 0.02) supporting assignment of oxidation and reduction processes.**

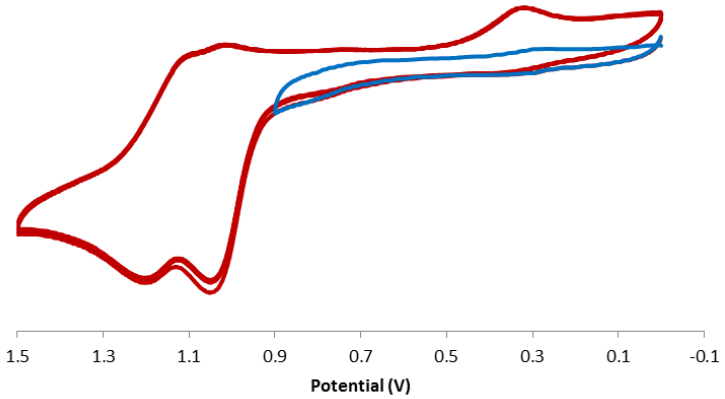


**Figure 5.6**: **Cyclic voltammagram of 3 with five complete cycles from 0 to 1.5V (red) and one cycle from 0 to 0.9V (blue) indicating dependence of cathodic peak on oxidations at higher potential. Performed in acetonitrile using 0.1M [n-Bu$_4$N][PF$_6$] electrolyte with a scan rate of 0.1V/s.**

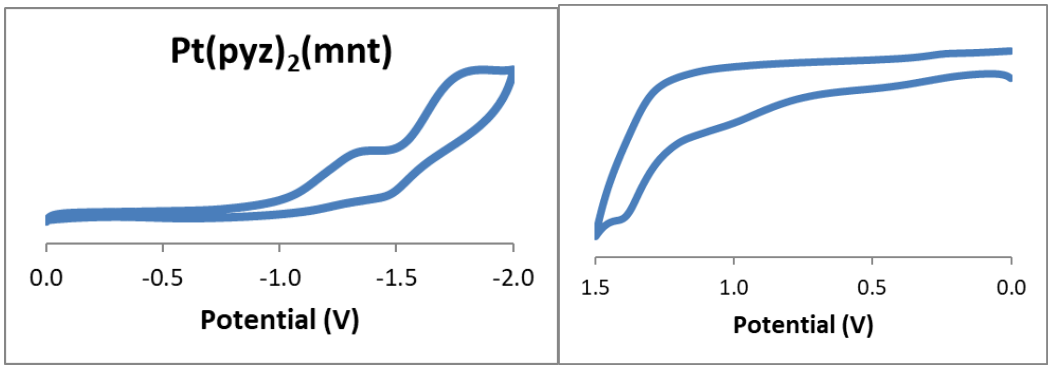


**Figure 5.7**: **Cyclic voltammagrams of 1 in THF using 0.1M [n-Bu$_4$N][PF$_6$] electrolyte with a scan rate of 0.1V/s.**

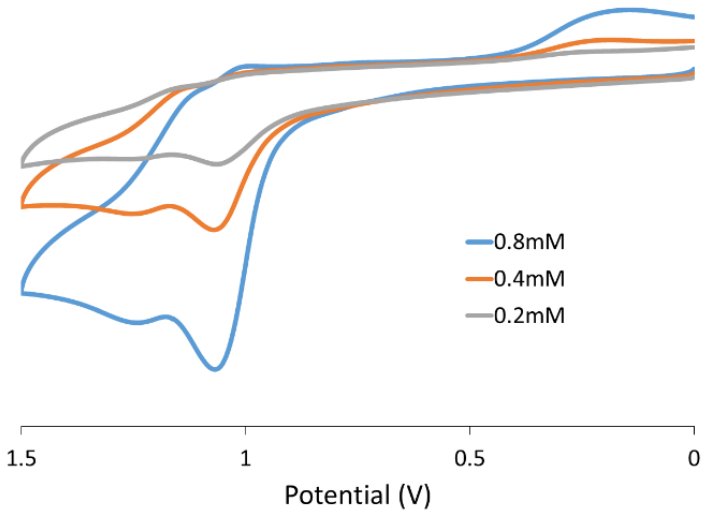


**Figure 5.8: Cyclic voltammagram of 3 with increasing concentrations (0.2mM, 0.4mM, and 0.8mM) indicating concentration dependence of cathodic peak at 0.32V. Performed in acetonitrile using 0.1M [n-Bu$_4$N][PF$_6$] electrolyte with a scan rate of 0.1V/s.**

The electronic absorption spectra of compounds **1**-**3** (**Figure 5.9**) exhibit two types of bands: stronger absorption bands ($\varepsilon$ ~ $10^4$ $M^{-1}cm^{-1}$) in the mid-UV region attributable to intraligand $^1\pi$-$\pi^*$ transitions, and weaker bands ($\varepsilon$ ~ $10^3$ $M^{-1}cm^{-1}$) in the near-UV extending into the visible region. For the latter bands, we adopt Eisenberg's assignment of mixed metal-(donor)ligand to (acceptor)ligand charge transfer, $^1$MMLL'CT (i.e., platinum dithiolate charge transfer to pyrazine or pyridyl-based ligands).[20] This lowest-energy absorption is tunable based on the identity of the $\kappa^1$-*NN* ligand, which is manifest in the absorption maxima herein ($\lambda_{max}$ = 372, 377, and 388 nm for **1**, **2** and **3**, respectively). These band assignments are not only supported by previous work in the field, but also through a computational analysis of the calculated absorption spectra for **1**-**3** (**Figure 5.10**). In all computationally studied complexes, the majority of the transitions and bands can be assigned as intraligand charge transfer states (LLCT) while the other bands are made up of MLL`CT states.

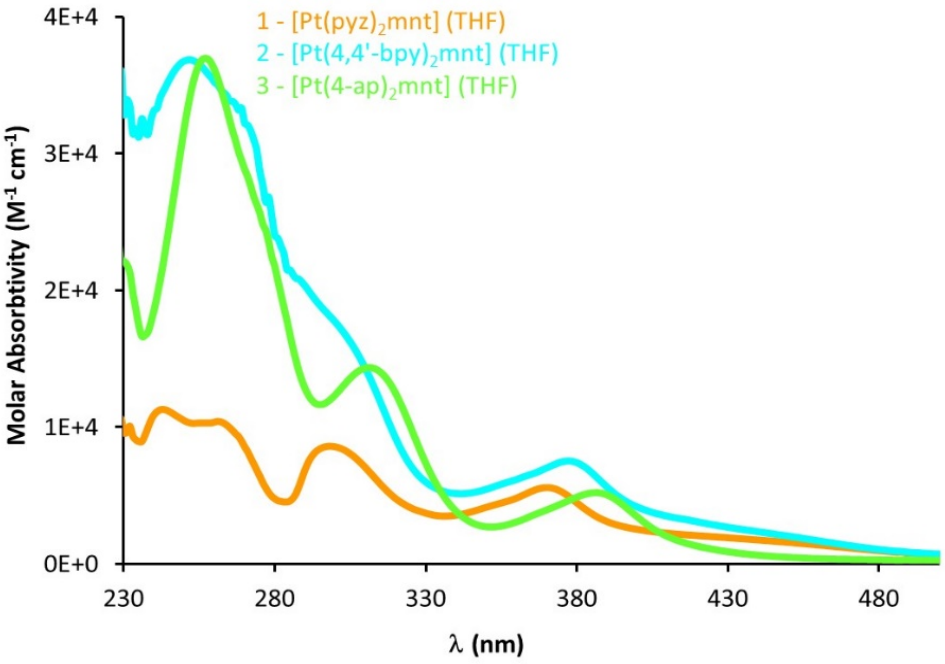


**Figure 5.9: Electronic adsorption spectra of compounds 1-3 exhibiting diimine-based $\pi$-$\pi^*$ absorptions in the mid-UV region and tunable MMLL'CT in the near-UV extending into the visible region.**

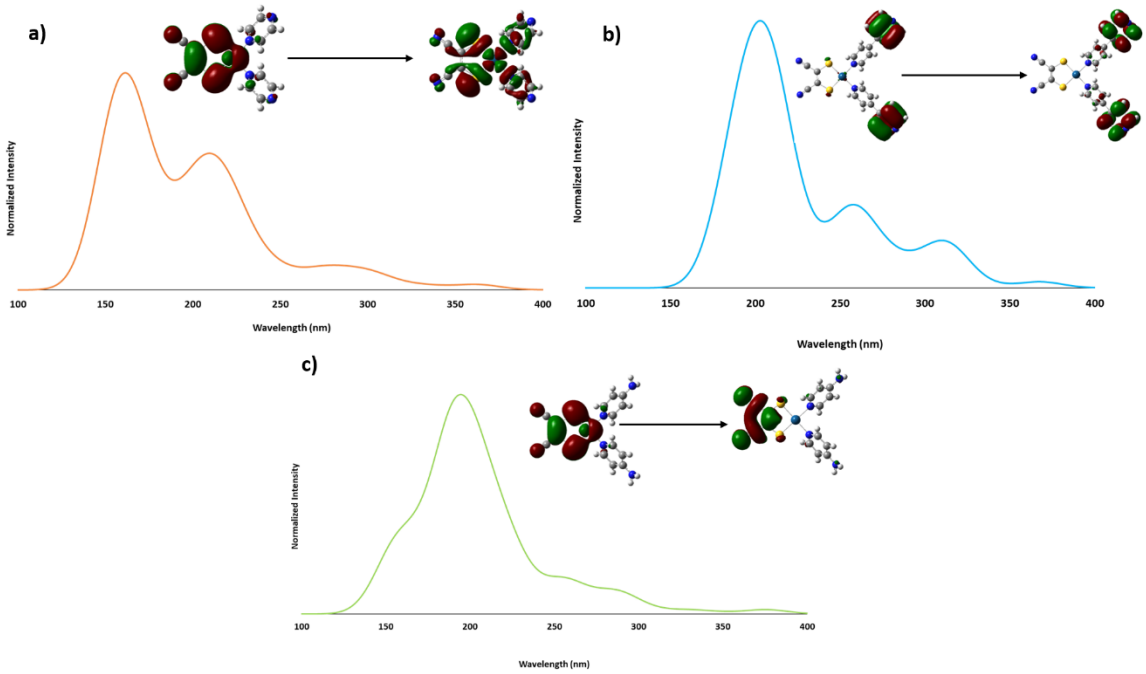


**Figure 5.10: Calculated absorption spectra of 1 (a), 2 (b) and 3 (c) with orbital contours for the transitions with the highest oscillator strength.**

All three complexes exhibit feeble luminescence that can be drastically enhanced upon cooling to cryogenic temperatures. **Figure 5.11** shows the emission and excitation spectra for all three complexes in glassy matrices at 77 K (lifetime data is summarized in **Table 5.6**), whereas the analogous spectra in the solid state are shown in **Figure 5.12** (summarized lifetime data in **Table 5.7**). The spectral resolution is significantly higher in the frozen glasses than in the solid state while the spectral energies are rather similar. The lifetimes of the emission bands were consistently and uniformly in the 10 µs regime, clearly suggesting phosphorescence (hence a $^3$MMLL'CT assignment), as expected for this type of complexes.[20] Typically, it would be assumed that the emissive state would be the lowest triplet, $T_1$. These complexes however exhibit $T_1$ states that are too low in energy to be responsible for the emission (i.e. – emission energies from the $T_1$ state are in the near-IR). DFT calculations show that the emissive state is from the second-

lowest triplet state, $T_2$, which has the expected MMLL`CT character. This emissive state has emission energies in the visible region (**Table 5.8**).

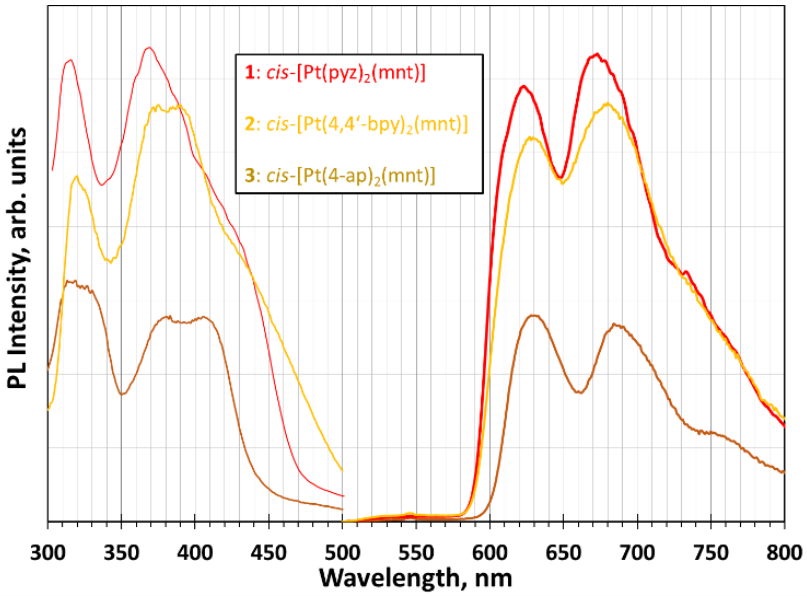


**Figure 5.11: Photoluminescence excitation (left/thinner curves) and emission (right/thicker curves) spectra for frozen glassy solutions of 1, 2, and 3 in acetone.**

**Table 5.6: Summary of lifetime data for frozen glassy solutions of 1 ($10^{-3}$ M), 2 ($10^{-4}$ M), and 3 ($10^{-3}$ M) in acetone.**

| cis-[Pt(pyz)$_2$(mnt)] | | cis-[Pt(4,4`-bpy)$_2$(mnt)] | | cis-[Pt(4-ap)$_2$(mnt)] | |
|---|---|---|---|---|---|
| $\lambda_{ex}/\lambda_{em}$ | LT (μs) | $\lambda_{ex}/\lambda_{em}$ | LT (μs) | $\lambda_{ex}/\lambda_{em}$ | LT (μs) |
| 314-622 | 37.77 ± 3.069e-1 | 318-623 | 31.72 ± 3.773e-1 | 315-630 | 25.04 ± 3.068e-1 |
| 314-672 | 36.84 ± 4.470e-1 | 318-650 | 30.27 ± 2.015e-1 | 315-660 | 23.66 ± 2.343e-1 |
| 314-730 | 38.36 ± 3.547e-1 | 318-675 | 30.89 ± 3.560e-1 | 315-685 | 25.04 ± 2.607e-1 |
| 370-622 | 38.35 ± 2.177e-1 | 390-623 | 32.99 ± 2.380e-1 | 315-710 | 24.19 ± 1.532e-1 |
| 370-672 | 36.58 ± 1.750e-1 | 390-650 | 29.97 ± 2.767e-1 | 377-630 | 26.7 ± 8.692e-2 |
| 370-730 | 34.61 ± 7.300e-1 | 390-675 | 32.3 ± 2.413e-1 | 377-660 | 25.13 ± 1.261e-1 |
| 420-622 | 38.33 ± 2.151e-1 | 430-623 | 32.16 ± 1.318e-1 | 377-685 | 26.36 ± 1.688e-1 |
| 420-672 | 36.15 ± 3.490e-1 | 430-650 | 28.32 ± 2.258e-1 | 406-630 | 25.94 ± 1.018e-1 |
| 420-730 | 37.05 ± 2.947e-1 | 430-675 | 30.18 ± 1.939e-1 | 406-660 | 24.56 ± 1.186e-1 |
| | | | | 406-685 | 26.35 ± 1.080e-1 |

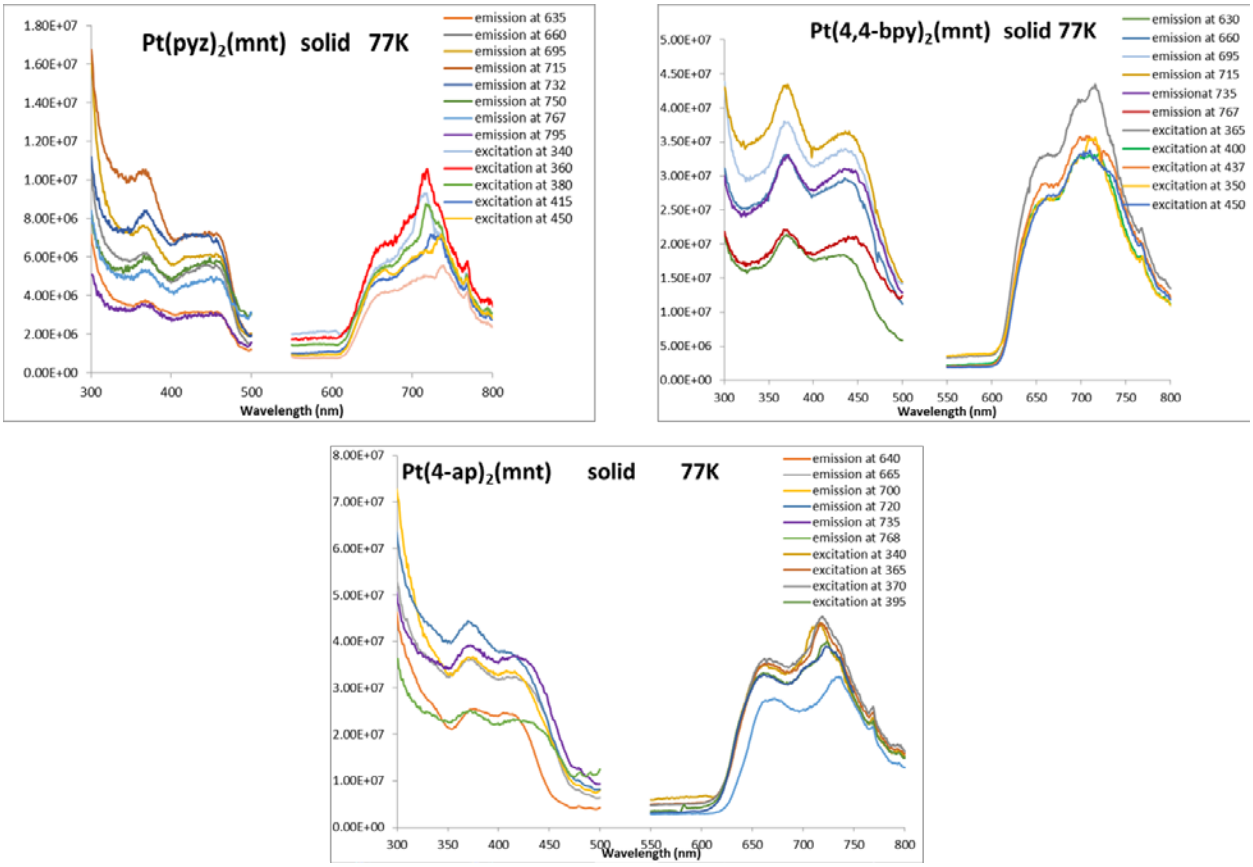


**Figure 5.12: Photoluminescence excitation (left/thinner curves) and emission (right/thicker curves) spectra for solid samples of 1, 2, and 3 at 77K.**

**Table 5.7: Summary of lifetime data for solid samples of 1, 2, and 3 at 77K.**

| cis-[Pt(pyz)$_2$(mnt)] | | cis-[Pt(4,4`-bpy)$_2$(mnt)] | | cis-[Pt(4-ap)$_2$(mnt)] | |
|---|---|---|---|---|---|
| $\lambda_{ex}/\lambda_{em}$ | LT (µs) | $\lambda_{ex}/\lambda_{em}$ | LT (µs) | $\lambda_{ex}/\lambda_{em}$ | LT (µs) |
| 360-635 | 9.208 ± 1.621e-1 | 365-630 | 14.4 ± 1.386e-1 | 370-665 | 7.834 ± 1.281e-1 |
| 360-660 | 8.818 ± 2.002e-1 | 365-660 | 15.03 ± 1.031e-1 | 370-700 | 7.743 ± 1.377e-1 |
| 360-695 | 10.48 ± 8.543e-2 | 365-695 | 13.35 ± 6.438e-2 | 370-720 | 8.343 ± 1.484e-1 |
| 360-715 | 10.68 ± 8.580e-2 | 365-715 | 13.4 ± 1.283e-1 | 370-735 | 8.216 ± 1.184e-1 |
| 360-732 | 9.991 ± 1.590e-1 | 365-735 | 14.49 ± 1.142e-1 | 370-740 | 7.735 ± 9.914e-2 |
| 360-750 | 9.879 ± 1.880e-1 | 365-767 | 13.33 ± 1.545e-1 | 370-768 | 7.21 ± 1.600e-1 |
| 450-635 | 9.76 ± 1.677e-1 | 437-630 | 14.16 ± 1.170e-1 | 410-665 | 7.953 ± 9.414e-2 |
| 450-660 | 10.57 ± 9.549e-2 | 437-660 | 14.21 ± 1.131e-1 | 410-700 | 8.313 ± 1.667e-1 |
| 450-695 | 10.67 ± 8.082e-2 | 437-695 | 13.15 ± 9.819e-2 | 410-720 | 7.781 ± 1.435e-1 |

| cis-[Pt(pyz)$_2$(mnt)] | | cis-[Pt(4,4`-bpy)$_2$(mnt)] | | cis-[Pt(4-ap)$_2$(mnt)] | |
|---|---|---|---|---|---|
| $\lambda_{ex}/\lambda_{em}$ | LT (μs) | $\lambda_{ex}/\lambda_{em}$ | LT (μs) | $\lambda_{ex}/\lambda_{em}$ | LT (μs) |
| 450-715 | 11.04 ± 1.313e-1 | 437-715 | 13.93 ± 1.256e-1 | 410-735 | 8.127 ± 1.711e-1 |
| 450-732 | 10.89 ± 9.182e-2 | 437-735 | 11.99 ± 1.436e-1 | 410-740 | 7.568 ± 2.068e-1 |
| 450-750 | 10.88 ± 1.419e-1 | 437-767 | 11.97 ± 1.251e-1 | 410-768 | 8.618 ± 4.323e-1 |

**Table 5.8: Comparison of calculated emission energies from the $T_1$ and $T_2$ states and excitation energy from $S_0 \rightarrow T_1$.**

| | $T_1$ (emission in nm) | $T_2$ (emission in nm) | $S_0 \rightarrow T_1$ (nm) |
|---|---|---|---|
| ***1*** | 1311 | 659 | 568 |
| ***2*** | 1080 | 712 | 568 |
| ***3*** | 1027 | 587 | 556 |

The excitation bands correspond to the spin-forbidden direct absorption transition to the $^3$MMLL'CT triplet state of the same $^1$MMLL'CT lower-energy absorption bands (based on band energy). There is a red shift in the absorption or PL excitation bands, that is reproduced computationally (**Table 5.8**), that is consistent with the trend of the $\kappa^1$-*NN* ligands ability to act as a $\pi$-acceptance (trend increases from 4-ap (**3**) < pyz (**1**) < 4,4'-bpy (**2**)), which is consistent with previous work.[21, 22] The presence of only one *N*-heterocyclic nitrogen atom in the aromatic ring, and an electron-donating $NH_2$ group in **3**, renders weaker $\pi$-acceptance and blue-shifted absorption/excitation bands. The addition of a second N-heterocyclic aromatic ring in 4,4'-bpy of **2** expands the $\pi$ conjugation beyond that seen in **1**, leading to **2** having better $\pi$-accepting behavior. Interestingly, however, the emission bands are essentially indifferent to the $\kappa^1$-*NN* ligand identity, i.e. they do not follow the same trend seen in the corresponding absorption/excitation bands. This is a qualitatively different result from that known for Pt(diimine)(dithiolate) complexes, whose emission and absorption energies correlate with one

another. We hypothesize that the steric factor is more significant than the electronic factor for the excited state distortion in **1**-**3** given that two $\kappa^1$-*NN* ligands rearrange more easily than one $\kappa^2$-*NN* ligand bonded as one unit to the Pt(II) center in these [Pt(II)(dithiolate)(diimine)] complexes.

## 5.4 Commentary on Divergent vs Convergent Pt(II)-Diimine Complexes

While this study has focused on divergent Pt(II)-diimine complexes, there are plenty of already known convergent complexes. Computationally, it is easier to achieve more accurate structures for these convergent complexes given the rigid nature of their structure (**Table 5.9**). Due to the rigid nature of this structure, the bond lengths and angles are much closer than those calculated for the divergent ligands. In addition to this rigidity, the N-Pt-N angle is smaller for the convergent complex than the divergent complexes (88.3° and 86.6° for **1** and **3**, respectively vs 79.9°). The bond lengths are similar in the convergent complex to the divergent complexes, with only slight decreases in the Pt-S and Pt-N bond lengths. Additionally, the convergent complexes are completely planar, with the dihedral angle between the imine rings being 0.0° and in the same plane as the mnt ring.

**Table 5.9**: **Select bond lengths, angles and torsion angles for [Pt(2,2'-bpy)(mnt)].**

| Bond Length (Å) | | | Angle (°) | | |
|---|---|---|---|---|---|
| | Experimental | Theoretical | | Experimental | Theoretical |
| *Pt1—S2* | 2.243 | 2.303 | *S1—Pt1—S2* | 89.8 | 89.2 |
| *Pt1—S1* | 2.249 | 2.303 | *N5—Pt1—S1* | 95.8 | 96.1 |
| *Pt1—N5* | 2.047 | 2.101 | *N5—Pt1—S1* | 175.0 | 96.1 |
| *Pt1—N3* | 2.035 | 2.101 | *N3—Pt1—N5* | 79.9 | 78.6 |

| Bond Length (Å) | | | Angle (°) | | |
|---|---|---|---|---|---|
| | Experimental | Theoretical | | Experimental | Theoretical |
| *S1—C2* | 1.734 | 1.756 | *C1—S2—Pt1* | 103.8 | 103.8 |
| *S2—C1* | 1.730 | 1.756 | *C1—C2—S1* | 121.0 | 121.6 |
| *N1—C3* | 1.139 | 1.187 | Torsion Angle (°) | | |
| *C2—C4* | 1.436 | 1.450 | | Experimental | Theoretical |
| *C2—C1* | 1.367 | 1.392 | *PtS2C2—N3 Ring* | 3.59 | 0.00 |
| *C4—N2* | 1.136 | 1.187 | *PtS2C2—N5 Ring* | 2.09 | 0.00 |
| *C3—C1* | 1.431 | 1.450 | *N3Ring—N5 Ring* | 4.51 | 0.00 |

The electron density of the SOMO-1 is localized on the dithiolate ligand for the divergent pyridyl ligands, while for the convergent complex, [Pt(2,2'-bpy)(mnt)], the SOMO-1 is not localized on the dithiolate and has some electron density on the $\kappa^2$-bpy ligand (**Figure 5.13**). The SOMO for the doublet anion for the convergent complex possesses a SOMO that is comparable to that of **3**, where there is some electron density on the mnt ligand but it is mostly localized on the pyridyl ligand. These similarities in the orbital analysis lead to oxidation and reduction potentials that are comparable to those seen for **1**, **2** and **3** (**Table 5.6**).

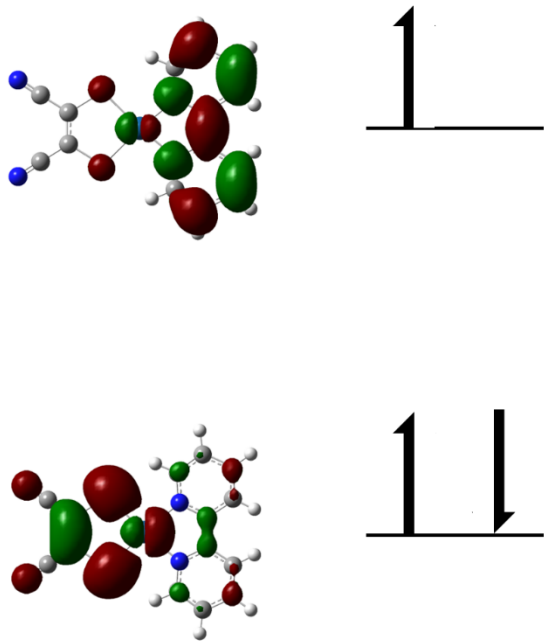

| | Oxidation | | Reduction | |
|---|---|---|---|---|
| | $E^{abs}_{calc}$ (V) | $E^{abs}_{exp.}$ (V) | $E^{abs}_{calc}$ (V) | $E^{abs}_{exp.}$ (V) |
| [Pt(mnt)(bpy)] (in DMF) | 5.39 | 5.76 | 3.49 | 3.29 |

**Figure 5.13: SOMO and SOMO-1 for the convergent [Pt(2,2'-bpy)(mnt)] complex along with experimental oxidation and reduction values taken from ref. 48 and calculated oxidation and reduction potentials.**

Similar to the divergent complexes, the convergent complex exhibits two types of electron transitions in the calculated absorption spectrum. A detailed orbital analysis revealed there to be intraligand charge transfer (π-to-π* transitions that are pyridyl based) as well as MMLL`CT states that involve the transfer of electron density from the Pt(mnt) moiety to the diimine ligand (both types of transitions are depicted below in **Figure 5.13**). These transition types are consistent with previous literature[44] as well as with the characteristics seen for the divergent complexes in both character and the energy range in which the transitions occur.

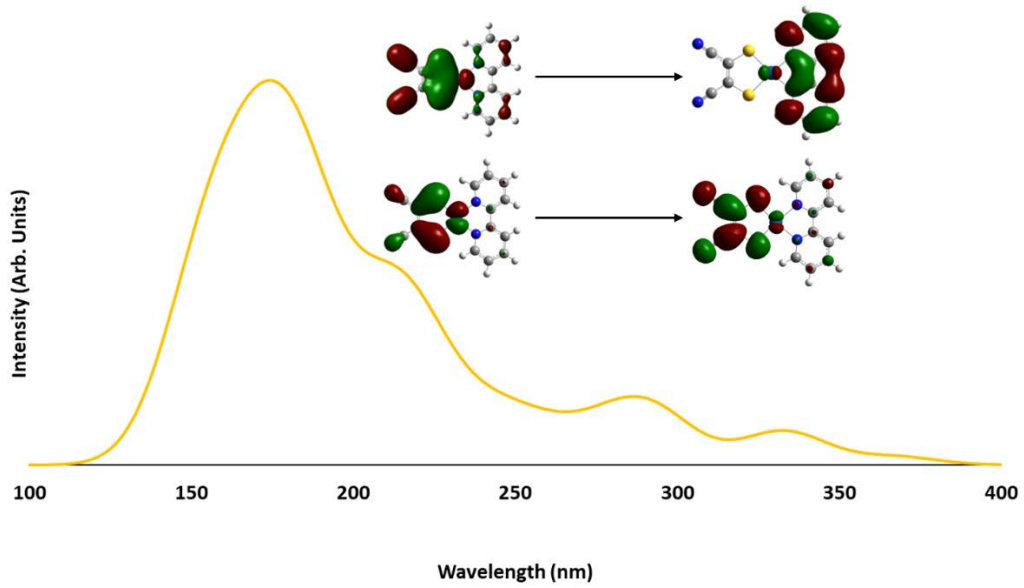


**Figure 5.14: Calculated absorption spectra of [Pt(2,2'-bpy)(mnt)] with orbital contours for the transition with the highest oscillator strength.**

Finally the convergent complex has an emissive state that is similar to the divergent complexes. The convergent complexes emissive state is shown to have the same character of MMLL`CT. The emissive state for the convergent complex is also the $T_2$ instead of the $T_1$. However, the excitation energy is significantly red-shifted from the divergent complexes (749 nm vs around 550 nm for the divergent complexes). However, the $T_2$ emission energy falls in the range of the divergent complex emission energies, being blue-shifted from **1** and **2** (644 vs 659 and 712 respectively) but red-shifted from **3** (587 nm).

## 5.5 Conclusions

A series of neutral Pt($\kappa^1$-*NN*)$_2$(mnt) and ion-paired [Pt($\kappa^1$-*NN*)$_4$][Pt(mnt)$_2$] complexes have been synthesized and characterized for their molecular and electronic structures. Representatives of the former, Pt($\kappa^1$-*NN*)$_2$(mnt) complexes have been found to exhibit luminescence and redox properties akin to those that are characteristic of the diverse

platinum(II) diimine-dithiolate family. This is the case despite having two non-chelating imine ligands as opposed to a chelating diimine such as 2,2'-bpy. The new complexes also exhibit the potential to extend the coordination core by shifting the coordination mode from a $\kappa^1$-monotopic to a $\mu$-bridging mode. As such, these new complexes hold promise as building blocks for supramolecular compounds, MOFs and other coordination polymers with photophysical and/or electrochemical functions.

## 5.6 Acknowledgements

This work was supported by the Welch Foundation (AD-0007, BWS) and (B-1542, MAO) and the U S National Science Foundation (CHE-1413641) (MAO). The SMART-1000 diffractometer was provided by generous donations from Bruker and Austin College. Calculations were completed on a super computer at the University of North Texas supported by the National Science Foundation (CHE-1531468). We are grateful to Dr. Vladimir Nesterov and Prof. Guido Verbeck from the University of North Texas for helpful discussions on X-ray crystallography and MS measurements at the Laboratory of Imaging Mass Spectrometry, respectively.

## 5.7 References

1. Balzani, V.; Bergamini, G.; Marchioni, F.; Ceroni, P. Ru(II)-bipyridine complexes in supramolecular systems, devices and machines. **2006**.

2. Schelter, E. J.; Karadas, F.; Avendano, C.; Prosvirin, A. V.; Wernsdorfer, W.; Dunbar, K. R. A Family of Mixed-Metal Cyanide Cubes with Alternating Octahedral and Tetrahedral Corners Exhibiting a Variety of Magnetic Behaviors Including Single Molecule Magnetism. *J. Am. Chem. Soc.*, **2007**, 129(*26*), 8139-8149.

3. Klosterman, J. K.; Iwamura, M.; Tahara, T.; Fujita, M. Energy Transfer in a Mechanically Trapped Exciplex. *J. Am. Chem. Soc.*, **2009**, 131(*27*), 9478-9479.

4. Sautter, A.; Kaletaş, B. K.; Schmid, D. G.; Dobrawa, R.; Zimine, M.; Jung, G.; van Stokkum, I. H. M.; De Cola, L.; Williams, R. M.; Würthner, F. Ultrafast Energy-Electron Transfer Cascade in a Multichromophoric Light-Harvesting Molecular Square. *J. Am. Chem. Soc.*, **2005**, 127(*18*), 6719-6729.

5. Corma, A.; García, H.; Llabrés i Xamena, F. X. Engineering Metal Organic Frameworks for Heterogeneous Catalysis. *Chem. Rev.*, **2010**, 110(*8*), 4606-4655.

6. Cook, T. R.; Zheng, Y.-R.; Stang, P. J. Metal–Organic Frameworks and Self-Assembled Supramolecular Coordination Complexes: Comparing and Contrasting the Design, Synthesis, and Functionality of Metal–Organic Materials. *Chem. Rev.*, **2013**, 113(*1*), 734-777.

7. Guo, Z.; Kobayashi, T.; Wang, L.-L.; Goh, T. W.; Xiao, C.; Caporini, M. A.; Rosay, M.; Johnson, D. D.; Pruski, M.; Huang, W. Selective Host–Guest Interaction between Metal Ions and Metal–Organic Frameworks Using Dynamic Nuclear Polarization Enhanced Solid-State NMR Spectroscopy. *Chem. - Eur. J.*, **2014**, 20(*49*), 16308-16313.

8. Cui, J.; Xu, Z. An electroactive porous network from covalent metal–dithiolene links. *Chem. Commun.*, **2014**, 50(*30*), 3986-3988.

9. Ghosh, S.; Mukherjee, P. S. Self-Assembly of a Nanoscopic Prism via a New Organometallic $Pt_3$ Acceptor and Its Fluorescent Detection of Nitroaromatics. *Organometallics*, **2008**, 27(*3*), 316-319.

10. Flynn, D. C.; Ramakrishna, G.; Yang, H.-B.; Northrop, B. H.; Stang, P. J.; Goodson, T. Ultrafast Optical Excitations In Supramolecular Metallacycles with Charge Transfer Properties. *J. Am. Chem. Soc.*, **2010**, 132(*4*), 1348-1358.

11. Mauro, M.; Aliprandi, A.; Cebrián, C.; Wang, D.; Kübel, C.; De Cola, L. Self-assembly of a neutral platinum(II) complex into highly emitting microcrystalline fibers through metallophilic interactions. *Chem. Commun.*, **2014**, 50(*55*), 7269-7272.

12. Eisenberg, R.; Gray, H. B. Noninnocence in Metal Complexes: A Dithiolene Dawn. *Inorg. Chem.*, **2011**, 50(*20*), 9741-9751.

13. Espa, D.; Pilia, L.; Makedonas, C.; Marchiò, L.; Mercuri, M. L.; Serpe, A.; Barsella, A.; Fort, A.; Mitsopoulou, C. A.; Deplano, P. Role of the Acceptor in Tuning the Properties of Metal [M(II) = Ni, Pd, Pt] Dithiolato/Dithione (Donor/Acceptor) Second-Order Nonlinear Chromophores: Combined Experimental and Theoretical Studies. *Inorg. Chem.*, **2014**, 53(*2*), 1170-1183.

14. Smucker, B. W.; Hudson, J. M.; Omary, M. A.; Dunbar, K. R. Structural, Magnetic, and Optoelectronic Properties of (Diimine)(dithiolato)platinum(II) and -palladium(II) Complexes and Their Charge-Transfer Adducts with Nitrile Acceptors. *Inorg. Chem.*, **2003**, 42(*15*), 4714-4723.

15. Islam, A.; Sugihara, H.; Hara, K.; Singh, L. P.; Katoh, R.; Yanagida, M.; Takahashi, Y.; Murata, S.; Arakawa, H.; Fujihashi, G. Dye Sensitization of Nanocrystalline Titanium Dioxide with Square Planar Platinum(II) Diimine Dithiolate Complexes. *Inorg. Chem.*, **2001**, 40(*21*), 5371-5380.

16. Browning, C.; Hudson, J. M.; Reinheimer, E. W.; Kuo, F.-L.; McDougald, R. N.; Rabaâ, H.; Pan, H.; Bacsa, J.; Wang, X.; Dunbar, K. R.; Shepherd, N. D.; Omary, M. A. Synthesis, Spectroscopic Properties, and Photoconductivity of Black Absorbers Consisting of Pt(Bipyridine)(Dithiolate) Charge Transfer Complexes in the Presence and Absence of Nitrofluorenone Acceptors. *J. Am. Chem. Soc.*, **2014**, 136(*46*), 16185-16200.

17. Pintus, A.; Aragoni, M. C.; Bellec, N.; Devillanova, F. A.; Lorcy, D.; Isaia, F.; Lippolis, V.; Randall, R. A. M.; Roisnel, T.; Slawin, A. M. Z.; Woollins, J. D.; Arca, M. Structure–Property Relationships in $Pt^{II}$ Diimine-Dithiolate Nonlinear Optical Chromophores Based on Arylethylene-1,2-dithiolate and 2-Thioxothiazoline-4,5-dithiolate. *Eur. J. Inorg. Chem.*, **2012**, 2012(*22*), 3577-3594.

18. Zhang, J.; Du, P.; Schneider, J.; Jarosz, P.; Eisenberg, R. Photogeneration of Hydrogen from Water Using an Integrated System Based on $TiO_2$ and Platinum(II) Diimine Dithiolate Sensitizers. *J. Am. Chem. Soc.*, **2007**, 129(*25*), 7726-7727.

19. Zheng, B.; Sabatini, R. P.; Fu, W.-F.; Eum, M.-S.; Brennessel, W. W.; Wang, L.; McCamant, D. W.; Eisenberg, R. Light-driven generation of hydrogen: New chromophore dyads for increased activity based on Bodipy dye and Pt(diimine)(dithiolate) complexes. *Proc. Natl. Acad. Sci.*, **2015**, 112(*30*), E3987-E3996.

20. Cummings, S. D.; Eisenberg, R. Tuning the Excited-State Properties of Platinum(II) Diimine Dithiolate Complexes. *J. Am. Chem. Soc.*, **1996**, 118(*8*), 1949-1960.

21. Moorcraft, L. P.; Jack, L. A.; Jennings, J. R.; Peter, L. M.; Yellowlees, L. J.; Robertson, N. Synthesis and properties of $[Pt(4\text{-}CO_2CH_3\text{-}py)_2(dmit)]$ and $[Pt(4\text{-}NO_2\text{-}py)_2(mnt)]$: Exploring tunable Pt dyes. *Polyhedron*, **2009**, 28(*18*), 4084-4090.

22. Moorcraft, L. P.; Morandeira, A.; Durrant, J. R.; Jennings, J. R.; Peter, L. M.; Parsons, S.; Turner, A.; Yellowlees, L. J.; Robertson, N. Synthesis and properties of $[Pt(4\text{-}CO_2CH_3\text{-}py)_2(mnt)]$: comparison of pyridyl and bipyridyl-based dyes for solar cells. *Dalton Trans.*, **2008**, *48*), 6940-6947.

23. Derry, P. J.; Wang, X.; Smucker, B. W. Tetra-pyrazine-platinum(II) bis-(tetra-fluoro-borate) acetonitrile hemisolvate. *Acta Crystallogr., Sect. E: Struct. Rep. Online* **2008**. 64(*Pt 11*) m1449.

24. F. Wendt, O.; K. Kaiser, N.-F.; I. Elding, L. Acetonitrile and propionitrile exchange at palladium(II) and platinum(II) †. *J. Chem. Soc., Dalton Trans.*, **1997**, *24*), 4733-4738.

25. Davison, A.; Holm, R. H.; Benson, R. E.; Mahler, W. Metal Complexes Derived from cis-1,2-dicyano-1,2-ethylenedithiolate and Bis(Trifluoromethyl)-1,2-dithiete. Inorganic Syntheses. **1967**. Muetterties, E. L., Mc-GrawHill Inc.

26. Bruker(2007). SAINT. Bruker AXS Inc. Madison, Wisconsin, USA.

27. Bruker(2007). SADABS. Bruker AXS Inc. Madison, Wisconsin, USA.

28. Bruker(2007). XPREP. Bruker AXS Inc. Madison, Wisconsin, USA.

29. Bourhis, L. J.; Dolomanov, O. V.; Gildea, R. J.; Howard, J. A. K.; Puschmann, H. The anatomy of a comprehensive constrained, restrained refinement program for the modern computing environment - Olex2 dissected. *Acta Crystallogr., Sect. A: Found. Crystallogr.*, **2015**, 71(*1*), 59-75.

30. Dolomanov, O. V.; Bourhis, L. J.; Gildea, R. J.; Howard, J. A. K.; Puschmann, H. OLEX2: a complete structure solution, refinement and analysis program. *J. Appl. Crsytallogr.*, **2009**, 42(*2*), 339-341.

31. M. J. Frisch, G. W. T., H. B. Schlegel, G. E. Scuseria, M. A. Robb, J. R. Cheeseman, G. Scalmani, V. Barone, G. A. Petersson, H. Nakatsuji, X. Li, M. Caricato, A. Marenich, J. Bloino, B. G. Janesko, R. Gomperts, B. Mennucci, H. P. Hratchian, J. V. Ortiz, A. F. Izmaylov, J. L. Sonnenberg, D. Williams-Young, F. Ding, F. Lipparini, F. Egidi, J. Goings, B. Peng, A. Petrone, T. Henderson, D. Ranasinghe, V. G. Zakrzewski, J. Gao, N. Rega, G. Zheng, W. Liang, M. Hada, M. Ehara, K. Toyota, R. Fukuda, J. Hasegawa, M. Ishida, T. Nakajima, Y. Honda, O. Kitao, H. Nakai, T. Vreven, K. Throssell, J. A. Montgomery, Jr., J. E. Peralta, F. Ogliaro, M. Bearpark, J. J. Heyd, E. Brothers, K. N. Kudin, V. N. Staroverov, T. Keith, R. Kobayashi, J. Normand, K. Raghavachari, A. Rendell, J. C. Burant, S. S. Iyengar, J. Tomasi, M. Cossi, J. M. Millam, M. Klene, C. Adamo, R. Cammi, J. W. Ochterski, R. L. Martin, K. Morokuma, O. Farkas, J. B. Foresman, and D. J. Fox Gaussian 09 Revision E01. **2016**.Wallingford, CT, USA.

32. Becke, A. D. Density-functional exchange-energy approximation with correct asymptotic behavior. *Physical Review A*, **1988**, 38(*6*), 3098-3100.

33. Miehlich, B.; Savin, A.; Stoll, H.; Preuss, H. Results obtained with the correlation energy density functionals of becke and Lee, Yang and Parr. *Chem. Phys. Lett.*, **1989**, 157(*3*), 200-206.

34. Zhao, Y.; Truhlar, D. G. The M06 suite of density functionals for main group thermochemistry, thermochemical kinetics, noncovalent interactions, excited states, and transition elements: two new functionals and systematic testing of four M06-class functionals and 12 other functionals. *Theor. Chem. Acc.*, **2008**, 120(*1*), 215-241.

35. Cundari, T. R.; Stevens, W. J. Effective core potential methods for the lanthanides. *The Journal of Chemical Physics*, **1993**, 98(*7*), 5555-5565.

36. Stevens, W. J.; Basch, H.; Krauss, M. Compact effective potentials and efficient shared-exponent basis sets for the first- and second-row atoms. *The Journal of Chemical Physics*, **1984**, 81(*12*), 6026-6033.

37. Stevens, W. J.; Krauss, M.; Basch, H.; Jasien, P. G. Relativistic compact effective potentials and efficient, shared-exponent basis sets for the third-, fourth-, and fifth-row atoms. *Canadian Journal of Chemistry*, **1992**, 70(*2*), 612-630.

38. Zheng, Y.-R.; Stang, P. J. Direct and Quantitative Characterization of Dynamic Ligand Exchange between Coordination-Driven Self-Assembled Supramolecular Polygons. *J. Am. Chem. Soc.*, **2009**, 131(*10*), 3487-3489.

39. Willermann, M.; Mulcahy, C.; Sigel, R. K. O.; Cerdà, M. M.; Freisinger, E.; Sanz Miguel, P. J.; Roitzsch, M.; Lippert, B. Pyrazine as a Building Block for Molecular Architectures with $Pt^{II}$. *Inorg. Chem.*, **2006**, 45(*5*), 2093-2099.

40. Melnik, M.; Holloway, C. E. Stereochemistry of platinum coordination compounds. *Coord. Chem. Rev.*, **2006**, 250(*17*), 2261-2270.

41. Adams, C. J.; Fey, N.; Parfitt, M.; Pope, S. J. A.; Weinstein, J. A. Synthesis, structures and properties of a new series of platinum–diimine–dithiolate complexes. *Dalton Trans.*, **2007**, *39*), 4446-4456.

42. Makedonas, C.; Mitsopoulou, C. A.; Lahoz, F. J.; Balana, A. I. Synthesis, Characterization, and Crystal Structure of the Pd(phen)(bdt) Complex. A DFT and TDDFT Study of Its Ground Electronic and Excited States Compared to Those of Analogous Complexes. *Inorg. Chem.*, **2003**, 42(*26*), 8853-8865.

43. Connick, W. B.; Gray, H. B. Photooxidation of Platinum(II) Diimine Dithiolates. *J. Am. Chem. Soc.*, **1997**, 119(*48*), 11620-11627.

44. Bevilacqua, J. M.; Eisenberg, R. Synthesis and Characterization of Luminescent Square-Planar Platinum(II) Complexes Containing Dithiolate or Dithiocarbamate Ligands. *Inorg. Chem.*, **1994**, 33(*13*), 2913-2923.

45. Wei, C. H.; Hingerty, B. E.; Busing, W. R. Structure of tetrakis(pyridine)platinum(II) chloride trihydrate: unconstrained anisotropic least-squares refinement of hydrogen and non-hydrogen atoms from combined X-ray-neutron diffraction data. *Acta Crystallogr., Sect. C: Struct. Chem.*, **1989**, 45(*1*), 26-30.

46. Geary, E. A. M.; Yellowlees, L. J.; Jack, L. A.; Oswald, I. D. H.; Parsons, S.; Hirata, N.; Durrant, J. R.; Robertson, N. Synthesis, Structure, and Properties of [Pt(II)(diimine)(dithiolate)] Dyes with 3,3‘-, 4,4‘-, and 5,5‘-Disubstituted Bipyridyl: Applications in Dye-Sensitized Solar Cells. *Inorg. Chem.*, **2005**, 44(*2*), 242-250.

47. Nesterov, V. N.; Reinheimer, E. W.; Smucker, B. W. (2,2`-Bipyridine)(1,2-dicyanoethene-1,2-dithiolato)platinum(II). *IUCrData*, **2019**, 4 (x190158).

48. Lazarides, T.; McCormick, T. M.; Wilson, K. C.; Lee, S.; McCamant, D. W.; Eisenberg, R. Sensitizing the Sensitizer: The Synthesis and Photophysical Study of Bodipy−Pt(II)(diimine)(dithiolate) Conjugates. *J. Am. Chem. Soc.*, **2011**, 133(*2*), 350-364.

49. Zuleta, J. A.; Bevilacqua, J. M.; Proserpio, D. M.; Harvey, P. D.; Eisenberg, R. Spectroscopic and theoretical studies on the excited state in diimine dithiolate complexes of platinum(II). *Inorg. Chem.*, **1992**, 31(*12*), 2396-2404.

50. Zuleta, J. A.; Burberry, M. S.; Eisenberg, R. Platinum(II) diimine dithiolates. New solution luminescent complexes. *Coordination Chemistry Reviews*, **1990**, 97(47-64.

51. Koopmans, T. Über die Zuordnung von Wellenfunktionen und Eigenwerten zu den Einzelnen Elektronen Eines Atoms. *Physica*, **1934**, 1(*1*), 104-113.

52. Guasch, J.; Grisanti, L.; Souto, M.; Lloveras, V.; Vidal-Gancedo, J.; Ratera, I.; Painelli, A.; Rovira, C.; Veciana, J. Intra- and Intermolecular Charge Transfer in Aggregates of Tetrathiafulvalene-Triphenylmethyl Radical Derivatives in Solution. *J. Am. Chem. Soc.*, **2013**, 135(*18*), 6958-6967.

53. Pap, J. S.; Benedito, F. L.; Bothe, E.; Bill, E.; DeBeer George, S.; Weyhermüller, T.; Wieghardt, K. Dimerization Processes of Square Planar $[Pt^{II}(tbpy)(dithiolato^{\bullet})]^{+}$ Radicals. *Inorg. Chem.*, **2007**, 46(*10*), 4187-4196.

54. Spanggaard, H.; Prehn, J.; Nielsen, M. B.; Levillain, E.; Allain, M.; Becher, J. Multiple-Bridged Bis-Tetrathiafulvalenes: New Synthetic Protocols and Spectroelectrochemical Investigations. *J. Am. Chem. Soc.*, **2000**, 122(*39*), 9486-9494.

55. Spruell, J. M.; Coskun, A.; Friedman, D. C.; Forgan, R. S.; Sarjeant, A. A.; Trabolsi, A.; Fahrenbach, A. C.; Barin, G.; Paxton, W. F.; Dey, S. K.; Olson, M. A.; Benítez, D.; Tkatchouk, E.; Colvin, M. T.; Carmielli, R.; Caldwell, S. T.; Rosair, G. M.; Hewage, S. G.; Duclairoir, F.; Seymour, J. L.; Slawin, A. M. Z.; Goddard Iii, W. A.; Wasielewski, M. R.; Cooke, G.; Stoddart, J. F. Highly stable tetrathiafulvalene radical dimers in [3]catenanes. *Nat. Chem.*, **2010**, 2(870.

56. Zanello, P. Inorganic Electrochemistry. **2003**. The Royal Society of Chemistry.

57. Schindler, J. W.; Adamson, A. W. Emission quenching and photochemistry of aqueous tetracyanoplatinate(2-). *Inorg. Chem.*, **1982**, 21(*12*), 4236-4240.

# CHAPTER 6

# CONCLUSIONS AND FUTURE WORK

## 6.1 Spin-Orbit Splitting in Gold(I) Alkylphosphine Complexes

### 6.1.1 Conclusions

The spin-orbit splitting of $[AuTPA_3]Cl$ and $[AuTPA_3]I$ (where TPA = 1,3,5-triaza-7-phosphaadamntane) have been observed and resolved through the use of cryogenic temperature photoluminescent measurements. The splitting between the spin-orbit microstates has been determined to be about 4500 $cm^{-1}$ for the chloride complex while the splitting is increased to 6500 $cm^{-1}$ upon exchanging the chloride counterion for iodide. This degree of spin-orbit splitting has not been previously reported for any transition metal complex to the knowledge of the author. These complexes are of particular interest due to the fact that the spin-orbit splitting results in emission bands that span the visible light region of the electromagnetic radiation spectrum. These complexes are anticipated to lead to promising applications in the world of light devices, such as organic light emitting diodes (OLEDs).

### 6.1.2 Future Work

The complexes studied have halides as counterions which are known to be non-innocent counterions.[1] Given these counterions, the emission and excitation spectra have been shown to be halide dependent, with the degree of spin-orbit splitting changing depending upon the identity of the counterion. In order to test the spin-orbit splitting of just $[AuL_3]^+$, the halides should be switched with counterions that will not interact with the Au(I) center in the excited state. Examples of these counterions are $PF_6^-$, $BF_4^-$, or $Ph_4B^-$. These counterions have been used

to synthesis gold(I) complexes before but never to study the spin-orbit splitting of gold(I) complexes.

In order to determine the usefulness of these complexes for use in devices, thin film studies would be the next step. The optical band gap of these complexes has been determined via the excitation spectra for the solid materials, which is important for solar cell applications. However, for lighting devices, these materials need to be made into thin films and the electric band gap needs to be determined. The band gaps determined from the electrical band gap will be higher in energy than the optical band gaps.[2] This would require electrical conductivity measurements and can also be determined computationally through solid state calculations or band calculations, which is offered through the ADF package. These methods could be used to determine whether the material acts as a p- or n-type semiconductor and could be used to help determine what type of semiconductor this material would need to be layered with as shown below in **Figure 6.1**.

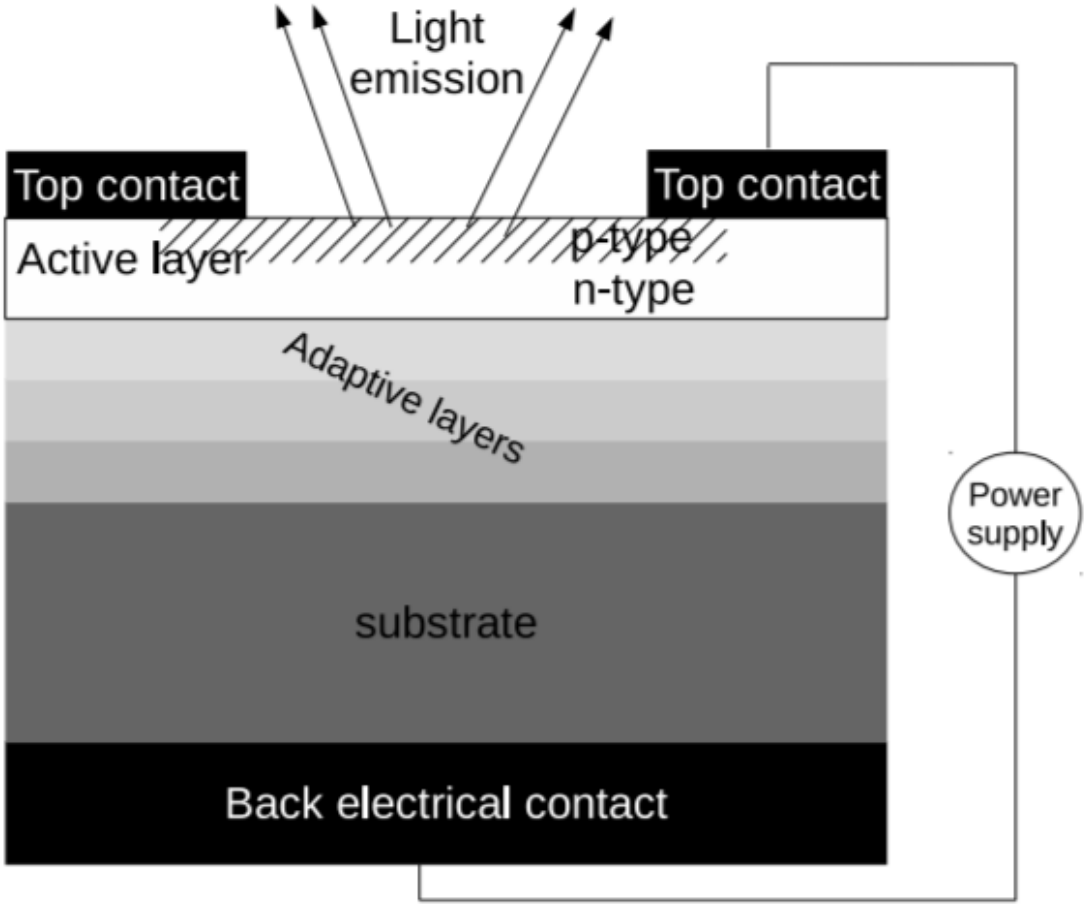


**Figure 6.1: Schematic of a lighting device with the active layer being composed of a p- and n-type semiconductor.[2]**

Another experimental value that will be important for lighting devices is the quantum yield of these complexes which have not been studied. Quantum yield is the measurement of the emitted photons versus absorbed photons. This value gives information on the radiative decay rate (Γ) versus the non-radiative decay rate ($k_{nr}$), leading to a measurement of how effective the material works as a chromophore (**Equation 6.1**). Recently, the synthesis of the first three-coordinate N-heterocyclic carbene complex was synthesized and found to have a high quantum yield.[3] While these complexes demonstrated excitation and emission transition types that are

reliant upon the NHC, they still demonstrated a small degree of metal center excitation and emissions.

$$Q = \frac{\Gamma}{\Gamma + k_{nr}} \qquad \text{Equation 6.1}$$

## 6.2 21st Century Alchemy: Cupriphication of Gold to Sensitize $d^{10}$-$d^{10}$ Metal-Metal Bonds and Near-Unity Phosphorescence Quantum Yields

### 6.2.1 Conclusions

In conclusion, a novel synthesis method for the preparation heterobimetallic $Au_2Cu$, $Cu_2Au$ and stacking complexes is hereby documented and discussed for the first time. Crystallographic, far-IR, and dispersive DFT methods data reinforce the formation of a *bona fide* polar-covalent bond between Cu(I) and Au(I) atoms of the {[$Au_2$(μ-$C^2$,$N^3$-EtIm)$_2$Cu(μ-3,5-($CF_3$)$_2$Pz)]}$c_2$ hexanuclear dimer-of-trimer **4a**, whereas the analogous [$Au_2$(μ-$C^2$,$N^3$-BzIm)$_2$Cu(μ-3,5-($CF_3$)$_2$Pz)] (**1**) and [$Au_2$(μ-$C^2$,$N^3$-MeIm)$_2$Cu(μ-3,5-($CF_3$)$_2$Pz)] (**3a**) species are found to exhibit cupro-aurophilic as opposed to aurophilic or cuprophilic non-covalent metal···metal interactions. The reaction mechanism occurring is not completely understood but it likely proceeds *via* π-acid/π-base interactions - a well-known chemistry for this type of complexes. The reduced symmetry in the $Au_2Cu$ compounds has been demonstrated to attain greater extinction coefficient in solution and higher solid-state photoluminescence quantum yield than those for the homometallic complexes, indeed approaching unity for **3a** and **4a**, which opens promising applications of such materials in OLEDs as light-emitting layers and/or inorganic LEDs as down-conversion phosphors.

### 6.2.2 Future Work

While this complex has been studied extensively to determine the bonding character in the ground state, the excited state properties of this complex remain to be studied. Given the small distance between the Au and Cu centers, it is unlikely this bond will shorten or strengthen in the excited state. It is more likely that in the excited state there will be an elongation of this bond and while the ground state is accurately described by a hexanuclear complex, the excited state maybe a dodecanuclear complex. The complexity involved with these calculations are related purely to the size of the molecules and the approach of having all 12 metal centers involved in the calculations.

The calculations in this chapter focused on the gas phase and as such have neglected the effects of the solid state packing. For the ground state, this was determined to ne a non-issue given the crystal structure shows each hexanuclear dimer as a separate unit, but given the hypothesis of the excited state, these same approximations may not be appropriate. Solvation issues are not as big a factor for this complex given the fact that the study focused on the solid state properties. This complex also exhibited high quantum yield, which led to thin film studies that show this material to be promising for lighting devices. However, the electrical bandgap has not been determined for this complex, and so electrical conductivity studies are needed to justify the use of this complex as a semiconductor.

Looking forward to other complexes, this work has opened the door for the studying of closed shell metals to possess metal-metal bonds. This work was pre-dated by the discovery of a Pt-Au dative bond[4] which also opens the door to study metal-only lewis pairs. Current work in the field has led to the discovery of dative interactions between Lewis base complexes of Fe(0),

Ru(0), Pt(0) and the Lewis acid of Ag(I).[5-7] To further this work, a more extensive study needs to be undertaken of complexes containing a combination of π-acceptor ligands (such as CO, CN, phosphines, carbenes, etc.) and σ-donor ligands, starting by modeling known complexes.

## 6.3 Oxidative Addition of Haloacids and Dihalogens to Trinuclear Cyclic Coinage Metal Complexes and Photoinduced Reductive Elimination of $X_2$ and $H_2$

### 6.3.1 Conclusions

Oxidative addition reactions of cyclic trinuclear complexes with dihalogens has been a field of interest since 1977 starting with the work done by Balch. The use of these compounds to produce hydrogen gas has not been studied previously to the authors knowledge. This work shows the expected trends in oxidative addition, with the more π-basic trimers resulting in more favorable oxidative additions, and the expected energetics of reductive elimination of hydrogen gas and dihalogen gas when the substrates are the asymmetric hydrohalic acids. Time-dependent DFT results show the possibility of UV light to be used as a trigger to produce hydrogen gas through the transfer of electron density from the Au(III) centers of the adduct to the hydrogen bond. The most promising results are for the combination of the AuIm trimer with either HBr or HI, given the strongly allowed transitions, indicated by large oscillator strengths. For both of these acids, there is a red-shifting of the absorption energy leading to the elimination of the hydrogen gas, compared to the other trimers. The major transitions for these complexes are comprised completely with these Au(III) to hydrogen charge transfer states, while other complex and acid combinations also lead to other metal to ligand charge transfer states involving the halogens as well as the bridging ligands. This work demonstrates the possibility of the use of UV light to add

the production of hydrogen gas through the utilization of oxidative addition reactions of cyclic trinuclear gold(I) complexes.

### 6.3.2 Future Work

While these trinuclear complexes have been studied experimentally,[8-12] the experimental work has focused on the oxidative addition of dihalogens to the gold containing complexes. The experimental work has focused on the oxidative addition being carried out in chloroform As far as the author is aware, there has been no work for conducted on addition of the hydrohalic acids, let alone the photoinduced reductive elimination of either substrate. Most of the studied trimers can be substituted to increase the solubility of the trimers in water, which would be necessary for the addition of the hydrohalic acids.

Another point for these complexes is that the overall thermochemistry supports previously hypothesized reaction pathways[13] but the complexes transition barriers have not been investigated. The main goal of this work was to hypothesize whether hydrogen gas production could occur from these complexes with asymmetrical substrates. Since this hypothesis has been shown to be a reasonable assumption from the thermochemical data, a thermodynamic or kinetic study should be completed for these complexes. This would include the calculation of transition state barriers for both the supposed $S_N2$ and $S_N1$ reaction pathways expected for the dihalogens and hydrohalic acids, respectively.

For these complexes to be used in devices for hydrogen gas production, they must retain reactivity when made into thin films. While there has been ridgidochromatic shifting seen for Au(I) complexes upon thin film development[14-18] and there have been studies on the electrical

conductivity of these trimers when developed into thin films[19] but the reactivity of these molecules for oxidative addition reactions has not been undertaken to the knowledge of the author.

Another note is that these calculations have been completed on the monomer of trimers and in the gas phase, which has excluded the effects of the extended chain structure seen in the experimental crystal structure, as well as neglected the solvent interactions that may occur between the substrates and the solvent. Although the implicit solvation method would apply the desired electric field, the fact that the some of the substrates may have hydrogen bond interactions may point to the need for either a combination of explicit and implicit solvation techniques or the use of just the explicit solvation model. The solvents to study would be water given that hydrohalic acids are aqueous solutions, but may need to be extended to include the solvents the trimers are soluble in, such as chloroform for the AuCb trimer[9] as well as benzene, toluene or pyridine for the AuPz trimers[12, 20, 21] and dichloromethane for AuIm.[22, 23] Recent work in the Omary group has led to the solubility of certain AuTz complexes being soluble in water, opening the door for the trimer with successful heavy metal sensing also a candidate for hydrogen gas production. In order for the oxidative addition reactions to take place, there must be a disruption of the aurophilic interactions seen for these complexes. While this has been seen experimentally[12] the energetics of this process have not been studied computationally.

## 6.4 Luminescent, Redox-Active (Dithiolato)Bis(Imine)Platinum(II) Divergent Complexes With Exchangeable Imine Ligands: An Experimental/Computational Study Versus Their (Diimine)(Dithiolato)Platinum(II) Convergent Congeners

### 6.4.1 Conclusions

A series of neutral Pt($\kappa^1$-*NN*)$_2$(mnt) and ion-paired [Pt($\kappa^1$-*NN*)$_4$][Pt(mnt)$_2$] complexes have been synthesized and characterized for their molecular and electronic structures. Representatives of the former, Pt($\kappa^1$-*NN*)$_2$(mnt) complexes have been found to exhibit luminescence and redox properties akin to those that are characteristic of the diverse platinum(II) diimine-dithiolate family. This is the case despite having two non-chelating imine ligands as opposed to a chelating diimine such as 2,2'-bpy. The new complexes also exhibit the potential to extend the coordination core by shifting the coordination mode from a $\kappa^1$-monotopic to a $\mu$-bridging mode. As such, these new complexes hold promise as building blocks for supramolecular compounds, MOFs and other coordination polymers with photophysical and/or electrochemical functions.

### 6.4.2 Future Work

As discussed, the monotopic ligands studied in this work allow for these complexes to be used as building blocks for supramolecular compounds such as MOFs and other coordination polymers. This work has already led to production of some Pt based MOF materials[24, 25] as well as Pt(POP) based materials.[26]

MOFs are of particular interest given their porous nature which allows for them to be used for gas storage and transportation. MOFs are specifically analyzed based on their ability to absorb gas into their pores and can even be used to absorb oils and contaminates to clean spills and to clean fracking water. Recent studies in the Omary lab have led to the discovery of the

ability of MOFs to clean fracking water which offers environmental applications as well as industrial applications.

## 6.5 References


1. Barakat, K. A.; Cundari, T. R.; Omary, M. A. Jahn−Teller distortion in the phosphorescent excited state of three-coordinate Au(I) phosphine complexes. *J. Am. Chem. Soc.*, **2003**, 125(*47*), 14228-14229.

2. Petit, M.; Michez, L.; Raimundo, J.-M.; Dumas, P. Electrical and optical measurements of the bandgap energy of a light-emitting diode. *Phys. Ed.*, **2016**, 51(*2*), 025003.

3. Visbal, R.; Ospino, I.; López-de-Luzuriaga, J. M.; Laguna, A.; Gimeno, M. C. N-Heterocyclic carbene ligands as modulators of luminescence in three-coordinate gold(I) complexes with spectacular quantum yields. *J. Am. Chem. Soc.*, **2013**, 135(*12*), 4712-4715.

4. Baya, M.; Belío, Ú.; Fernández, I.; Fuertes, S.; Martín, A. Unusual metal–metal bonding in a dinuclear Pt–Au complex: snapshot of a transmetalation process. *Angew. Chem. Int. Ed.*, **2016**, 55(*24*), 6978-6982.

5. Yamaguchi, T.; Yamazaki, F.; Ito, T. A helical metal−metal bonded chain via the Pt→Ag dative bond. *J. Am. Chem. Soc.*, **2001**, 123(*4*), 743-744.

6. Braunschweig, H.; Dewhurst, R. D.; Hupp, F.; Kaufmann, C.; Phukan, A. K.; Schneider, C.; Ye, Q. Gauging metal Lewis basicity of zerovalent iron complexes via metal-only Lewis pairs. *Chem. Science*, **2014**, 5(*10*), 4099-4104.

7. Braunschweig, H.; Brunecker, C.; Dewhurst, R. D.; Schneider, C.; Wennemann, B. Lewis Acid binding and transfer as a versatile experimental gauge of the Lewis basicity of $Fe^0$, $Ru^0$, and $Pt^0$ complexes. *Chem. - Eur. J.*, **2015**, 21(*52*), 19195-19201.

8. White-Morris, R. L.; Olmstead, M. M.; Attar, S.; Balch, A. L. Intermolecular interactions in polymorphs of trinuclear gold(I) complexes: Insight into the solvoluminescence of $AuI_3(MeNCOMe)_3$. *Inorg. Chem.*, **2005**, 44(*14*), 5021-5029.

9. Balch, A. L.; Doonan, D. J. Mixed valence gold chemistry: Stepwise oxidation of a cyclic trigold(I) complex. *J. Organomet. Chem.*, **1977**, 131(*1*), 137-146.

10. Balch, A. L.; Nagle, J. K.; Oram, D. E.; Reedy, P. E. Oxidative additions and luminescence involving iridium-gold-iridium chains formed by binding of gold(I) to the metallamacrocycle $Ir_2Cl_2(CO)_2[\mu\text{-}Ph_2PCH_2As(Ph)CH_2PPh_2]_2$. *J. Am. Chem. Soc.*, **1988**, 110(*2*), 454-462.

11. Vickery, J. C.; Olmstead, M. M.; Fung, E. Y.; Balch, A. L. Solvent-stimulated luminescence from the supramolecular aggregation of a trinuclear gold(I) complex that displays extensive intermolecular Au̇Au interactions. *Angew. Chem., Int. Ed.*, **1997**, 36(*11*), 1179-1181.

12. Vickery, J. C.; Balch, A. L. X-ray crystallographic studies of the products of oxidative additions of iodine to cyclic trinuclear gold(I) complexes: Directional effects for Au−I···I−Au interactions. *Inorg. Chem.*, **1997**, 36(*26*), 5978-5983.

13. Teets, T. S.; Nocera, D. G. Photocatalytic hydrogen production. *Chem. Commun.*, **2011**, 47(*33*), 9268-9274.

14. Donamaría, R.; Gimeno, M. C.; Lippolis, V.; López-de-Luzuriaga, J. M.; Monge, M.; Olmos, M. E. Tuning the luminescent properties of a Ag/Au tetranuclear complex featuring metallophilic interactions via solvent-dependent structural isomerization. *Inorg. Chem.*, **2016**, 55(*21*), 11299-11310.

15. Fernández, E. J.; López-de-Luzuriaga, J. M.; Olmos, M. E.; Pérez, J.; Laguna, A.; Lagunas, M. C. A family of Au−Tl loosely bound butterfly clusters. *Inorg. Chem.*, **2005**, 44(*17*), 6012-6018.

16. Fernández, E. J.; Laguna, A.; López-de-Luzuriaga, J. M. Luminescence in complexes with Au(I)-Tl(I) interactions. *Coord. Chem. Rev.*, **2005**, 249(*13-14*), 1423-1433.

17. Rawashdeh-Omary, M. A. Remarkable alteration of photophysical properties of cyclic trinuclear complexes of monovalent coinage metals upon interactions with small organic molecules *Comments Inorg. Chem.*, **2012**, 33(*3-4*), 88-101.

18. Zhang, X.; Li, B.; Chen, Z.-H.; Chen, Z.-N. Luminescence vapochromism in solid materials based on metal complexes for detection of volatile organic compounds (VOCs). *J. Mater. Chem.*, **2012**, 22(*23*), 11427-11441.

19. McDougald, R. N.; Chilukuri, B.; Jia, H.; Perez, M. R.; Rabaâ, H.; Wang, X.; Nesterov, V. N.; Cundari, T. R.; Gnade, B. E.; Omary, M. A. Molecular and electronic structure of cyclic trinuclear gold(I) carbeniate complexes: Insights for structure/luminescence/conductivity relationships. *Inorg. Chem.*, **2014**, 53(*14*), 7485-7499.

20. Minghetti, G.; Banditelli, G.; Bonati, F. Metal derivatives of azoles. 3. The pyrazolato anion (and homologs) as a mono- or bidentate ligand: Preparation and reactivity of tri-, bi-, and mononuclear gold(I) derivatives. *Inorg. Chem.*, **1979**, 18(*3*), 658-663.

21. Raptis, R. G.; Murray, H. H.; Fackler, J. P., Jnr The structure of [Au-[μ]-{3,5-$(C_6H_5)_2C_3HN_2$}]$_3Cl_2$: A trinuclear mixed-valence gold pyrazolate complex. *Acta Crystallogr., Sect. C: Struct. Chem.*, **1988**, 44(*6*), 970-973.

22. Bonati, F.; Burini, A.; Rosa Pietroni, B.; Bovio, B. Reactions of symmetric C-imidazolylgold(I) leading to Au1 carbene complexes or mixed valence or AuIII imidazolyl derivatives. Crystal structure of [1-benzyl-3-(carboethoxy)imidazolin-2-yliden]chlorogold(I). *J. Organomet. Chem.*, **1991**, 408(*2*), 271-280.

23. Bovio, B.; Burini, A.; Pietroni, B. R. Reactions of trimeric 1-benzyl-2-gold(I)imidazole leading to AuI carbene complexes. Crystal structure of [1-benzyl-3-benzoyl-imidazolin-2-yliden]chlorogold(I). *J. Organomet. Chem.*, **1993**, 452(*1*), 287-291.

24. Braglia, L.; Borfecchia, E.; Martini, A.; Bugaev, A. L.; Soldatov, A. V.; Øien-Ødegaard, S.; Lønstad-Bleken, B. T.; Olsbye, U.; Lillerud, K. P.; Lomachenko, K. A.; Agostini, G.; Manzoli, M.; Lamberti, C. The duality of UiO-67-Pt MOFs: Connecting treatment conditions and encapsulated Pt species by operando XAS. *Phys. Chem. Chem. Phys.*, **2017**, 19(*40*), 27489-27507.

25. Szeto, K. C.; Lillerud, K. P.; Tilset, M.; Bjørgen, M.; Prestipino, C.; Zecchina, A.; Lamberti, C.; Bordiga, S. A thermally stable Pt/Y-based metal−organic framework: Exploring the accessibility of the metal centers with spectroscopic methods using $H_2O$, $CH_3OH$, and $CH_3CN$ as probes. *J. Phys. Chem. B*, **2006**, 110(*43*), 21509-21520.

26. Zheng, X.; Wang, L.; Pei, Q.; He, S.; Liu, S.; Xie, Z. Metal–organic framework@porous organic polymer nanocomposite for photodynamic therapy. *Chem. Mater.*, **2017**, 29(*5*), 2374-2381.